Creep properties of cementitious materials : effect of water and microstructure : An approach by microindentation

Qing Zhang

Thèse de Doctorat
Université Paris-Est

École Doctorale: SIE
Discipline: Matériaux et Structures

Présentée par
Qing ZHANG

Propriétés mécaniques des matériaux cimentaires: effet de l'eau et de la microstructure, une approche par microindentation

Soutenue publiquement à l'École des Ponts ParisTech
le 13 Févier, 2014

James J. BEAUDOIN	Professeur, University of Ottawa	Rapporteur
Bernhard PICHLER	Professeur, TU Vienna	Rapporteur
Jean-Noël ROUX	ICPEF, IFSTTAR	Directeur de thèse
Matthieu VANDAMME	IPEF, École des Ponts ParisTech	Examinateur
Ellis GARTNER	Docteur, Lafarge	Examinateur
Bruno ZUBER	Docteur, Lafarge	Examinateur

Laboratoire Navier
École des Ponts ParisTech
77455 Champs-sur-Marne

I would like to dedicate this thesis to my loving parents ...

Acknowledgements

I thank my supervisors Dr. Matthieu Vandamme, Dr. Ellis Gartner, Dr. Bruno Zuber and Dr. Jean-Nöel Roux for their guidances in the PhD research project.

I thank my family and my friends for their continuous supports, especially during my three years' doctoral studies.

Many thanks to various supports (including funding) from Lafarge Research Center. Thank Gilles Chanvillard, Pipat Termkhajornkit, Jeffrey Chen, Rémi Barbarulo, QuocHuy Vu, Arnaud Delaplce, Gabriel Pham and Bruno Huet for their fruitful advices and for those interesting discussions on the thesis. I thank my lovely colleagues: Hervé Noyalet, Fabienne Begaud, Sandrine Brun, Sylvette Chiale, Catherine Bouillon, Karine Jacquemet, Marc Fouilhe, Sara Scapol, Françoise Tardy and Agnès Monier for their helps, supports and for the good moments that we passed together.

Creep properties of cementitious materials: effect of water and microstructure. An approach by microindentation

Abstract

Cementitious materials such as concrete, cement and gypsum are widely used in construction, as the raw materials of which they are made are abundant on Earth. Such trend is unlikely to change in the coming decades. But these materials suffer from creep. The creep of cementitious materials is a complex issue. On one hand, in cementitious materials creep is often coupled with other phenomena such as drying, hydration and cracking, and can be influenced by various parameters such as temperature, level of stress, water content and mix design. On the other hand, measuring creep by traditional macroscopic creep testing is time-consuming (creep test on concrete is recommended to be carried out over several months in order to provide a reliable characterization of long-term creep) and tedious, since experimental parameters need to be well controlled over extensive periods of time.

This thesis studied microindentation at the scale of cement paste or gypsum plaster for the assessment of long-term basic creep properties of cementitious materials, by comparing creep functions obtained by minutes-long microindentation testing with those obtained with macroscopic creep experiments which lasted up to years. For cement paste, the comparison was made at the scale of concrete with the aid of upscaling tools. The study validated that minutes-long microindentation testing can provide a measurement of the long-term creep properties of cementitious materials.

With the validated indentation technique, we studied the effect of microstructure (i.e., the distribution and the spatial organization of

phases) and of water on long-term basic creep of cementitious materials. The effect of microstructure was studied on materials such as C_3S pastes and C_2S pastes as well as on compacts of synthetic C-S-H, portlandite (CH) and their mixtures prepared by compaction of powders. For all samples considered, we identified the right micromechanical model that allows predicting the results. The choice of micromechanical model was consistent with microstructural observations.

The effect of relative humidity was studied by conditioning and testing some of those materials (i.e., C_3S paste, compact of C-S-H, and compact of CH) in various relative humidities ranging from 11% to 94%. Relative humidity had a significant effect on creep: for all materials tested, a greater humidity led to a greater creep. The compact of portlandite was the most sensitive to relative humidity, probably because creep occurs at interfaces between portlandite crystals. For C_3S paste, a linear relation was identified between long-term creep properties and water content at relative humidities ranging from 11% to 75%.

Finally, we proposed micromechanical models that allow predicting long-term basic creep properties of cementitious materials with a wide range of volume fraction of crystalline phase and over a wide range of relative humidities.

Keywords: creep, cementitious materials, microindentation, microstructure, relative humidity

Propriétés mécaniques des matériaux cimentaires: effet de l'eau et de la microstructure, une approche par microindentation

Résumé

Les matériaux cimentaires tels que le béton, le ciment et le plâtre sont largement utilisés dans la construction, les matières premières dont ils sont faits étant abondantes sur Terre. Cette tendance ne devrait pas changer dans les prochaines décennies. Mais ces matériaux subissent l'impact du fluage. Le fluage des matériaux cimentaires est une problématique complexe. D'une part, dans les matériaux cimentaires, le fluage est souvent couplé avec d'autres phénomènes tels que le séchage, l'hydratation et la fissuration, et peut être influencé par différents paramètres comme la température, le niveau de contrainte, la teneur en eau et la formulation. D'autre part, la mesure du fluage par un test macroscopique traditionnelle du fluage requiert du temps (il est recommandé de réaliser l'essai de fluage du béton sur plusieurs mois afin de donner une caractérisation fiable du fluage à long terme) et s'avère fastidieuse, puisque les paramètres expérimentaux doivent être bien contrôlés sur de longues périodes de temps.

Cette thèse étudie la microindentation à l'échelle de la pâte de ciment ou du plâtre pour évaluer les propriétés de fluage propre à long terme des matériaux cimentaires, en comparant les fonctions de fluage obtenues par des tests de microindentation de quelques minutes avec celles obtenues par des expériences macroscopiques de fluage réalisées pendant de longues années. Pour la pâte de ciment, la comparaison a été faite à l'échelle du béton à l'aide d'une certaine homogénéisation. L'étude a validé le fait que un test de microinden-

tation de quelques minutes peut fournir une mesure des propriétés à long terme de matériaux cimentaires.

Une fois validée la technique d'indentation, nous avons étudié l'effet de la microstructure (c'est-à-dire la distribution des phases) et celui de l'eau sur le fluage propre à long terme des matériaux cimentaires. L'effet de la microstructure a été étudiée sur des matériaux tels que des pâtes de C_3S et de C_2S ainsi que sur des compacts de C-S-H synthétique, de portlandite (CH) et leurs mélanges préparés par compression de poudres. Une attention particulière a été consacrée à créer des compacts avec de grandes fractions volumiques de phase cristalline. Pour tous les échantillons examinés, nous avons identifié le bon modèle micromécanique qui permette de prédire les résultats. Le choix du modèle micromécanique concorde avec les observations microstructurales.

L'effet de l'humidité relative a été étudié par le conditionnement et l'indentation de certains de ces matériaux (par exemple la pâte de C_3S, de compact de C-S-H et de compact de CH) dans différents humidité relative allant de 11% à 94%. L'humidité relative a eu un effet significatif sur le fluage : pour tous les matériaux testés, une plus grande humidité a conduit à un fluage plus important. Le compact de portlandite fut le plus sensible à l'humidité relative, sans doute parce que le fluage se produit au niveau des interfaces entre les cristaux de portlandite. Pour la pâte de C_3S, une relation simple a été identifiée entre les propriétés de fluage à long terme et la teneur en eau.

Enfin, nous avons proposé des modèles micromécaniques qui permettent la prédiction des propriétés de fluage à long terme de matériaux cimentaires avec une large gamme de fraction volumique de phase cristalline et sur une gamme d'humidités relatives étendue.

Mots clés: fluage, matériaux cimentaires, microindentation, microstructure, humidité relative

Propriétés mécaniques des matériaux cimentaires: effet de l'eau et de la microstructure, une approche par microindentation

Résumé long

Les matériaux cimentaires sont largement utilisés dans la construction, les matières premières dont ils sont faits étant abondantes sur Terre. Cette tendance ne devrait pas changer dans les prochaines décennies. Mais ces matériaux subissent l'impact du fluage. Le fluage des matériaux cimentaires est une problématique complexe. D'une part, dans les matériaux cimentaires, le fluage est souvent couplé avec d'autres phénomènes tels que le séchage, l'hydratation et la fissuration, et peut être influencé par différents paramètres comme la température, le niveau de contrainte, la teneur en eau et la formulation. D'autre part, la mesure du fluage par un test macroscopique traditionnelle du fluage requiert du temps (il est recommandé de réaliser l'essai de fluage du béton sur plusieurs mois afin de donner une caractérisation fiable du fluage à long terme) et s'avère fastidieuse, puisque les paramètres expérimentaux doivent être bien contrôlés sur de longues périodes de temps.

Initié par Lafarge Centre de Recherche et Laboratoire Navier à École des Ponts ParisTech , le projet de recherche vise les objectifs suivants . Tout d'abord, le projet vise à trouver une réponse claire sur la validité des tests de fluage indentation pour la mesure des propriétés de fluage sur des matériaux cimentaires. Le deuxième objectif est de mieux comprendre le fluage des matériaux cimentaires. Deux sous-objectifs sont identifiés. Dans ciment Portland, de deux types distincts de composants existent : composant amorphe tel que le silicate de calcium hydraté, c'est à dire, C-S-H, et des composants cristallins tels que

portlandite et particules de clinker non hydraté. La microstructure des matériaux à base de ciment peut être caractérisée par la proportion de ces composants et de leur organisation spatiale. Le premier objectif est d'étudier par l'effet de la microstructure, à savoir la distribution de proportion et de l'organisation spatiale des minéraux, sur le fluage de base à long terme des matériaux cimentaires. Bien que certaines études ont montré que la teneur en eau a un effet sur les propriétés de fluage des matériaux cimentaires, avec les données disponibles dans la littérature, l'influence de la quantité d'eau sur base de longue durée propriétés de fluage des matériaux cimentaires n'est pas claire. Ainsi, le second objectif est d'étudier l'effet de l'eau sur le fluage propre à long terme.

La thèse se compose de quatre parties. La première partie est une introduction qui présente le contexte de la recherche (chapitre 1) et une revue de la littérature sur les tests de fluage (chapitre 2). A partir de l'analyse d'indentation (chapitre 3), la partie II traite de la validation de l'indentation pour la mesure de fluage sur divers matériaux à base de ciment, à savoir, la pâte de ciment (chapitre 4) et plâtre (chapitre 5). Une fois la technique des tests de pénétration est validée, la partie III se concentre sur la caractérisation de la façon dont à long terme des propriétés de fluage de base de matériaux cimentaires sont influencés par la microstructure et de l'eau. L'effet de la microstructure est examinée en consultant les matériaux obtenus par hydratation , tels que C_3S et C_2 pâtes (chapitre 6) et par compactage de poudre, c'est-à-compacts (chapitre 7). L'effet de l'eau est étudiée sur les pâtes et les pactes qui ont atteint l'équilibre hygral avec des humidités relatives différentes (chapitre 8). La partie III se termine par le chapitre 9, dans lequel nous utilisons l'approche micromécanique pour construire des modèles qui permettent de prédire à long terme des propriétés de fluage de base de matériaux cimentaires en fonction de la microstructure et de l'humidité relative. Les modèles sont validés par des résultats expérimentaux. Partie IV est un déterminant dont nous présentons les principaux résultats, les contributions, les limites et perspectives (chapitre 10).

La thèse commence par un résumé général du projet de recherche (chapitre 1). Le chapitre démarre par une introduction au problème traité par le sujet de recherche, c'est-à-dire le fluage des matériaux cimentaires. L'introduction est suivie ensuite par les objectifs de recherche ainsi que les bénéfices scientifiques et industriels. Le chapitre se termine par un aperçu de la thèse.

Le chapitre 2 présente une revue de la littérature sur les matériaux cimentaires et leur fluage. Les matériaux cimentaires sont des matériaux multi-échelles et poreux. Dès lors, le fluage de ces matériaux intervient à différentes échelles et peut être largement influencé par la présence d'eau en porosité. Les effets liés au changement d'humidité, à la teneur en eau, à la température, au niveau de contrainte et à la formulation sur le fluage des matériaux cimentaires ont été examinés sur la base d'études récentes. L'origine du fluage des matériaux cimentaires est probablement due à une combinaison de mécanismes. Le comportement du fluage des matériaux cimentaires à court et long terme est contrôlé par différentes cinétiques et peut être causé par différents mécanismes. Pour la prédiction du fluage, un regard a été porté sur les modèles les plus répandus.

Le chapitre 3 est dédié à la présentation de la technique d'indentation. Nous commençons par présenter un test d'indentation typique et l'appareil d'indentation utilisé dans l'étude. Puis nous présentons l'analyse pour évaluer le module d'indentation M et la dureté d'indentation H issus d'un test d'indentation. Enfin, nous élargissons l'analyse aux calculs des propriétés de fluage à partir d'un test d'indentation.

Le chapitre 4 est consacré à comparer des tests de fluage par microindentation de quelques minutes sur de la pâte de ciment avec des tests de fluage macroscopique de plusieurs années sur le béton d'une part et de plusieurs mois sur la pâte de ciment d'autre part (toutes les tests de fluage macroscopique par compression uniaxiale ont été réalisés par Le Roy [1996]. Pour l'ensemble de ces tests, après une période transitoire, la fonction de fluage a été décrite de façon satisfaisante par une fonction logarithmique du temps. Les périodes transitoires

non logarithmiques ont duré plusieurs jours à l'échelle macroscopique, mais seulement quelques secondes à l'échelle de la microindentation. Les modules de fluage (qui définissent donc le taux de fluage logarithmique à long terme) des échantillons de béton ont été estimés à partir de la microindentation réalisée à l'échelle des pâtes de ciment en combinaison avec des modèles micromécaniques. Ces estimations se sont révélées être proportionnelles au module de fluage mesuré sur les échantillons de béton par des tests de macroscopie uni axiale usuelle, montrant ainsi que la microindentation de quelques minutes peut permettre de mesurer les propriétés de fluage à long terme des matériaux cimentaires.

Le chapitre 5 s'intéresse à comparer des tests de fluage par microindentation de quelques minutes avec des tests de fluage par macroscopie de plusieurs jours, c'est-à-dire des test de fluage par flexion sur du plâtre – un matériau cimentaire cristallin. Une partie de ces tests de fluage par flexion a été conduite par Pachon-Rodriguez [2011]. Les fonctions de fluage propre spécifique ont été mesurées à la fois par microindentation et par flexion. Qualitativement, des tendances comparables ont été obtenues avec ces deux types des tets. Quantitativement, pour toutes les tests par indentation, après une période transitoire, la fonction de fluage propre spécifique était bien décrite par une fonction logarithmique du temps. Comme ce qui a été fait au chapitre 4, nous retenons le module de fluage C_i et le temps caractéristique par indentation τ_i pour caractériser la fonction de fluage. Les fonctions de fluage propre spécifique obtenues pas flexion n'ont jamais été des fonctions logarithmiques du temps. En revanche, ces fonctions de fluage ont été bien décrites par la somme d'une fonction logarithmique du temps et d'une fonction linéaire. La fonction logarithmique a été caractérisée par un module de fluage en flexion et un temps caractéristique en flexion. Pour la plupart des échantillons, les modules de fluage du plâtre mesurés par indentation ont été pratiquement (soit 4 échantillons sur 6) en parfaite concordance avec les modules de fluage en flexion mesurés par flexion, ce qui prouve que l'indentation est une technique validée pour caractériser les propriétés de fluage des

matériaux cimentaires. Par contre et comme cela a été le cas avec le ciment Portland, le temps caractéristique requis pour atteindre la cinétique de fluage logarithmique s'est avéré bien inférieur par indentation que par flexion, ce qui montre que l'indentation de quelques minutes permet d'obtenir rapidement la cinétique logarithmique des matériaux cimentaires. La partie non logarithmique du fluage propre spécifique du plâtre observé par test de flexion est probablement due au fait que, durant le text de flexion, une partie de l'échantillon est en tension.

Après avoir validé la technique d'indentation pour la mesure de fluage sur des matériaux cimentaire, dans le chapitre 6, nous appliquons cette technique pour étudier les propriétés de fluage des matériaux cimentaires. Les propriétés mécaniques telles que le module de Young E, la dureté d'indentation H ainsi que les propriétés de fluage, à savoir le module de fluage C_i et le temps caractéristique τ_i sur des pâtes C_3S et C_2S, ont été obtenues par microindentation. La microstructure des pâtes testées a été caractérisée par la fraction volumique de chaque phase déduite à partir du degré d'hydratation estimé à partir de la mesure du retrait chimique. Nous avons établi une relation linéaire entre le module de fluage C_i et la dureté d'indentation H ainsi qu'une fonction de puissance entre le module de fluage C_i et le module de Young E. La relation entre les propriétés mécaniques et la fraction volumique de chaque phase est explorée en traçant simplement les propriétés mécaniques en fonction de la fraction volumique de chaque phase. Nous abordons également l'effet de la porosité sur ces propriétés mécaniques. Les résultats confirment que E, H et C_i augmentent lorsque le degré d'hydratation augmente. La proportion de chaque phase et les propriétés mécaniques des pâtes C_3S et C_2S seront utilisées ultérieurement dans le chapitre 9 pour valider le modèle micromécanique.

Le chapitre 7 est consacré à la présentation d'une étude sur les propriétés mécaniques d'échantillons présentant une porosité similaire mais des fractions volumiques de C-S-H et de CH différentes. Ces

échantillons ont été préparés par compactage de poudre. La masse volumique a été déterminée à partir des masses et des dimensions des échantillons et la densité des poudres. Tous les échantillons ont été conditionnés sous 11% d'humidité relative ou bien sous conditions saturées en eau. Les propriétés mécaniques de ces compacts ont été caractérisées par microindentation. Nous avons trouvé une amélioration claire du module de Young E, de la dureté d'indentation H et du module de fluage C_i des compacts quand la fraction volumique de CH sous 11% d'humidité relative augmentait au cur du solide, tandis que dans des conditions saturées en eau aucune augmentation sensible n'était observée. Nous avons aussi constaté que les propriétés mécaniques des compacts telles que définies ci-dessus sous 11% d'humidité relative étaient nettement supérieures à celles observées dans des conditions saturées en eau, ce qui a permis de démontrer l'impact important de l'eau sur les propriétés mécaniques des compacts. Pour les échantillons avec une quantité élevée de CH, le temps caractéristique d'indentation τ_i soit le temps requis pour atteindre la cinétique de fluage logarithmique, s'est révélé plus important dans des conditions saturées en eau que sous une humidité relative de 11%.

Dans le chapitre 8, la pâte C_3S, le compact de C-S-H et le compact de CH en équilibre hydrique selon des niveaux d'humidité relative différents ont été testés par microindentation. Pour l'ensemble des matériaux étudiés, il a été observé que la dureté d'indentation H diminuait quand l'humidité relative augmentait. Le module de Young E de la pâte C_3S s'est quant à lui révélé constant à des niveaux d'humidité relative différents, tandis que pour le compact de CH et de C-S-H, une baisse du module de Young E était observée à des humidité relatives élevées. Le module de fluage C_i a baissé de manière générale avec une hausse d'humidité relative. Pour le compact de CH, la baisse du module C_i s'est vérifiée sur l'ensemble d'humidités relatives considérés, alors que pour la pâte C_3S et le compact de C-S-H, nous avons identifié une humidité relative critique en dessous lequel le module C_i variait. En combinant nos observations avec la con-

naissance de base sur la saturation partielle des solides poreux, nous pouvons conclure que le fait de désaturer les pores capillaires n'a eu aucun effet sur le module de fluage mais que le fait de désaturer les pores dans C-S-H était par contre responsable des variations observées sur le module de fluage à des niveaux d'humidité relative variables. Autrement dit, l'eau dans le C-S-H est responsable du fluage propre à long terme de la pâte C_3S et du compact de C-S-H. Pour tous les échantillons analysés, il a été constaté une évolution fragmentée du temps caractéristique d'indentation en fonction de l'humidité relative: il semble qu'il existe une humidité relative critique au-delà duquel τ_i est une fonction décroissante de l'humidité relative et en-deçà duquel τ_i est une fonction croissante de l'humidité relative. Sur la pâte C_3S, en considérant les données sur le module de fluage et l'isotherme de désorption, une relation linéaire reliant le module de fluage et le teneur en eau a été trouvée pour une humidité relative compris entre 11% et 75%.

Avec tous les résultats expérimentaux collectés dans les chapitres avant, une approche micromécanique est utilisée pour interpréter les résultats expérimentaux et pour modéliser l'effet de la microstructure et de l'eau sur le fluage dans le chapitre 9. En considérant les propriétés mécaniques et la distribution de chaque phase des matériaux obtenue par des expériences, nous proposons un modèle de mise à l'échelle pour les pâtes C_3S et C_2S et un autre modèle pour les compacts. Les modèles proposés sont aussi utilisables pour le module de Young E. Pour la pâte C_2S et les compacts, le choix du modèle est guidé par les informations sur la microstructure obtenues par MEB. L'effet de l'humidité relative est en outre intégré aux différents modèles proposés.

La thèse finie par le chapitre 10, dans lequel nous présentons un résumé des principales conclusions du projet de recherche. Sur la base de ces conclusions et des contributions, plusieurs limites et perspectives sont détaillées.

Contents

Nomenclature

Greek alphabet

β	correcting parameter for Galin-Sneddon solution
$\boldsymbol{\epsilon}(\underline{x})$	strain tensor in representative volume element
$\boldsymbol{\Sigma}(\underline{X})$	stress tensor at homogenized scale
$\boldsymbol{\sigma}(\underline{x})$	stress tensor in representative volume element
$\boldsymbol{\xi}$	displacement vector
$\boldsymbol{E}(\underline{X})$	strain tensor at homogenized scale
$\boldsymbol{I}$	second unit tensor
ϵ_f	flexural strain, 1
ϵ_{ir}	irreversible strain due to creep, 1
ϵ_r	reversible creep strain due to creep, 1
$\Gamma(t)$	gamma function
$\mathbb{I}$	four-order unit tensor
Ω	volume occupied by representative volume element
Φ	diameter, mm
ϕ	porosity, 1
ρ	density, kg/m

σ_{fmax}	flexural strength, Pa
σ_f	flexural stress, Pa
τ_f	bending characteristic time, s
τ_H	duration of the holding phase of indentation test, s
τ_i	indentation characteristic time, s
τ_L	duration of the loading phase of indentation test, s
τ_U	duration of the unloading phase of indentation test, s
τ_u	uniaxial compression characteristic time, s
θ	half-cone angle, °

English alphabet

$\mathbb{A}$	localization tensor
$\mathbb{A}_r$	mean localization tensor of phase r
$\mathbb{C}$	stiffness tensor
$\mathbb{C}_{hom}$	homogenized stiffness tensor
$\mathbb{C}_r$	stiffness tensor of phase r
$\mathbb{P}$	Hill's tensor
$\mathbb{S}$	Eshelby's tensor
RH	relative humidity, %
$\underline{X}$	space variable at homogenized scale
$\underline{x}$	space variable within representative volume element
b	width, m
c/s	cement-to-silica ratio, 1

C_d	deviatoric creep modulus, Pa
C_f	flexural creep modulus, Pa
C_i	contact creep modulus, Pa
C_u	uniaxial creep modulus, Pa
C_v	volumetric creep modulus, Pa
D	deflection, m
d	depth, m
D_0	instantaneous deflection, m
E	Young's modulus, Pa
E_0	Young's modulus at moment of loading, Pa
E_{eff}	effective modulus, Pa
f_r	volume fraction of phase r, Pa
G	shear modulus, Pa
g	geometry coefficient of monomial indentation probe, 1
g_0	geometry coefficient of monomial indentation probe, 1
G_{hom}	homogenized shear modulus, Pa
G_r	shear modulus of phase r, Pa
$J(t)$	creep compliance, Pa
$J_f(t)$	flexural creep compliance, Pa
$J_u(t)$	uniaxial creep compliance, Pa
K	bulk modulus, Pa
K_{hom}	homogenized bulk modulus, Pa

K_r	bulk modulus of phase r, Pa
l	span of two supports in a bending test, m
$L(t)$	contact creep compliance, Pa
l_{heter}	characteristic length of heterogeneity, m
l_{RVE}	characteristic length of representative volume element, m
l_{sample}	characteristic length of sample, m
M	indentation modulus, Pa
m	mass, g
m_a	mass of absorbed water, g
M_m	molar mass, g/mol
P	load, N
P_{max}	maximum load, N
r	radius, m
S	contact stiffness, N/m
s	complex number in Laplace domain
S_{ch}	chemical shrinkage, mL/g
T	temperature, °C
t	time, s
t'	time starting from loading, s
V	volume, m^3
w/c	water-to-cement mass ratio, 1
w/h	water-to-hemihydrate mass ratio, 1

Other Symbols

$\langle\rangle$	average operator
$\mathcal{L}$	Laplace transform operator
div	divergence operator
tr	trace operator

List of Figures

List of Tables

Part I

Introduction

Chapter 1

General presentation

Résumé *Ce chapitre est un résumé général du projet de recherche. Le chapitre démarre par une introduction au problème traité par le sujet de recherche, c'est-à-dire le fluage des matériaux cimentaires. L'introduction est suivie ensuite par les objectifs de recherche ainsi que les bénéfices scientifiques et industriels. Le chapitre se termine par un aperçu de la thèse.*

Abstract *This chapter is a general summary of the research project. The chapter starts with an introduction to the problem addressed by the research, i.e., the creep of cementitious materials. The introduction is followed by the research objectives and the scientific and industrial benefits. The chapter ends with an outline of the thesis.*

1.1 Context

1.1.1 Concrete for construction

Concrete is a composite material composed of coarse granular material (aggregates or fillers) embedded in a hard matrix of material (cement or binder) that fills the space between the aggregates and glues them together [Li, 2011].

Concrete is widely used all over the world: in mass, twice as much as steel, wood, plastics, and aluminum combined. Concrete is the most used man-made material in the world, with nearly three tons used annually per person [World Business Council for Sustainable Development, 2013]. In terms of effectiveness, price and performance, concrete can hardly be replaced by other existing building materials. Currently over 20 billion tons of concrete are produced per year and by 2050, the use of concrete is predicted to reach four times the 1990 level.

1.1.2 Creep of concrete

Creep is a time-dependent deformation occurring under and induced by, a constant sustained stress [Neville, 1971]. Since the first publication on the creep of reinforced concrete in 1907 [Hatt, 1907], the creep of concrete has been studied for more than 100 years but its fundamental mechanism is still rather poorly understood. For instance, in the past 10 years, the term “creep” appeared in 14% of original research papers published in the journal ‘Cement and Concrete Research’.

Creep can be either beneficial or detrimental for a concrete structure. On one hand, creep can bring a beneficial effect by relieving undesirable stresses due to strains imposed by shrinkage or extreme initial temperature. Thus in certain occasions, thanks to creep, the risk of cracking can be reduced [Fédération Internationale du Béton, 2013]. On the other hand, creep can reduce the beneficial effects of stresses artificially imposed for improving the serviceability of a structure. In the case of pre-stressed concrete, creep causes a loss of pre-stress over time in structure which reduces the serviceability of the structure [Magura et al., 1963]. Last but not least, the long-term reliability of structures may be largely affected by creep as creep increases by an important factor the initial deformations of a concrete structure [Bažant and Panula, 1980]. Either beneficial

or detrimental, creep plays an important role in concrete structure in terms of stability, serviceability and durability, both at short term and long term. The calculation of time-dependent deformations is recommended by most widely used codes for design of concrete structures, such as the ACI code, the fib model code, the GL2000 code, etc.

1.1.3 The complexity of creep of concrete

Creep of concrete is a complex issue for several reasons. Firstly, due to the fact that cement and concrete are multi-scale heterogeneous materials: creep can be observed at different scales ranging from that of concrete to cement paste, down to individual hydration products. Secondly, creep is sensitive to a variety of parameters: moisture, temperature, stress level, curing condition and mix design (i.e., water-to-cement ratio, admixture, aggregates) can influence creep [Neville, 1971]. Thirdly, cementitious materials are obtained by hydration of binders, and the hydration can last months to years. As a consequence, cementitious materials evolve with time and the creep properties depend on the age at which a given material is tested. Because of those various reasons, in the past century, despite major successes, the phenomenon of creep (and shrinkage) is still far from being fully understood [Bažant, 2001].

The difficulties in measuring creep at macroscopic scale by classical mechanical testing (compressive, tensile, bending) somehow make the issue even more complicated. Indeed, in order to provide a reliable prediction of long-term creep, creep testing on concrete is recommended to be carried out over hundreds of days [Jirásek and Dobruskỳ, 2012; Le Roy, 1996]. With such a long duration of test, experimental parameters as temperature, applied load and moisture content and distribution within the sample are difficult to control.

1.1.4 Potential for measuring creep by indentation testing

Indentation or hardness testing has long been used for characterization and quality control of materials [VanLandingham, 2003]. The indentation technique is used more and more widely for characterizing the mechanical properties of materials at very small scales: microindentation for testing on the scale of micrometer and nanoindentation on the scale of nanometer. Recently, different studies show

the possibility of measuring viscous properties by indentation, on cementitious materials [Davydov et al., 2011; Pichler and Lackner, 2009; Vandamme and Ulm, 2009, 2013]. Compared with conventional macroscopic creep testing, indentation creep testing is carried out at a much smaller microscopic scale but under a much higher stress. How to compare the result with traditional macroscopic creep testings on cementitious materials is still unclear.

1.2 Research motivation and objectives

Initiated by Lafarge Research Center and Laboratoire Navier at École des Ponts ParisTech, the research project has the following objectives.

Firstly, the project aims at finding a clear answer on the validity of indentation creep testing for the measurement of creep properties on cementitious materials [1]. The word "validate" here in our context refers to testing new methods developed by Vandamme [2008] on indentation creep with respect to classical macroscopic creep experiments.

The second objective is to better understand creep of cementitious materials. Two sub-objectives are identified:

- In Portland cement, two distinct types of components exist: amorphous component such as calcium silicate hydrate, i.e., C-S-H and crystalline components such as portlandite and unhydrated clinker particles. The microstructure of cementitious materials can be characterized by the proportion of those components and their spatial organization. The first objective is to study the effect of microstructure, i.e., the proportion distribution and the spatial organization of minerals, on long-term basic creep of cementitious materials.

- Though some studies showed that water content has an effect on the creep properties of cementitious materials [Acker and Ulm, 2001; Bažant et al.,

[1] Hydraulic binder is a material (with or without an aggregate) that provides plasticity, cohesive, and adhesive properties when it is mixed with water. Those properties are necessary for its placement and formation into a rigid mass. The term cementitious material refers to the material created by mixing hydraulic binder with water, i.e., via hydration reaction. In the thesis, the term "cementitious material" can refer to cement paste, concrete, C_3S and C_2S pastes, gypsum plaster and compacted samples made of component(s) of a cement paste.

1973; Cilosani, 1964; Wittmann, 1970], with the available data in literature, the influence of amount of water on long-term basic creep properties of cementitious materials is unclear. So the second objective is to study the effect of water on long-term basic creep.

1.3 Industrial and scientific benefits

In parallel of fulfilling those objectives mentioned above, there are some additional useful results that can be brought by our research, both on the basis of industrial application and that of research.

- A fast, (i.e., minutes-long) and well-controlled experimental technique to measure the long-term basic creep behavior of cementitious materials
- Fundamental understandings on the long-term basic creep properties of cementitious materials influenced by their microstructures and by the amount of water
- A model to predict the long-term basic creep behavior of cementitious materials as a function of relative humidity and of their microstructure

1.4 Outline of thesis

The thesis consists of four parts. Part I is an introductory part which provides the context of research (chapter 1) and a literature review on creep testing (chapter 2). Starting with indentation analysis (chapter 3), the part II deals with the validation of indentation for the measurement of creep on various cementitious materials, i.e., cement paste (chapter 4) and gypsum plaster (chapter 5). Once the technique of indentation testing is validated, part III focuses on characterizing how the long-term basic creep properties of cementitious materials are influenced by microstructure and water. The effect of microstructure is scrutinized by looking at both materials obtained by hydration, such as C_3S and C_2S pastes (chapter 6) and by compaction of powder, i.e., compacts (chapter 7). The effect of water is studied on pastes and compacts that achieved hygral equilibrium with various

relative humidities (chapter 8). The part III ends with chapter 9 in which we use micromechanical approach to build models that predict the long-term basic creep properties of cementitious materials as a function of microstructure and of relative humidity. The models are validated with experimental results. Part IV is a conclusive one in which we present the main findings, contributions, limitations and perspectives (chapter 10).

Chapter 2

Bibliographic study

Résumé *Ce chapitre présente une revue de la littérature sur les matériaux cimentaires et leur fluage. Les matériaux cimentaires sont des matériaux multi-échelles et poreux. Dès lors, le fluage de ces matériaux intervient à différentes échelles et peut être largement influencé par la présence d'eau en porosité. Les effets liés au changement d'humidité, à la teneur en eau, à la température, au niveau de contrainte et à la formulation sur le fluage des matériaux cimentaires ont été examinés sur la base d'études récentes. L'origine du fluage des matériaux cimentaires est probablement due à une combinaison de mécanismes. Le comportement du fluage des matériaux cimentaires à court et long terme est contrôlé par différentes cinétiques et peut être causé par différents mécanismes. Pour la prédiction du fluage, un regard a été porté sur les modèles les plus répandus.*

Abstract *This chapter gives a literature review on cementitious materials and the creep of those materials. Cementitious materials are multi-scale and porous materials. Therefore, creep of those materials happens at different scales and can be largely influenced by the presence of water in porosity. The effects of moisture change, water content, temperature, stress level and mix design on creep of cementitious materials were reviewed based on recent studies. The origin of creep of cementitious materials is probably due to a combination of mechanisms. The short-term and long-term creep behaviors of cementitious materials are controlled by different kinetics and may be due to different mechanisms. For creep prediction, a glance was given at the most widespread models.*

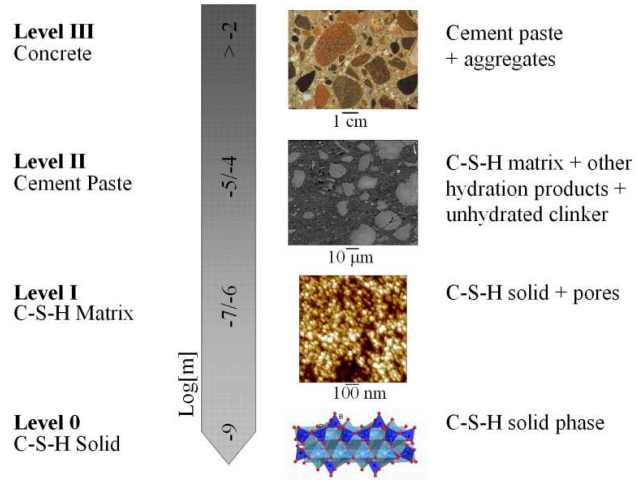

Figure 2.1: Multi-scale view of concrete [Vandamme, 2008].

2.1 Cementitious materials

Cementitious materials are multi-scale materials. For example, concrete by nature is highly heterogeneous over a large range of length scales. In engineering application, concrete is a composite made of aggregates (e.g., sand, gravel, fiber) and binder (e.g., cement) which bonds the aggregates together. At a smaller scale than concrete, cement paste can be regarded as a composite of unhydrated clinker, hydrated products and voids. The unhydrated clinker consists of various calcium silicates, including tricalcium silicate (Ca_3SiO_5 or C_3S), dicalcium silicate (Ca_2SiO_4 or C_2S) and tricalcium aluminate ($3CaO{\cdot}Al_2O_3$, C_3A), calcium aluminoferrite as other common components. The hydrated products in cement paste may include calcium silicate hydrates (C-S-H), calcium hydroxide (CH), calcium sulfoaluminates, ettringite and monosulfate with various sizes and geometries. Each hydrate has its own microstructure. Hydrates with complicated microstructures such as C-S-H are widely studied as a heterogeneous material with substructures at smaller scales. A multi-scale plotting of concrete is presented in Fig. 2.1.

Cementitious materials are porous materials, due to the voids present at different scales in those materials. According to Mehta and Monteiro [2006], classified by the sizes, the following voids in a cement paste can be found: the porosity in C-S-H, the capillary porosity, and air voids. The dimensional range

of those voids in cement paste is presented in Fig. 2.2.

The pore size distribution in C-S-H is till studied intensively today, but various terminologies can be already found in literature to classify the pores in C-S-H, such as: "interlayer pores"(1nm) and "gel pores"(3nm) given by Feldman and Sereda [1970]; "intraglobular pores"(1nm) and two types of "globule pores"(1-10nm) from the model of Tennis and Jennings [2000]. The lengths in parentheses were the characteristic sizes of the corresponding pores given by Muller et al. [2012]. In following chapters, we apply the terms from Feldman and Sereda [1970] for the pores in C-S-H.

The porosity at different scales may have various influences on the properties of cementitious materials. The porosity in C-S-H may contribute to drying shrinkage and creep; the capillary porosity may contribute to the strength and permeability while the small capillary porosity may contribute to drying shrinkage and creep [Mehta and Monteiro, 2006]. As a consequence, the quantity, the size distribution and the connectivity of porosity influence the physical and mechanical properties of cementitious materials. The mechanical behavior of porous materials is significantly influenced by the pore fluid. As the fluid in porosity is naturally water or, more precisely, saturated aqueous solution of minerals, the mechanical behaviors of cementitious materials could be sensitive also to moisture change which replaces water with moist air for instance.

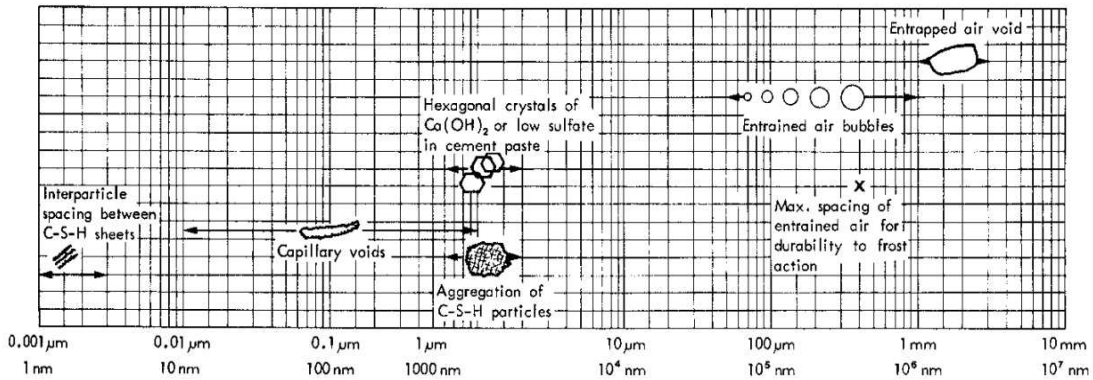

Figure 2.2: Dimensional range of solids and pores in a hydrated cement paste [Mehta and Monteiro, 2006].

2.2 Terminologies of deformations

Since this thesis is focused mainly on time-dependent deformations, this section is dedicated to define the time-dependent deformations to which cementitious materials are submitted.

Neville et al. [1983] precisely defined creep as 'a deformation occurring under, and induced by, a constant sustained stress'. Cementitious materials can shrink even with absence of applied loads and these deformations are called shrinkage, when temperature is constant [Bažant and Wittmann, 1982].

Depending on whether there is moisture exchange with external environment or not, shrinkage can be categorized as drying shrinkage and autogeneous shrinkage. Drying shrinkage refers to the contracting of a hardened concrete mixture due to the loss of water. [Tazawa, 1998] defines autogeneous shrinkage as the deformation occurring without moisture transfered to the exterior surrounding environment, and without external load: it is affiliated with the hydration of cement particles. During the very first hours after mixing, autogeneous shrinkage is fully attributed to chemical shrinkage [Holt, 2005], which is the volume change due to the difference between the volume occupied by the products of hydration and that of mixture of water and clinker. Once cement is hardened, autogeneous shrinkage can result from self-desiccation [Tazawa and Miyazawa, 1995], which is the localized drying resulting from a decreasing relative humidity in the concrete's internal pores [Holt, 2005].

As a consequence of the existence of shrinkage, the experimentally measured time-dependent deformation ϵ_{total} of a cementitious material by applying a constant load contains not only the instantaneous deformation as elastic deformation (denoted as $\epsilon_{elastic}$), and time-dependent deformation of total creep (noted as ϵ_{creep}) but also the shrinkage deformation (denoted as ϵ_{sh}). Though Hua [1995] and Sicard et al. [1996] showed that creep and shrinkage of cementitious materials are not independent phenomena and one may interact with the other, the assumption of superposition of deformation of creep and shrinkage stays the principal method to interpret experimental results and also to model creep deformations:

$$\epsilon_{total}(t) = \epsilon_{elastic} + \epsilon_{creep}(t) + \epsilon_{sh}(t) \tag{2.1}$$

At constant temperature, the creep strain of cementitious materials can be further

classified by whether drying occurs or not:

- Basic creep strain, denoted as ϵ_b, is termed as the time-dependent deformation without moisture change and at constant temperature [Bažant and Wittmann, 1982].
- Drying creep strain, denoted as ϵ_d, is defined as the excess of creep at drying over the sum of shrinkage and basic creep [Bažant and Yunping, 1994].

At variable temperature, an extra term called thermal transitional creep strain is introduced. The thermal transitional creep strain, denoted as ϵ_T, is the extra deformation due to temperature change. With the above definitions, the total creep strain can be expressed by Eq. 2.2 as the sum of basic creep strain, drying creep strain and transitional creep strain if one supposes that different creep deformations are additive:

$$\epsilon_{creep} = \epsilon_b + \epsilon_d + \epsilon_T \tag{2.2}$$

There exists also other ways to categorize the creep deformations of cementitious materials. Here, we will mention the two commonly applied classifications:

- irreversible creep and reversible creep
- short-term creep and long-term creep

Depending on whether the creep deformation can be recovered or not by complete unloading, creep can be divided as reversible creep strain (the part that can be recovered from complete unloading, denoted as ϵ_r) and irreversible creep strain (the part of creep that can not be recovered from complete unloading, denoted as ϵ_{ir}):

$$\epsilon_{creep} = \epsilon_{ir} + \epsilon_r \tag{2.3}$$

The creep strains are often normalized by applied load. The term 'specific creep' as one may find in much literature is defined as the creep strain divided by applied stress. For the convenience of illustration below, we also define a term "specific basic creep" as the specific creep without strains due to drying or temperature change. The specific creep equals to the specific basic creep if there is no drying

or temperature change. For drying creep strain and thermal transitional strain one can define their corresponding specific strains.

The creep of cementitious materials can also be phenomenologically classified as short-term creep and long-term creep. The term of "short-term creep" and "long-term creep" appear very often in various studies, yet definition is not very clear. The "short-term creep" on an experimental basis refers to the creep behavior measured in relatively short duration, which can vary from 1 day to 1 month [Bernard et al., 2003; Guo et al., 2005; Jo et al., 2007; Khadraoui, 2012; Tamtsia and Beaudoin, 2000] by macroscopic creep testing. On the other hand, the term "long-term creep" refers to a test duration that may vary from 3 months to years [Chami et al., 2009; Han and Yang, 2003; Jo et al., 2007; Li et al., 2012; Manzi et al., 2013; Miàs et al., 2013; Salau, 2003]. On the basis of creep kinetics, short-term creep and long-term creep are used to present different kinetics of creep. The short-term creep kinetics last only a few days, while the long-term kinetics is characterized by a pronounced aging without an asymptote [Ulm et al., 1999]. One can notice that the long-term creep or short-term creep may refer to different time scales on the basis of testing or on the basis of creep kinetics.

To characterize the creep behavior of cementitious materials, apart from using time-dependent creep deformation, one can also use creep function and creep compliance. The creep function, also called specific creep strain, is the creep deformation normalized by applied stress. The creep function has the same unit as compliance (ability to comply with deformation forces). Talking about the compliance, there is another term called creep compliance J, which is also widely used to characterize the creep behavior of cementitious materials. The creep compliance can be written as the sum of the instantaneous compliance at the moment of applying a load and the creep function. For example, the uniaxial creep compliance J_u equals to the instantaneous elastic compliance, i.e., the reciprocal of Young's modulus $1/E_0$ at the moment of loading plus a creep function $f(t)$:

$$J_u(t) = 1/E_0 + f(t) \tag{2.4}$$

2.3 Creep testing on cementitious materials

This section gives a brief introduction on experimental approaches that provide access to the creep properties of cementitious materials.

Creep testing on cementitious materials at macroscopic scale focuses on how the specimen deforms macroscopically when subjected to a specific type of loading. The scale of test is much larger than the characteristic length of the heterogeneity of material: so when a macroscopic creep testing is done on cement paste, one measures the creep properties of cement paste, similarly when macroscopic creep testing is done on concrete, one measures the creep properties of concrete. Classical mechanical testings as compression, bending, tensile and, very rarely, torsion, were investigated to measure creep under different stress conditions. The choice of testing method is also influenced by the loading conditions to which cementitious materials in service are subjected.

Compressive testing is the most applied testing method for cement and concrete. There has been an increasing attention on tensile creep of cementitious materials in the past 20 years, partly due to the fact that tensile creep is even more poorly understood, to the appearance of new formulations of concretes with reinforcement of fiber that improves its tensile strength; and to the fact that the tensile testing helps to better understand cracking issues of cementitious materials, especially for early ages, during drying. Tensile creep is mainly measured by tensile testing. Bending testing is also widely used for reinforced concrete beams and boards, gypsum plaster etc.

Compressive testing is an experimental testing method for the determination of mechanical behaviors of materials under a compressive load. The most applied compressive testing for creep test is uniaxial creep testing. To study the mechanical behavior of a sample under uni-dimensional stress on sample to test, an uniaxial compressive test is often conducted by loading the test specimen between two plates, and then applying a force to the specimen by approaching the two cross-heads. To study the mechanical behavior of a sample under three-dimensional stress, a triaxial compressive test can be conducted by applying hydraulic pressure to the surrounding surface of material as well as a vertical compressive load which could be applied by cross-heads. During the test, the specimen is compressed, and deformation versus the applied load is recorded.

Figure 2.3: Photo of uniaxial compressive creep testing machine [Lee et al., 2006].

The compression test can be used to determine elastic limit, proportional limit, yield point, yield strength, compressive strength as well as time-dependent deformation under compression. To measure creep by compressive testing, a targeted load is achieved rapidly and it is then held constant for the whole duration of creep test. The applied load, deformation as well as time are recorded. For cementitious materials as cement paste, mortar and concrete, the applied load is often proportional to the strength of the material at the moment of testing, e.g., 30% of its compressive strength at the beginning of the compressive creep experiment. A schematic uniaxial compressive creep apparatus is presented in Fig. 2.3.

Tensile testing is also a common experimental method for determining the mechanical behaviors of materials under axial tensile loading. The tests are conducted by fixing the specimen to the test apparatus and then applying a force to the specimen by separating the testing machine cross-heads. Data from the test are used to determine tensile strength, yield strength, and modulus of elasticity. To measure creep by tensile testing, a target load is reached and held constant for the duration of creep test. The load applied, deformation as well as time are recorded. For cementitious materials, the load applied during creep is often proportional to the tensile strength of the material at the moment of testing, which is much lower than load applied in compressive creep test due to the fact

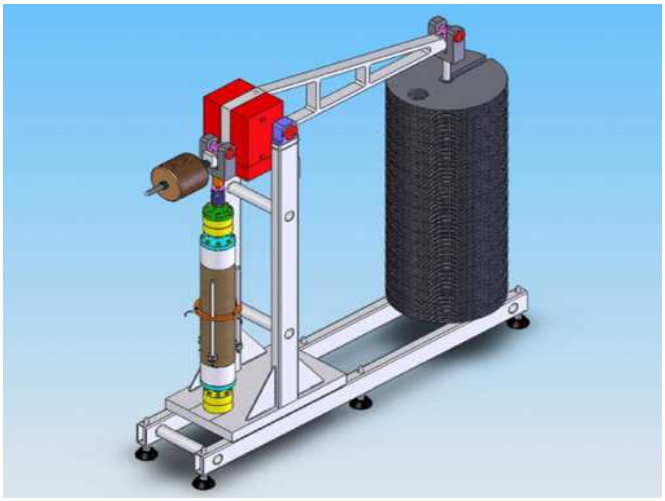

Figure 2.4: Schema of tensile creep machine with dead weight [Rossi et al., 2013b].

that the tensile strength is much lower than compressive strength for common cementitious materials. A schematic uniaxial tensile creep apparatus is presented in Fig. 2.4.

Bending testing is used to characterize the mechanical behavior of the slender structural element subjected to an external load applied perpendicularly to a longitudinal axis of the element. A bending test can give access to the Young's modulus, flexural stress, flexural strain and the flexural stress-strain response of the material. The most common applications are three-point bending test and four-point bending test. Both deformations in region where material is in tension or compression can be recorded. Apart from deformation, the deflection is also commonly measured in a bending test, from which the flexural strain can be calculated. When bending test is used to measure time-dependent deformation, a constant load is applied and held till the end of test. However, in the literature, we could hardly find any in which the deformation due to shrinkage is subtracted. A schematic three-point bending creep apparatus is presented in Fig. 2.5.

Apart from the techniques mentioned in this section at macroscopic scale, instrumental indentation technique is nowadays routinely used to measure mechanical properties at much smaller scales: nanoindentation at the scale of nanometer or microindentation at the scale of micrometer. The technique of indentation is applied on various materials for the determination of mechanical properties.

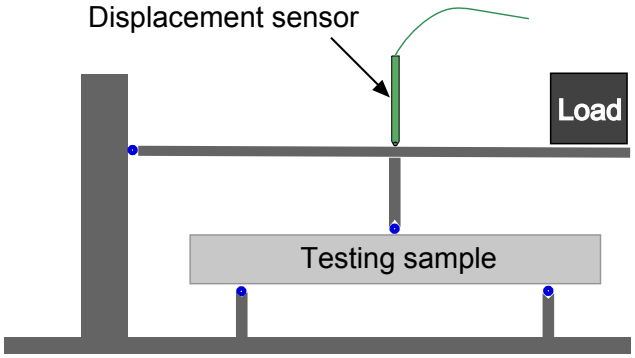

Figure 2.5: Schema of bending creep testing machine with dead weight.

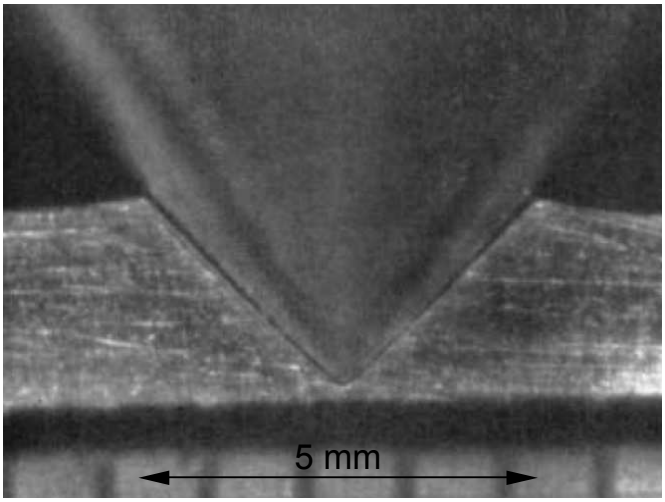

Figure 2.6: Indentation test on duralumin with a tungsten carbide conical indenter [Testwell and Tabor, 1961].

In an indentation test, a probe of known geometry and mechanical properties is penetrated into the surface of the material under test, as presented in Fig. 2.6. The load applied to the probe and the depth of the indenter with respect to the indented surface and the time are continuously recorded. Several methods were developed by different researchers to analyze the load-depth curve in order to obtain mechanical properties such as indentation modulus or indentation hardness [Bhattacharya and Nix, 1988; Cheng and Cheng, 2004; Doerner and Nix, 1986; Oliver and Pharr, 1992, 2004]. The indentation modulus is related to the elastic properties of the tested material, while indentation hardness is mostly –but not only– governed by the plastic properties and strength of tested material. Recently, high attention has been paid on indentation for time-dependent properties, both on analytical development [Guin et al., 2002; Hidenari et al., 2005; Ogbonna et al., 1995; Oyen, 2004; Sargent and Ashby, 1992; Seltzer and Mai, 2008; Shahsavari R, 2009; Vandamme and Ulm, 2006; Zhang et al., 2004] and experimental study. Measuring creep by indentation in particular has been shown on polymers [Beake, 2006; Lu et al., 2003; Maxwell et al., 2011; VanLandingham et al., 2005; Zhang et al., 2005], metalloids [Poisl et al., 1995], metals [Chen et al., 2001; Dorner et al., 2003; Fujiwara and Otsuka, 2001; Geranmayeh and Mahmudi, 2005; Ma and Yoshida, 2003; Mahmudi et al., 2009; Peng et al., 2007; Takagi et al., 2010; Tewari et al., 2004; Wang et al., 2005] and cementitious materials [Davydov et al., 2011; Pichler and Lackner, 2009; Vandamme and Ulm, 2009, 2013].

2.4 Review of experimental results on creep of cementitious materials

The creep properties of cementitious materials are influenced by various factors. By a rough classification, such factors fall into two categories: external factors such as relative humidity, temperature, loading (age of loading, duration of loading, type of loading, level of stress) and intrinsic factors such as strength, characteristics of binder (porosity, hydration degree, hydrates), presence of additional products (silica fume, fiber, superplasticizer), characteristics of aggregates (nature, fraction, size distribution). In this section, attention will be paid on the effects of some of the above mentioned factors on the creep function (with or/and

without drying) of cementitious materials, based on experimental results from former studies. We recall that the creep function is a time-dependent function of creep strain normalized by applied stress in a creep experiment.

2.4.1 Effects of moisture on creep properties of cementitious materials

The amount of water in cementitious materials has an effect on the basic creep strain of cementitious materials. Without many results existing in literature, it seems that for mortar and hardened cement and concrete, the higher the amount of water, the higher the specific basic creep strain. Cilosani [1964] studied the creep behavior of pre-dried mortar beams which then reached equilibrium in various relative humidities and found the deflection (proportional to basic creep strain) is higher when the relative humidity is higher, while in very dry conditions, deflection of mortar seemed to be time-independent. At the scale of cement (see Fig. 2.7), Bažant et al. [1973] showed the basic creep of hydrated cement paste sample first conditioned in lime water and then conditioned in 75% for 1 day and then tested at 75% relative humidity is lower than the sample conditioned in lime water and tested at relative humidity of 99%. As presented in Fig. 2.7, if one substracts shrinkage from the total deformation, sample c (at 75% relative humidity) creeps less than samlpe a (at 99% relative humidity). On concrete, Acker and Ulm [2001] found concrete which has dried to the state where evaporable water had been totally eliminated was not subject to creep, as presented in Fig. 2.8.

The moisture change has an effect on the creep properties of cementitious materials. At the scale of concrete, Pickett [1942] found that ordinary concrete under load and at same time being dried presented a higher deformation than that of sample under load without drying. This phenomenon was later called Pickett effect. Pickett [1942] also found the amount and rate of total deformation, i.e., creep plus shrinkage in concrete under load to depend on the rate of drying. Many studies were carried out in the last century on the drying creep of cementitious materials as cycles of moisture change happen for most concrete structures in service and the Pickett effect was confirmed by various studies [Bažant et al., 1973; Bissonnette and Pigeon, 1995; Kamen et al., 2006; Rossi et al., 2013b; Schrage and Springenschmid, 1996; Vandewalle, 2000].

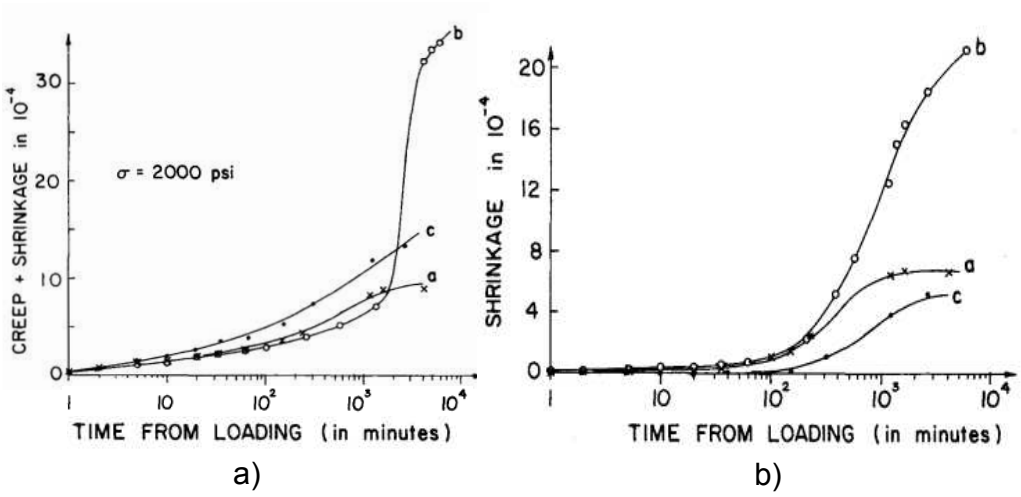

Figure 2.7: a) Total deformation and b) shrinkage deformation of thin cement paste tested in different hygral conditions: sample *a* at 99% relative humidiy, sample *b* at relative humidities varying from 99% to 75% within a day; and for sample *c*: at 75% humidity. [Bažant et al., 1973].

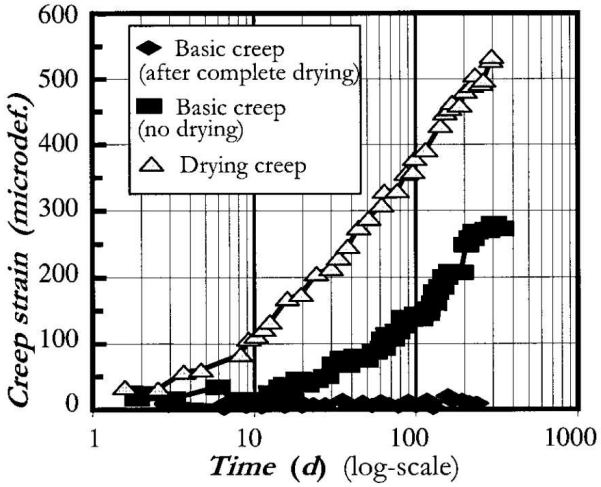

Figure 2.8: Basic creep strain of concrete samples with complete drying before and without drying before creep testing, compared with drying creep strain on similar sample, figure from [Acker and Ulm, 2001].

Schrage and Springenschmid [1996] found that the characteristics of drying creep strain of high strength concrete was different from normal concrete: tested in the same environment, the drying creep of high strength concrete seemed to stabilize faster than normal concrete samples.

The above mentioned experiments studied the drying creep of concrete in environment with constant relative humidity and temperature. What happens if samples are submitted to variable relative humidities and temperatures? Seasonal variation of relative humidity and temperature influence the creep properties of cementitious materials. Vandewalle [2000] measured the total creep strain of concrete samples prepared in different seasons and submitted to creep test when their compressive strengths reached the same value (the age of test may be different among samples cured in different seasons). The amplitude of total creep of samples that were submitted to seasonal variable relative humidity were found to be similar with samples that were tested in constant relative humidity and temperature.

Last but not least, Tamtsia and Beaudoin [2000] found the history of drying may also influence the basic creep of cement paste. As presented in Fig. 2.9, compressive creep testing was done to hydrated cement samples with 3 different drying histories: dried at 42% relative humidity and resaturated in 100% relative humidity, D-dried (vacuum drying to the equilibrium vapor pressure above ice at 79°C and resaturated in 100% relative humidity) saturated sample without drying. The basic creep strain of cement sample is found to be the least for the sample without drying.

2.4.2 Effect of temperature on creep properties of cementitious materials

The effects of temperature on the creep properties of cementitious are threefold: first, during hydration, temperature influences the hydration of cementitious materials and microstructure development of those materials thus influences the creep properties of those materials; second, cementitious materials under load in higher temperature show higher creep, probably due to the breakages and restorations of bond [Bažant et al., 2004].

Within a certain range, by increasing the temperature during sample curing,

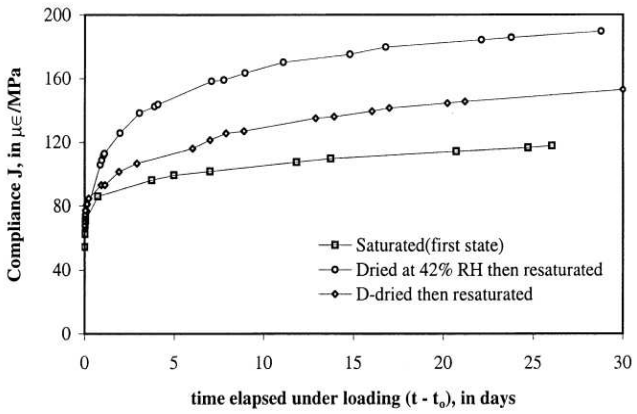

Figure 2.9: Compliance function of hydrated cement paste (w/c=0.5) after re-saturation from different drying pre-treatments [Tamtsia and Beaudoin, 2000].

the hydration process is accelerated so that cementitious materials gain a higher degree of maturity within the same time of hydration [Taylor, 1997], thus enhances the mechanical performance at given age. This conclusion is supported by the result of Sakata [1993]: when the curing temperature varies within 5°C to 35°C, creep strain is found to be lower when curing temperature is higher. On the other hand, higher curing temperature may also lead to microstructure change of cementitious materials such as the density change of C-S-H in Portland cement [Escalante-Garcia and Sharp, 1998] and change of distribution of porosity [Kjellsen et al., 1990a] thus higher curing temperature may lead to weaker mechanical properties, including a higher amplitude of creep: as found by Vu et al. [2012], the basic creep strain at given time is higher for samples cured in high temperatures than that of samples cured in lower temperatures (varying from 60°C to 90°C).

Experimental results also support that, at least within a certain range of temperatures, higher temperature leads to a larger basic creep. For instance, the basic creep strain of cement samples cured in room temperature was found to be higher at 38°C than at 24°C [Bažant et al., 1976] at given time. Similar tendency was found by York et al. [1970] on concrete , who measured the basic creep at age of 90 days at 24°C and 65.6°C; and likewise by Kommendant et al. [1976] who tested concrete samples cured in room temperature and loaded at age of 28 days

and 90 days in temperatures of 23°C, 43°C, and 71°C as well as by Shkoukani and Walraven [1993] who found that, at given time, the basic creep strain of concrete samples cured in 20°C increased with the temperature during creep experiment (testing was performed at 20°C, 40°C and 60°C).

The change of temperature introduces the transitional thermal creep strain (defined in section 2.2) and thus influences the creep properties of materials. Fahmi et al. [1972] studied creep properties of hollow cylindrical micro-concrete specimens by compression, at 50% and 100% relative humidities. Some of these specimens were subjected to a sustained load during 37 days at 23°C, and then heated to 60°C. The transitional thermal creep was observed when temperature change was varied.

2.4.3 Effect of stress level on creep

It seems to be generally accepted that creep strains are proportional to the applied stress when the applied stress is below a certain value [Atrushi, 2003]. An example of linear response of basic creep of concrete with respect to applied stress level can be found from the result of Lee et al. [2006], as presented in Fig. 2.10. The high performance concrete samples were prepared with water-to-cement ratio of 0.3 and loaded at age of 1 day at four stress levels, i.e., 10%, 20%, 30% and 40% of 1-day compressive strength. The specific basic creep strains are quite similar, which indicates that the basic creep is linear to applied load for a stress level of up to 40% of the 1-day compressive strength for high performance concrete tested at early age. However, many studies showed that creep strain is no longer proportional to the applied stress (or in other words the specific creep functions at different load levels are different) when this applied stress is above a critical value.

De Schutter and Taerwe [2000] found the basic creep of hardening normal concrete is non-linear to applied load and the non-linearity is more obvious if the age of loading is earlier: normal concrete samples were tested at ages varying from 0.5 day to 14 days, with two different stress levels (20% and 40% of compressive strength at age of loading); the specific basic creep was higher for samples tested at 40% of compressive strength than those tested at 20% and this non-linearity becomes less evident for the samples loaded at larger ages. From the result of

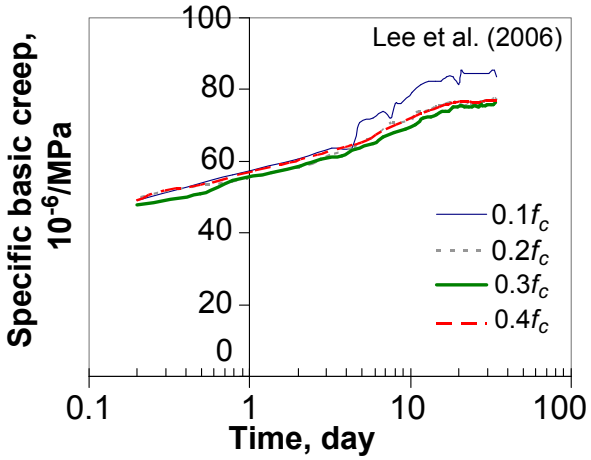

Figure 2.10: Specific basic creep of concrete tested at the age of 1 day under four stress levels from 10% compressive strength ($0.1f_c$) to 40% of compressive strength ($0.4f_c$). Adapted from [Lee et al., 2006].

De Schutter and Taerwe [2000], the critical stress level should be below 40% of its compressive strength at loading, and this limit increases with the age of loading. For creep behavior of normal concrete obtained by tensile creep testing, similar observation was found. Bissonnette and Pigeon [2000] found similar specific basic creep of concrete tested at age of 7 days under stress level of 30% and 50% of 7-day tensile strength. Østergaard et al. [2001] found also by tensile creep testing that the specific basic creep functions of normal concrete samples loaded at age of 1 day with two different stress levels (25% or 45% of 1-day tensile strength) are different. Combining the results from the two studies, the non-linearity of basic creep from tensile testing lies between 25% and 45% of tensile strength at very early age and increases to higher than 50% of tensile strength at maturer ages.

The non-linear limit for high performance concrete at early age should be higher than 40% judging from the result of Lee et al. [2006] (see in Fig. 2.10). Kamen et al. [2007] observed that the non-linearity of basic creep of high performance concrete was below 55% of 7-day strength for test started at concrete age of 7 days. Rossi et al. [2013a] showed that the non-linearity of basic creep of high performance concrete tested at 28 days should be below 75% of 28-day strength. Ranaivomanana et al. [2013] showed non-linear basic creep should start below 50% of 28-day strength of high performance concrete. Based on all observations

above, it seems to us that the limit to non-linear creep with respect to stress level lies somewhere between 40% to 50% of the compressive strength at moment of loading.

To summarize, the limit above which the basic creep is no longer linear (the critical stress level) seems to depend on the age of loading and also on the type of concrete:

- The critical stress level seems to be higher when load is applied in maturer ages.
- The critical stress level seems to be higher for high performance concrete than that of normal concrete.

2.4.4 Effect of mix design on creep

In the following part, the effect of mix design parameters such as water-to-cement ratio, additions and fraction as well as nature of aggregate on creep will be discussed.

The specific creep can be reduced by reducing water-to-cement ratio. By reducing water-to-cement ratio from 0.5 to 0.28, the specific basic creep of cement paste after 3 months loading was reduced by 50% [Le Roy, 1996]. Similar trend was found by Wiegrink et al. [1996] on concrete samples with various water-to-cement ratio but constant volume fractions of aggregate. Wiegrink et al. [1996] also found the specific creep of concrete decreases with water-to-cement ratio on concrete samples under the same condition of drying.

By adding silica fume or fly ash or replacing part of cement clinker with those materials, the basic creep can be reduced. For instance, at various water-to-cement ratios, with 10% (silica-to-cement ratio) of addition of silica fume, the basic creep strain is reduced [Le Roy, 1996]. Also, for high performance concrete samples made with blended cement, replacing 10% mass of cement clinker with silica fume reduces the total creep of concrete [Li and Yao, 2001]. Tikalsky et al. [1988] found that replacing the binder with up to 35% of fly ash reduced the total creep, and the creep reducing effect depended on the type of fly ash used.

By adding blast furnace, specific basic creep is reduced [Li and Yao, 2001]. Replacing 30% mass of cement by ultra fine blast furnace slag, the specific total

creep of high performance concrete is reduced [Li and Yao, 2001]. Alexander [1994] studied the properties of blended cement concrete containing blast furnace slag by compressive creep testing. For unsealed prisms, addition of slag had no significant influence on total creep, while the specific basic creep strain was reduced by more than 40%.

Brooks and Johari [2001] showed that, at constant water-to-cement ratio, by adding metakaolin, both basic creep and total creep of concrete were reduced and the creep-reduction effect became more obvious by increasing metakaolin-to-cement ratio from 5% to 15%.

Adding fiber can help to reduce total creep. Mangat and Azari [1986] tested hardened concrete and mortar with and without addition of steel fibers at the age of 28 days by compressive creep testing and found that the addition of steel fibers reduced total creep. Similarly, total creep of ultra high performance concrete tested at age of 7 days at 40% of tensile creep was found to be reduced by adding 2% of steel fibers [Garas et al., 2009].

The effect of the volume fraction and the nature of aggregates on concrete creep were studied. Le Roy [1996] found that, by increasing the volume of aggregates, specific creep of concrete samples tested at various ages (1 day, 3 days, 7 days and 28 days) was reduced. The nature of the aggregates may have an influence on creep. Indeed, Alexander [1996] measured the total creep of concrete made with various types of aggregates at age of 28 days and the influence of the aggregates was linked to their absorption property and to their stiffness. Domingo-Cabo et al. [2009] measured the total creep strain of concrete samples with very similar 28-day strength but with different type of aggregates. The concrete sample with recycled coarse aggregates showed higher total creep deformation than concrete with normal coarse aggregates.

2.5 Creep theories of cementitious materials

Various creep theories were proposed in the last century. For example: mechanical deformation theory, plastic theory, viscous and visco-elastic theory, elastic after-effect theory, solid solution theory, seepage theory, micro-cracking theory, consolidation theory, solidification theory and long-term aging theory. It is generally agreed that none of the proposed theories is capable to explain all experimental

observations and possibly several mechanisms are involved in the creep of cementitious materials. According to ACI Committee [1999], the main mechanisms of creep are the following:

- Viscous flow of the cement paste caused by sliding or shear of the gel particles.
- Consolidation due to seepage and redistribution of pore water under stress.
- Delayed elasticity due to the cement paste acting as a restraint on the elastic deformation of the skeleton formed by the aggregate and gel crystals.
- Microcracking

Viscous shear theory was proposed by Thomas [1937]. Concrete is composed of a viscous phase, i.e., the cement paste and an inert phase, i.e., the aggregates. When a load is applied to concrete, the stresses in the paste are gradually transferred to the aggregates. As the stresses in the paste decrease with time, the rate of deformation also decreases. Such decrease is consistent with the experimental observations. At the scale of paste, Ruetz [1968] proposed a so-called adsorption theory, according to which creep occurs through the slip between C-S-H particles with inter-layer water acting as a lubricant.

The water seepage theory was proposed by Lynam [1934]. The theory is based on the observation that hardened cement paste is a rigid gel composed of a solid phase and a liquid phase. The application of an external load leads to a change of internal liquid pressure in concrete [Lea and Lee, 1947]. Due to this pressure, creep happens when water is squeezed out of the pores and moves into areas of unhindered adsorption [Powers, 1968]. With this movement, stresses originally applied on water are then progressively transferred to the solid phase. Bissonnette and Pigeon [2000] complete that creep is a result of the establishment of a new equilibrium between the rigid gel and its environment.

Another potentially significant creep mechanism is microcracking. The exact definition of microcracking is seldom mentioned in literature, yet one may consider that microcracking refers to the cracking happening within a representative elementary volume. Microcracking was mentioned 4 decades ago [Ishai and Coheno, 1968; Slate and Hover, 1984]. At high stress level microcracking

could result in additional strains reaching up to 10% or even 25% of the total time-dependent strain [Neville et al., 1983]. The time dependence of the growth of microcraks may be the source of nonlinear part of creep of concrete [Bažant, 1993]. The theory of microcracking was emphasized again recently by Rossi et al. [2012]: they proposed that microcracking was the main mechanism responsible for the basic creep of hardened concrete. This proposition was based on the experimental observation of a linear relationship between basic creep and acoustic events during creep tests.

As mentioned in section 2.2, the short-term and long-term creep of cementitious materials can be distinguished in terms of mechanisms (or kinetics). The creep at short term of concrete is due to short-term aging that can be explained by solidification theory [Bažant and Prasannan, 1989a,b]. This solidification theory explains the age dependence of creep compliance of concrete as a result of an increase of the macroscopic stiffness of the material. For concrete, the increase of stiffness is a result of the changes in the proportions of each phase in concrete due to the hydration of cement paste. However, the long-term volume growth history that gives a good description of the age effect on creep does not agree with the known volume growth history of the hydration products of cement [Bažant et al., 1997], so the long-term creep should involve a new mechanism, namely microprestress theory [Bažant et al., 1997]. According to this theory, the origin of creep of hardened cement gel is considered as the shear slips happening in the gel microstructure, driven by the breaks of interatomic bond which are highly localized sites under a very high tensile stress. Creep is thus the macroscopic result of numerous breaks of interatomic bond happening at different times at different overstressed sites.

Another candidate to explain the creep of cementitious materials is the so called theory of dissolution and precipitation under pressure (or pressure solution theory), which is considered as the most important one to explain the time-dependent deformation of rocks [Raj, 1982; Rutter, 1983; Rutter and Elliott, 1976; Weyl, 1959]. The theory demonstrates the macroscopic creep as a result of the geometry change of the solid matrix (e.g. crystals) at microscopic scale. The geometry change is realized by mass transfer which can be regarded as a three-step process: the dissolution of solid under pressure, the diffusion of dissolved mass through the interface of crystals or their aggregates [Coble, 1963] in a very

thin liquid film [Renard and Ortoleva, 1997] and finally the precipitation at new sites. The rate of creep is thus controlled by the step with lowest rate [De Meer and Spiers, 1999; De Meer et al., 1997]. Pachon-Rodriguez et al. [2011] showed recently that dissolution and precipitation under pressure is the main mechanism of creep of gypsum plaster. Pachon-Rodriguez et al.[submitted] showed the theory could also play a role in the creep of Portland cement.

2.6 Creep prediction

2.6.1 Assumptions and limitations

Several predictive models for creep and shrinkage of cementitious materials were proposed in the past in scientific papers and/or in technical guidance documents of national and international associations. Though the assumptions might vary from one model to another, we note a few common ones as follows:

- The total creep strain and shrinkage strains are additive. Creep strain is determined by subtracting the measured shrinkage strains from the measured total strains.
- For compressive creep testing, if the applied stress is less than 40% of the compressive strength of concrete at the age of loading, the total creep strain is proportional to the applied stress.
- The basic creep strain and drying creep strain are additive: drying creep strain can be obtained by subtracting basic creep strain from total creep strain.

The above assumptions must be used with caution and according to the specific conditions considered, which we do not discuss further in this section. The limitations of creep predictive models are twofold: understanding of the phenomenon and availability of data to nourish the models. Due to the complexity of creep phenomenon, widely applied creep models, such as ACI 209, fib model and GL2000 are still largely based on phenomenological approaches with simplified assumptions and empirical equations. In contrast, the most complex model

B3 includes parameters with more physical meanings. For the design of important structures, the long-term creep behavior is of great interest, but most creep data are on relatively short time spans. In the RILEM database, only 8% data includes creep curves with durations of more than 6 years, and ony 5% includes creep curves with durations of more than 12 years [Carreira and Chiorino, 2012]. Furthermore, a large proportion of data is from laboratory experiments in which the characteristics of the samples are quite different from those used in engineering applications. Last but not least, there exists inconstency between some experiemental data and the dispersion of results is quite high. On the other hand, efforts were made recently by Wendner et al. [2013] to extend the experimental database for the calibration of model: the database used to calibrate the new B4 model is three times as large as the RILEM database.

2.6.2 Models and comparison

In this section, we take a closer look at the widely applied models on creep prediction, namely the ACI model, B3 model, fib model (2010) and GL2000 model.

Approved in 1997, the ACI 209R-92 model is the current standard code recommended by American Concrete Institute (ACI). The model is empirical, based on experimental results of shrinkage and creep tests on standard concrete samples which were 300mm in height and 150mm in diameter. The total creep strain is obtained from the compliance function, which is a function of the age of the sample and of the time since loading.

The fib model code (2010) is successor of the CEB model codes of 1990 and 1999. The fib model differs slightly from the earlier CEB models which were based on a team work coordinated by Muller and Hilsdorf in 1990. The GL2000 model was originally proposed by Gardner and Lockman [2001] and then slightly modified by Gardner [2004].

The B3 model was developed by Bažant and Baweja [2000], based on the BP model proposed in 1978 and on the BP-KX model proposed in 1991. Compared with the models mentioned above, the B3 model is the most complicated predictive creep model. The complexity can be readily observed from the number of input parameters (as presented in table 2.1). The B3 model is the only model

Necessary information	ACI 209	B3	fib	GL 2000
Aggregate in concrete	-	X	-	-
Cement content in concrete	-	X	-	-
Type of cement	X	X	X	X
Curing conditions	X	X	-	-
Loading age	X	X	X	X
Compressive strength at loading age	-	-	-	X
Young's modulus at loading age	-	-	X	X
Drying start age	-	X	-	-
Compressive strength at 28 days	X	X	X	X
Young's modulus of concrete at 28 days	X	X	-	-
Relative humidity	X	X	X	X
Shape of specimen	-	X	-	-
Volume to surface ratio	X	X	X	-
Water content	-	X	-	-

Table 2.1: Input parameter of different creep prediction models

which includes a logarithmic part in the compliance function, while the other models are only power law functions, which leads to a creep curve distinct from those predicted by other models especially at long term. The long-term creep rate predicted by the B3 model decreases with $1/t$, where t is the time since the application of loading. This long-term creep rate decreases in $1/t^{0.4}$, $1/t^{0.7}$ and $1/t^2$ for ACI model, GL2000 model and fib model respectively.

From a comparison of these models based on the standard statistical indicators and the complete database, Bažant and Li [2008] conclude that the B3 model is the most accurate, followed by the GL 2000 model.

2.7 Chapter conclusions

Cementitious materials are multi-scale and porous materials. Therefore, creep of those materials happens at different scales and can be influenced by the presence of water in porosity. The effect of various parameters on creep was reviewed based on recent and less recent studies. The main conclusions are as follows:

- Moisture change leads to a higher total creep as a consequence of the occurrence of drying creep. A higher water content leads to a higher basic creep.

- Below a critical stress, basic creep strains are proportional to the applied load. However, above this critical stress, the basic creep strains are no longer proportional to the applied load. The critical value seems to increase with the age of loading and is higher for high performance concrete than normal concrete with the same loading age.
- Adding or replacing cement clinker with a certain proportion of silica fume, fly ash, metakaolin or fiber can reduce the specific creep.
- A higher water-to-cement ratio leads to a higher specific basic creep and total creep.
- A higher volume fraction of aggregates results in a lower specific basic creep.

The creep of cementitious materials is probably due to a combination of mechanisms. The short-term and long-term creep behavior of cementitious materials appear to exhibit different kinetics and may be due to different mechanisms.

For creep prediction, a glance was given at the most widespread models, at their common assumptions and at their complexity.

Part II

Microindentation creep test on cementitious materials - validation for measuring creep of cementitious materials by microindentation

Chapter 3

Indentation technique

Résumé *Ce chapitre est dédié à la présentation de la technique d'indentation. Nous commençons par présenter un test d'indentation typique et l'appareil d'indentation utilisé dans l'étude. Puis nous présentons l'analyse pour évaluer le module d'indentation M et la dureté d'indentation H issus d'un test d'indentation. Enfin, nous élargissons l'analyse aux calculs des propriétés de fluage à partir d'un test d'indentation.*

Abstract *This chapter is dedicated to present the indentation technique. We start by presenting a typical indentation test and the indentation apparatus used in the study. And then we present the analysis for the assessment of the indentation modulus and the indentation hardness from an indentation test. Lastly, we extend the analysis to the back-calculation of creep properties from indentation testing.*

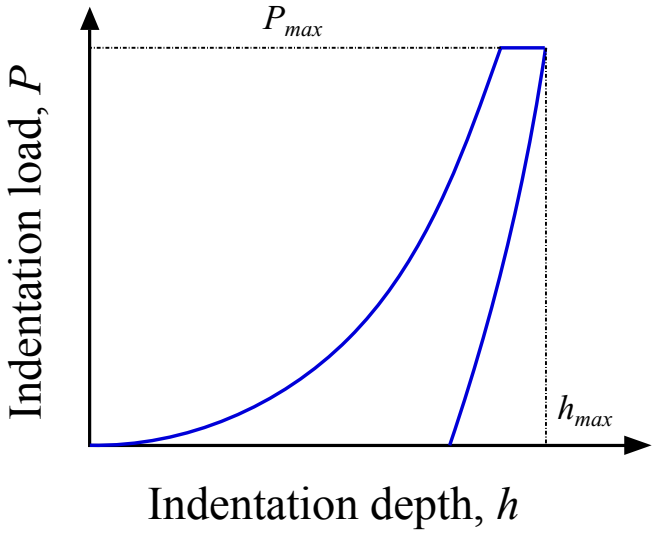

Figure 3.1: Schematic load-depth curve from an indentation test

3.1 Indentation test

A typical indentation test consists of three phases: the loading phase, the holding phase and the unloading phase. In the loading phase, a small probe, i.e., the indentation probe gets into contact with the surface of testing material, a load P is applied to the probe and is increased to a maximum value P_{max}. Due to the application and increment of load, the indentation probe penetrates into the surface of material being tested. In the holding phase, the maximum load is maintained for a given duration. In the unloading phase, the indentation probe is withdrawn from the surface and the load applied is decreased to zero. The applied load P, the depth of penetration h (with a maximum value h_{max}) and the time t are recorded during the test. A schematic presentation of load-depth curve from an indentation test is presented in Fig. 3.1. The load-depth curve can be obtained from an indentation test which can be used for calculating the mechanical properties of tested materials.

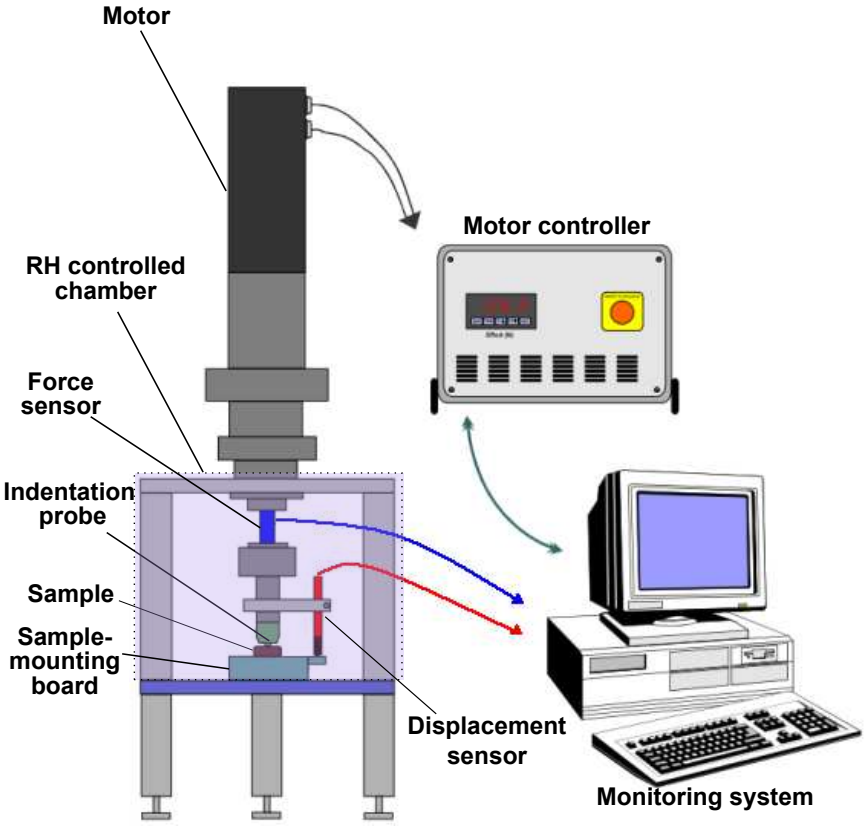

Figure 3.2: Indentation apparatus in Lafarge Research Center.

3.2 Indentation apparatus in Lafarge Research Center

Fig. 3.2 displays a schematic presentation of the indentation apparatus in Lafarge Research Center. The apparatus is used for all the indentation testing experiments that will be mentioned later in the thesis. As shown in Fig. 3.2, the indentation apparatus is equipped with a motor controller, a monitoring system and an indentation platform which consists of a displacement sensor, a force sensor and sample-mounting board. The apparatus is placed in a laboratory where the temperature is precisely controlled at 23°C±0.2°.

The apparatus is also equipped with removable chamber for relative humidity control, during indentation. As presented in Fig. 3.3, relative humidity is con-

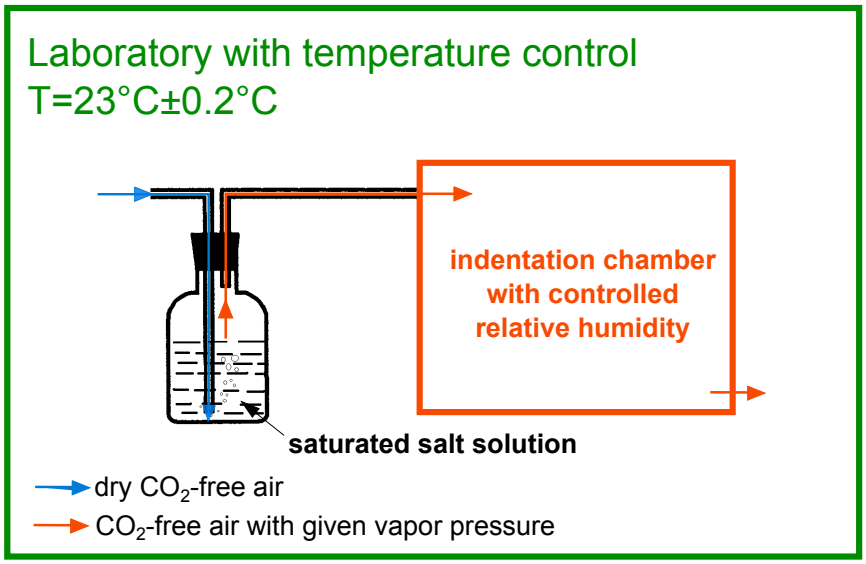

Figure 3.3: Schematic presentation of a simple system to control relative humidity during indentation testing.

trolled in this way: dry CO_2-free air is pumped into saturated salt solution and comes out as humidified air with the water vapor concentration in equilibrium with that near the solution-air boundary. The humidified air is sent into indentation chamber where the relative humidity achieves the same value as the relative humidity of humidified air, after certain time.

The frame compliance of the indentation apparatus was calibrated according to the ASTM E2546 -7 [2007].

3.3 Assessment of indentation modulus and indentation hardness

3.3.1 Indentation modulus

The mechanical problem involved in indentation testing is a typical problem of contact mechanics: the indentation probe penetrates into a flat surface and then is withdrawn from the surface of material of interest. The indentation of an elastic half-space by a rigid flat punch and conical probe was first solved by Love

[1927]. The solution for a rigid axisymmetric indentation probe was developed later by Galin et al. [1961]. This solution is based on the assumption of both small displacement and small deformation. The boundary conditions were set as: stress-free surface outside of the contact area; friction-free surface inside the contact area. For indentation probe with a monomial shape that is characterized by $z = g_0 r^g$ with r being the radius, g_0 and g being geometry coefficients, the following solution links the indentation load P to indentation depth h via effective modulus E_{eff} and parameters depending on the geometry of indenter.

$$P = \frac{2}{(\sqrt{\pi} g_0)^{1/g}} \frac{g}{1+g} \frac{\Gamma(\frac{g+1}{2})}{\Gamma(\frac{g+2}{2})}^{1/g} \cdot E_{eff} \cdot h^{1+1/g} \tag{3.1}$$

where $\Gamma(x) = \int_0^\infty t^{x-1} \exp(-t) dt$ is the Euler Gamma function. To avoid repeating long equation, we introduce a parameter $\varphi = \frac{2}{(\sqrt{\pi} g_0)^{1/g}} \frac{g}{1+g} \frac{\Gamma(\frac{g+1}{2})}{\Gamma(\frac{g+2}{2})}^{1/g}$ and Eq. 3.1 can be rewritten as:

$$P = \varphi E_{eff} \cdot h^{1+1/g} \tag{3.2}$$

A differentiation of the equation above with respect to the indentation depth h gives [Bulychev et al., 1975]:

$$S = \frac{dP}{dh} = \frac{2}{\sqrt{\pi}} E_{eff} \sqrt{A_c} \tag{3.3}$$

where S is the contact stiffness defined by $S = dP/dh$, and A_c is the projected contact area (or briefly, contact area) between the indentation probe and the indented surface. The parameter E_{eff} is called effective modulus or reduced modulus and can be linked to Young's modulus by the following equation:

$$\frac{1}{E_{eff}} = \frac{1-\nu_{in}^2}{E_{in}} + \frac{1-\nu^2}{E} \tag{3.4}$$

where ν_{in} and ν are the Poisson's ratio of the indentation probe and that of the tested material, respectively; E_{in} and E are the Young's modulus of indentation probe and that of the tested material, respectively.

For a rigid indentation probe Eq. 3.4 can be simplified as the following ex-

pression, in which M is termed as indentation modulus:

$$E_{eff} \cong \frac{E}{1-\nu^2} = M \tag{3.5}$$

As one can see from the equation above, similar to other elastic moduli such as Young's modulus and bulk modulus, the indentation modulus is an elastic modulus.

However, the assumption of small perturbation, i.e., small displacement and small deformation, is a very strong assumption. Firstly, infinite stresses occur at the tip of a conical indenter, thus assuming small deformation is erroneous. Secondly, by supposing small displacement, the initial configuration and the actual configuration are merged and the boundary condition is expressed in the initial configuration for the derivation of Galin-Sneddon solution, while during indentation, when a shape indentation probe, gets in touch with the surface being tested, the surface is obviously rotated: the assumption of small deformation is thus inaccurate.

Though Eq. 3.3 is not accurate, this formula is quite handy to use. To correct the deviation of Eq. 3.3, a parameter β was introduced and Eq. 3.3 can be rewritten as:

$$S = \beta(\theta, \nu)\frac{2}{\sqrt{\pi}}E_{eff}\sqrt{A_c} \tag{3.6}$$

By dimension analysis, the factor β is shown to depend only on the Poisson's ratio ν and the geometry of indenter characterized by the half-cone angle θ. Hay et al. [1999] found that β is always greater than 1 and proposed the following equation to calculate β:

$$\beta = \pi\frac{\frac{\pi}{4} + 0.1548\frac{1-2\nu}{4-4\nu}\cot\theta}{(\frac{\pi}{2} - 0.8312\frac{1-2\nu}{4-4\nu})^2} \tag{3.7}$$

Cheng and Cheng [2004] found with finite element modeling that β is almost independent of the plastic properties of the material and that its value should be between 1.04 and 1.12.

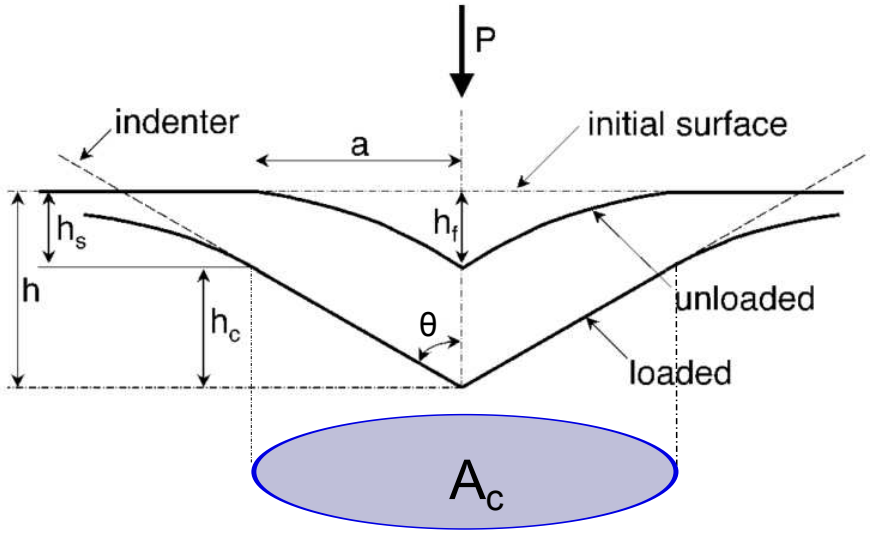

Figure 3.4: Schematic representation of a section through an indentation showing various parameters used in Oliver and Pharr method, schematic adapted from [Oliver and Pharr, 1992].

3.3.2 Determination of projected contact area

To determine the Young's modulus with Eq. 3.6, one needs to find out the projected contact area A_c. Stilwell and Tabor [1961] found that when withdrawing the indentation probe from indented surface, the diameter of the indent changes little: the projected area of residual indent on the surface of tested material is thus comparable with the maximum contact area during indentation test. With this observation, measuring the size of the residual indent left on the surface of tested sample after indentation test can give an estimation of the contact area A_c. In practice, determining the contact area by measuring directly the size of indent on the surface of tested material can be operator-dependent and may lead to poor estimations with materials that exhibit sink-in phenomena, i.e., the indented material around the indentation probe sinks below its original surface [Bhushan and Li, 2003]. At the same time, various indirect methods were proposed by different researchers to determine the projected contact area, among which the most widely applied one is the method of Oliver and Pharr [1992]. As presented in Fig. 3.4, the indentation depth h can be decomposed into two parts: a depth h_c over

Indentation probe	**Shape area function**
Spherical	$-\pi h_c^2 + 2R\pi h_c$
Flat punch	πR^2
Vickers and Berkovich	$24.5 h_c^2$

Table 3.1: Theoretical contact area function of different indentation probes

which the indentation probe is in contact with the indented surface and a depth h_s over which the probe is not in contact with the indented surface:

$$h = h_c + h_s \tag{3.8}$$

The following derivation is suitable for a conical indentation probe. Applying the solution of Sneddon [1965], the depth h_s over which the probe is not in contact of the indented surface can be linked to the residual depth h_f of the indent after withdrawing the indentation probe:

$$h_s = \frac{\pi - 2}{\pi}(h - h_f) = \frac{\pi - 2}{2\pi}\frac{P}{S} \tag{3.9}$$

Deriving from Sneddon's load-displacement relation expressed in Eq. 3.2 and applying it for a conical indentation probe yields:

$$h_c = h_{max} - \epsilon \frac{P_{max}}{S_{max}} \tag{3.10}$$

where $S_{max} = \frac{dP}{dh}|_{P=P_{max}}$ is the maximum contact stiffness at the maximum load, the parameter ϵ depends on the geometry of the indentation probe and is equal to 0.72 for a conical indentation probe. By performing similar derivation, one would obtain $\epsilon = 1$ for a flat punch probe and $\epsilon = 0.75$ for a paraboloid of revolution. Eq. 3.10 thus offers a method to estimate the contact depth between indenter and indented surface. This equation assumes that the surface area beyond the contact points is conformed to the elasticity solution, which is only possible if no piling-up occurs during the test. The estimation of h_c based on this method could thus be poor for materials with piling-up during indentation. The function $A_c(h_c)$ is called the shape area function and depends on the geometry of the indentation probe. This shape area function is given for various probes in Tab. 3.1. In practice, the area functions may differ from the theoretical ones. Especially for

probes with sharp apex (e.g., Berkovich probe) used at sub-micrometric depths, as a consequence of the imperfection of the peak of probe. To take into account this imperfection, a polynomial contact area function was introduced by Oliver and Pharr [1992] as follows:

$$A_c = \sum_{n=0}^{4} h_c^{2^{1-n}} = 24.5h_c^2 + k_1 h_c + k_2 h_c^{\frac{1}{2}} + \cdots + k_8 h_c^{\frac{1}{128}} \tag{3.11}$$

where k_1,..., k_8 are parameters that can be calibrated by indentation on materials with known mechanical properties. The above function has no physical meaning but was proposed for its ability to fit data over a wide range of depths.

We introduce a contact radius a_c which is defined by the following equation:

$$a_c = \left(\frac{A_c}{\pi}\right)^{1/2} \tag{3.12}$$

In case of axisymmetric indentation, contact radius a_c equals to the radius of the projected contact area. This radius will be used later in section 3.4.

3.3.3 Indentation hardness

The indentation hardness H is the average pressure below the indenter, defined by the following equation:

$$H = \frac{P_{max}}{A_c} \tag{3.13}$$

From the above equation, indentation hardness H can be obtained experimentally if one knows the maximum load and the contact area. The concept of hardness can be backtracked to the 18^{th} century by a French scientist named Réaumur who devised a scratching method for hardness comparison in 1722. One century later Mohs devised the ordinal Mohs scale of hardness circa. One of the earliest example of engineering application of indentation methods using the material hardness appeared in the work of Brinell, published in an international congress in Paris [Brinell, 1901]. By pushing a small ball of hardened steel or tungsten carbide against the surface of the specimen, Brinell empirically correlated the shape of impression with the strength of the metal alloys. Indeed, studies showed that the indentation hardness can be related to the strength of

material. Tabor suggested a factor of 3 [Tabor, 2000] between indentation hardness H and the tensile strength σ_t for metals: $H \approx 3\sigma_t$. Based on this result, the indentation hardness is often interpreted as a snapshot of the strength or the plastic properties of the indented material. However, the physical meaning of indentation hardness is still under debate and is known to depend on the elastic properties of the indented material also [Cheng and Cheng, 2004]. The main issue to use indentation hardness to back-calculate the plastic or strength properties lies in the non-unique solutions of the reverse analysis [Chen et al., 2007].

3.4 Assessment of creep properties from an indentation

Indentation test can also be used to measure the creep properties of materials. This section is dedicated to explain how a creep function can be back-calculated from indentation experimental data. We will first consider the case of an indentation into a linear viscoelastic material and then the case of an indentation into a plastic linear viscoelastic material.

3.4.1 Indentation into a linear viscoelastic material

For materials with a linear viscoelastic behavior, the stress history can be related to the corresponding strain history by convolution integrals with time-dependent elastic moduli or creep compliances [Salençon, 1981]. The volume stress history $\boldsymbol{\sigma}_v(t)$ (where $\boldsymbol{\sigma}_v = \frac{1}{3}\text{tr}(\boldsymbol{\sigma})\boldsymbol{I}$, tr is the trace operator and $\boldsymbol{I}$ the second order unit tensor) is related to the volume strain history $\boldsymbol{\epsilon}_v(t)$ (where $\boldsymbol{\epsilon}_v = \text{tr}(\boldsymbol{\epsilon})\boldsymbol{I}$) by the stress convolution integral:

$$\boldsymbol{\sigma}_v(t) = \int_0^t K(t-\tau)\frac{d}{d\tau}\boldsymbol{\epsilon}_v(\tau)d\tau \tag{3.14}$$

where $K(t)$ is called the volume relaxation modulus. The deviatoric strain history $\boldsymbol{\sigma}_d(t)$ (where $\boldsymbol{\sigma}_d = \boldsymbol{\sigma} - \boldsymbol{\sigma}_v$) is related to the deviatoric strain history $\boldsymbol{\epsilon}_d(t)$ by the

stress convolution integral:

$$\boldsymbol{\sigma}_d(t) = \int_0^t G(t-\tau)\frac{d}{d\tau}\boldsymbol{\epsilon}_d(\tau)d\tau \tag{3.15}$$

where $G(t)$ is called the shear relaxation modulus. The Laplace transform of the stress convolution integral of linear isotropic viscoelasticity gives the following equation:

$$\mathcal{L}(\boldsymbol{\sigma}_v(t)) = s \cdot \mathcal{L}(K(t))\mathcal{L}(\boldsymbol{\epsilon}_v(t)) \tag{3.16}$$

and

$$\mathcal{L}(\boldsymbol{\sigma}_d(t)) = s \cdot \mathcal{L}(G(t))\mathcal{L}(\boldsymbol{\epsilon}_d(t)) \tag{3.17}$$

where $\mathcal{L}$ is the Laplace transform operator. For a time-dependent function $f(t)$, the Laplace transform $\mathcal{L}(f(t))$ of $f(t)$ is given by the following equation:

$$\mathcal{L}(f(t)) = \int_0^\infty f(t)e^{-st}dt \tag{3.18}$$

where s is the Laplace parameter and it can be a complex number. A function that leans the same viscous deformation as the volumetric relaxation modulus $K(t)$ is the volumetric creep compliance $J_v(t)$, which links the volume strain history to the volume stress history through the following strain convolution integral [Salençon, 1981]:

$$\epsilon_v(t) = \int_0^t J_v(t-\tau)\frac{d}{d\tau}\sigma_v(\tau)d\tau \tag{3.19}$$

A function that bears the same viscous deformation as the shear relaxation modulus $G(t)$ is the deviatoric creep compliance $J_d(t)$ which links the deviatoric strain history to the deviatoric stress history through the following strain convolution integral [Salençon, 1981]:

$$\epsilon_d(t) = \int_0^t J_d(t-\tau)\frac{d}{d\tau}\sigma_d(\tau)d\tau \tag{3.20}$$

Applying a Laplace transform to Eq. 3.19 and Eq. 3.20 yields:

$$\mathcal{L}(\epsilon_v(t)) = s \cdot \mathcal{L}(J_v(t))\mathcal{L}(\sigma_v(t)) \tag{3.21}$$

$$\mathcal{L}(\epsilon_d(t)) = s \cdot \mathcal{L}(J_d(t))\mathcal{L}(\sigma_d(t)) \tag{3.22}$$

Combining Eq. 3.16 and Eq. 3.21 gives the relation of $K(t)$ and $J_v(t)$ in Laplace domain:

$$s \cdot \mathcal{L}(J_v(t)) = \frac{1}{s \cdot \mathcal{L}(K(t))} \tag{3.23}$$

Combining Eq. 3.17 and Eq. 3.22 yields the relation of $G(t)$ and $J_d(t)$ in Laplace domain:

$$s \cdot \mathcal{L}(J_d(t)) = \frac{1}{s \cdot \mathcal{L}(G(t))} \tag{3.24}$$

Therefore, relaxation moduli and creep compliances are inverse of each other, in the sense of the convolution integrals.

Upon indentation by a rigid indentation probe, an indentation test on an elastic material yields an indentation modulus. If indentation is performed on a linear viscoelastic material, and if the indentation is performed infinitely fast, the measured indentation modulus is noted as M_0, this indentation modulus is an elastic property of the indentation viscoelastic material. Analogously to Eq. 3.14 and Eq. 3.15, applying the correspondence principle of viscoelasticity to the elastic indentation for Eq. 3.2 and for a rigid indentation probe yields:

$$P(t) = \varphi \int_0^t M(t-\tau)\frac{d}{d\tau}h^{1+1/g}(\tau)d\tau \tag{3.25}$$

where $M(t)$ is termed indentation relaxation modulus . Applying a Laplace transform to the equation above yields:

$$\mathcal{L}(P(t)) = \varphi s \mathcal{L}(M(t))\mathcal{L}(h^{1+1/g}(t)) \tag{3.26}$$

We define a parameter $l(t)$ which is homogeneous to compliance:

$$l(t) \overset{def}{=} \frac{\varphi}{P_{max}}h^{1+1/g}(t) \tag{3.27}$$

Performing Laplace transform to the above equation yields:

$$\mathcal{L}(l(t)) = \frac{\varphi}{P_{max}}\mathcal{L}(h^{1+1/g}(t)) \tag{3.28}$$

Considering a Heaviside step loading:

$$P(t) = P_{max}\mathcal{H}(t) \tag{3.29}$$

where $\mathcal{H}(t)$ the Heaviside step function and performing Laplace transform to the above equation yields:

$$\mathcal{L}(P(t)) = P_{max}/s \tag{3.30}$$

Combining the equation above with Eq. 3.26 and Eq. 3.28 yields:

$$\mathcal{L}(l(t)) \overset{\mathcal{H}(t)}{=} \mathcal{L}(L(t)) \tag{3.31}$$

where $L(t)$ satisfies the following equation in Laplace domain:

$$s \cdot \mathcal{L}(L(t)) = \frac{1}{s \cdot \mathcal{L}(M(t))} \tag{3.32}$$

By analogy, the function $L(t)$ is therefore called the contact creep compliance. For a creep test with Heaviside step load, rewriting Eq. 3.31 in time domain yields the time-dependent contact creep compliance expressed in following equation [Vandamme et al., 2011]:

$$L(t) = \frac{\varphi}{P_{max}} h(t)^{1+1/g} \tag{3.33}$$

With the the above equation, one can back-calculate the contact creep compliance with the time-indentation depth, the maximum load and the information on the geometry of the indentation probe.

3.4.2 Indentation into a plastic linear viscoelastic material

Under shape indentation probe, plasticity occurs because of concentration of stress at the tip of indentation probe, even at the lowest loads. Because of this plasticity, the penetration of the indentation probe into the material is not only due to linear viscoelastic effects, so that Eq. 3.33 can no more be used to back-calculate creep properties from indentation data. Therefore, one needs an alternative method to back-calculate creep properties in such case of indentation into a plastic linear viscoelastic material.

By introducing a fictitious indentation test with an instantaneous loading phase, an instantaneous unloading phase and an instantaneous-reloading-and-holding phase, Vandamme et al. [2011] derived a method to back-calculate creep properties from an indentation in which time-independent plasticity occurs. Here we briefly present the derivation to obtain the contact creep compliance $L(t)$, which will be used in the analysis of experimental results presented in following chapters. Note that the main assumption in their derivation is that time-independent plasticity occurs only during the loading phase but not during the holding or unloading phases.

Their demonstration starts by writing, in the case of elastic indentation, the contact radius a_c as a function of indentation depth:

$$a_c = f(h) \tag{3.34}$$

The analytical expression of function f is generally unknown. But as one will find out later, knowing explicitly the expression of f is not necessary in the derivation. Integrating Eq. 3.6 with respect to indentation depth h yields:

$$P = 2MF(h) \tag{3.35}$$

where $F(h)$ is the primitive function of $f(h)$ for which $F(0)$=0. Rewriting Eq. 3.35 in the time domain for a linear viscoelastic material by applying the correspondence principle, one obtains:

$$P(t) = 2\int_0^t M(t-\tau)\frac{d}{d\tau}F(h(\tau))d\tau \tag{3.36}$$

Performing Laplace transform to Eq. 3.36, one obtains:

$$\mathcal{L}(P(t)) = 2s \cdot \mathcal{L}(M(t))\mathcal{L}(F(h(t))) \tag{3.37}$$

In the case of a step load, combining Eq. 3.32, Eq. 3.30 and Eq. 3.37, one obtains the following equation which links the contact creep compliance $L(t)$ to indentation data in Laplace domain:

$$\mathcal{L}(L(t)) = \frac{2}{P_{max}}\mathcal{L}(F(h(t))) \tag{3.38}$$

Performing inverse Laplace transform on the equation above, one obtains the time-dependent contact creep compliance in the time domain as a function of indentation depth during the holding phase:

$$L(t) = \frac{2F(h(t))}{P_{max}} \tag{3.39}$$

After differentiating Eq. 3.39 with respect to time, one obtains the relation of interest [Vandamme et al., 2011]:

$$\dot{L}(t) = \frac{d}{dt}\frac{2F(h(t))}{P_{max}} = \frac{2f(h(t)) \cdot \dot{h}(t)}{P_{max}} = \frac{2a_c(t)\dot{h}(t)}{P_{max}} \tag{3.40}$$

which links the derivative of the contact creep compliance to the rate of penetration of the indentation probe during the holding phase. For flat punch indentation probe, as the contact radius a_c is constant, Eq. 3.40 can be written as:

$$\dot{L}(t) = \frac{2a_c\dot{h}(t)}{P_{max}} \tag{3.41}$$

For other indentation probes, $a_c(t)$ evolves with h_c, but Eq. 3.41 can also be reasonably applied if $a_c(t)$ does not change too much during the holding phase. Because of apparatus limitations such as thermal drift, after some time the rate of penetration can no more be accurately measured, so that the durations of holding phase are typically limited to several minutes. For nanoindentation performed on cement paste by a Berkovich indentation probe, the contact radius $a_c(t)$ over a 180s holding phase is estimated to vary about 5% [Vandamme, 2008]. Therefore, assuming that the contact radius remains constant during the holding phase is realistic. The contact radius during holding can therefore be estimated by the contact radius at the start of unloading and can be estimated by the Oliver and Pharr's method mentioned in section 3.3.

Integrating Eq. 3.41 with respect to time from the beginning of holding phase yields:

$$L(t) - L(0) = L(t) - \frac{1}{M_0} = \frac{2a_c\Delta h(t)}{P_{max}} \tag{3.42}$$

where $\Delta h(t)$ is the change of indentation depth during the holding phase. The difference $L(t) - L(0)$ between the contact creep compliance $L(t)$ and the recip-

rocal of indentation modulus $L(0) = 1/M_0$ at the moment of loading is termed the contact creep function.

The used of Eq. 3.41 or Eq. 3.42 to back-calculate creep properties enables to obtain a contact compliance that is a material property. The use of linear viscoelastic formula such as Eq. 3.33 can yield, in case of indentation with sharp probe, a contact creep compliance that may not be representative of the properties of tested material because of the occurrence of plasticity. As one may see in following chapters, Eq. 3.42 will be applied to back-calculate the creep properties from indentation tests.

3.5 Chapter summary

In this chapter, we presented the indentation technique and the associated analysis for the assessment of indentation modulus and indentation hardness. We also presented how to back-calculate creep properties from indentation experimental data. We derived formulae valid in the case of indentation into a linear viscoelastic material (see section 3.4.1). However, those formulae are not useful in the case of indentation with a sharp probe, in which time-independent plasticity occurs even at small load. In such case, the contact creep compliance must be back-calculated with a formula applicable when time-independent plasticity occurs, as is the case with Eq. 3.41 or Eq. 3.42. In the following chapters, we will make use of those equations to back-calculate creep properties from indentation creep experiments.

Chapter 4

Comparative study on cement paste and concrete

Résumé *Ce chapitre est consacré à comparer des tests de fluage par microindentation de quelques minutes sur de la pâte de ciment avec des tests de fluage macroscopique de plusieurs années sur le béton d'une part et de plusieurs mois sur la pâte de ciment d'autre part (toutes les tests de fluage macroscopique par compression uniaxiale ont été réalisés par Le Roy [1996]. Pour l'ensemble de ces tests, après une période transitoire, la fonction de fluage a été décrite de façon satisfaisante par une fonction logarithmique du temps. Les périodes transitoires non logarithmiques ont duré plusieurs jours à l'échelle macroscopique, mais seulement quelques secondes à l'échelle de la microindentation. Les modules de fluage (qui définissent donc le taux de fluage logarithmique à long terme) des échantillons de béton ont été estimés à partir de la microindentation réalisée à l'échelle des pâtes de ciment en combinaison avec des modèles micromécaniques. Ces estimations se sont révélées être proportionnelles au module de fluage mesuré sur les échantillons de béton par des expérimentations de macroscopie uni axiale usuelle, montrant ainsi que la microindentation de quelques minutes peut permettre de mesurer les propriétés de fluage à long terme des matériaux cimentaires.*

Abstract *This chapter is dedicated to comparing minutes-long microindentation creep experiments on cement paste with years-long macroscopic creep experiments on concrete and months-long macroscopic creep experiments on cement*

paste. All the macroscopic uniaxial creep experiments were carried out by Le Roy [1996]. For all experiments, after a transient period the creep function was well captured by a logarithmic function of time, the amplitude of which is governed by a so-called creep modulus. The non-logarithmic transient periods lasted for days at the macroscopic scale, but only for seconds at the scale of microindentation. The creep moduli (which thus govern the rate of the long-term logarithmic creep) of concrete samples were estimated from the microindentation performed at the scale of the cement pastes in combination with micromechanical models. Those estimates were proportional to the creep modulus measured on the concrete samples by regular macroscopic uniaxial testing, thus proving that minutes-long microindentation can provide a measurement of the long-term creep properties of cementitious materials.

4.1 Chapter introduction

This chapter is dedicated to verify whether an estimation of the macroscopic creep behavior of concrete samples can be inferred from microindentation tests performed at the scale of the cement paste. With this objective, we compared minutes-long microindentation creep experiments on cement paste samples with months-long macroscopic uniaxial creep experiments on cement paste samples and years-long macroscopic uniaxial creep experiments on concrete samples. All the macroscopic uniaxial creep experiments were carried out by Le Roy [1996], a brief summary on materials and associated methods will be given later in this chapter to facilitate the comparison.

4.2 Materials and methods

4.2.1 Materials

Cement samples were prepared with materials identical to those used in [Le Roy, 1996]. So in this section, both materials used in [Le Roy, 1996] for compressive creep testing and the materials used here for indentation will be mentioned and compared.

All cement paste samples and concrete samples were made with Portland cement (class CEM I 52.5). Both clinkers from Saint Vigor (Lafarge, France) and from Saint-Pierre-la-Cour (Lafarge, France) were used, which contain different amounts of tricalcium aluminate (see Tab. 4.1). Concrete samples and cement samples for uniaxial creep testing were manufactured in 1992, while cement samples for microindentation creep testing were manufactured in 2011. Clinkers from Saint Vigor used in 1992 and in 2011 were from the same factory, as was the case for clinkers from Saint-Pierre-la-Cour. The composition of the clinkers used in the various samples is provided in Tab. 4.1, while their physical properties are provided in Tab. 4.2. Although the clinkers used in the samples for uniaxial testing and for microindentation testing were manufactured about 20 years apart, the composition and the specific gravity of the two batches differed very little from each other. The proportion of the main phases in the clinkers used to prepare cement pastes for microindentation testing is given in Tab. 4.3.

	year	CaO	SiO_2	Al_2O_3	Fe_2O_3	SO_3	LOI[(a)]
cement from Saint Vigor	1992	64.25	22.49	3.60	4.00	2.50	1.48
	2011	64.76	20.87	3.58	4.45	2.45	1.06
cement from Saint-Pierre-la-Cour	1992	65.30	19.72	4.98	2.71	3.36	1.30
	2011	63.94	20.06	4.93	2.86	3.67	1.45
silica fume from Laudun	1992	-	87.00	-	-	-	3.09
	2011	-	93.31	-	-	-	3.43

Table 4.1: Mass percentage of chemical components in the clinkers and silica fume used in this study. Data is provided by manufacturer. For clinker and silica fume, respectively, only mass percentages greater than 1% and than 3% are given.
(a) LOI: loss on ignition.

	year	specific surface ($m^2.g^{-1}$)	specific gravity ($g.cm^{-3}$)
cement from Saint Vigor	1992	0.35	3.17
	2011	0.35	3.18
cement from Saint-Pierre-la-Cour	1992	-	-
	2011	0.45	3.11
silica fume from Laudun	1992	17.6	2.20
	2011	21.3	-

Table 4.2: Physical properties of clinker and silica fume used in this study. Data is provided by manufacturer.

In some samples, silica fume was used as an additive. Both silica fume used in 1992 and in 2011 were from Laudun (France). As can be observed in Tab. 4.1, from one set to the other the content of SiO_2 varied by about 6%. And Tab. 4.2 shows that the specific gravity of the silica fume used in 2011 was about 20% greater than that of the silica fume used in 1992. To some samples a superplasticizer was added (see Tab. 4.4), the solid content of which was 30.5% and the effective component of which was melamine.

cement	C_3S	C_2S	C_3A	C_4AF	gypsum
Saint Vigor (2011)	60.0	22.4	1.20	12.9	1.30
Saint-Pierre-la-Cour (2011)	59.9	17.6	7.40	9.40	0.30

Table 4.3: Proportion of the main phases in the clinkers used in 2011 to prepare cement paste samples for microindentation testing, determined by Rietveld X-ray diffraction quantification. Data is from the manufacturer (Lafarge).

The mix formulation of the various samples is given in Tab. 4.4. Cylindrical concrete samples were prepared in 1992 with seven various mix formulations. For each formulation, four samples were dedicated to uniaxial strength testing (the diameter of these samples was 110mm and their height was 220mm), one sample was dedicated to autogenous shrinkage testing (the diameter of this sample was 160mm and its height was 1000mm), and the last sample was dedicated to uniaxial creep testing the geometry of this sample was the same as that of the sample dedicated to autogenous shrinkage). The mix formulations of those concretes differed by the water-to-cement ratio w/c, the mass ratio s/c of silica fume to clinker, and the volume fraction of aggregates (i.e., of sand and gravel).

Six groups of cylindrical cement paste samples were prepared in 1992 with a diameter equal to 20mm and a height equal to 160mm. For each group, two samples were prepared: one was used for autogenous shrinkage test and the other one for uniaxial creep test. The mix formulations of those pastes differed by the water-to-cement ratio w/c, the mass ratio s/c of silica fume to clinker, and the type of clinker used (from Saint Vigor or from Saint-Pierre-la-Cour). Samples with identical mix formulations and geometry were prepared again in 2011 for microindentation creep test. In addition, the cement paste P33-1SV (see Tab. 4.4 for sample designation) was also prepared for microindentation testing, although paste with this mixing formulation was not tested by uniaxial test: by doing so, all cement pastes used in both cement pastes and concretes in 1992 were manufactured again in 2011 for microindentation test.

Samples were prepared according to the following procedure. For cement paste samples the mixing consisted in:

- add the solid raw materials, the water, and one third of the superplasticizer and mix for 3 minutes;
- add the rest of superplasticizer and mix for 2 minutes;

For concrete samples the mixing consisted in:

- add the solid raw materials and mix for 1 minute;
- add water and one third of the superplasticizer and mix for 1 minute;
- add the rest of the superplasticizer;

sample	**cement**	w/c	s/c	p/c	f_{agg} (%)	**1992**	**2011**
P28-0SV	Saint Vigor	0.28	0.0	1.5%	-	X	X
P38-0SV	Saint Vigor	0.38	0.0	0.0%	-	X	X
P50-0SV	Saint Vigor	0.50	0.0	0.0%	-	X	X
P28-1SV	Saint Vigor	0.28	0.1	1.5%	-	X	X
P33-1SV	Saint Vigor	0.33	0.1	1.5%	-		X
P38-1SV	Saint Vigor	0.38	0.1	1.5%	-	X	X
P38-0LC	Saint-Pierre -la-Cour	0.38	0.0	1.5	-	X	X
B28-1	Saint Vigor	0.28	0.1	4.7%	71.0	X	
B38-1	Saint Vigor	0.38	0.1	4.9%	71.3	X	
B50-0	Saint Vigor	0.50	0.0	0.0%	70.5	X	
B33-1A	Saint Vigor	0.33	0.1	4.9%	67.3	X	
B33-1B	Saint Vigor	0.33	0.1	4.9%	69.5	X	
B33-1C	Saint Vigor	0.33	0.1	4.8%	71.5	X	
B33-1D	Saint Vigor	0.33	0.1	4.9%	73.1	X	

Table 4.4: Mix formulations of cement paste samples (the denomination of which starts with the letter P) and concrete samples (the denomination of which starts with the letter B) prepared in this study. w/c denotes the water-to-cement mass ratio; s/c stands for the mass ratio of silica fume to clinker; p/c denotes the superplasticizer to cement ratio; f_{agg} denotes the volume fraction of aggregates (i.e., gravel and sand) in concrete. Samples prepared in 1992 were used for uniaxial creep experiments; samples prepared in 2011 were used for microindentation creep experiments.

For both cement paste samples and concrete samples:

- pour mixture into molds;
- evacuate embedded gas bubbles by vibrating sample on a vibration table;
- unmould sample 24 hours after mixing and envelop in 2 layers of self-sealing aluminum paper;
- conserve samples at 20°C±1°C and at a relative humidity 50% ± 5% till testing.

For cement paste samples only, right after vibration the samples were rotated for 15 hours after mixing in order to prevent any segregation.

4.2.2 Uniaxial compressive creep experiments on concrete and cement

In this section we give some descriptions of the uniaxial compressive creep experiments from Le Roy [1996] to facilitate the comparison. More details can be found in [Le Roy, 1996].

On the concrete samples, basic creep was measured up to 15 years. This basic creep was obtained by performing in parallel autogenous shrinkage test on one sample and creep test on another sample with identical mix formulation and geometry. The autogenous shrinkage test started 24 hours after casting. During this test, no load was applied to the sample and the axial strain due to shrinkage or the shrinkage strain $\epsilon_s(t)$ was measured over time. The creep test by uniaxial compression started 28 days after casting. During creep test, a uniaxial compressive stress σ_u equal to 30% of the 28-day uniaxial compression strength was applied and kept constant over time, and the axial strain $\epsilon_t(t)$ was measured over time. The reference time $t = 0$ corresponds to the time at which the load was applied for the creep experiments, i.e., to 28 days after casting. The compression strength was obtained on a distinct sample with the same mix formulation and the same geometry just before the commencement of the creep test, by following the then-used French standard NFP 18-406. The duration of the tests varied from 150 days to 5230 days for the various samples. All tests were performed in sealed conditions at 20°C ± 2°C.

On the cement paste samples, basic creep was measured, again by performing in parallel an autogenous shrinkage test and a creep test on samples with identical mix formulation and geometry. Autogenous shrinkage experiments started 24 hours after mixing. Creep experiments under uniaxial compression started 28 days after casting. The axial stress applied on sample P50-0SV was 9.4 MPa (i.e., about 28% of its compressive strength 28 days after mixing). For all other cement paste samples, the applied stress was 15.6 MPa (i.e., about 13% to 22% of their compressive strengths 28 days after mixing). The duration of the creep test was of about 100 days for all samples. All tests were performed in sealed conditions at 20°C ± 2°C.

As already mentioned in section 2.4.2, at constant temperature, the basic creep $\epsilon_b(t)$ can be obtained as the difference between the total axial strain $\epsilon_t(t)$ measured on the cement paste sample under load and the shrinkage strain $\epsilon_s(t)$ due to autogenous shrinkage and measured on the cement paste sample subjected to no load: $\epsilon_b(t) = \epsilon_t(t) - \epsilon_s(t)$. From the measured basic creep strain, the uniaxial creep functions $J_u(t)$ of the various cement paste samples were obtained with Eq. 4.2. Here the reference time $t = 0$ also corresponds to the time at which the load was applied for the creep experiments, i.e., to 28 days after casting.

As mentioned in section 3.4, similar to Eq. 3.19, a linear viscoelastic material subjected to a known uniaxial stress $\sigma_u(t)$ applied over positive time $t > 0$, the resulting uniaxial strain $\epsilon_u(t)$ can be calculated through the uniaxial creep compliance $J_u(t)$ with [Salençon, 1981]:

$$\epsilon_u(t) = \int_0^t J_u(t-\tau)\dot{\sigma_u}(\tau)d\tau \tag{4.1}$$

where $\dot{f}$ stands for the time derivative of a function f. At time $t = 0$, the uniaxial creep compliance must be equal to: $J_u(t = 0) = 1/E_0$, where E_0 is the elastic Young's modulus of material. The function $J_u(t) - J_u(0) = J_u(t) - 1/E_0$ is known as the uniaxial creep function.

For mature concrete subjected to negligible variations of temperatures, linear viscoelasticity is expected to apply reasonably well, as long as the applied stresses increase or slightly decrease over time [Huet et al., 1982]. For such materials, which can also be subjected to drying-induced shrinkage or autogenous shrinkage, the correct strain to consider in Eq. 4.1 is the so-called basic creep strain $\epsilon_b(t)$.

From the uniaxial experiments here performed on concrete samples, this basic creep strain $\epsilon_b(t)$ was obtained as the difference between the total axial strain $\epsilon_t(t)$ measured on the concrete sample under load and the axial strain $\epsilon_s(t)$ due to autogenous shrinkage and measured on the concrete sample subjected to no load: $\epsilon_b(t) = \epsilon_t(t) - \epsilon_s(t)$. Since the load was kept constant over time during the macroscopic creep experiments, a direct use of Eq. 4.1 shows that the uniaxial basic creep compliance $J_u(t)$ of the concrete samples could be obtained with the following formula:

$$J_u(t) = \frac{\epsilon_b(t)}{\sigma_u} = \frac{\epsilon_t(t) - \epsilon_s(t)}{\sigma_u} \tag{4.2}$$

The creep experiments started 28 days after casting, so that we neglected the aging feature of the viscous behavior. The reference time $t = 0$ corresponds to the time at which the load was applied for the creep experiments. For concrete samples B28-1, B33-1A, B33-1B, and B33-1D, the shrinkage experiments were terminated between 1289 and 1338 days after loading. For these samples, subsequent autogenous shrinkage was estimated by extrapolating the experimental data with the function $\epsilon_s = \epsilon_s^\infty (t/t_0)^a / ((t/t_0)^a - b)$, in which $t_0 = 1$ day and the parameters ϵ_s^∞, a and b were fitted for each sample.

4.2.3 Microindentation creep experiments on cement paste

Microindentation tests with different holding duration were carried out on cement samples carried out at age of 28 days after casting. One day before testing, the samples were moved into the room in which the indentation apparatus was located and the temperature was controlled at 23°C. About five minutes before testing, a 10-millimeters-thick disk was cut from the median part of the cylindrical sample. The surface to be indented was then polished with 4 pads of silicon carbide (SiC) paper with decreasing particle size. Polishing lasted for about 3 minutes, without any contact with water or other solvents. With respect to the polishing procedure recommended by Miller et al. for nanoindentation testing of cementitious materials [Miller et al., 2008], the duration of the procedure we used here was much shorter. Indeed, since the scale of microindentation testing is much larger than that of nanoindentation testing, our requirements on surface roughness were much less strict than for those authors. In addition, a rapid

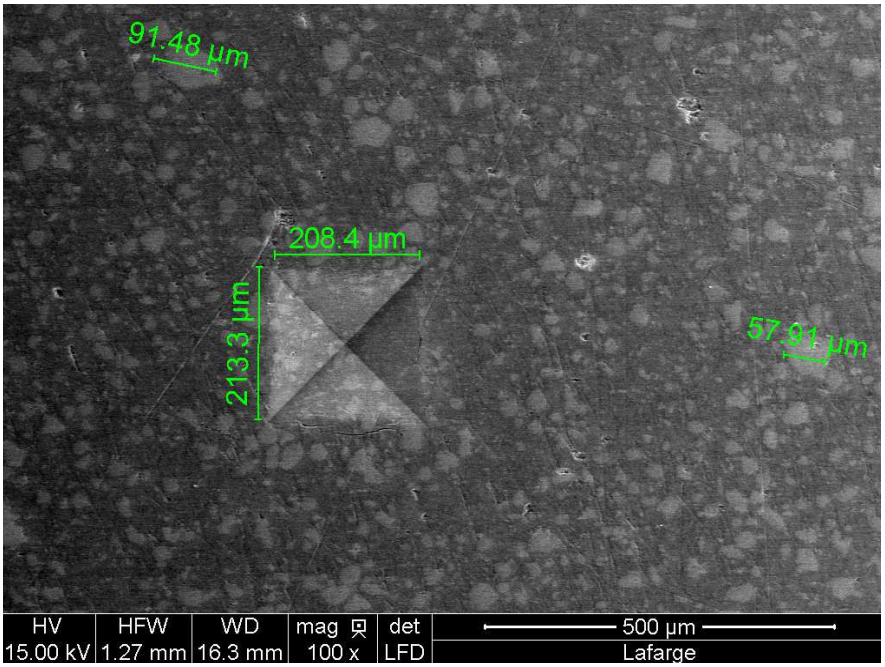

Figure 4.1: Scanning electron microscopy picture of the surface of an indented cement sample.

procedure also allowed to minimize drying. A typical surface with a typical indent is presented in Fig. 4.1. As can be observed, the scale of the indent is greater than the characteristic scale of the microstructure of the cement paste: thus, the performed microindentation tests provided the mechanical properties of the cement paste itself (and not of the individual phases of which this cement paste is constituted).

On each sample, 10 microindentation tests were performed with a Vickers indenter probe and a maximal applied force of 20N. For each indent, the load was increased linearly over time in 15 seconds, kept constant during the holding phase, and decreased linearly over time back to zero in 15 seconds. Out of the 10 indents performed on each sample, 5 were with a relatively short 20-seconds-long holding phase, while 5 were performed with a relatively long 300-seconds-long holding phase. Indentation test with a 20-seconds-long holding phase enabled to measure the reduced modulus E_{eff}; on supposing Poisson's ratio $v = 0.2$, the Young's modulus of cement paste was calculated (see section 3.3). The Young's modulus of cement paste samples is presented in Fig. 4.5.

Indenter	Vickers
Maximum indentation load P_{max}	20N
Maximum indentation depth h_{max}	35-87µm
Holding duration τ_H	20 seconds, 5 minutes or 30 minutes
Temperature	23°±0.2°
Relative humidity	91%±2%

Table 4.5: Experimental parameter settings of indentation experiments on cement paste.

Indents with a 300-seconds-long holding phase enabled to measure the creep properties of the paste. The contact creep function $L(t)-L_0$ can then be obtained by applying Eq. 3.42.

On sample P38-0SV, one indentation creep experiment with a 1800-seconds-long holding phase was also performed in order to determine the shape of the creep function at longer term. For this last experiment, the maximal load still was 20 N, the duration of the loading phase 15s, and the duration of the unloading phase 15s.

The internal relative humidity of cement paste cured in sealed conditions at temperature of 20°C varies from 90% to 98% at the age of 28 days [Jiang et al., 2005; Saengsoy et al., 2008]. Therefore, in order to avoid drying during testing, all microindentation creep experiments were performed in an environment with a relative humidity equal to 91% ± 2% and temperature equal to 23°C ± 0.2°C. By doing so, we expect drying-induced strains to be negligible with respect to the strains induced by creep. Moreover, at the age of 28 days, the autogenous shrinkage of cement over the duration of the 5-minutes-long creep phase can be neglected with respect to the strains induced by creep. As a consequence, the contact creep compliance $L(t)$ is expected to characterize the basic creep of the cement paste. A summary of indentation experimental parameters is presented in Tab. 4.5.

4.3 Results

4.3.1 Creep functions of compressive tests and indentation tests

Figure 4.2 displays the uniaxial basic creep functions $J_u(t) - 1/E_0$ of the cement paste samples obtained by uniaxial compression. In this figure, $t = 0$ stands for the time at which loading was applied. For samples with no addition of silica fume, creep increased with the water-to-cement ratio w/c. For samples with 10% of silica fume added, varying the water-to-cement ratio w/c from 0.28 to 0.38 hardly varies amplitude of creep. For a given water-to-cement ratio (i.e., $w/c = 0.28$ or $w/c = 0.38$), adding 10% of silica fume decreases creep. For given mix proportions, changing the clinker (i.e., using a clinker from Saint Vigor (sample P38-0SV) or from Saint-Pierre-la-Cour (sample P38-0SL) slightly modified the creep of the paste: however, after a few days, the difference between the two basic creep functions mostly remained constant over time, which means that the difference between the creep of those two pastes was mostly due to the time-dependent behavior of the pastes during the first days of loading.

The basic creep functions of the concrete samples obtained by uniaxial compression are displayed in Fig. 4.3. In a consistent manner with the results obtained on cement pastes, this figure shows that basic creep of concrete increased with the water-to-cement ratio w/c. A comparison of the results for samples B33-1A, B33-1B, B33-1C, and B33-1D shows that, globally, creep decreases when the volume fraction of aggregates increases, though scattering hides this trend partially for sample B33-1B.

4.3.2 Direct comparison of microindentation on cement paste with uniaxial compression on cement paste

In this section, we aim at comparing results obtained by microindentation test with results obtained by regular macroscopic uniaxial testing, both in terms of elastic properties and in terms of creep properties.

Assuming a Poisson's ratio $\nu = 0.20$ for the samples, Eq. 3.5 enabled to calculate the Young's modulus E_0 of the indented cement pastes. The Young's

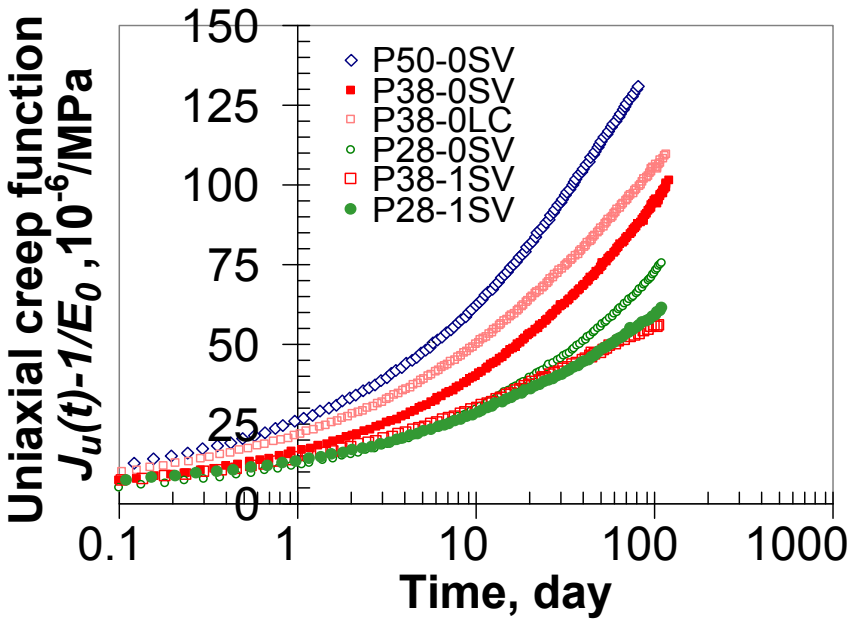

Figure 4.2: Uniaxial basic creep functions of cement paste samples obtained by uniaxial compressive creep testing [Le Roy, 1996].

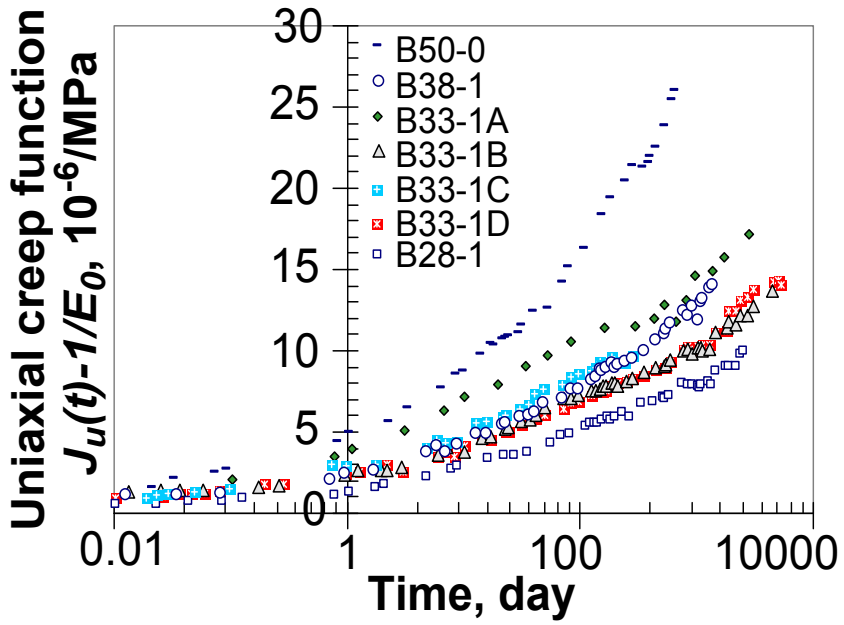

Figure 4.3: Uniaxial basic creep functions of concrete obtained from uniaxial compressive creep testing [Le Roy, 1996].

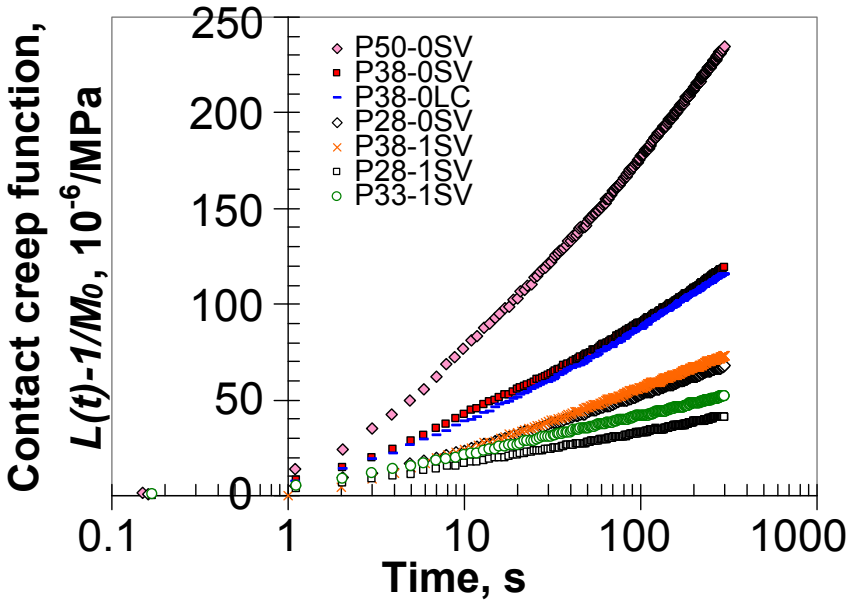

Figure 4.4: Contact creep functions $L(t) - 1/M_0$ of cement paste samples obtained by microindentation. For each sample, out of the 5 experiments performed, only the median curve is displayed.

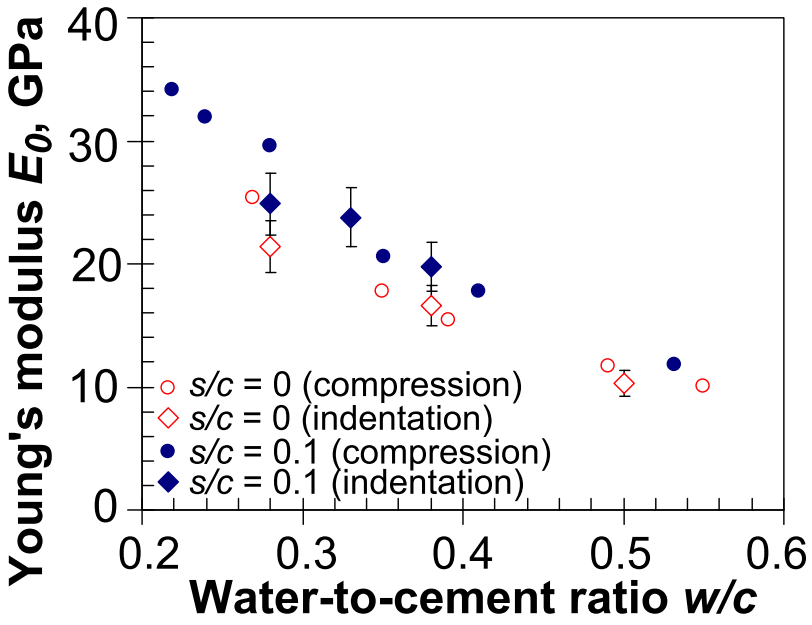

Figure 4.5: Young's modulus E_0 of the cement paste samples, determined by indentation test when assuming a Poisson's ratio $\nu = 0.20$ and determined by macroscopic uniaxial compression test. s/c stands for the mass ratio of silica fume to clinker. Experimental data for compression is from Marchand [1992].

modulus of the cement samples manufactured in 1992 were measured by Marchand [1992] by regular macroscopic compression. Both sets of data are displayed in Fig. 4.5. The agreement between the Young's modulus of the cement pastes prepared in 2011 for indentation test and of the cement pastes prepared in 1992 for uniaxial testing is excellent, which proves that, by using similar raw materials and protocols of preparation, very similar cement pastes were prepared, although almost 20 years apart.

We now aim at comparing directly the creep functions obtained by uniaxial test and by microindentation test. In order to do so, we focus on sample P38-0SV, on which a microindentation creep experiment with a 1800-seconds-long holding phase was performed. Both the derivative dL/dt with respect to time of the contact creep function obtained by microindentation test and the derivative dJ_u/dt of the uniaxial creep function obtained by macroscopic uniaxial test are displayed in Fig. 4.6. One readily observes that, over the half hour compared,

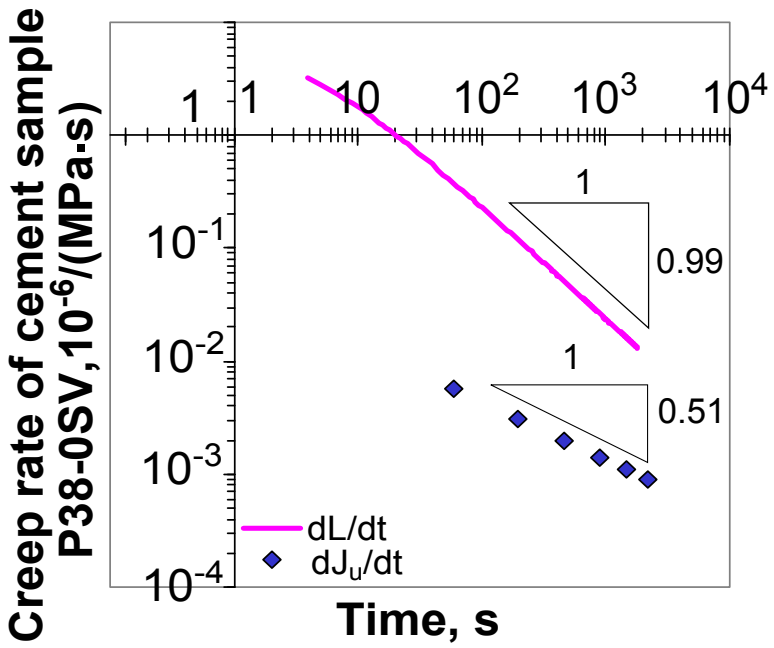

Figure 4.6: Derivatives with respect to time of the contact creep compliance obtained by microindentation test and of the uniaxial creep compliance obtained by macroscopic compression test on cement paste sample P38-0SV.

the rates measured by the two techniques differed by one or even two orders of magnitude. In addition, a linear regression of this figure in a log-log scale shows that, from 1 minute to 30 minutes, the rate of the creep function measured by uniaxial test decreased as $t^{-0.51}$ while the rate of the creep function measured by microindentation test decreased as $t^{-0.99}$. From this simple comparison directly on creep function, we conclude that the microindentation technique does not give the same creep function as macroscopic uniaxial test.

4.3.3 Comparison of long-term logarithmic kinetics of creep

From the microindentation creep data on cement pastes displayed in Fig. 4.4, one observes very clearly that, on the last two decades of the test, creep was logarithmic with respect to time. For the microindentation performed on sample P38-0SV with a 1800-seconds-long holding phase, creep was logarithmic on almost 3 decades (see Fig. 4.7c). Although less clearly, such logarithmic kinetics of creep can also be observed on about one decade for what concerns the uniaxial

creep data on cement paste (see Fig. 4.2) and on about one to two decades for the data on concrete (see Fig. 4.3). Moreover, this kinetics is reminiscent of the long-term basic creep of cementitious materials, which, as proposed by Bažant and others, can be well modeled by a logarithmic function of time [Bažant and Baweja, 1995; Ulm et al., 1999]. Therefore, those observations suggest that not only years-long uniaxial creep experiments on concrete and months-long uniaxial creep experiments on cement paste, but more surprisingly, also minutes-long microindentation creep experiments on cement paste were all long enough in order to reach the long-term creep of the tested material, which exhibits a logarithmic kinetics.

In order to compare quantitative parameters, we fitted the measured creep data with logarithmic functions. More precisely, the indentation creep function obtained on cement paste was fitted with:

$$L(t) - \frac{1}{M_0} = \frac{\ln(t/\tau_i + 1)}{C_i} \tag{4.3}$$

The uniaxial creep function obtained by uniaxial compression was fitted with:

$$J_u(t) - \frac{1}{E_0} = \frac{\ln(t/\tau_u + 1)}{C_u} \tag{4.4}$$

The parameters C_i and C_u are termed contact creep modulus and uniaxial creep modulus, respectively. The greater they are, the lower the amplitude of creep is. In the case of uniaxial test, in order to differentiate between values obtained for cement paste and for concrete, the following notations are used: when the fit is performed for cement paste, the fitted parameters τ_u and C_u are noted as $\tau_{u,cem}$ and $C_{u,cem}$, respectively; when the fit is performed for concrete, the fitted parameters τ_u and C_u are noted as $\tau_{u,con}$ and $C_{u,con}$, respectively.

With such a choice of fitting functions, each creep function is condensed into 2 parameters: a characteristic time (noted τ_u when obtained from uniaxial test and τ_i when obtained from indentation test) and a creep modulus (noted C_u when obtained from uniaxial test and C_i when obtained from indentation test). The characteristic time characterizes the time at which creep starts exhibiting a logarithmic kinetics. The creep modulus governs the rate of this long-term kinetics:

sample	$\tau_{u,cem}$ **(day)**	τ_i **(second)**
P28-0SV	4.8	2.2±0.6
P38-0SV	3.7	3.2±0.7
P50-0SV	2.6	2.4±0.8
P28-1SV	2.1	1.5±0.4
P33-1SV	-	1.3±0.4
P38-1SV	0.9	2.4±0.6
P38-0LC	2.1	3.3±0.3
sample	$\tau_{u,con}$ **(day)**	
B28-1	2.2	-
B38-1	2.5	-
B50-0	2.3	-
B33-1A	0.2	-
B33-1B	1.4	-
B33-1C	0.5	-
B33-1D (data until 5320 days)	2.8	-
B33-1D (data until 1800 days)	1.1	-

Table 4.6: Characteristic time τ_u obtained by uniaxial compression creep experiment and τ_i obtained by indentation creep experiment.

$$\frac{dJ_u}{dt} \approx \frac{1}{C_u t} \text{ if } t \gg \tau_u \tag{4.5}$$

$$\frac{dL}{dt} \approx \frac{1}{C_i t} \text{ if } t \gg \tau_i \tag{4.6}$$

Figure 4.7 displays the best fits obtained with the functions introduced in Eqs. (4.3) and (4.4). The best-fit parameters are presented in Tab. 4.6, Tab. 4.7, and Tab. 4.8. Tab. 4.6 shows that the characteristic time needed to reach logarithmic kinetics varied tremendously with the type of solicitation: this characteristic time was on the order of a day for uniaxial creep experiments on cement paste or on concrete, but was on the order of a second for the microindentation creep experiments on cement paste. Said otherwise, microindentation enabled to reach the logarithmic kinetics of creep orders of magnitude faster than regular macroscopic test.

The contact creep modulus C_i fitted on the microindentation creep experiments on cement paste and the uniaxial creep modulus $C_{u,cem}$ fitted on the

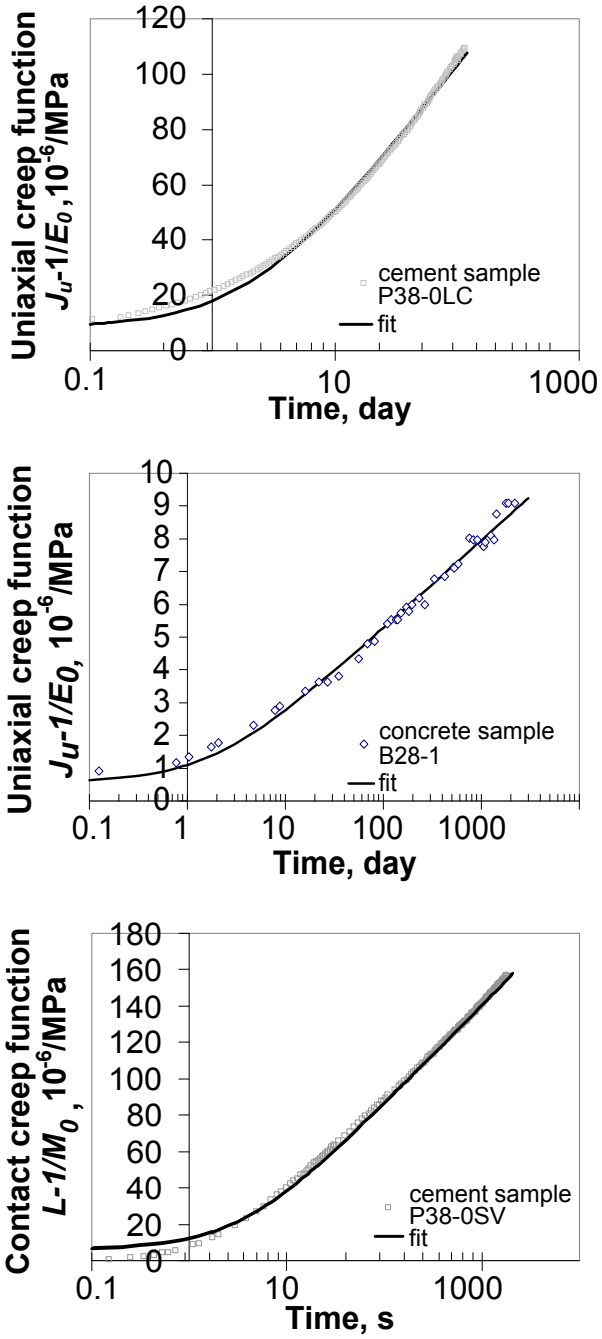

Figure 4.7: Examples of basic creep functions and of the best fits obtained with Eq. 4.3 or Eq. 4.4: a) uniaxial creep function obtained by uniaxial compression of cement paste P38-0LC, b) uniaxial creep function obtained by uniaxial compression of concrete B28-1, and c) contact creep function obtained by microindentation of cement paste P38-0SV.

sample	$C_{u,cem}$ **(GPa)**	C_i **(GPa)**
P28-0SV	47.89	75.16
P38-0SV	39.42	39.68
P50-0SV	29.49	20.89
P28-1SV	75.16	124.5
P33-1SV	-	104.5
P38-1SV	94.10	67.46
P38-0LC	40.86	39.74

Table 4.7: Contact creep modulus C_i obtained by microindentation creep experiment on cement paste and uniaxial creep modulus $C_{u,cem}$ obtained by uniaxial compression creep experiment on cement paste.

uniaxial creep experiments on cement paste are given in Tab. 4.7 and displayed in Fig. 4.8 with respect to each other. Fitting a linear relation to the experimental data through zero yielded $C_i = 1.172 C_{u,cem}$ with an average distance of the data points to the fitted line of 13.7 GPa. At least, the contact creep moduli and the uniaxial creep moduli were of the same order of magnitude, while the creep functions measured uniaxially and by indentation differed by more than one order of magnitude (see Fig. 4.8). However, given the relative poorness of the fit displayed in Fig. 4.8, we conclude that the logarithmic creep measured by microindentation did not enable us to precisely retrieve the amplitude of the logarithmic creep measured by macroscopic uniaxial test on cement paste.

The contact creep moduli C_i were measured at the scale of cement pastes, while the uniaxial creep moduli $C_{u,con}$ were measured at the scale of concrete: those two sets of moduli can therefore not be directly compared. In order to make a comparison possible, results obtained at the scale of cement paste must be upscaled to the scale of concrete. We performed this upscaling by using homogenization techniques within the frame of linear viscoelasticity. For details on how to perform homogenization of materials that creep logarithmically with respect to time, we refer to section 9.2 and the work of Vandamme and Ulm [2013]. In particular, these authors showed that, if a cement paste creeps logarithmically with respect to time in the long term, the concrete of which it is made (i.e., a mixture of creeping cement paste with non-creeping aggregates) should also creep logarithmically in the long term. Also, they showed that, if the cement paste creeps deviatorically in the long term, a concrete made with this paste

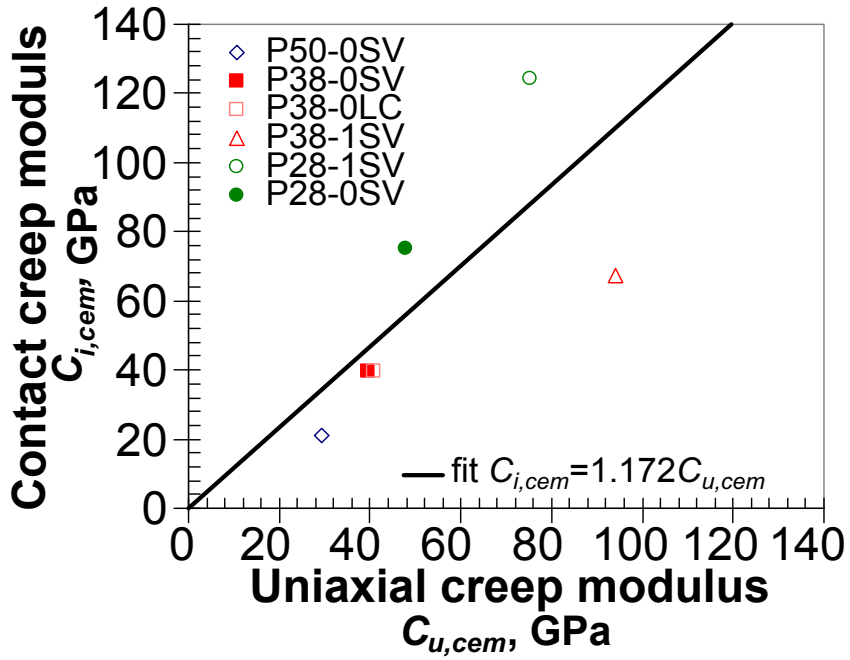

Figure 4.8: Uniaxial creep modulus $C_{u,cem}$ versus contact creep modulus C_i for cement paste samples.

should also creep deviatorically in the long term. Making use of a Mori-Tanaka scheme, which is well adapted to matrix-inclusions morphologies, they showed that the contact creep modulus $C_{i,con}$ of the concrete can be estimated from the contact creep modulus C_i of the cement paste with:

$$C_{i,con} = C_i \frac{2 + 3f_{agg}}{2(1 - f_{agg})} \tag{4.7}$$

where f_{agg} is the volume fraction occupied by the aggregates in the concrete.

Applying above equation, for each concrete sample, we estimated its contact creep modulus $C_{i,con}$ from the contact creep modulus C_i measured on the cement paste of which this concrete was made. Tab. 4.8 provides both this contact creep modulus $C_{i,con}$ estimated by microindentation tests performed at the scale of the paste and the uniaxial creep modulus $C_{u,con}$ measured by uniaxial compression of the concrete sample. Figure 4.9a displays those two creep moduli with respect to each other for all concrete samples. Fitting a linear relation to the experimental data through zero yielded $C_{i,con} = 1.064 C_{u,con}$ with an average distance of the

sample	$C_{u,con}$ **(GPa)**	$C_{i,con}$ **(GPa)**
B28-1	823.6	886.5
B38-1	524.8	486.4
B33-1A	644.3	642.2
B33-1B	711.1	699.8
B33-1C	705.0	759.9
B33-1D (data until 5320 days)	617.6	814.4
B33-1D (data until 1800 days)	751.0	
B50-0	247.3	145.7

Table 4.8: Uniaxial creep modulus $C_{u,con}$ measured by uniaxial compression creep experiments on concrete and contact creep modulus $C_{i,con}$ of concrete estimated from microindentation creep experiments performed on cement paste.

data points to the fitted line of 45.7 GPa. Even better than the comparison result on cement paste, the creep modulus of various concrete samples estimated by microindentation compared well with the creep moduli measured by macroscopic creep test, in spite of an extra step of homogenization.

The main discrepancy between creep modulus of the concrete samples measured by uniaxial test and estimated from microindentation test at the scale of the cement paste was for sample B33-1D. The uniaxial creep function of this sample, already displayed in Fig. 4.3 together with the uniaxial creep functions of all other concrete samples tested, is displayed again in Fig. 4.10. On this latter figure, one can clearly observe that the creep function of this concrete exhibited a nice logarithmic dependency on time after about a dozen of days, but that the creep rate sharply increased after about 1800 days. Wondering whether the data gathered after 1800 days was still fully representative of the basic creep of the sample, we performed again the analysis of the data on this sample, by considering only data points up to 1800 days. A fit of the function given in Eq. 4.4 to this new set yielded a new uniaxial creep modulus $C_{u,con} = 751.0$ GPa and a new characteristic time $\tau_{u,con} = 1.1$ day for this sample. The $C_{i,con}$-versus-$C_{u,con}$ relationship with this corrected uniaxial creep modulus is displayed in Fig. 4.9b. One can observe that the correlation between uniaxial creep modulus measured by macroscopic uniaxial test and contact creep modulus estimated by microindentation at the scale of the cement paste is now much better. Fitting a linear relation to the corrected experimental data through zero yielded $C_{i,con} = 1.031 C_{u,con}$ with

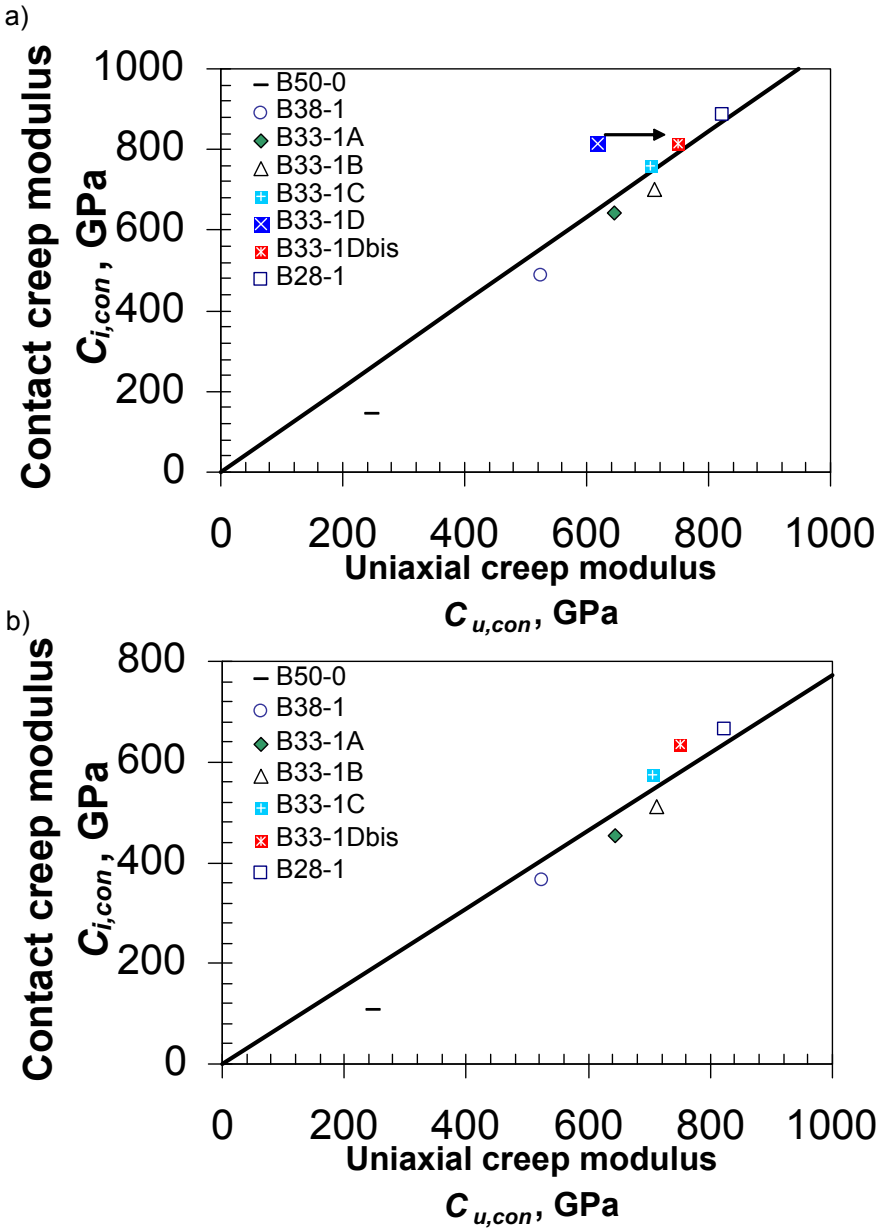

Figure 4.9: Uniaxial creep modulus $C_{u,con}$ measured by uniaxial compression creep experiments on concrete versus contact creep modulus $C_{i,con}$ of concrete estimated from microindentation creep experiments performed on cement paste, by considering, for the upscaling from cement paste to concrete, a) a Mori-Tanaka scheme and b) the upscaling model of Vu et al. [2010].

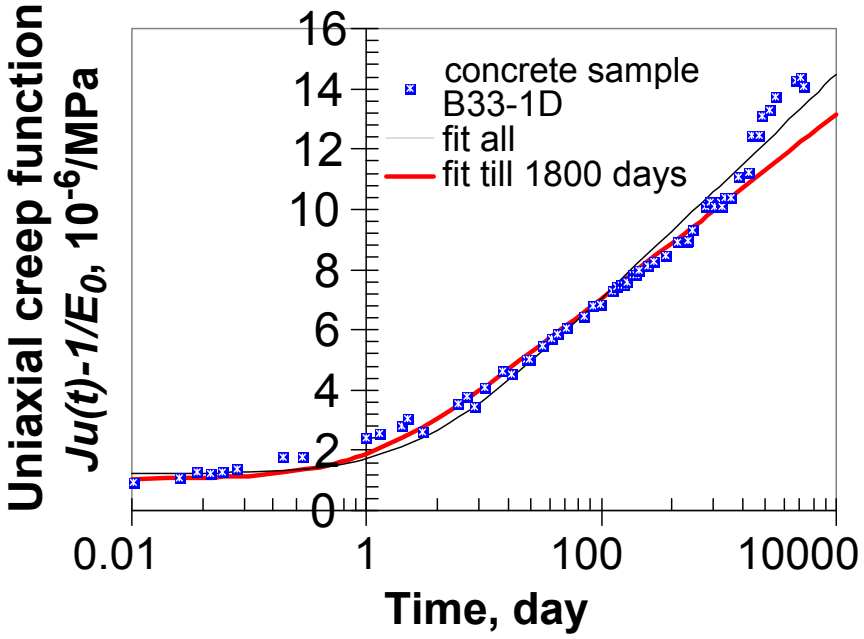

Figure 4.10: Basic creep function of concrete sample B33-1D, together with Eq. 4.4 fitted on all data points and with Eq. 4.4 fitted on data points until 1800 days only.

an average distance of the data points to the fitted line of 32.8 GPa: the agreement between direct measurements of long-term creep properties of concrete and estimations based on microindentation tests at the scale of the cement paste is now excellent.

4.4 Discussion

4.4.1 On the coefficient between contact and uniaxial creep modulus

For concrete, an excellent agreement was found between macroscopic measurements and estimates based on microindentation tests (see Fig. 4.9a), and the coefficient that enables to translate a contact creep modulus $C_{i,con}$ into a uniaxial creep modulus $C_{u,con}$ was found to be equal to $C_{u,con} = 0.970 C_{i,con}$. Why such a coefficient? In elasticity the indentation modulus M_0 is linked to the Young's

modulus E_0 through Eq. 3.5. Considering that, in the long term, the material of interest (here concrete) is linear viscoelastic and creeps only deviatorically, i.e., with no volume change (thus the Poisson's ratio $\nu = 0.5$), an application of the s-multiplied Laplace transform to Eq. 3.5 yields the theoretical relation $C_{u,con} = (1 - 0.5^2)C_{i,con} = 0.75C_{i,con}$. Therefore, we observe a discrepancy between the theoretical coefficient and the one used experimentally to convert the contact creep modulus into a uniaxial one. As will be seen in the next section, this discrepancy may be explained by the choice of homogenization scheme that we used to estimate the contact creep modulus of the concrete from the one of the paste.

4.4.2 On the choice of homogenization scheme

In order to predict the creep of concrete from the creep of the paste measured by indentation, we needed to employ a homogenization scheme, namely the Mori-Tanaka scheme (see Eq. 4.7). At high volume fractions of inclusions, the estimation given by the scheme is less accurate [Ghossein and Lévesque, 2012]. Therefore, one may want to try other schemes. As an alternative, we employed the upscaling model proposed by Vu et al. [2010] for bidisperse suspensions of noncolloidal particles in yield-stress fluids. For such suspensions, the shear modulus G of the suspension is related to the shear modulus G_0 of the suspending fluid through $G/G_0 = (1 - f/f_m)^{-1.43}$, where f is the volume fraction of the particles and f_m a critical volume fraction at which the elastic properties diverge. Adapting their model to our problem of a concrete made of non-creeping aggregates, we translated their formula for viscous properties as: $C_{i,con} = C_i(1 - f_{agg}/f_{agg,m})^{-1.43}$ or $C_{u,con} = 0.75C_i(1 - f_{agg}/f_{agg,m})^{-1.43}$, where $f_{agg,m}$ is the critical volume fraction of aggregates above which creep properties should diverge. Fitting this relation to the experimental measurements yielded very satisfactory results for a critical volume fraction $f_{agg,m} = 90.4\%$ of aggregates. For such parameter, a linear fit through zero of the relation $C_{u,con}$-versus-$0.75C_{i,con}$ yielded $C_{u,con} = 0.978 \times 0.75C_{i,con}$ with an average distance of the data points to the fitted line of 48.4 GPa (see Fig. 4.9b). Therefore, we conclude that the discrepancy observed with the Mori-Tanaka scheme (i.e., the fact that the coefficient of proportionality observed between the measured uniaxial creep

modulus of concrete and the contact creep modulus of concrete predicted with the Mori-Tanaka scheme did not correspond to the value 0.75 expected theoretically) is likely due to the fact that the Mori-Tanaka scheme is not adapted to systems with high volume fractions of inclusions. At such high volume fractions, the upscaling model proposed by Vu et al. Vu et al. [2010] may be more relevant. However, in turn, one should note that the use of the Mori-Tanaka scheme requires the knowledge of the mechanical properties of the individual phases and of their volume fractions only, while the use of the upscaling model of Vu et al. [2010] requires the additional knowledge of a critical volume fraction $f_{agg,m}$ of aggregates.

4.4.3 On the ability of indentation to characterize long-term creep

The comparison in the previous section shows that a 5-minutes-long microindentation test at the scale of the cement paste enables to quantitatively predict the long-term logarithmic creep kinetics of a concrete sample. This result, although already proposed by Vandamme and Ulm [2009], is surprising, since this long-term logarithmic kinetics is only reached after days at the scale of macroscopic samples, or even after years at the scale of structures [Bažant et al., 2011]. According to Vandamme and Ulm [2009], the ability to characterize long-term creep kinetics so fast by microindentation is apparently not due to the fact that microindentation probes a much smaller volume than macroscopic experiments, or probe those volumes at much higher strains than regular macroscopic test. They proposed the tentative explanation that this ability is due to the fact that microindentation probes the material at much greater stresses than macroscopic test. In our study, for uniaxial creep experiments, we observed no significant difference between the characteristic time needed to reach a logarithmic kinetics of creep on cement paste or on concrete (see Table 4.6). This observation further suggests that the characteristic time needed to reach a logarithmic kinetics of creep is not governed by the size of the system; on the other hand, the difference in the size of the concrete samples (the length of which was 1000mm and the diameter of which was 160mm) and of the cement paste samples (the length of which was 160mm and the diameter of which was 20mm) may have been not

sufficient to observe significant differences between the characteristic times for the two sets of samples. In addition, since this characteristic time did not differ much between cement samples and concrete samples, we can also conclude that the heterogeneity of the system does not modify the duration needed to reach a long-term creep: indeed, concrete samples are more heterogeneous than cement paste samples, in the sense that concrete is itself a mixture of cement paste with aggregates.

4.4.4 On the quality of the creep experiments

The quality of the correlation between microindentation results and macroscopic uniaxial results was much better at the scale of the concrete than at the scale of the cement paste (see Figs. 4.8 and 4.9). Such a result is quite surprising, since comparing results at the scale of a concrete sample required to homogenize results obtained by microindentation at the scale of the cement paste: by doing so, since homogenization schemes such as the Mori-Tanaka scheme only provide estimates of the homogenized properties, one could have expected that the quality of the correlation would have been worse at the scale of the concrete than at the scale of the cement paste. Our opinion is that the relatively poor correlation on cement paste samples is due to the difficulty of performing creep experiments on cement samples. In general, performing creep experiments on cementitious materials is tricky and, even when great care is taken, a dispersion of the long-term creep results of about 16.5% can be expected on concrete samples tested 28 days after casting [Clément and Le Maou, 2000]. For younger samples, this dispersion is rather on the order of 20% [Clément and Le Maou, 2000]. On cement paste samples, even more dispersion should be expected, since preparing the samples proves to be very delicate, in spite of the fact that cement paste samples are smaller than concrete samples. An example of such a difference in the difficulty of preparing both sets of specimen is the fact that cement paste samples needed to be rotated for a few hours after casting in order to prevent segregation, while concrete samples did not.

In order to obtain Fig. 4.9b from Fig. 4.9a, we needed to perform a new analysis of the creep data of sample B33-1D. For this sample, instead of considering all the data available on the 5320 days (i.e., about 14.5 years), we only

considered data on about 1800 days (i.e., about 5 years), because of a kink in the data at about 1800 days, that we considered as spurious (see Fig. 4.10). Although the spuriousness of this kink can be discussed, we want to underline how difficult and tedious running creep experiments on such long periods is. Since the objective of such experiments is to measure basic creep, on several years the temperature must be well controlled and all hygric exchanges must be prevented. The difficulty is also enhanced by the fact that basic creep strain is measured by difference between the strains measured on a loaded sample and on an unloaded sample (see section 4.2.2): therefore, basic creep will be correctly measured only if temperature is well controlled and hygric exchanges are prevented for both samples, thus increasing the risks of experimental error. In our present study, experimental error due to temperature variations must have been negligible, since all samples for compressive creep experiments and autogenous shrinkage experiments were located in the same room and thus at the same temperature. In contrast, since upon years drying can occur even for samples tightly sealed with self-sealing aluminum foil [Toutlemonde and Le Maou, 1996], experimental error due to long-term drying can not be discarded, in particular for sample B33-D.

As an alternative to tedious years-long macroscopic experiments, minutes-long microindentation testing would prove to be very handy. And our work showed that such microindentation testing makes it possible to characterize precisely the long-term logarithmic kinetics of creep of cementitious materials. As a counterpart, this result means that microindentation testing cannot give access to the short-term kinetics of those materials. Consequently, microindentation testing should be used as a complement to shorter macroscopic creep experiments: the macroscopic experiments would enable to characterize the short-term creep of the material and should be sufficiently long to reach the long-term logarithmic kinetics of creep; while microindentation tests run in parallel would enable to characterize the rate of this logarithmic kinetics of creep. For practical use, other sources of creep (e.g., drying creep) would need to be added to the long-term basic creep determined in such a manner.

4.5 Chapter conclusions

This chapter was dedicated to compare microindentation creep experiments on cement paste with macroscopic uniaxial creep experiments on both cement paste and concrete. Samples for uniaxial experiments were manufactured in 1992, while samples for indentation test were manufactured in 2011. Although the two sets of samples were prepared almost 20 years apart, we used virtually the same raw materials and employed the same procedures of preparation, so that the mechanical properties of both sets of cement pastes could be expected to be very close to each other (see Fig. 4.5).

Uniaxial creep experiments lasted for years on concrete samples and for months on cement paste samples. In contrast, microindentation creep experiments (performed at the scale of cement paste) only lasted for minutes. The creep rates measured by microindentation differed by one to two orders of magnitude from the creep rates measured during the first three minutes of the macroscopic uniaxial experiments (see Fig. 4.6): microindentation did not provide access to the short-term creep of the tested cement pastes.

For all experiments, after a transient period, the basic creep was well captured by a logarithmic function of time. The amplitude of the rate of this logarithmic kinetics of creep depends on a creep modulus, called uniaxial creep modulus for uniaxial creep experiments and contact creep moduli for microindentation creep experiments. We compared the contact creep modulus with the uniaxial creep moduli. The comparison with macroscopic uniaxial experiments on concrete required to homogenize the microindentation results: this homogenization was performed within the frame of linear viscoelasticity. Contact creep moduli of concrete were in an almost perfect agreement with uniaxial creep moduli measured by regular macroscopic test (see Fig. 4.9b). This result shows that the rate of long-term creep of concrete can be quantitatively inferred from minutes-long microindentation experiments at the scale of the paste. However, the coefficient of proportionality observed between measured uniaxial creep moduli and predicted contact creep moduli did not correspond to the value expected theoretically: this discrepancy was attributed to the inaccuracy of the Mori-Tanaka scheme for systems with high volume fraction of inclusions. At such high volume fractions, the upscaling model proposed by Vu et al. [2010] may be more relevant.

The measured contact creep moduli compared worse with the uniaxial creep moduli on cement paste (see Fig. 4.8). We attributed this less good agreement to the difficulty of measuring basic creep of cement pastes by regular macroscopic test. Several factors can make this measurement tricky: difficulty of preparing homogeneous samples (which need to be rotated after mixing), need to perform two experiments in parallel (since basic creep is obtained by subtracting autogenous shrinkage to total creep), difficulty of preventing hydric exchanges with the surroundings over long periods of time and scattering due to a smaller volume compared with concrete.

The characteristic time needed to reach a logarithmic kinetics of creep was of a few days with macroscopic uniaxial test and of a few seconds by microindentation test. This striking observation –that small scale test enables to reach long-term creep of cementitious materials orders of magnitude faster than macroscopic test –was already observed at the scale of nanoindentation test [Vandamme and Ulm, 2013]. This surprising feature is apparently not due to the fact that microindentation or nanoindentation probes small volumes, or probe those volumes at large strains, or probe volumes that are less heterogeneous than macroscopic ones. In contrast, a tentative explanation proposed by Vandamme and Ulm [2013] is that indentation test probes volumes at very large stresses, thus allowing for a very fast redistribution of internal stresses within the solid.

This comparative study shows that microindentation tests provide access to the long-term kinetics of creep of cementitious materials in minutes. As a counterpart, such microindentation tests do not allow to characterize the short-term creep of those materials. From an engineering perspective, microindentation test could prove very beneficial, when used in parallel with regular macroscopic test: the latter should only last long enough in order to measure the short-term kinetics of creep, while the rate of the long-term logarithmic creep would be characterized by microindentation. By doing so, the whole creep function of cementitious materials could be measured precisely, and in a more convenient and faster way than is done today.

Chapter 5

Comparative study on gypsum

Résumé *Ce chapitre s'intéresse à comparer des tests de fluage par microindentation de quelques minutes avec des tests de fluage par macroscopie de plusieurs jours, c'est-à-dire des tests de fluage par flexion sur du plâtre – un matériau cimentaire cristallin. Une partie de ces tests de fluage par flexion a été conduite par Pachon-Rodriguez [2011]. Les fonctions de fluage propre spécifique ont été mesurées à la fois par microindentation et par flexion. Qualitativement, des tendances comparables ont été obtenues avec ces deux types des tests. Quantitativement, pour toutes les tests par indentation, après une période transitoire, la fonction de fluage propre spécifique était bien décrite par une fonction logarithmique du temps. Comme ce qui a été fait au chapitre 4, nous retenons le module de fluage C_i et le temps caractéristique par indentation τ_i pour caractériser la fonction de fluage. Les fonctions de fluage propre spécifique obtenues pas flexion n'ont jamais été des fonctions logarithmiques du temps. En revanche, ces fonctions de fluage ont été bien décrites par la somme d'une fonction logarithmique du temps et d'une fonction linéaire. La fonction logarithmique a été caractérisée par un module de fluage en flexion et un temps caractéristique en flexion. Pour la plupart des échantillons, les modules de fluage du plâtre mesurés par indentation ont été pratiquement (soit 4 échantillons sur 6) en parfaite concordance avec les modules de fluage en flexion mesurés par flexion, ce qui prouve que l'indentation est une technique validée pour caractériser les propriétés de fluage des matériaux cimentaires. Par contre et comme cela a été le cas avec le ciment Portland, le temps caractéristique requis pour atteindre la cinétique de*

fluage logarithmique s'est avéré bien inférieur par indentation que par flexion, ce qui montre que l'indentation de quelques minutes permet d'obtenir rapidement la cinétique logarithmique des matériaux cimentaires. La partie non logarithmique du fluage propre spécifique du plâtre observé par test de flexion est probablement due au fait que, durant le test du fluage par flexion, une partie de l'échantillon est en tension.

Abstract *This chapter is dedicated to comparing minutes-long microindentation creep experiments with days-long macroscopic creep experiments, i.e., three-point bending creep experiments on gypsum plaster –a crystalline cementitious material. Part of bending creep experiments were carried out by Pachon-Rodriguez [2011]. The specific basic creep functions of gypsum samples were measured both by indentation and by three-point bending. Qualitatively, similar trends were found with both indentation creep testing and three-point bending creep testing. Quantitatively, for all indentation experiments, after a transient period, the specific basic creep of gypsum measured by indentation testing was well captured by a logarithmic function of time. As was done in chapter 4, we apply the creep modulus C_i and indentation characteristic time τ_i to characterize the contact creep function. The specific basic creep functions obtained by three-point bending were never logarithmic with respect to time. In contrast, those creep functions were well captured by the sum of a logarithmic function of time and of a linear one. The logarithmic function was characterized by a flexural creep modulus and a flexural characteristic time. For most samples, the contact creep moduli of gypsum measured by indentation were in perfect agreement with the flexural creep moduli measured by flexural bending creep testing for samples without additives, which further proves that indentation is a validated technique to characterize creep properties of cementitious materials. In contrast, as was the case with Portland cement, the characteristic time needed to reach the logarithmic creep kinetics of creep was much lower by indentation testing than that by bending, which shows that minutes-long indentation testing provides a rapid access to the logarithmic kinetics of cementitious materials. The non-logarithmic part of specific basic creep of gypsum observed by bending test is likely due to the fact that, during bending creep testing part of the specimen is in tension.*

5.1 Chapter introduction

Gypsum plasters ($CaSO_4 \cdot 2H_2O$) were almost certainly the first examples of 'hydraulic cement' known to mankind, with evidence for their use in construction going back well over 9000 years [Gartner, 2009]. They are still widely used in modern construction.

The raw material needed to prepare gypsum plaster can be easily obtained by heating gypsum ($CaSO_4 \cdot 2H_2O$) to temperatures of 115-140°C at which it dehydrates to produce a micro crystalline solid known formally as β-hemihydrate ($CaSO_4 \cdot 1/2H_2O$). Gypsum plasters can be prepared by simply mixing the powdered hemihydrate with water: the hemihydrate reacts with water and gypsum is formed, as presented by the following chemical reaction formula:

$$(2CaSO_4 \cdot H_2O) + 3H_2O \rightarrow 2(CaSO_4 \cdot 2H_2O) \tag{5.1}$$

This reaction happens more rapidly than the hydration of Portland cement: at room temperature, the reaction completes after several hours (see Fig. 5.1 from Jaffel et al. [2006]). So, sometimes, it is quite convenient to use gypsum plaster as a reference material for research on cementitious materials. The hydrated gypsum plaster is a polycrystalline material. Generally, the microstructure of pure gypsum plaster without additives is considered as an assembly of randomly distributed needle-shaped gypsum crystals, with typically 20µm in length and a characteristic size of 1µm for the cross-section. Those crystals bridge with each other, forming a network and thus contribute to the mechanical properties of gypsum plaster [Shchukin and Amelina, 1992].

The mechanical properties of gypsum plaster can be influenced by the following parameters:

- Porosity: the porosity of gypsum plaster used in construction with water to hemihydrate ratio w/h=0.8 is around 50%. As for any porous media, its mechanical properties are higly influenced by its porosity.
- Relative humidity or water content: compared with dry condition, in wet condition an evident drop of Young's modulus and strength was observed in various studies [Andrews, 1946; Badens et al., 1999; Meille, 2001; Padevět et al., 2011]. The influence of relative humidity is even more drastic on the

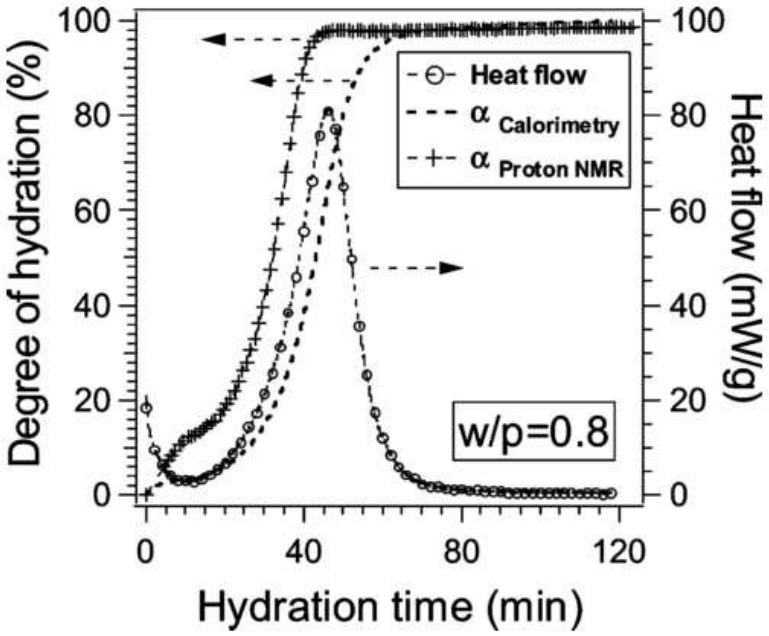

Figure 5.1: Degrees of hydration obtained by NMR and isothermal calorimetry, at 25°C, and isothermal heat flow over time [Jaffel et al., 2006].

creep properties of gypsum: dry gypsum nearly does not creep while wet gypsum creeps significantly.

- Additives: by adding additives to gypsum plaster during its hydration, the mechanical properties can be improved [Amathieu and Boistelle, 1986] and the time-dependent deformation due to creep can be reduced [Pachon-Rodriguez, 2011]. The improvement might be due to a change of the morphology of gypsum crystals and the change of interface properties between crystals. Pachon-Rodriguez [2011] found the creep deformation of gypsum plaster can also be reduced by immersing it in solutions with additives: and the change is probably due the change of diffusion coefficient of gypsum in those solutions.

In this chapter, we aim at validating the use of indentation testing to measure creep properties on gypsum plaster. The reasons for choosing gypsum plaster for such validation were manyfold:

- Gypsum plaster samples are easy and fast to prepare because its hydration

is fast.

- Macroscopic creep testing is easier to carry out than for cement paste samples because there is no need to perform shrinkage experiments in parallel with the creep experiment due to the fact that gypsum plaster exhibits negligible shrinkage.
- Creep results can vary drastically by simply varying relative humidity or adding additives.
- Hardened gypsum paste appears to be a purely crystalline material. It is generally believed that the origin of long-term creep in Portland cement paste lies in the amorphous phase C-S-H [Acker and Ulm, 2001; Bažant et al., 1997], while for gypsum without the presence of this amorphous phase, the origin may be completely different. The validating of indentation creep testing on crystalline material such as gypsum is thus necessary.

The validation will be performed by comparing indentation creep testing and bending creep testing, as a complement to what has been done in chapter 4, in which indentation creep testing was compared with compressive creep testing. The rationale for doing so is that the way of loading might influence the creep properties that one can get from the experiment. Therefore, the comparison between bending creep testing will give us some hint on whether indentation can be used to predict creep properties under more complex types of loading.

5.2 Materials and methods

5.2.1 Sample preparation

The hemihydrate calcium sulphate used in experiment was a product from Lafarge. The chemical composition is given in Tab. 5.1. Samples with different water-to-hemihydrate (i.e., hemihydrate calcium sulphate) ratio w/h were prepared. Samples for both indentation tests and bending tests were prepared by the following procedure:

- At a temperature of 23°C, add the powdered hemihydrate to a given quantity of deionized water within 30s while stirring.

Chemical component	$CaSO_4 \cdot 1/2H_2O$	$CaCO_3$	SiO_2	$CaSO_4 \cdot 2H_2O$	$CaSiO_2$
Mass percentage (%)	96	2.5	1.0	0.3	0.2

Table 5.1: Chemical component of the hemihydrate calcium sulphate used for the preparation of gypsum sample.

- Seal the container containing the mixture and install it into a vacuum mixing unit, in which low pressure is applied in order to get out air initially trapped in the mixture in the vacuum mixing unit and stir for 2 minutes.
- Keep the mixture in container for an additional 1 minute before molding, which enables to improve the fluidity for molding.
- Pour out the mixture into molds made of polyvinyl chloride.
- Vibrate the mold filled with the mixture to expel air created during molding.
- Seal the mold in plastic bags for 1 hour.
- Demold and seal the samples in plastic bag for 24 hours.
- Put the samples into oven with constant temperature (45°) to dry samples during 48 hours.
- Get gypsum samples out of oven and condition them under 50% relative humidity or immersing them in various solutions for at least 2 weeks, at a temperature of 23°.

Already mentioned in section 5.1, the porosity, the relative humidity (or the water content), and the additives can influence the creep properties of gypsum plaster. In order to obtain a wide range of data for comparison, we varied the following parameters in sample preparation and conditioning: the water-to-hemihydrate ratio w/h, in order to vary the porosity of sample; and the environment of conditioning, in order to vary the water content is sample as well as the absorbed additives. The labellings of gypsum plaster samples, their porosity and the environment in which they were conditioned are given in Tab. 5.2.1.

In total, six groups of sample were prepared and in each group there were 4 identical samples. The porosities ϕ of gypsum samples were calculated with the

Label	w/h	**Porosity** ϕ	**Condition environment**
G07	0.7	52%	50%±5% relative humidty
G08	0.8	56%	50%±5% relative humidty
G09	0.9	59%	50%±5% relative humidty
G08-G	0.8	56%	immersed in gypsum solution
G08-T	0.8	56%	immersed in Trilon-P solution
G08-P	0.8	56%	immersed in phosophate solution

Table 5.2: Labeling, water-to-hemihydrate ratio w/h, porosity ϕ of gypsum samples and environment in which they were conditioned.

volume V, the mass m of dried gypsum sample, the density of gypsum crystal (ρ_{gc}=2.32g·cm^{-1}), with the following equation:

$$\phi = 1 - \frac{m/V}{\rho_{gc}} \tag{5.2}$$

All solutions used for immersing gypsum samples were initially saturated with gypsum. The effective mass concentration of Trilon-P and phosphate (sodium trimetaphosphate) in respective solutions prepared with each of those additives was 2.3g/L. See more details on the additives in [Pachon-Rodriguez, 2011].

After conditioning, both bending tests and indentation tests were performed on the six groups of samples. Firstly, bending creep experiments were performed, then indentation creep experiments were performed on the same samples.

5.2.2 Bending experiments

The bending experiments on sample labeled as G08-G, G08-T and G08-P, i.e., gypsum samples with w/h=0.8, immersed in various solutions were carried out by Pachon-Rodriguez [2011].

After conditioning, the flexural strength σ_{fmax} was measured on three identical samples from the same group. The bending test for measuring the flexural strength was carried out by a mechanical testing apparatus without controlling relative humidity. We took the average value from the three tests as the flexural strength of gypsum sample for bending creep test. Then bending creep experiments were performed in the same environment as that for sample conditioning, i.e., either at 50% relative humidity or in immersed conditions. As already men-

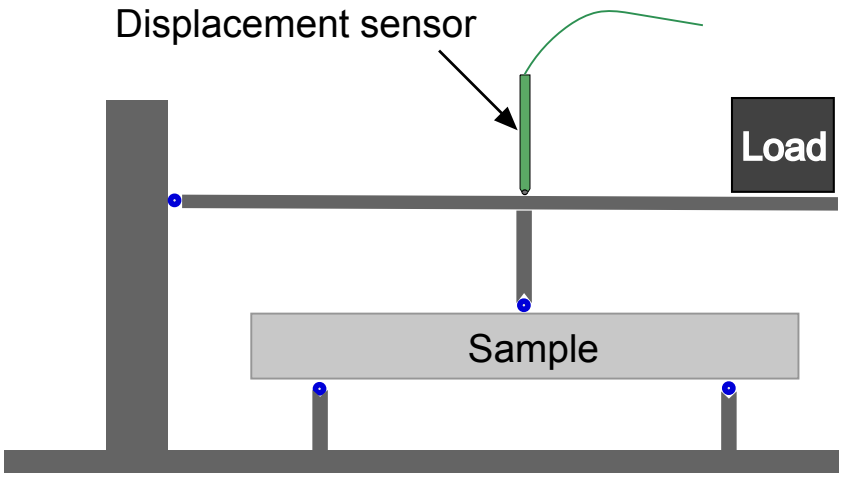

Figure 5.2: Schematic figure of the apparatus used for three-point bending creep testing.

	Room condition	**Immersed condition**
Stress level	$20\%\sigma_{fmax}$	$20\%\sigma_{fmax}$
Duration of test t_b	about 10 days	about 10 days
Temperature	23°C±0.2°C	23°C±0.2°C
Relative humidity	50%±5%	immersed in solution

Table 5.3: Experimental parameter setting during bending creep testing.

tioned in chapter 4, the creep of cementitious materials is not linear to applied load if the applied load is too high, therefore a load of only 20% of the flexural strength was applied during bending creep test. All the bending creep tests lasted about 10 days and the time-dependent deflection $D(t)$ of gypsum beams was measured. A summary of experimental parameters is given in Tab. 5.3.

In the elastic range, the Young's modulus E can be determined by bending testing by the following expression:

$$E = \frac{\sigma_f}{\epsilon_f} \tag{5.3}$$

where σ_f and ϵ_f denote the flexural stress and the flexural strain, respectively. Similarly to the derivation performed in chapter 4, applying linear viscoelasticity, the flexural strain history $\epsilon_f(t)$ can be linked to the flexural stress σ_f by flexural compliance J_f:

$$\epsilon(t) = \int_0^t J_f(t-\tau)\frac{d}{d\tau}\sigma(\tau)d\tau \tag{5.4}$$

In the Laplace domain, one has: $s\mathcal{L}(E) = [s\mathcal{L}(J_f)]^{-1}$. For a three-point bending test on a beam with rectangular cross section, the flexural strain and flexural stress can be expressed as:

$$\sigma_f(t) = \frac{3P(t)l}{2bd^2} \tag{5.5}$$

where P denotes the applied force on mid-span, l denotes support span, b and d denote the width and depth of tested beam. The flexural strain is obtained from the acquired data as:

$$\epsilon_f(t) = \frac{6dD(t)}{l^2} \tag{5.6}$$

where D denotes the deflection at midspan. Applying a Laplace transform to Eq. 5.4, Eq. 5.5 and Eq. 5.6, in case of a step loading $\mathcal{L}(P(t))=P_{max}/s$ where P_{max} is the applied step load, and then applying an inverse Laplace transform, one can find the following expression which links the flexural compliance J_f to the measured deflection $D(t)$:

$$J_f(t) = \frac{4bd^3}{l^3 P_{max}}D(t) \tag{5.7}$$

The basic creep function obtained by bending creep testing is then $J_f(t) - 1/E_0$, which can be calculated with the following equation:

$$J_f(t) - 1/E_0 = \frac{4bd^3}{l^3 P_{max}}(D(t) - D_0) \tag{5.8}$$

where D_0 and E_0 denote the instantaneous deflection and the Young's modulus at the moment of loading, respectively. In practice, to obtain the specific basic creep function $J_f(t)-1/E_0$, knowing the Young's modulus at the moment of loading E_0 is not necessary, as one can simply work with the increment of deflection $D(t)-D_0$ during the creep phase. As the hydration of gypsum is almost complete after 24 hours in room temperature [Jaffel et al., 2006], the time-dependent deformation

due to hydration of hemihydrate Calcium sulfate $CaSO_4 \cdot 0.5H_2O$ during the creep phase can be ignored. Said otherwise, the chemical or autogenous shrinkage is negligible during the creep phase. Adding that no drying happened during our bending tests, so the measured total deformation equals to basic creep.

5.2.3 Indentation experiments

After bending creep test, prism gypsum samples were cut into cubes and tested by indentation. Indentation experiments were done on both gypsum samples conditioned in 50% relative humidity and those immersed in various solutions. A summary of indentation parameters is given in Tab. 5.4. The parameters were fixed according to the following principles:

- To prevent drying during indentation test, the hygral conditions during test were controlled to be the same or very similar to those for sample conditioning: for samples conditioned in 50% relative humidity, the environment during indentation was controlled as the same relative humidity; for samples immersed in solutions, the relative humidity during indentation test was controlled at 100%.

- Flat punch indentation probes with diameter Φ=0.5mm and Φ=1.0mm were used. The advantage of flat punch probe, compared with Vickers probe is that, the contact area during holding phase is constant, so Eq. 3.42 holds without approximation. On the other hand, it is difficult to ensure a perfect contact between the surface of tested material and the surface of indentation probe. Nevertheless, the equipped flat punch indentation probes are suitable for gypsum plaster, as the material is soft and thus the flat punch probes can penetrate easily into its surface under loads within the capacity of the force sensor of the indentation apparatus. As the gypsum samples in wet conditions are even softer than those in room condition, to keep the similar maximum load, a probe with a diameter Φ=1.0mm was used.

- The maximum indentation depth was chosen to be high enough to ensure a complete contact between the surface of probe and the surface of tested material.

	Room condition	**Wet condition**
Temperature	23°C±0.2°C	23°C±0.2°C
Relative humidity	50%	100%
Indentation probe	flat punch, Φ=0.5mm	flat punch, Φ=1mm
Maximum depth	200µm	200µm
Maximum load	2.0N to 7.0N	1.9N to 3.2N
Holding duration	10min	5min

Table 5.4: Summary of the experimental parameters of indentation experiments in room condition and wet condition.

Sample	$\boldsymbol{\sigma_{fmax}}$**(MPa)**	$\boldsymbol{H}$**(MPa)**	$\boldsymbol{E}$**(GPa)**
G07	4.90±0.15	35.7±2.8	4.48±0.62
G08	3.65±0.11	18.1±0.9	2.57±0.23
G09	2.71±0.12	14.5±3.3	2.40±0.28
G08-G	2.09±0.12	2.62±0.28	1.52±0.29
G08-T	2.27±0.07	2.85±0.41	2.09±0.33
G08-P	2.29±0.18	3.69±0.44	1.66±0.56

Table 5.5: Mechanical properties measured by three-point bending testing or indentation testing.

- The duration of the holding phase for gypsum plaster samples in room condition was prolonged to 10 minutes in order to get more information on the creep phase as gypsum does not creep much in this condition.

On each sample, five repeats of indentations were performed. The contact creep function $L(t) - 1/M_0$ was obtained by applying Eq. 3.42. With no drying and ignorable shrinkage during indentation creep test, the contact creep function $L(t) - 1/M_0$ represents the basic creep of gypsum. The Young's modulus E indentation hardness H were obtained as the average value from the five tests by applying Eq. 3.13 and Eq. 3.6.

5.3 Results and discussion

5.3.1 Flexural strength, indentation hardness and Young's modulus of gypsum samples

A summary of mechanical properties measured by indentation and three-point bending is presented in Tab. 5.5. The following trends can be found for the evolution of the flexural strength σ_{fmax}, the Young's modulus E and the indentation hardness H of tested gypsum samples in function of experimental parameters:

- σ_{fmax}, E and H decreased with an increasing water-to-hemihydrate ratio. Indeed, increasing water-to-hemihydrate ratio resulted in an increase of the porosity and thus a decrease of σ_{fmax}, E and H.
- σ_{fmax}, E and H decreased after immersing samples in solutions.
- With the presence of additive (Trilon-P or phosphate) E and H were increased. The increase of E was more evident for sample immersed in solution with Trilon-P than that for sample immersed in solution with phosphate, while the increase of indentation hardness was more evident for sample immersed in solution with phosphate than that for sample immersed in Trilon-P.

5.3.2 Qualitative comparison of creep function

The specific basic creep of gypsum samples with various water-to-hemihydrate ratios conditioned at 50% relative humidity are presented in Fig. 5.3. Results from the two testing technique show a very little difference on the specific basic creep functions between samples with water-to-hemihydrate ratios varying from 0.7 to 0.9.

As one can see from Fig. 5.3b, the measurement of indentation shows some noise, due to the fact that very little change of indentation depth happened in creep test. The comparison shows both indentation testing and bending testing give the same qualitative trend of creep behavior of gypsum: by varying water-to-hemihydrate ratio from 0.7 to 0.9, the creep functions are similar: the amplitude of creep functions measured by indentation creep testing during 10 minutes in

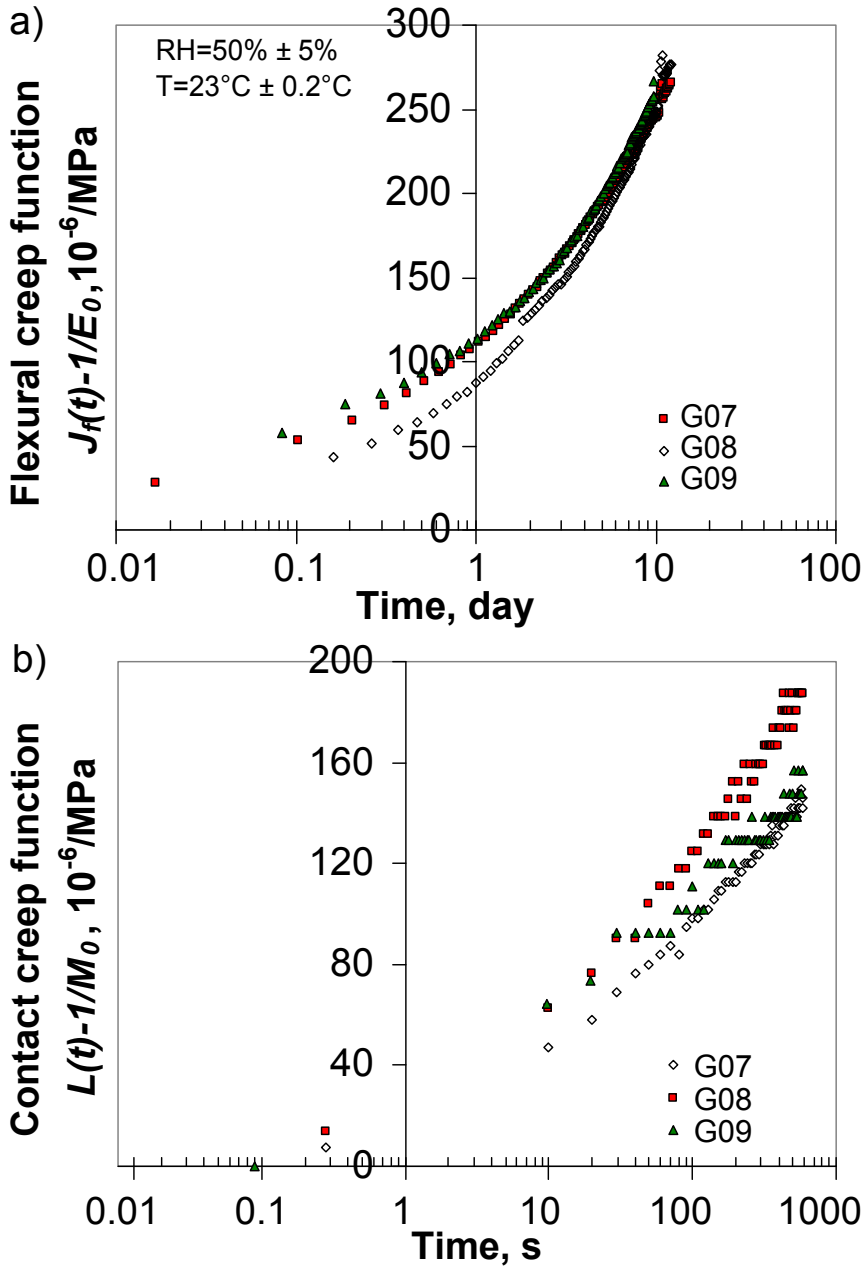

Figure 5.3: Creep functions of gypsum samples conditioned in 50% relative humidity measured by a) indentation creep testing and b) three-point bending testing at 50% relative humidity, at 23°C.

50% relative humidity only varies from 150Pa^{-1} to 187Pa^{-1}, while that of flexural functions measured by bending creep testing only varies from 266Pa^{-1} to 276Pa^{-1}.

The specific basic creep functions of gypsum samples immersed in different aqueous solutions are presented in Fig. 5.4b. As one can see from this figure, the specific basic creep of gypsum was reduced by immersing in solutions with additives (Trilon-P and phosphate). At the same effective mass concentration studied, the additive phosphate shows a higher effect on reducing the specific basic creep of gypsum when compared with the additive Trilon-P. These observations are perfectly in agreement with that from bending creep testing, as presented in Fig. 5.4b. On the other hand, the creep-reducing effect by phosphate seems less evident by indentation creep testing than bending creep testing on gypsum: the amplitude of specific basic creep is reduced by phosphate by a factor of 100 from bending creep testing, while a factor of 10 was seen from the result of indentation creep testing.

Gypsum creeps much more in wet condition than that of dry condition. As presented in Fig 5.5, creep functions of this sample, after immersion in solution saturated with gypsum, increased by a factor of 100, when compared with that obtained at 50% relative humidity.

To summarize, the above comparisons on creep functions obtained by the two techniques showed that, by varying formulation and the condition environment, similar trends of evolution of creep functions could be found with both indentation creep testing and three-point bending creep testing. Therefore qualitatively, indentation creep testing is a validated technique to measure the basic creep properties of gypsum.

5.3.3 Quantitative comparison of creep parameters

In order to have a quantitative comparison, one can apply Eq. 4.3, i.e., $L(t) - 1/M_0 = \ln(t/\tau_i+1)/C_i$, to fit experimental contact creep function $L(t)-1/M_0$. As presented in Fig. 5.6, applying Eq. 4.3 to fit experimental data yields satisfactory result, except at early time when systematic deviations can be found between the best-fit curve and experimental data. Applying Eq. 4.3, the contact creep function of gypsum is thus controlled by a characteristic time by indentation test, i.e., τ_i and the contact creep modulus C_i.

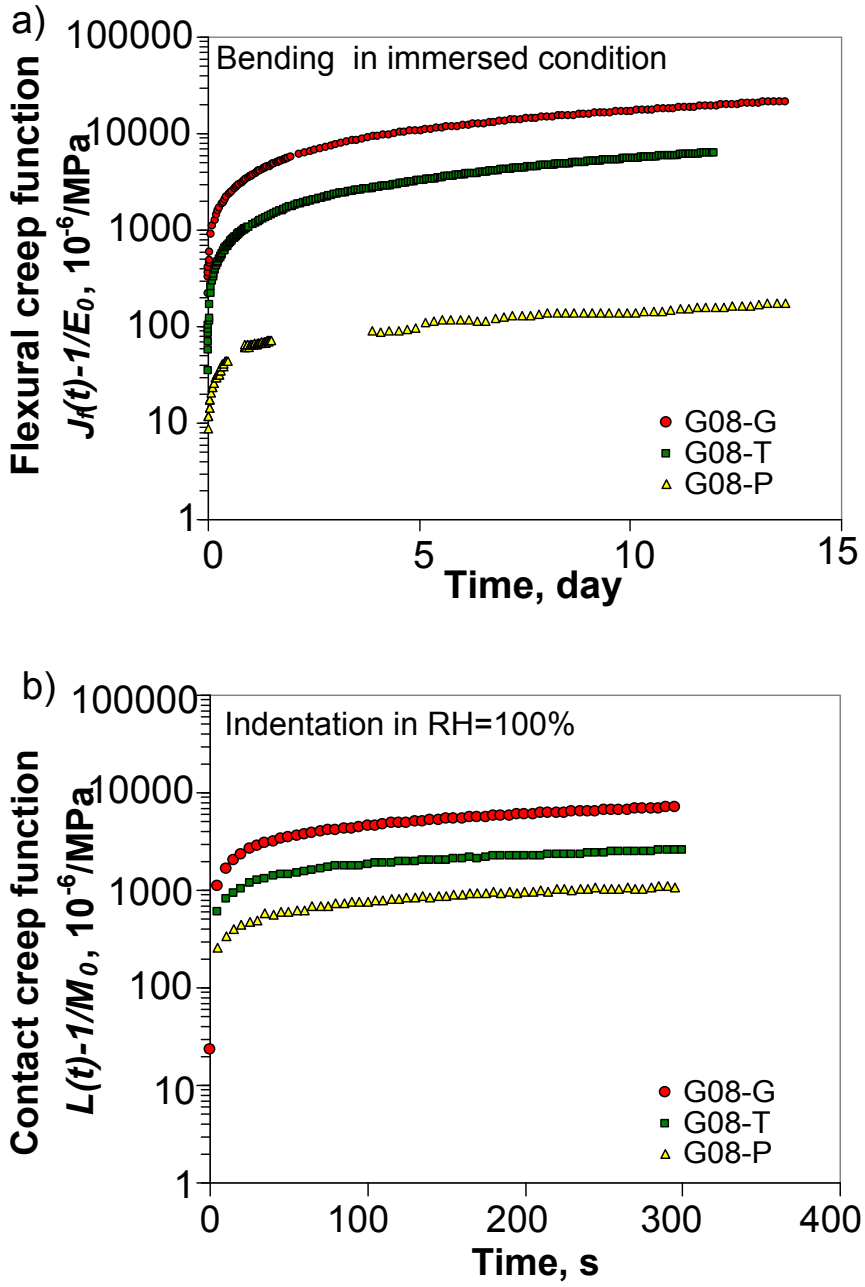

Figure 5.4: Summary of a) flexural creep functions from three-point bending creep testing in immersed conditions (results from [Pachon-Rodriguez, 2011]) and b) contact creep functions from indentation creep testing in 100% relative humidity on gypsum samples immersed in various solutions: G08-T immersed in Trilon-P solution, G08-P immersed in phosphate solution and G08-G immersed in gypsum solution.

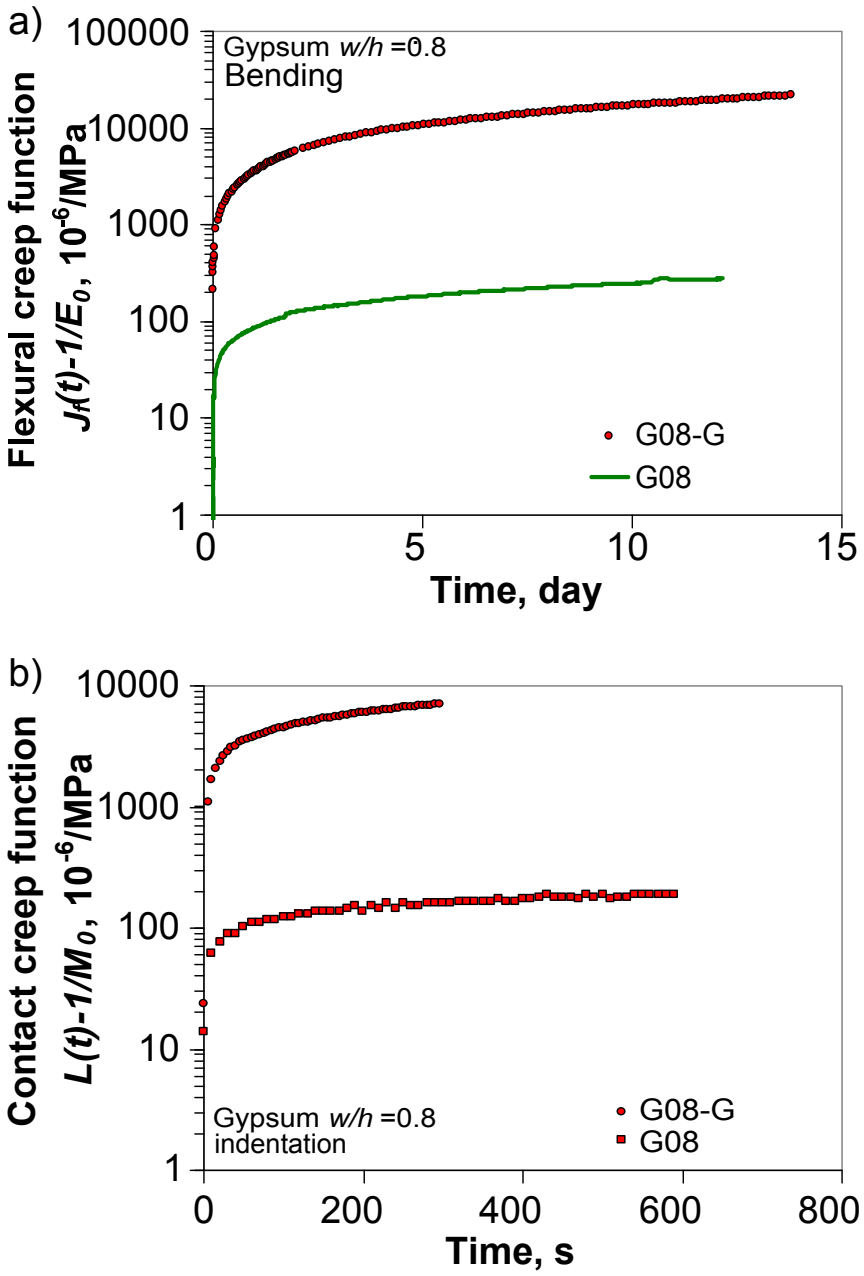

Figure 5.5: Effect of water content on creep properties of gypsum observed by a) bending testing b) indentation testing. Sample G08-G was immersed in solution saturated with gypsum, sample G08 was conditioned in 50% relative humidity. Data of bending testing on sample G08-G in immersed conditions is from [Pachon-Rodriguez, 2011].

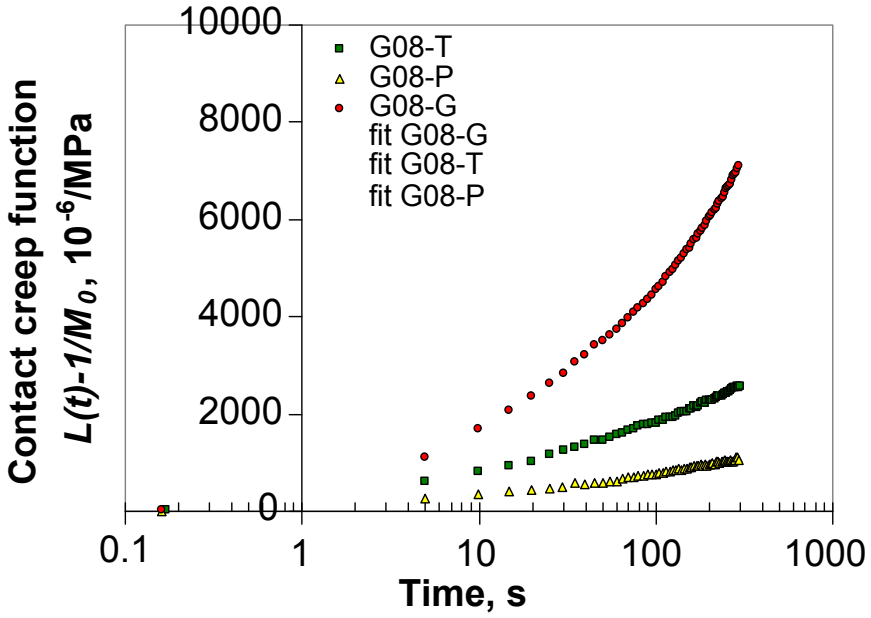

Figure 5.6: Summary of contact creep functions from indentation creep testing and their corresponding fits with Eq. 4.3, on gypsum samples immersed in various solutions: G08-T immersed in Trilon-P solution, G08-P immersed in phosphate solution and G08-G immersed in gypsum solution.

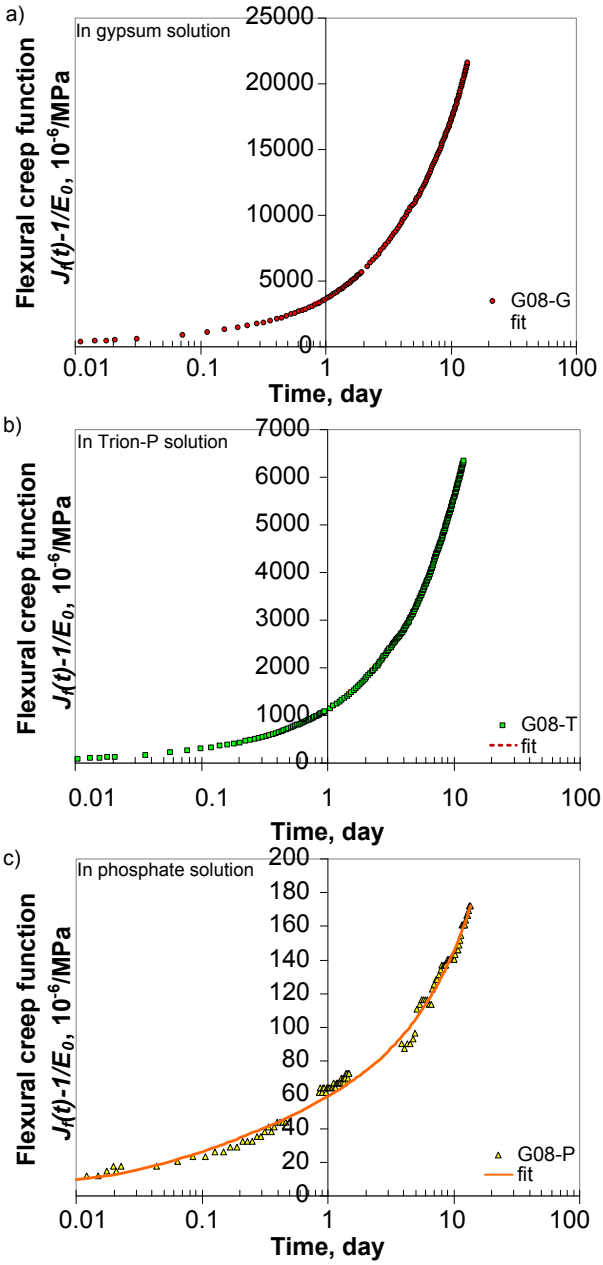

Figure 5.7: Summary of flexural creep functions from three-point bending creep testing and their corresponding fits with Eq. 5.9, on gypsum samples immersed in various solutions: G08-T immersed in Trilon-P solution, G08-P immersed in phosphate solution and G08-G immersed in gypsum solution.

On the other hand, a much more evident curvature of creep function from bending can be found in logarithmic time scale (see in Fig. 5.7 and 5.3a, when comparing with that from indentation (see in Fig. 5.6 and 5.3b, which indicates that the creep functions from bending are never logarithmic with respect to time. In order to capture the characteristics of those curves, we decompose the flexural creep function into a logarithmic part and an additive non-logarithmic part. The logarithmic part is characterized similarly as contact creep function by a characteristic time τ_f, termed as flexural characteristic time and a creep modulus C_f termed as flexural creep modulus. The non-logarithmic part is a linear function characterized by a creep rate λ. The flexural creep function can thus be written as:

$$J_f(t) - \frac{1}{E_0} = \frac{\ln(t/\tau_f + 1)}{C_f} + \lambda t \tag{5.9}$$

The flexural creep modulus C_f controls creep rate of the logarithmic part of flexural creep function. The higher the value of C_f is, the lower the long-term creep rate is, for the logarithmic part of flexural creep function. Yet, with the presence of the linear part of flexural creep function, the amplitude and rate of long-term flexural creep function is no longer dominated by the logarithmic term but by the linear term: with Eq. 5.9, the long-term flexural creep function is controlled by the linear term with the parameter λ. Choosing a linear function for the non-logarithmic part is completely due to practical reasons: linear function is simple to use and at the same time gives very good fitting results (See Fig. 5.7).

The parameters of creep functions from the two testing techniques are presented in Tab. 5.6. The parameters were obtained by best-fitting experimental results with proposed creep functions (Eq. 4.3 for indentation results and Eq. 5.9 for bending results).

As one may readily see from Tab. 5.6, for 4 samples out of 6, i.e., G07, G08 and G09 (conditioned at 50% relative humidity) and G08-G (immersed in solution saturated with gypsum), the creep moduli measured by indentation creep testing are very close to those by three-point bending creep testing. For samples immersed in solutions with additives, i.e., G08-T and G09-P, the creep moduli measured by indentation creep testing are different from those measured by three-point bending creep testing. The difference is small for G08-T, the sample immersed in solution with Trilon-P but as high as 38 times for G08-P, the sample

	Bending			Indentation	
Sample	C_f**(GPa)**	τ_f**(s)**	λ **(MPa/s)**	C_i**(GPa)**	τ_i **(s)**
G07	28.02	5.83×10^{3}	7.16×10^{-11}	33.94±3.79	9.34±3.54
G08	27.89	1.13×10^{4}	1.07×10^{-10}	28.52±5.11	8.59±3.71
G09	42.34	1.23×10^{3}	1.23×10^{-10}	39.78±9.59	3.40±3.62
G08-G	0.37	2.40×10^{4}	1.10×10^{-8}	0.39±0.19	29.0 ±19.1
G08-T	2.41	6.46×10^{4}	4.54×10^{-9}	1.42±0.43	18.7 ±11.0
G08-P	76.20	2.27×10^{3}	7.25×10^{-11}	2.01±0.83	13.4 ±10.1

Table 5.6: Summary of creep functions parameters from bending creep testing and indentation creep testing. Sample G07, G08 and G09 were conditioned and tested in 50% relative humidity; Sample G08-G,G08-T and G08-P were immersed in solutions, tested in immersed conditions by bending and at 100% relative humidity by indentation.

immersed in solution with phosphate.

For the characteristic time, τ_i from indentation creep testing is in the order of 10s, varying from 3.4s to 29s for different samples, while τ_f from bending testing varies from 1130s to 64600s. The characteristic times from the two testing techniques are thus not quantitatively comparable at all. However, the evolution of characteristic time with respect to the condition environments is comparable: comparing sample G08 with G08-G, G08-T and G08-P, by immersing sample in solutions, characteristic time from the two testing techniques is increased. On the other hand, for the samples immersed in various solutions, comparing sample G08-G without additive with G08-T with additive of Trilon-P, the trend of characteristic time is different according to the results from the two testing techniques: with presence of Trilon-P, bending testing shows an increase of characteristic time by a factor of 4 while indentation testing shows a decrease by a factor of 0.7.

The parameter λ seems to be influenced by water content: for all the samples conditioned in 50% relative humidity, the value of λ is in the order of 10^{-10}MPa/s while for sample G08-G immersed in solution without additive, λ increased by an order of 100. λ seems also to be influenced by additives: compared with G08-G immersed without aditive, λ is decreased with presence of Trilon-P by a factor of 2 while by a factor of 150 with the presence of phosphate.

5.3.4 Discussion

Qualitatively, for what concerns the creep properties of gypsum samples and their dependence on the formulation of sample and the conditioning environment, indentation and bending yield comparable results. Firstly, the creep functions of gypsum samples with water-to-hemihydrate ratio w/h of 0.7, 0.8 and 0.9 are quite similar, and this was confirmed by both indentation creep testing and three-point creep testing. As presented in Tab. 5.2.1 the porosity of those samples are quite similar, varying from 52% to 59%. So the similarity in creep functions for sample G07, G08 and G09 is probably due to the fact that the porosities of those samples are similar. Secondly, increasing the water content in gypsum by immersing sample in solution leads to a higher creep, and this was also confirmed by the two testing techniques. Lastly, by immersing gypsum samples in solutions with additives can reduce the creep of those samples, and this was, again, confirmed by the two testing techniques.

For quantitative comparison, the contact creep function was characterized by a logarithmic function with two parameters namely the contact creep modulus C_i and indentation characteristic time τ_i; the flexural creep function was characterized by a logarithmic function plus a linear one. The logarithmic part was characterized by two parameters namely the flexural creep modulus C_f and bending characteristic time τ_f, while the linear part was characterized by the parameter λ.

The quantitative comparison of the creep parameters obtained by indentation and that obtained from bending was fairly good: for samples conditioning at 50% relative humidity and immersed in solution without additives, the creep moduli from the two testing techniques are highly comparable, as one can see from Tab. 5.6. On the other hand, the characteristic time needed to achieve logarithmic creep on gypsum was much shorter for indentation creep testing than for macroscopic creep testing. Therefore, indentation creep testing is validated as a fast technique which gives rapid acess to logarithmic creep kinetics.

Note that, the observation of logarithmic creep for gypsum is not only limited to indentation testing: indeed, De Meer and Spiers [1997], De Meer et al. [1997] and De Meer and Spiers [1999] obtained also logarithmic creep functions of compacted gypsum aggregates by compression. In those studies, uniaxial com-

pressive creep testing was carried out on compacted gypsum aggregates under water-saturated conditions. As presented in Fig. 5.8, the creep function, which is proportional to the time-dependent uniaxial strain, of gypsum aggregate samples with various average grain size and under various stress levels are logarithmic respect to time. However, since the experiments of De Meer were performed on compacted gypsum aggregates, the observed logarithmic creep may be due to the fact that the samples are made of an assembly of grains, rather than the viscous properties of the gypsum grain themselves.

But why is there a non-logarithmic term in flexural creep function? What does this term stand for?

Firstly, the non-logarithmic part of flexural function could be due to cracking or microcracking promoted by bending. Cementitious materials are quasi brittle materials with large difference in compressive strength and tensile strength. Under bending testing, there is a region under tensile stress, which is favorable for cracking at local scale, i.e., within the representative elementary volume.

Secondly, the non-logarithmic part of flexural creep function on material scale could be due to the presence of tensile creep of gypsum under bending. Indeed, during a bending creep test, regions with compressive and tensile stresses co-exist and both of those regions contribute to the measured time-dependent deflection $D(t)$ and thus contribute to the flexural creep function. In other words, the flexural creep function includes the contribution of both tensile creep and compressive creep. And it may well be that the compressive creep function of gypsum differs significantly from its tensile creep function. In contrast, for indentation creep testing, high compressive stress is applied on samples: the creep function measured by indentation is more representative of compressive creep.

The comparison on creep modulus worked less well for sample G08-T immersed in solution with Trilon-P and did not work at all for sample G08-P which was immersed in solution with phosphate. Such discrepancy could be explained if Trilon-P and phosphate were acting in different manners on compressive creep and tensile creep of gypsum.

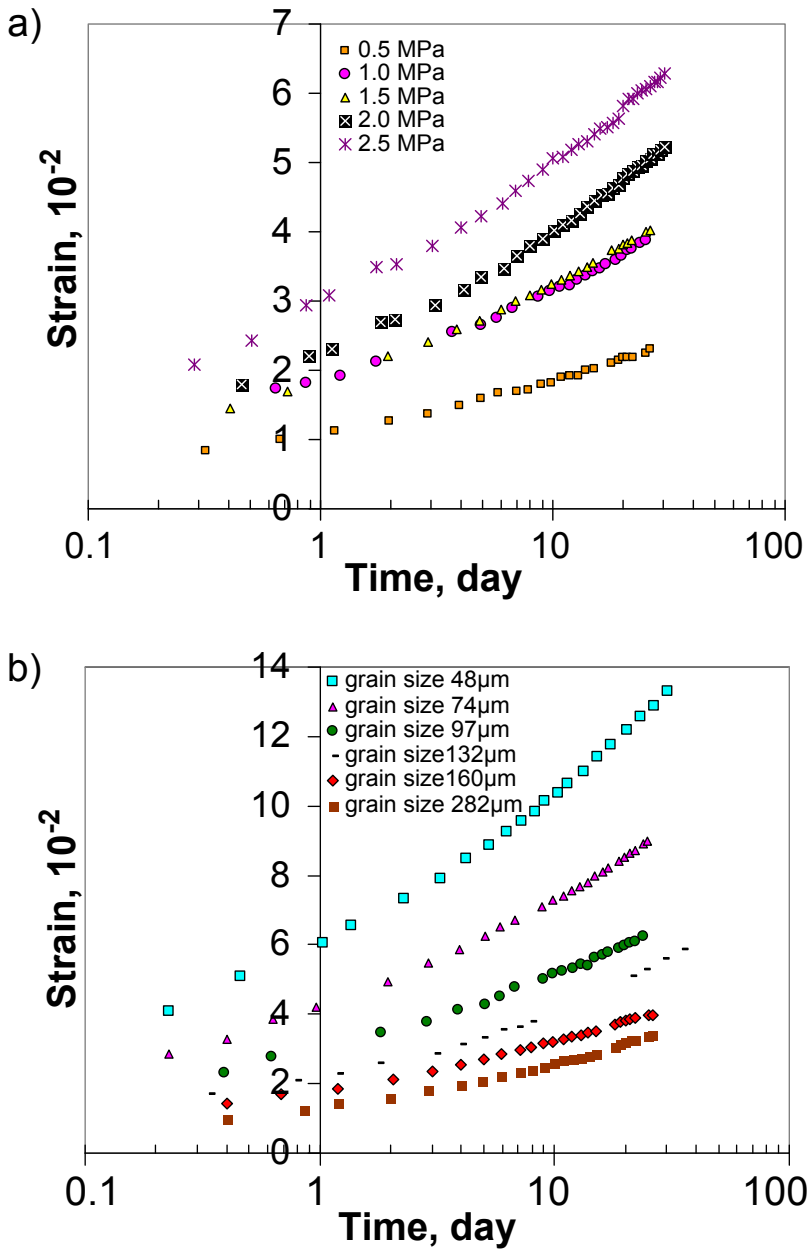

Figure 5.8: Time-dependent uniaxial strain obtained by uniaxial compressive creep testing in water-saturated condition on gypsum aggregates samples a) tested at different compressive stress levels b) with different average size of gypsum grains [De Meer and Spiers, 1997].

5.4 Chapter conclusions

This chapter was dedicated to compare microindentation creep experiments with macroscopic three-point bending creep testing on gypsum plaster. In total six groups of samples with either difference in water-to-hemihydrate ratio w/h or conditioning environment were tested by the two techniques. Three-point bending creep experiments lasted for more than 10 days. In contrast, microindentation creep experiments only lasted for minutes. The specific basic creep of gypsum samples was captured through a contact creep function for indentation creep testing and through a flexural creep function for three-point bending creep testing, respectively.

Qualitatively, indentation creep testing enables to capture the trends observed with bending creep testing on the creep properties: light dependence on the water-to-hemihydrate ratio in the range of water-to-hemihydrate ratio considered, effect of hygral condition, creep-reducing effect of additives. The qualitative comparison also confirms the effect of water and additives on the specific basic creep of gypsum which were already observed in former studies:

- The higher the water content in gypsum, the higher the specific basic creep of gypsum plaster.
- With the presence of additives Trilon-P and phosphate, specific basic creep of gypsum is largely reduced.

For quantitative comparison, analytical functions were fitted to the experimental creep functions in order to back-calculate creep parameters. For all indentation experiments, after a transient period, the specific basic creep of gypsum measured by indentation testing was well captured by a logarithmic function of time. The contact creep modulus C_i and the indentation characteristic time τ_i were the two parameters used to characterize the contact creep function. The creep function measured by bending was fitted with the sum of a logarithmic function of time and a linear one. The flexural creep modulus C_f and the flexural characteristic time τ_f controlled the logarithmic part of creep, while a third parameter λ controlled the linear part. Due to the presence of linear term in the flexural creep function, the long-term behavior of this creep function is no longer

controlled by the logarithmic term but the linear one. The non-logarithmic behavior of specific creep function of gypsum obtained by three-point bending creep testing may be explained by the presence of tensile creep during bending creep testing.

The comparison showed that the creep moduli of gypsum measured by indentation were almost in perfect agreement with those measured by bending for sample conditioned in environment without additives. The sample immersed in solution with phosphate is an exception: a difference of factor of 30 between the contact modulus measured by indentation and flexural modulus measured by bending was found. The comparison also showed that the characteristic time needed to reach a logarithmic kinetics of creep for bending testing was at least 1000 times as high as that for indentation creep testing. Therefore, the access to logarithmic kinetics of creep is accelerated by indentation creep test when compared with bending creep testing.

So far, the minutes-long indentation creep testing is validated as a testing technique to measure the long-term logarithmic creep of cementitious materials. In the following chapters, the technique will be applied to study the effect of microstructure and water on the long-term basic creep properties of cementitious materials.

Part III

Effect of microstructure and relative humidity on long-term basic creep of cementitious materials

Chapter 6

Creep properties of C_3S and C_2S pastes

Résumé *Dans ce chapitre, nous appliquons la technique d'indentation validée pour étudier les propriétés de fluage des matériaux cimentaires. Les propriétés mécaniques telles que le module de Young E, la dureté d'indentation H ainsi que les propriétés de fluage, à savoir le module de fluage C_i et le temps caractéristique τ_i sur des pâtes C_3S et C_2S, ont été obtenues par microindentation. La microstructure des pâtes testées a été caractérisée par la fraction volumique de chaque phase déduite à partir du degré d'hydratation estimé à partir de la mesure du retrait chimique. Nous avons établi une relation linéaire entre le module de fluage C_i et la dureté d'indentation H ainsi qu'une fonction de puissance entre le module de fluage C_i et le module de Young E. La relation entre les propriétés mécaniques et la fraction volumique de chaque phase est explorée en traçant simplement les propriétés mécaniques en fonction de la fraction volumique de chaque phase. Nous abordons également l'effet de la porosité sur ces propriétés mécaniques. Les résultats confirment que E, H et C_i augmentent lorsque le degré d'hydratation augmente. La proportion de chaque phase et les propriétés mécaniques des pâtes C_3S et C_2S seront utilisées ultérieurement dans le chapitre 9 pour valider le modèle micromécanique.*

Abstract *In this chapter, we apply the validated indentation technique to study the creep properties of cementitious materials. Mechanical properties such as*

Young's modulus E, indentation hardness H and creep properties, i.e., contact creep modulus C_i and characteristic time τ_i, of hydrating C_3S and C_2S pastes were obtained by microindentation testing. The microstructure of the tested pastes was characterized by the volume fraction of each phase inferred from the hydration degree estimated from chemical shrinkage measurement. We found a linear relationship between contact creep modulus C_i and indentation hardness H and a power-law relation between contact creep modulus C_i and Young's modulus E. The relation between mechanical properties and the volume fraction of each phase was explored by simply plotting mechanical properties versus the volume fraction of each phase. We also discussed the effect of porosity on these mechanical properties. The results confirm that E, H and C_i increased with increasing degree of hydration. The proportion of each phase and mechanical properties of C_3S and C_2S pastes will be further used in chapter 9 to validate micromechanical model.

6.1 Chapter introduction

Microindentation creep testing was validated quantitatively for measuring the creep properties of cementitious materials in chapter 4 and chapter 5. In the following chapters, this validated technique will be applied to study the creep properties of cementitious materials to get a better understanding of creep, i.e., to study the influence of microstructure and water on creep.

Assessing that we aim at studying the effect of microstructure on creep is a very general statement. To make it more precise, the microstructure of cementitious materials can be regarded as an assembly of different phases. Two pieces of information are thus important for characterizing the microstructure: the volume fraction of each phase and the spatial organization of those phases. So the problem can be formulated more precisely as: how the volume fraction of each phase and the organization of each phase influence the creep properties of the material studied.

Microindentation testing enables to measure the mechanical properties at the scale of the paste. Various experimental techniques provide the volume fraction of each phase and some information on how the phases are organized in space. Combining the mechanical properties from indentation and the information on the volume fraction of each phase in a paste, the effect of microstructure on creep may be decoded.

In this chapter, we use pastes of C_3S and C_2S for the purpose of studying the effect of microstructure on creep. Tricalcium silicate (also called alite, Ca_3SiO_5 or C_3S in abbreviation) and β-dicalcium silicate (C_2S, Ca_2SiO_4 or belite) are the major components in Portland cement clinker. When mixing C_3S or C_2S with water, chemical reactions indicated in Eq. 6.1 or in Eq. 6.1, referred to generally as "hydration reactions" occur, and produce Portlandite (CH) and calcium silicate hydrate (C-S-H). The reactions can be expressed as follows:

$$C_3S + (3 - x + m)H \rightarrow (3 - x)CH + C_x\text{-}S\text{-}H_m \tag{6.1}$$

$$C_2S + (2 - y + n)H \rightarrow (2 - y)CH + C_y\text{-}S\text{-}H_n \tag{6.2}$$

As presented in Fig 6.1, at the scale of micrometer, crystals of Portlandite are embedded in a matrix of C-S-H while the areas with conglomeration of small

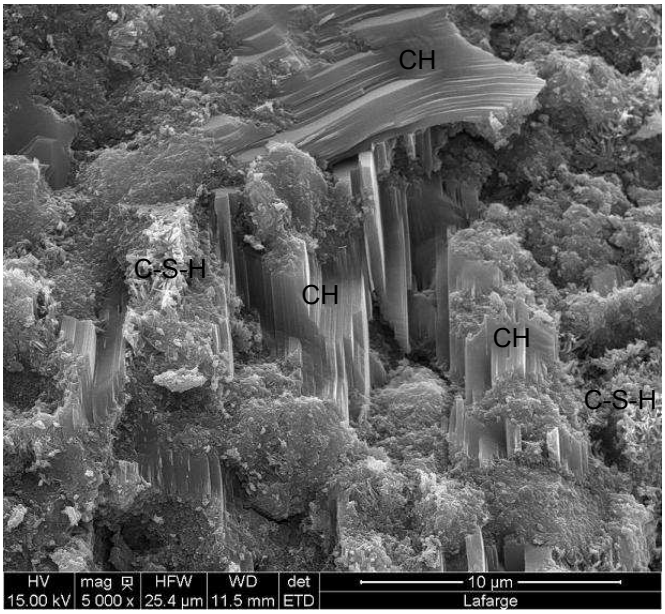

Figure 6.1: Fracture surface of hydrated C_3S paste at age of 90 days observed by scanning electron microscopy.

crystals are where one can find the presence of C-S-H. C-S-H is a complex hydration product. Though a lot of information on the structure of C-S-H at the atomic scale was obtained and refined in the last decade [Cong and Kirkpatrick, 1996; Jennings, 2000; Nonat, 2004; Richardson, 2004; Skinner et al., 2010; Taylor, 1986], the study of the structure of C-S-H is still ongoing. The average value of atomic calcium/silicon ratio (i.e., x in Eq. 6.1 or y in Eq. 6.2) of C-S-H in pure C_3S and C_2S paste and in ordinary Portland cement paste is between 1.7 and 1.8 [Richardson, 2000], and the ratio may vary locally. The molar water/silicon ratio (h/s, i.e., m in Eq. 6.1 or n in Eq. 6.2) may vary between 1.3 and 4 and is equal to 4 in water-saturated conditions [Brunauer, 1972; Feldman, 1972; Feldman and Sereda, 1968; Jennings, 2008; Powers and Brownyard, 1947; Thomas et al., 2001]. We apply the following hypotheses for the following calculations:

- The atomic calcium/silicon ratio is equal to 1.7 for both C-S-H produced by hydration of C_3S and C_2S; this ratio is constant in the range of ages investigated in this study, i.e., after 1 day of hydration.

- The molar water/silicon ratio h/s is equal to 4, for both C-S-H produced by hydration of C_3S and C_2S, as all the samples will be cured in water and

tested in condition without drying.

By applying a formula of $C_{1.7}$-S-H_4, the C-S-H phase represents the sum of C-S-H solid matrix and the porosity filled with water included in the chemical formula of $C_{1.7}$-S-H_4 (mainly the gel porosity). And consequently, what we call porosity does not include those pores included in the C-S-H phase. By applying the two hypotheses, Eq. 6.1 and Eq. 6.2 can be rewritten as:

$$C_3S + 5.3H \rightarrow 1.3CH + C_{1.7}\text{-S-}H_4 \tag{6.3}$$

$$C_2S + 4.3H \rightarrow 0.3CH + C_{1.7}\text{-S-}H_4 \tag{6.4}$$

As one can see from Eq. 6.3 and Eq. 6.4, the stoichiometric proportions of CH and C-S-H produced by the hydration of C_2S or C_3S differ from each other. Moreover, for a C_3S paste or C_2S paste under hydration, the proportions of hydrated products i.e., CH and C-S-H, and that of unhydrated clinker (C_3S or C_2S) evolve with time. Thus, by performing indentation testing on C_3S pastes and C_2S pastes at various ages of hydration, one measures the mechanical properties of pastes with various proportions of CH, C-S-H, unhydrated clinker and porosity.

As indentation creep testing takes only a few minutes, after about one day of hydration, the change of microstructure of tested materials during indentation testing can be ignored. As indentation creep testing gives access to long-term creep properties of the tested cementitious materials, the creep properties measured are the long-term creep properties of a paste with given unchanging microstructure i.e., with given proportion of C-S-H, CH, unhydrated clinker and porosity. So, thanks to the rapidity of indentation creep testing, the long-term creep properties of materials with various microstructures that do not evolve during creep experiment can be obtained and linked to their microstructures at the moment of test.

This chapter is dedicated to presenting the experimental study done C_3S pastes and C_2S pastes. The experimental settings as well as the results and their interpretation will be presented.

Material	Specific surface (cm^2/g)	Density (g/cm^3)
C_3S	5181	3.15
C_2S	4937	3.27

Table 6.1: Physical properties of C_3S and C_2S.

6.2 Materials and methods

6.2.1 Synthesis of pure C_3S and C_2S

Both C_2S and C_3S were synthesized at Lafarge Research Center by heating well mixed chemical reagent pure calcium carbonate ($CaCO_3$) and silica (SiO_2) with given stoichiometric proportion to high temperatures, i.e., with step increase from 1000°C to 1620°C for C_3S or from 1000°C to 1600°C for C_2S, during four hours. The following chemical reactions happen for C_3S and C_2S, respectively:

$$3CaCO_3 + SiO_2 \rightarrow Ca_3SiO_5 + 3CO_2 \uparrow \tag{6.5}$$

$$2CaCO_3 + SiO_2 \rightarrow Ca_2SiO_4 + 2CO_2 \uparrow \tag{6.6}$$

The products of the above chemical reaction were cooled rapidly to get desirable polymorph(s) of C_2S and C_3S. For C_3S, the quantity of free lime is controlled within 0.5% in mass proportion. For C_2S, the proportion of β-dicalcium silicate is close to unity yet very small quantities of α-dicalcium silicate is detectable by X-ray diffraction. The specific surface and the density of C_2S and C_3S used in this study are presented in Tab. 6.1.

6.2.2 Preparation of C_3S and C_2S paste samples

The following procedure was applied to prepare C_2S and C_3S pastes:

- at a temperature of 20°C, add powder of C_2S or C_3S to a given quantity of deionized de-CO_2 water in less than 30 seconds, while stirring with a spoon;
- seal the container with mixture and install it into a mixing unit and mix for 1 minute at a speed of 3000 rpm (revolutions per minute);
- stop mixing, unseal container and homogenize the mixture by retrieving the mixtures projected on inner wall of container;

sample	**material**	w/c
A50	C_3S	0.42
A42	C_3S	0.50
B42	C_2S	0.42

Table 6.2: Labeling and main control parameter of C_3S and C_2S paste samples.

- seal the container, mix for another 1 minute with the same speed;
- pour the mixture into cleaned cylinder molds (Φ=11mm, h=70mm) and vibrate molds in vibrating table for 10 seconds to eliminate the trapped air bubbles;
- seal molds and rotate the sealed mold in order to prevent any segregation. The rotation lasted for 15 hours and 3 days for C_3S and C_2S pastes before set respectively.

After rotation, all the samples were demolded and cured in deionized de-CO_2 water at 20°C till given ages. For each formulation, i.e., for a given type of clinker and a given water-to-cement ratio, 10 cylinder samples were prepared. The formulation and labeling of samples are given in Tab. 6.4.

6.2.3 Assessment of phase distribution in hydrating C_3S and C_2S pastes

The volumetric phase distribution in a cement paste is the volume fraction of each phase. As hydration proceeds, water reacts with clinker and produces hydration products. As presented in Fig. 6.2, the term 'cement' in the figure represents the volume of unreacted clinker; the term 'gel solid' represents the volume occupied by hydration products, the term 'capillary water' represents the volume of residual water, which is equal to the difference between initial water and water reacted with clinker, the term 'pores' refers to the volume of pores created inside a paste, as the hydration products occupy less space than the sum of volume of clinker and water from which it is formed within a closed cement paste system. The sum of volume fraction of pores and capillary water in Fig. 6.2 gives the porosity of the paste.

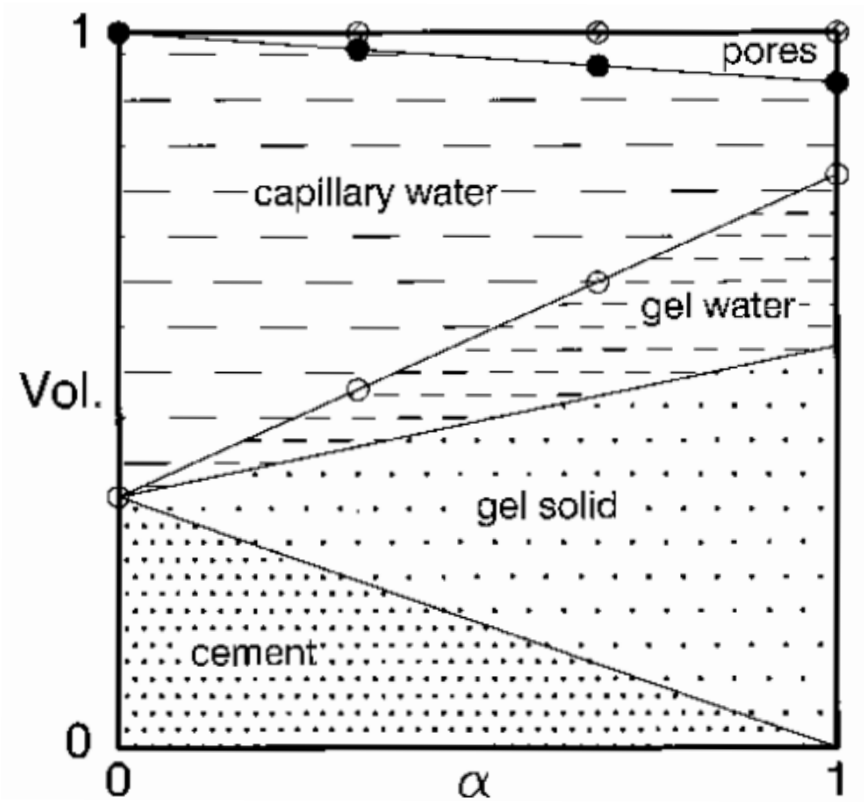

Figure 6.2: Volumetric phase distribution in a cement paste as a function of the degree of hydration α, at water-to-cement ratio of w/c=0.6. The diagram applies to a sealed hydration without exchange of water with the surroundings. Due to the high w/c, full hydration with degree of hydration $\alpha = 1$ of the cement can theoretically be obtained [Jensen and Hansen, 2001].

For a C_3S paste or a C_2S paste, the volumetric phase distribution is the porosity, the volume fraction of C-S-H, CH and unhydrated C_2S or unhydrated C_3S. The chemical reaction that happens when mixing water with C_3S or C_2S is indicated by Eq. 6.3 or Eq. 6.4, respectively. If one knows the quantity of reacted C_3S or C_2S, and the initial mass of reactant i.e., water and C_3S or C_2S, one can determine the mass of each phase. If the density of each phase is also known, the volume of each phase occupied by each phase can be found. We present next how to determine the volumetric phase distribution for a paste of C_3S. The method can be applied to C_2S similarly.

Suppose a mass m_0 of C_3S is mixed with water at a water-to-cement mass ratio of w/c, and that a fraction α of the initial mass of C_3S is reacted (thus, α is the degree of hydration of C_3S by definition). When the quantity of water is enough or in excess for consuming all the C_3S, i.e., $w/c \geq 0.42$ [Taylor, 1997], applying formula 6.3, the volume of water $V(H_2O)$, the volume of CH $V(CH)$, the volume of C-S-H $V(CSH)$ and the volume of unhydrated C_3S, $V(C_3H)$ can be given by:

$$V(C_3S) = \frac{(1-\alpha)m_0}{\rho(C_3S)} \tag{6.7a}$$

$$V(H_2O) = \frac{m_0 \cdot w/c - 5.3\frac{\alpha m_0}{M_m(C_3S)} \cdot M_m(H_2O)}{\rho(H_2O)} \tag{6.7b}$$

$$V(CSH) = \frac{\frac{\alpha m_0}{M_m(C_3S)} \cdot M_m(CSH)}{\rho(CSH)} \tag{6.7c}$$

$$V(CH) = \frac{1.3\frac{\alpha m_0}{M_m(C_3S)} \cdot M_m(CH)}{\rho(CH)} \tag{6.7d}$$

where $M_m(C_3S)$, $M_m(H_2O)$, $M_m(CSH)$, $M_m(CH)$ are the molar mass of C_3S, water, C-S-H and CH respectively, and $\rho(C_3S)$, $\rho(H_2O)$, $\rho(CSH)$ and $\rho(CH)$ are the density of C_3S, water, C-S-H and CH respectively. The molar mass of water, C_3S and CH phases are known unambiguously while that of C-S-H is still under debate. As presented in Eq. 6.2, when considering a formula of C-S-H being $C_{1.7}$-S-H_4, the molar mass of C-S-H $M_m(CSH)$ is thus known. With the above information, the volume of C-S-H, CH, C_3S and water can be found out for given degree of hydration α. By assuming that there is no bulk shrinkage from the start of mixing, the porosity ϕ of a C_3S paste sample at a given degree of hydration α

can be obtained with the following equation:

$$\phi = 1 - \frac{V(\mathrm{CSH}) + V(\mathrm{CH}) + V(\mathrm{C_3S})}{m_0/\rho(\mathrm{C_3S}) + (w/c \cdot (m_0/\rho(\mathrm{H_2O}))} \tag{6.8}$$

In order to know the degree of hydration α of a hydrating paste at given time, various experimental methods exist, such as quantitative X-ray diffraction analysis [Copeland et al., 1960], isothermal calorimetry [Monfore and Ost, 1900], scanning electron microscopy backscattered electron image analysis [Kjellsen et al., 1990b], chemical shrinkage [Parrott et al., 1990]. In the present study, the hydration degree of samples is determined by chemical shrinkage experiment.

As the volume occupied by the products of hydration is different from the initial volume occupied by reactant, along with chemical reaction, a macroscopic time-dependent volume change only due to chemical reaction can be observed. For C_3S and C_2S, as the products of hydration occupy less volume than the reactants, the total condensed phase of C_3S or C_2S shrinks. This time-dependent volume change per mass unit reactant is defined as chemical shrinkage [ASTM C-1608-07, 2007], denoted as $S_{ch}(t)$.

Note, however, that, after set, most of this volume change is not converted to any significant change in the bulk volume of the paste. Instead, if it is immersed in excess water, the paste sucks in liquid water to replace the missing volume. Thus, the volume of absorbed water is equal to the volume change due to chemical shrinkage. Therefore, by measuring the mass of absorbed water, the chemical shrinkage can be measured:

$$S_{ch}(t) = m_a/\rho(\mathrm{H_2O}) \tag{6.9}$$

where m_a is the mass of absorbed water at time t which starts when chemical reaction starts and $\rho(\mathrm{H_2O})$ is the density of water at given temperature. The experiments on measuring chemical shrinkage of C_3S paste and C_2S paste were carried out according to the internal experimental standard of Lafarge Research Center.

Knowing the time-dependent chemical shrinkage $S_{ch}(t)$, the hydration degree

α can be obtained by the following equation:

$$\alpha(t) = \frac{S_{ch}(t)}{S_{ch}^{\infty}} \tag{6.10}$$

where S_{ch}^{∞} is the chemical shrinkage when hydration is completed. For C_3S paste, combining the equation above with Eq. 6.7 one obtains:

$$\begin{aligned} S_{ch}^{\infty} = & \quad 1 - \frac{[V(C_3S) + V(H_2O) + V(CSH) + V(CH)]_{\alpha=1}}{[V(C_3S) + V(H_2O) + V(CSH) + V(CH)]_{\alpha=0}} \\ = & \quad 1 - \frac{w/c \cdot \frac{M_m(C_3S) - 5.3M_m(H_2O)}{\rho(H_2O)} + \frac{M_m(CSH)}{\rho(CSH)} + \frac{1.3M_m(CH)}{\rho(CH)}}{\frac{M_m(C_3S)}{\rho(H_2O)} + w/c \cdot \frac{M_m(C_3S)}{\rho(C_3S)}} \end{aligned} \tag{6.11}$$

Among all the parameters indicated in Eq. 6.7 and Eq. 6.11, the time-dependent chemical shrinkage $S_{ch}(t)$ can be obtained experimentally and the molar mass of each phase is known, as well as the density of CH, water and C_3S. A summary of density of different phases is given in Tab. 6.3. However, a difficulty lies in the density of C-S-H. The density of C-S-H in cement paste varies with the content of water bonded to C-S-H and may vary from from 1.83g/cm^3 to 2.85g/cm^3 [Feldman, 1972; Jennings, 2000, 2008; Powers and Brownyard, 1947]. The studies on the density of C-S-H in various hydraulic conditions are still ongoing. As already mentioned by Fernandez [2008], the degree of hydration α determined by chemical shrinkage with the method indicated above is quite sensitive to the value chosen for the density of C-S-H. In her study, the density of C-S-H was calibrated by fitting the time-dependent curve of the degree of hydration obtained by chemical shrinkage with that from scanning electron microscopy backscattered electron image analysis. According to her, the density of C-S-H in C_3S pastes varies from 2.04 g/cm^3 to 2.09 g/cm^3, depending on the fineness of C_3S. Those values are quite close to the value of 2.03 g/cm^3 given by Jennings [2008] for $C_{1.7}$-S-H_4. Here we apply a value of 2.06 g/cm^3 for the density of $C_{1.7}$-S-H_4 for the following calculation in this chapter.

The volume fraction of each phase can be calculated and, by dividing those volumes by the volume of the paste, the volumetric phase distribution can be determined.

phase	**C_2S**	**C_3S**	**H_2O**	**$C_{1.7}$-S-H_4**	**CH**
density (g/cm^3)	3.27	3.15	1.00	2.04	2.24
molar mass(g/mol)	172	228	18.0	227	74.0

Table 6.3: Density and molar mass of different phases in cement paste, used for the determination of volumetric phase distribution.

sample	**age of testing (day)**
A50	2, 4, 10, 21
A42	7, 15, 28, 56, 84
B42	3, 8, 13, 16, 28, 56

Table 6.4: Ages at testing of hydrating C_3S and C_2S pastes.

6.2.4 Microindentation creep testing on hydrating C_3S and C_2S pastes

Microindentation tests with different holding durations were carried out on C_2S and C_3S pastes samples at various ages. A summary of the ages at testing is presented in Tab. 6.4. About 10 minutes before testing, a 7-millimeters-thick disc was cut from the median part of the cylindrical sample. The surface to be indented was then polished according to the protocol mentioned in section 4.2.3, i.e., with 4 pads of silicon carbide paper with decreasing particle size. The polishing lasted for about 3 minutes, without any contact with water or any other solvent. Once polished, the sample to be tested was moved into the indentation chamber and fixed on the indentation platform. In the chamber, both the temperature and the relative humidity were controlled at 23°C±0.2°C and about 100%, respectively. As the temperature (23°C) in the chamber was slightly higher than curing temperature (20°C), several minutes were waited before starting indentation creep experiment which allows sample achieving the same temperature as in the testing chamber. As all samples were cured under water, the internal relative humidity was close to 100%. In order to eliminate the deformation due to drying, the relative humidity inside indentation chamber was controlled at about 100% by pumping in water-saturated CO_2-free air.

On each sample, 10 microindentation tests were performed with a Vickers indentation probe, including 5 repeats of test with 20-seconds-long holding phase to measure the Young's modus E and indentation hardness H and 5 tests with

Indentation probe	Vickers
Maximum indentation load P_{max}, N	5-20
Maximum indentation depth h_{max}, µm	50-100
Holding duration τ_H, s	20, 300 or 10000
Temperature	23°±0.2°
Relative humidity	100%

Table 6.5: Experimental parameter settings of indentation experiments on C_3S and C_2S pastes.

5-minutes-long holding phase to measure the contact creep function $L(t) - 1/M_0$. On sample A50 (C_3S paste with water-to-cement ratio w/c=0.5), at the age of 10 days, one indentation test with 10000s holding phase was carried out to give a glance at the shape of the creep function obtained by indentation.

The maximum load P_{max} applied on C_2S and C_3S varied from 5N to 20N. It was fixed in order to allow the maximal indentation depth h_{max} to be big enough but still smaller than the calibrated maximum depth for Vickers indentation probe, i.e., 100µm. For each indent, the load was increased linearly over time in 15 seconds, kept constant during the holding phase, and decreased linearly over time back to zero in 15 seconds. A summary of indentation parameter setting is presented in Tab. 6.5.

Mechanical properties such as Young's modulus E, indentation hardness H and contact creep function $L(t) - 1/M_0$ were calculated from the indentation experimental data by following the methods of analysis described in section 3.3. A Poisson's ratio $\nu = 0.25$ was used for obtained Young's modulus. An average value was calculated for E and H based on the 5 tests.

6.3 Results and discussion

6.3.1 Distribution of phases of hydrating C_3S and C_2S pastes

For the various tested samples, the degree of hydration α, the volume fraction f_{un} of unhydrated clinker, i.e., the volume fraction of C_3S for C_3S paste and that of C_2S for C_2S paste, the volume fraction f_{CSH} of C-S-H, the volume fraction f_{CH} of CH and porosity (which does not include the pores in the C-S-H phase) of different

sample	age (day)	α	f_{un}	f_{CSH}	f_{CH}	ϕ
A50	2	0.60	0.157	0.349	0.136	0.358
	4	0.68	0.124	0.398	0.156	0.322
	10	0.78	0.085	0.456	0.179	0.280
	21	0.85	0.058	0.498	0.194	0.250
A42	3	0.62	0.159	0.385	0.151	0.305
	8	0.76	0.101	0.474	0.185	0.241
	13	0.78	0.092	0.487	0.190	0.231
	16	0.83	0.070	0.521	0.203	0.207
	28	0.87	0.056	0.541	0.212	0.191
	56	0.89	0.050	0.550	0.215	0.185
B42	7	0.33	0.277	0.291	0.026	0.405
	15	0.40	0.248	0.354	0.032	0.366
	28	0.48	0.214	0.426	0.039	0.322
	56	0.56	0.182	0.493	0.045	0.280
	84	0.61	0.166	0.527	0.048	0.259

Table 6.6: Age of testing, degree of hydration α and phase distribution in hydrating C_3S paste, i.e., A50 with water-to-cement ratio w/c=0.5 and A42 with water-to-cement ratio w/c=0.42, and C_2S paste, i.e., B42 with water-to-cement ratio w/c=0.42.

pastes are listed in Tab. 6.6. Upon hydration, the volume fractions of C-S-H and CH increases while the porosity and the volume of unhydrated C_2S or unhydrated C_3S decrease. Indeed, the production of hydration product by chemical reaction fills the space of porosity thus an increase of volume of hydration product leads to a decrease of porosity. For samples with a given formulation, the evolution of each phase along with hydration is not independent. How the volume fractions of the various hydration products evolve upon hydration are linked to each other. For C_3S paste, the ratio f_{CSH}/f_{CH} of the volume fraction of C-S-H and of CH is found to be equal to 2.6 and for C_2S paste, the ratio is found to be equal to 11 at any time. The constance of this ratio is a consequence of assuming a constant density for C-S-H.

6.3.2 Mechanical properties of C_3S and C_2S pastes

The contact creep function was back-calculated by applying Eq. 3.42. For all the tested C_3S and C_2S pastes, the contact creep function was well captured y a

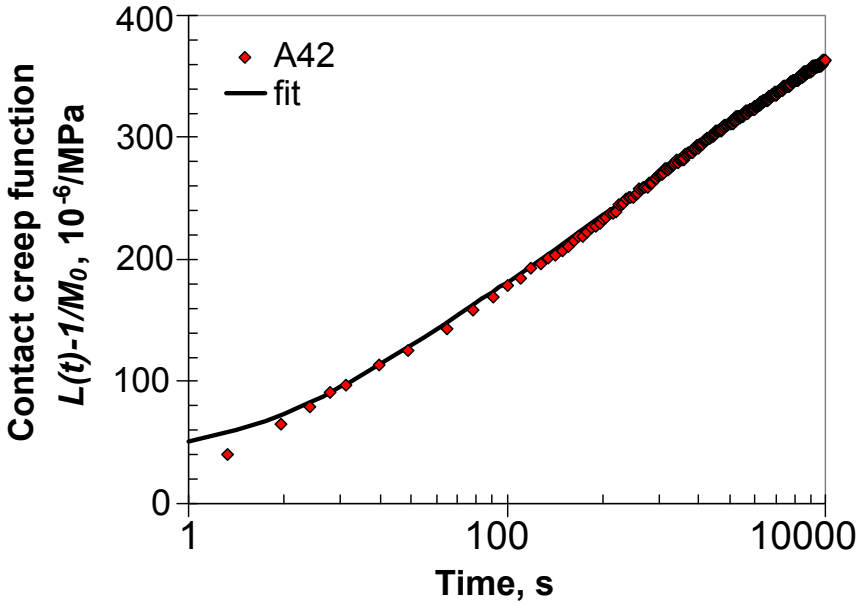

Figure 6.3: Contact creep function $L(t) - 1/M_0$ of C_3S paste sample A42 with water-to-cement ratio w/c=0.42 tested at age of 10 days with a 10000-seconds-long holding phase.

sample	**age (day)**	$\boldsymbol{E}$ **(GPa)**	$\boldsymbol{H}$ **(GPa)**	$\boldsymbol{C_i}$ **(GPa)**	$\boldsymbol{\tau_i}$ **(s)**
A50	2	5.00±0.40	0.104±0.004	8.56±0.71	0.7±0.2
	4	8.92±1.19	0.106±0.042	14.34±2.06	0.6±0.1
	10	11.35±0.44	0.154±0.036	25.48±5.39	1.3±0.3
	21	15.78±1.63	0.178±0.012	38.60±3.65	0.7±0.4
A42	3	6.49±0.56	0.094±0.011	18.78±3.45	0.7±0.3
	8	10.78±0.63	0.169±0.017	35.38±4.38	0.8±0.4
	13	11.27±2.75	0.234±0.039	35.78±3.09	1.6±0.2
	16	15.91±1.39	0.331±0.023	49.71±4.28	1.0±0.4
	28	19.15±1.27	0.327±0.019	51.02±1.91	1.7±0.7
	56	19.68±0.33	0.335±0.016	53.24±2.97	1.5±0.4
B42	7	2.62±0.23	0.021±0.003	3.44±0.95	2.4±1.4
	15	4.94±0.68	0.057±0.010	10.07±2.04	1.4±0.4
	28	8.44±0.60	0.121±0.011	19.43±3.24	1.0±0.9
	56	13.33±0.62	0.185±0.021	36.24±6.34	1.7±0.2
	84	17.46±3.56	0.280±0.076	43.10±3.73	1.5±0.5

Table 6.7: Mechanical properties of hydrating C_3S and C_2S pastes.

logarithmic function of time after a transition period. As presented in Fig 6.3, the logarithmic behavior of the creep function is confirmed also by an indentation creep experiment in which the holding indentation creep testing in which the holding phase was extended to 10000 seconds. As was the case with indentation creep experiments on cement paste, the contact creep function measured on C_3S and C_2S pastes were fitted with the logarithmic function given in Eq. 4.3. This fit yield, for each indentation creep experiment, a contact creep modulus C_i and an indentation characteristic time τ_i.

The Young's modulus E, the indentation hardness H, the contact creep modulus C_i and characteristic time τ_i obtained from indentation experiments are given in Tab. 6.7.

A general increase of Young's modulus, indentation hardness and indentation creep modulus is seen for all the samples with the progress of hydration. By plotting one mechanical property versus another, one can observe a potential correlation between those parameters. As presented in Fig. 6.4, despite the difference in water-to-cement ratio or type of clinker (C_3S or C_2S) and age of testing, within the standard deviation of experimental results, the $H(E)$, $C_i(H)$ and $C_i(E)$ relations seem to follow a single curve: data points nicely align around

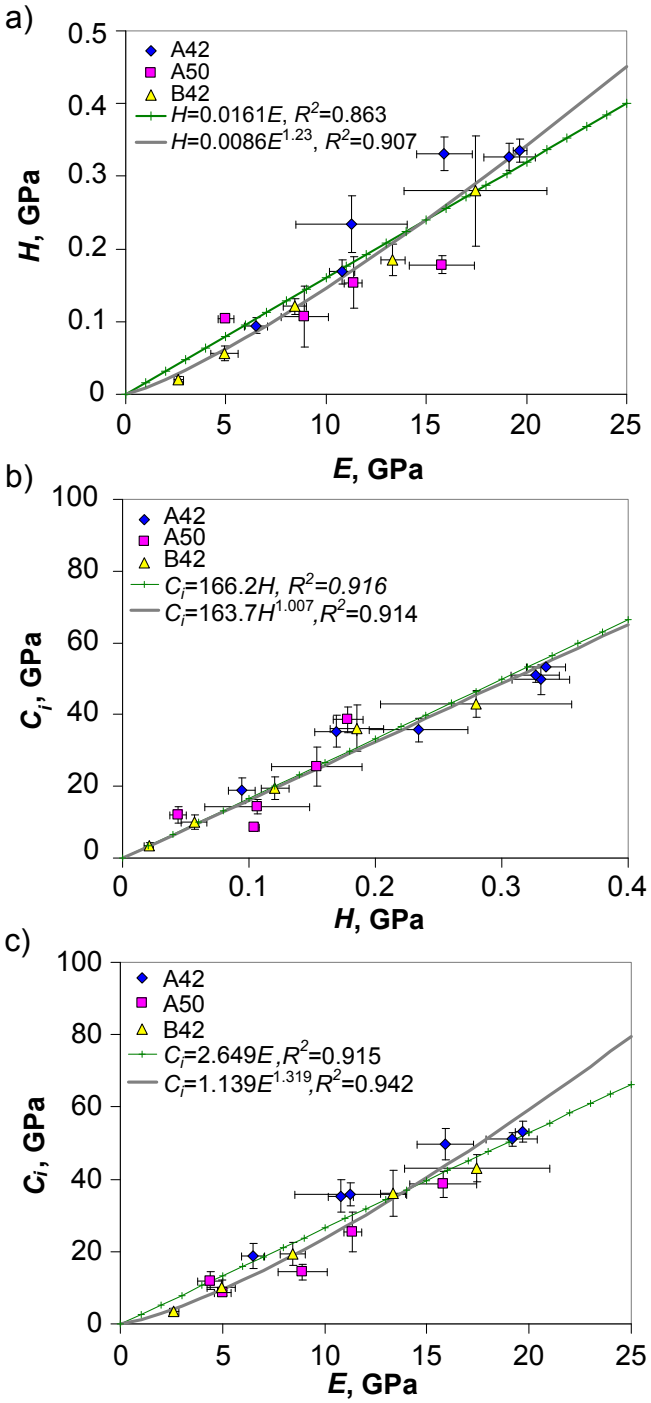

Figure 6.4: a) Indentation hardness H versus Young's modulus E, contact creep modulus C_i b) versus the Young's modulus E and c) versus the indentation hardness H from indentation tests performed on pastes of C_3S and C_2S.

master curves. Therefore, the relationship between C_i, E and H seems to be independent of the water-to-cement ratio, type of clinker and degree of hydration. Note however that data gathering around a single curve might no longer hold for other water-to-cement ratios or other raw materials. In any case, here with our results, it seems reasonable to fit all the data points with a single curve.

Performing a best-fit of the relation between H and E by power function and linear function yields $H/H_0 = 0.0086(E/E_0)^{1.23}$ (H_0=1MPa, E_0=1GPa) with $R^2 = 0.907$, and $H = 0.0161E$ with $R^2 = 0.863$, respectively. Performing a best-fit of the relation between C_i and E with a power function yields $C_i/C_0 = 1.139E/E_0^{1.319}$ (C_0=1GPa, E_0=1GPa), with a coefficient of determination $R^2 = 0.942$ and best-fit by linear function gives $C_i = 2.649E$, with $R^2 = 0.915$. Performing a best-fit of the relation between C_i and H by power function and linear function respectively yields $C_i/C_0 = 163.7(H/H_0)^{1.007}$ (C_0=1GPa, H_0=1MPa) with $R^2 = 0.914$, and $C_i = 162.2H$ with $R^2 = 0.916$. The fact that the exponent of power function fitted to the C_i(H) relationship was very close value to 1 and the coefficient of determination of the power function fit to this relation was close to that of the linear function proves a linear relationship between C_i and H. On the other hand, it seems that $H(E)$ and $C_i(E)$ relations follow a power law as the coefficient of determination R^2 of power function fit is higher than that of the linear fit function. Both the linear relation between contact creep modulus C_i and indentation hardness H and a power relation between contact creep modulus C_i and indentation hardness H were also observed by nanoindentation of the C-S-H phases in sub-stoichiometric Portland cement [Vandamme and Ulm, 2009].

6.3.3 Link between porosity and mechanical properties of C_3S and C_2S pastes

Cementitious materials are porous materials and their mechanical properties depend on their porosity. For all the samples, we plot the porosity versus the mechanical properties, as presented in Fig. 6.5. One can see from Fig. 6.5 that the contact creep modulus, the indentation hardness and the Young's modulus of all the samples tested decrease with the increment of porosity. However, when plotting the mechanical properties versus the porosity, data points do not gather

around a master curve, especially for Young's modulus. Therefore, the mechanical properties of C_2S paste and C_3S paste do not only depend on the porosity: solid phases affect those properties.

6.3.4 Link between volume fraction of solid phases and mechanical properties of C_3S and C_2S pastes

In Fig. 6.6 we plot the mechanical properties of C_3S and C_2S pastes in function of the volume fraction of C-S-H, of CH and of unhydrated C_3S. As presented in Fig. 6.6, an increase of the contact creep modulus, Young's modulus and indentation hardness of all the pastes is seen with the increment of the volume fraction of hydration products (C-S-H and CH) and with the decrease of volume fraction of unreacted clinker.

Clearly C_i, E and H do not depend only on the volume fraction of Portlandite f_{CH} or the volume fraction of unhydrated clinker: indeed, at a given volume fraction of portlandite or unhydrated clinker, the mechanical properties of different samples can significantly different from each other. In contrast, C_i, E and H of different samples with identical volume fraction of C-S-H are very close to each other. Therefore we conclude that for C_3S and C_2S pastes in the range of hydration degree and water-to-cement ratios considered, the mechanical properties of the pastes depend mostly on the volume fraction of C-S-H f_{CSH}: at a given volume fraction of C-S-H, the type of clinker and the water-to-cement ratio only have secondary effects.

6.4 Chapter conclusions

In this chapter, we obtained the volumetric phase distribution of C_3S and C_2S pastes with various testing ages, and different preparation formulations by acceding the hydration degree with chemical shrinkage and the mechanical properties by microindentation testing. We found a linear relationship between contact creep modulus C_i and indentation hardness H and a power-law relation between indentation hardness H and Young's modulus E and between contact creep modulus C_i and Young's modulus E. The relation between mechanical properties and the volume fraction of each phase was explored by simply plotting mechanical

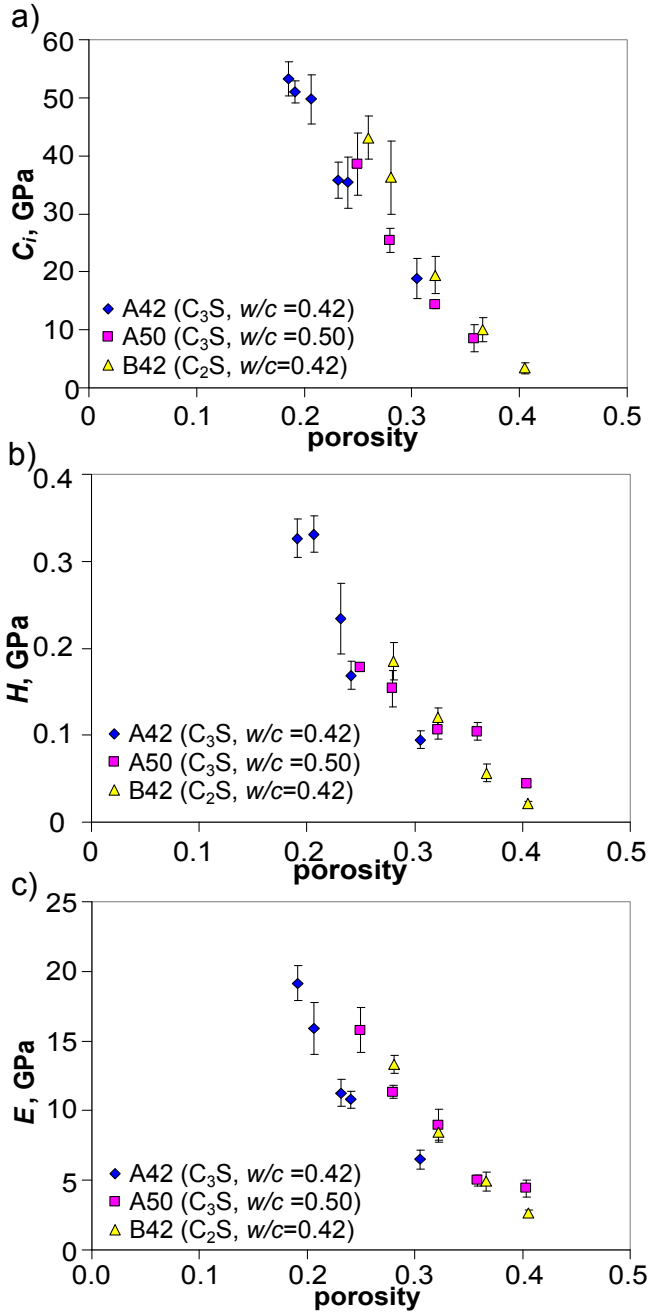

Figure 6.5: Porosity versus a) contact creep modulus C_i b) Young's modulus E and c) indentation hardness H of C_3S pastes and C_2S pastes.

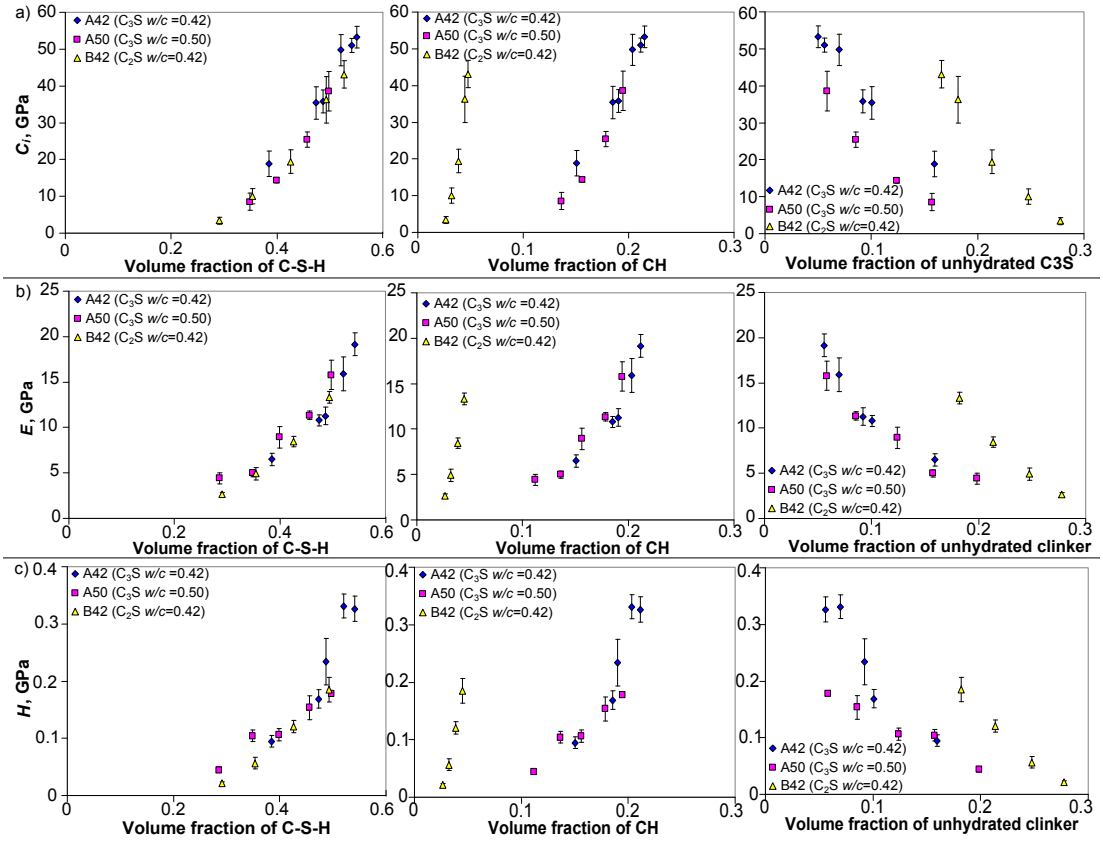

Figure 6.6: a) Contact creep modulus C_i, b) Young's modulus E, c) indentation hardness H versus volume fraction of C-S-H, that of CH and unhydrated clinker, i.e., C_3S for C_3S paste and C_2S for C_2S paste.

properties versus the volume fraction of each phase. The results confirm an increase of all the mechanical properties along with hydration. In a first order, the mechanical properties appear to depend either on the porosity or on the volume fraction of C-S-H. Therefore, for an empirical law, an indicator based on the porosity and the volume fraction of C-S-H may be applied to capture a global trend of C_i, E and H of C_3S paste and C_2S paste. However, the volume fractions of the various phases in C_3S and C_2S pastes do not evolve independently from each other: an increase of volume fraction of C-S-H and CH leads to a decrease of capillary porosity and the volume fraction of unreacted clinker. Therefore one cannot simply conclude from Fig. 6.5 and Fig. 6.6 that the lower the porosity is or the higher the volume fraction of C-S-H is, the higher C_i, E and H values of C_3S and C_2S pastes are: indeed, those variations of porosity or of volume of C-S-H hinder variations of the volume fractions of all phases in the paste and a variation of each phase is likely to have an influence on the macroscopic mechanical behavior. This will be discussed in chapter 9 by homogenization approach.

Chapter 7

Creep properties of compacts of CH, synthetic C-S-H and their mixtures

Résumé *Ce chapitre est consacré à la présentation d'une étude sur les propriétés mécaniques d'échantillons présentant une porosité similaire mais des fractions volumiques de C-S-H et de CH différentes. Ces échantillons ont été préparés par compactage de poudre. La masse volumique a été déterminée à partir des masses et des dimensions des échantillons et la densité des poudres. Tous les échantillons ont été conditionnés sous 11% d'humidité relative ou bien sous conditions saturées en eau. Les propriétés mécaniques de ces compacts ont été caractérisées par microindentation. Nous avons trouvé une amélioration claire du module de Young E, de la dureté d'indentation H et du module de fluage C_i des compacts quand la fraction volumique de CH sous 11% d'humidité relative augmentait au cur du solide, tandis que dans des conditions saturées en eau aucune augmentation sensible n'était observée. Nous avons aussi constaté que les propriétés mécaniques des compacts telles que définies ci-dessus sous 11% d'humidité relative étaient nettement supérieures à celles observées dans des conditions saturées en eau, ce qui a permis de démontrer l'impact important de l'eau sur les propriétés mécaniques des compacts. Pour les échantillons avec une quantité élevée de CH, le temps caractéristique d'indentation τ_i soit le temps requis pour atteindre la cinétique de fluage logarithmique, s'est révélé plus important*

dans des conditions saturées en eau que sous une humidité relative de 11%.

Abstract *This chapter is dedicated to presenting a study of the mechanical properties of samples with similar porosity but various volume fractions of C-S-H and CH. Those samples were prepared by compaction of powder. The volume fraction was obtained from masses and dimensions of the samples and density of powders. All samples were conditioned under 11% relative humidity or under water-saturated conditions. The mechanical properties of those compacts were characterized by microindentation testing. We found a clear enhancement of Young's modulus E, indentation hardness H and contact creep modulus C_i of compacts when increasing the volume fraction of CH in the skeleton of solid under 11% relative humidity, while under water-saturated conditions no significant increase was observed. We also found that the above mentioned mechanical properties of compacts at 11% relative humidity were much higher than those in water-saturated conditions, which showed a strong effect of water on the mechanical properties of compacts. For samples with significant amount of CH, the indentation characteristic time τ_i, i.e., the time needed to reach a logarithmic kinetics of creep, was found to be higher in water-saturated conditions than that at 11% relative humidity.*

7.1 Chapter introduction

In chapter 6, we studied the distribution of phases and the mechanical properties of hydrating C_3S and C_2S pastes. The porosity (which does not include the gel porosity in C-S-H solid) had an obvious influence on the mechanical properties of those pastes: as presented in Fig. 6.5, when the porosity became lower, the Young's modulus E, the indentation hardness H and creep modulus C_i became higher. Since the proportions of all phases in a hydrating C_3S or C_2S paste depend on each other and are directly linked to the degree of hydration, which itself is difficult to control, it is thus difficult to control the porosity and the volume fractions of those phases in a hydrating paste. The influence of the proportion of each phase on the mechanical properties is difficult to interpret without further modeling. In the present chapter, we aim at bypassing the difficulties encountered with C_3S and C_2S pastes by producing samples with various amounts of CH and C-S-H. To do so, we will work with samples obtained by compaction of powders at high pressure. Therefore, the creep properties of mixtures of CH and C-S-H with a wide range of mix proportions will be characterized by indentation.

Compression or compaction of powder is a technique for preparing rigid solid samples. By applying a pressure in the order of 100MPa, solid grains stick together and create a cohesive material. Sometimes, water is required during compression in order to get a cohesive material [Sereda and Feldman, 1963]. The properties of compacts of cementitious materials such as the Young's modulus, the hardness, the strength and the deformational change in various hygral conditions, the durability were studied by Sereda and Feldman [1963], Sereda et al. [1966], Soroka and Sereda [1970], Feldman and Beaudoin [1976], Beaudoin [1983], Beaudoin et al. [1998], Beaudoin et al. [2003]. As presented in Fig. 7.1, under 30% relative humidity, at a given porosity, the Young's modulus and the Vickers hardness of compacts made of hydrated cement powder (sample III in Fig. 7.1) and those of hydrated cement paste (sample I in Fig. 7.1) were found to be similar [Soroka and Sereda, 1970]. In terms of creep properties, the contact creep modulus C_i of C_3S paste and compacts of pure C-S-H, pure CH, pure gypsum and pure ettringite in equilibrium with water vapor at 11% relative humidity was studied by microindentation [Nguyen et al., 2013]. The porosity was found to be a parameter governing the contact creep modulus C_i. Yet, the creep properties of

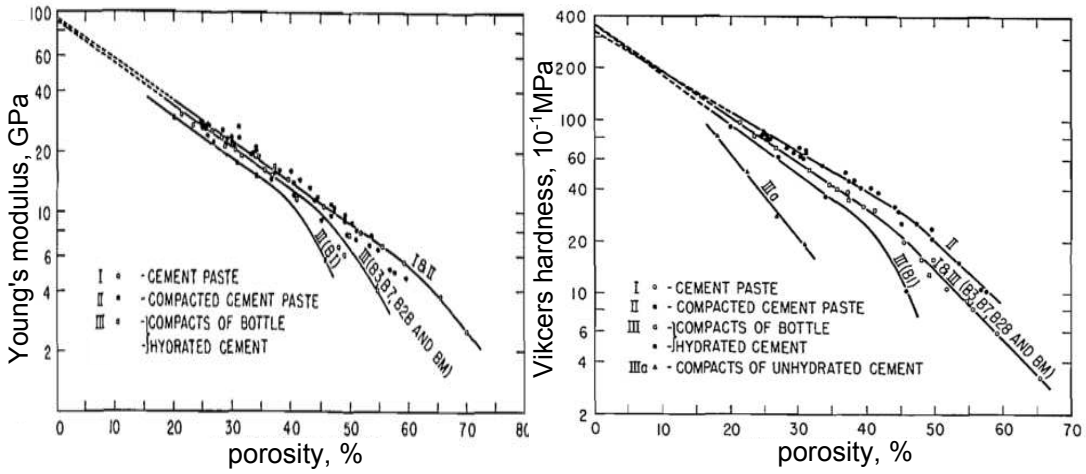

Figure 7.1: Young's modulus and Vickers hardness of hydrated cement pastes and compacts of hydrated cement [Soroka and Sereda, 1970]. I: hydrated cement paste; II: sliced and then compressed hydrated cement paste; III: compacts of hydrated cement powder. The porosity of samples was calculated from the weight, volume and degree of hydration, choosing 3.15g/cm^3 for the density of unhydrated cement clinker, and 2.6g/cm^3 for the density of hydration products.

compacted mixtures of C-S-H and CH and that of C_2S pastes were not discussed. In this chapter, we will apply the technique of compression of powder to prepare samples in order to obtain samples with the following characteristics:

- solid and homogeneous,
- with roughly similar capillary porosity,
- with a wide range of known volume fractions of crystalline phase (CH) and of amorphous phase (C-S-H).

With those samples obtained by compression of powder, as an extension of the study in chapter 6, this chapter aims at answering the following questions: for materials with similar porosity, how does the microstructure (i.e., the volume fractions of C-S-H and CH) influence the mechanical properties? To answer this question, various samples with similar porosity but wide range of volume fractions of C-S-H and CH are prepared and tested by microindentation testing. As the hygral conditions may influence the mechanical properties of cementitious materials, the samples will be conditioned and tested both under 11% relative humidty and under water-saturated conditions. As the compression process may lead to anisotropic samples, the isotropy of a sample will be verified by carrying out indentation tests on surfaces oriented in various directions.

7.2 Materials and methods

This section is dedicated to introducing the experimental method for preparing compacts and indentation testing on compacts. The experimental parameter settings and some results necessary for sample preparation are also presented in this section.

7.2.1 Preparation and characterization of synthetic C-S-H

Synthetic C-S-H was prepared by double decomposition of calcium nitrate with sodium silicate according to the following chemical reaction in aqueous conditions:

$$3Ca(NO_3)_2 + 2NaOH + 2Na_2SiO_3 + (m-1)H_2O \longrightarrow 3CaO \cdot 2SiO_2 \cdot mH_2O + 6NaNO_3 \tag{7.1}$$

where the actual value of parameter m is unknown.

The preparation method is based on the one used by Chen et al. [2004] and summarized as follows: a quantity of 0.05mol reagent-grade $Na_2SiO_3{\cdot}5H_2O$ and the same molar quantity of reagent-grade NaOH were dissolved in 125mL of boiled deionized water. A quantity of 0.075mol reagent-grade $Ca(NO_3)_2{\cdot}4H_2O$ was dissolved in 75 mL of boiled deionized water. The two solutions were stabilized for 3 hours in tightly sealed plastic containers in a laboratory in which the temperature was controlled at 20°C±1°C. The two solutions were mixed together and the mixture was stirred for 3 hours in a third tightly sealed plastic container in order to get a complete reaction that precipitates C-S-H. The precipitate was washed with 2L of saturated CH solution on a Buchner funnel under a continuous stream of nitrogen. After washing, the cream-like C-S-H was flushed with nitrogen and tightly sealed in a plastic container for storage. Special attention was paid during the preparation to avoid carbonation of C-S-H.

Due to the huge amount of water that exists in cream-like C-S-H, one cannot prepare C-S-H compact directly with the cream-like C-S-H. Part of the prepared cream-like C-S-H was dried at a pressure of about 10^{-2}mbar applied by a pump with a theoretical capacity of $2{\times}10^{-3}$mbar, for 72 hours in room temperature. The duration of drying was determined by measuring the mass evolution of C-S-H every 24 hours for a 5-day drying. The mass change was undetectable after 3-day drying. After drying, the cream-like C-S-H lost more than 90% of its initial mass, shrinked and agglomerated to form C-S-H grains. The C-S-H grains were ground by hand in glove box to get a fine powder that can all pass a 50µm sieve.

The synthetic C-S-H prepared by following the method mentioned above, i.e., by mixing solutions of sodium silicate and calcium salts at room temperature falls

into the category of C-S-H(I) [Taylor, 1997]. Compared with the C-S-H gel formed by the hydration of C_2S or C_3S, the nanostructure of C-S-H (I) is more highly ordered, while is still poorly crystallized when compared with the crystalline phases of C-S-H such as 1.4-nm tobermorite. Former experimental data showed that C-S-H (I) was a structurally imperfect form of 1.4nm tobermorite [Taylor, 1997].

The X-ray diffraction pattern obtained by X-ray diffraction experiment on the prepared dried C-S-H powder is presented in Fig 7.2, from which the following remarks can be found:

- The pattern is comparable with that of C-S-H (I) in [Taylor, 1997] (the peaks over the red bars in Fig 7.2), and thus confirms the prepared C-S-H is a type of C-S-H (I).
- The broad peaks over the red bars confirms that the prepared C-S-H is relatively poorly crystallized.
- The weak peaks over the blue bars are from portlandite. It means that only a trace amount of CH can be found in the C-S-H prepared, which cannot be avoided by applying the preparation method.

To characterize the atomic ratio of calcium/silicon in C-S-H, X-ray fluorescence accompanied with loss on ignition were performed on C-S-H powder. An atomic ratio of calcium/silicon equal to 1.4 was found, which is slightly lower than the theoretical value of 1.5.

7.2.2 Preparation of compacts

Compacts of pure C-S-H, pure CH and their mixtures (with 8 different proportions of the two phases) were prepared. The C-S-H compact was made with the ground fine C-S-H powder prepared with the procedure indicated in section 7.2.1. The CH compact was made with a fine powder of chemical reagent calcium hydroxide (puriss. p.a., Reag. Ph. Eur., $\geq$96%, a product from Sigma-Aldrich), no grinding was performed as the powder is very fine already. Mixtures were obtained by mixing given quantities of chemical reagent calcium hydroxide to C-S-H cream: thus, mixing was done in wet conditions which enabled to obtain more

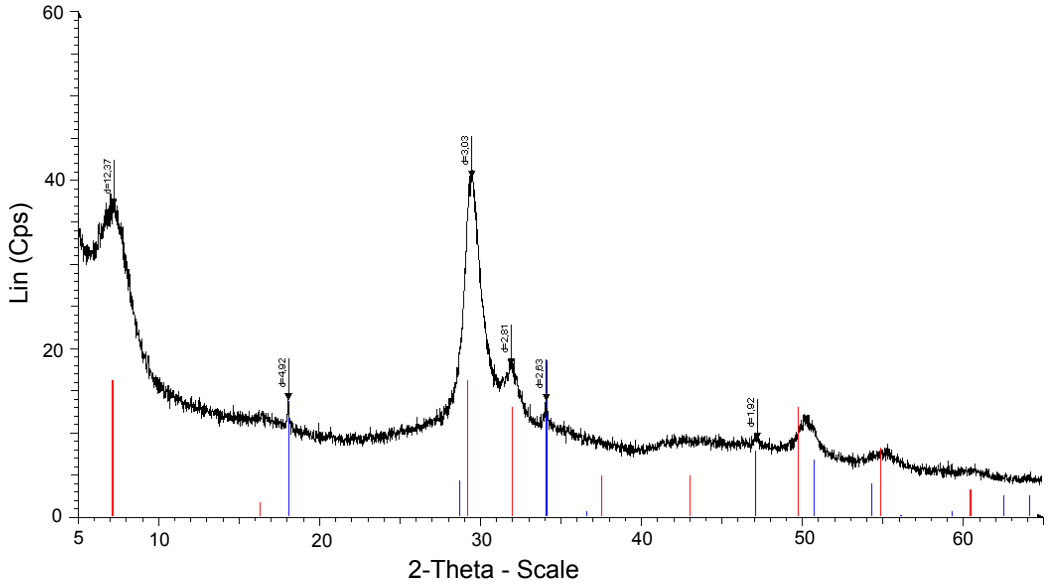

Figure 7.2: X-ray diffraction pattern of prepared C-S-H.

homogeneous mixtures than if mixing had been performed with dry powders of both CH and C-S-H. The mixture was then dried and ground to a fine powder by applying the same procedure as the one used to prepare fine C-S-H powder indicated in section 7.2.1.

A special compaction cell that resists to high pressures was customized for the preparation of compacts. As presented in Fig. 7.3, the mold consists of a cylinder hollow, two closely fitting cylindrical pistons so that powder can be sealed in the two pistons while water can pass through, and a third cylinder piston which serves to transfer the load applied from the press to the compaction cell. With the three pistons, cycles of compression can load on both the upper and lower sides of the sample. A procedure was adapted in order to get well compacted and homogeneous samples. Before compression, the powder was humidified with lime water, with a water-to-powder mass ratio of 0.5. The humidified powder was filled into the compacting mold in-between the two pistons. A load was applied to the upper piston, increased gradually up to 287MPa within 5 minutes and was held for 5 minutes. After the first load cycle, we turned over the cylindrical mold and applied a second cycle with the same loading procedure. During the compression cycle, some lime water was squeezed out of the compact and absorbed

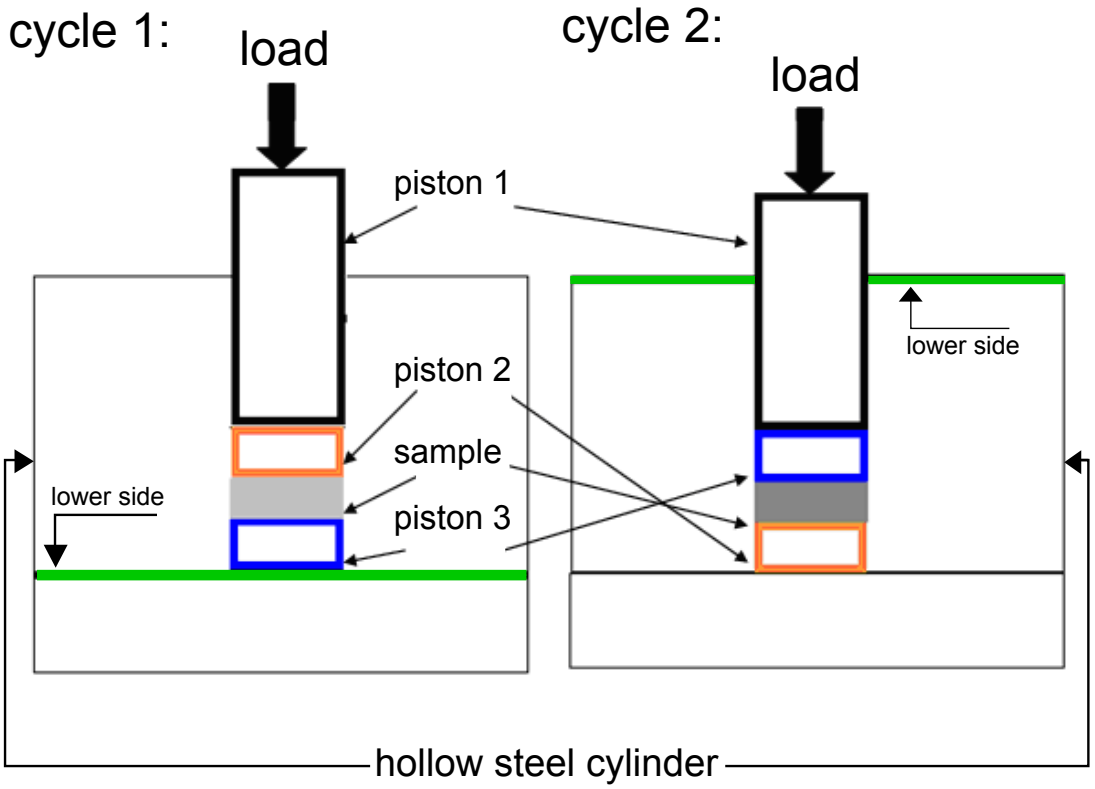

Figure 7.3: Schematic presentation of the compaction cell and of the compaction process. Between two cycles, the hollow cylinder mold is turned over for the load to be applied in two directions.

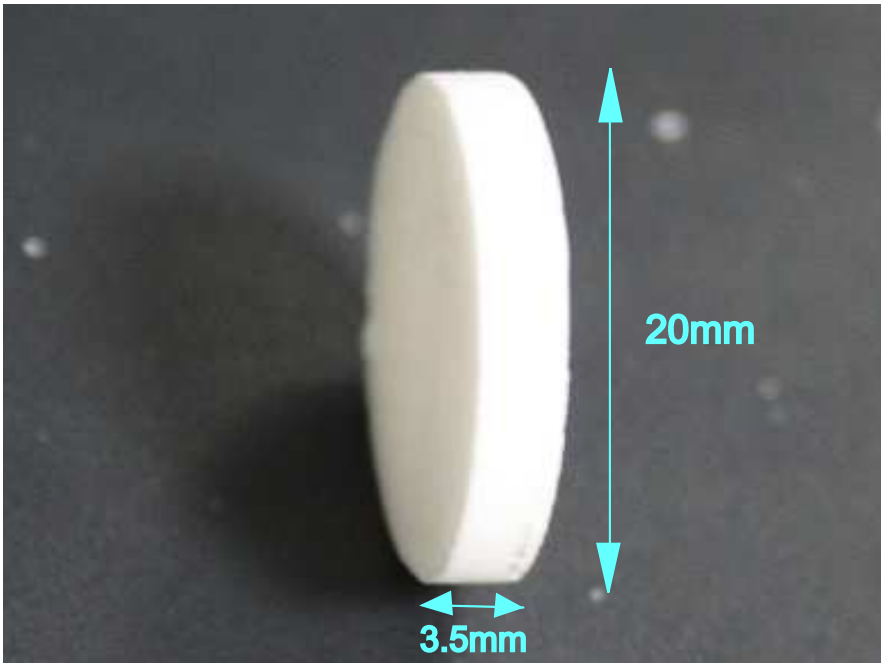

Figure 7.4: Compact of synthetic C-S-H.

with an absorbent paper. After two compressive cycles, the sample was carefully compressed out from the mold with a low pressure. By controlling the quantity of powder, a compact with characteristic dimensions of 20mm in diameter and 3.5mm in height could be obtained, as presented in Fig. 7.4.

After preparation, samples tested in saturated conditions were cured in lime water at 23°C for one week before being tested. Samples tested in dry conditions were conditioned under 11% relative humidity at 23°C for 3 months. As one will see later in chapter 8, after 3 months of conditioning under 11% relative humidity, the samples achieved moisture equilibrium with the conditioning environment. For samples conditioned in lime water, as they were not in contact with CO_2, the risk of carbonation during conditioning is low. For samples conditioned in 11% relative humidity, efforts were made to avoid carbonation during conditionning: after putting the samples into the desiccator, we pumped out the air from desiccator and then pumped in air without CO_2 into the desiccator and sealed the desiccator carefully.

7.2.3 Phase distribution in compacts

The following derivation was used to determine the volume fraction of each phase in a compact. The volume of a compact sample, noted as V_c, consists of the volume of solid (or the bulk volume), noted as V_s and the volume of voids, which is equal to the product of the porosity (noted as ϕ) with the volume of compact:

$$V_c = V_s + \phi \cdot V_c \tag{7.2}$$

For all compacts, the volume V_s of solid can be calculated from the mass and density of each powder:

$$V_s = \frac{m_{\mathrm{CSH}}}{\rho_{\mathrm{CSH}}} + \frac{m_{\mathrm{CH}}}{\rho_{\mathrm{CH}}} \tag{7.3}$$

where m_{CSH} and ρ_{CSH} are the mass and density of C-S-H powder, respectively, and m_{CH} and ρ_{CH} are the mass and the density of CH powder, respectively. For the compact of pure C-S-H, m_{CH}=0 and similarly for the compact of pure CH, m_{CSH}=0. Combining the two functions above, the volume of C-S-H and CH and the porosity of each compact can be obtained. Experimentally, the volume of compact V_c, the mass of C-S-H powder and/or mass of CH powder used to prepare a compact can be measured during sample preparation. The density of C-S-H powder and CH powder was measured by helium pycnometer by following the standard practice of Lafarge Research Center. The density of CH was measured as 2.25g/cm^3. The density of C-S-H powder ρ_{CSH} was measured as 2.21g/cm^3. As already stated in chapter 5, the density of C-S-H varies with the amount of water that is considered to be part of its basic structure. According to the colloid model for C-S-H [Jennings, 2008], at a density of 2.03g/cm^3 which is very close to the density of 2.06g/cm^3 that we used for the C-S-H in C_2S and C_3S paste, there are 4 moles of water in one mole of C-S-H; at a density of 2.20g/cm^3, which is very close to the density of synthetic C-S-H measured here, there are 3.14 moles of water in one mole of C-S-H. If we assume this relationship (between the density of C-S-H and the quantity of water in its basic structure) is applicable to the synthetic C-S-H, with a density of 2.21g/cm^3, for one mole of C-S-H, about 0.86 moles of water is dried out. And the porosity that we calculated with the density of 2.21g/cm^3 may include some of the gel porosity dried out from C-S-H.

Once all the other measurements on compacts were done, the porosity of the

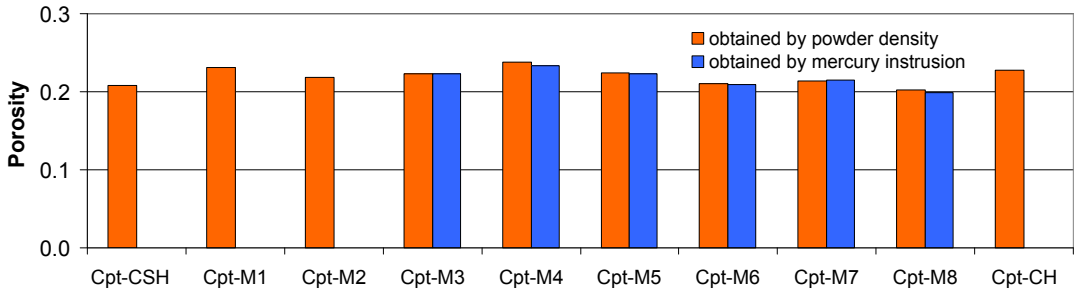

Figure 7.5: Porosity of compacts measured by different experimental techniques.

sample	f_{CSH}	f_{CH}	ϕ	$f_{CH}/(f_{CSH}+f_{CH})$
Cpt-CSH	0.792	0	0.208	0
Cpt-M1	0.691	0.078	0.231	0.102
Cpt-M2	0.637	0.146	0.217	0.186
Cpt-M3	0.521	0.256	0.222	0.330
Cpt-M4	0.475	0.288	0.237	0.378
Cpt-M5	0.391	0.386	0.223	0.496
Cpt-M6	0.254	0.538	0.209	0.680
Cpt-M7	0.203	0.584	0.213	0.742
Cpt-M8	0.172	0.626	0.202	0.784
Cpt-CH	0	0.773	0.227	1

Table 7.1: Phase distribution for compacts of C-S-H, CH and of their mixtures.

residual parts of the compacts were measured by mercury intrusion porosimetry by following the standard practice of Lafarge Research Center. This was not performed on all samples due to the insufficient quantity of residual parts of compacts necessary for a meaningful measurement. As presented in Fig. 7.5, the porosities measured by mercury intrusion porosimetry are close to those calculated based on the density of the powders and dimension of sample with the method mentioned above, which validated the above method to calculate the porosity of compacts. The volume fractions of the phases in compacts calculated by applying the method indicated in the present section is presented in Tab. 7.1. We observe that we prepared mixtures of C-S-H and CH with a wide range of relative volume fractions of C-S-H and CH.

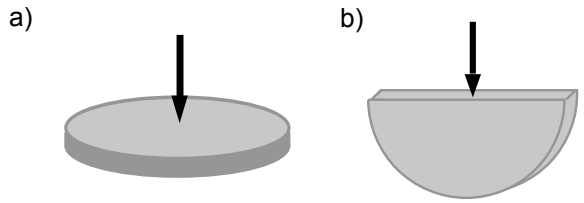

Figure 7.6: Schematic presentation of the surfaces of a disk-like compact.

7.2.4 Indentation experiments on compacts

Indentation testing was performed on the prepared compacts to measure their mechanical properties, including their creep properties. For each prepared disk-like compact, indentation testing was done on one of its flat surfaces, as presented in Fig. 7.6a. For the compact Cpt-M6 (see Tab. 7.1 for its composition), indentation testing was also done on the cross section, as presented in Fig. 7.6b, to check the isotropy of compact.

No polishing was performed on the compacts if indentation was performed on the top or bottom surface, the reasons are the following ones:

- The surfaces of the mold in contact with the compact were very smooth. As a consequence the surface of compact is very smooth.
- The scale of testing was relatively large: as will be seen later, the maximum indentation depth is around 35µm, from which the indented surface did not have to be very smooth.
- Moisture change and carbonation due to exposure to air during polishing could be avoided.

For sample Cpt-M6, on which indentation was also performed on a cross-section, the cross-section was polished by following the same procedure as mentioned in section 4.2.3. After conditioning, the sample to be tested was moved directly into the indentation chamber with controlled relative humidity and temperature and fixed on the indentation platform. For indentation tests on samples cured in lime water, the relative humidity was controlled at about 100% at 23°C±0.2°C by pumping water-saturated air into the indentation chamber. By doing so, the tested sample remained water-saturated during indentation test.

Indentation probe	Vickers
Maximum indentation load P_{max}, N	5 to 10
Maximum indentation depth h_{max}, µm	29-38
Holding duration τ_H, s	20 or 300
Temperature	23 °C ± 0.2°C
Relative humidity	100%, 11%

Table 7.2: Experimental parameter settings of indentation experiments on compacts.

For indentation tests on samples conditioned under 11% relative humdity at 23°C±0.2°C, the relative humidity in the indentation chamber was controlled at 11%±2% by pumping dry air into indentation chamber. Efforts were made to avoid carbonation during indentation: air pumped into the indentation chamber are CO_2-free which is from reconstituted bottled air without CO_2.

On each sample, 10 microindentation tests were performed with a Vickers indentation probe. The maximum force applied varied from 5N to 10N, which was adapted to generate a maximum depth around 35µm. For each indent, the load was increased linearly over time in 15 seconds, kept constant during the holding phase, and decreased linearly over time back to zero in 15 seconds. Out of the 10 indents performed on each sample, 5 were with a 20-seconds-long holding phase while 5 were performed with a 300-seconds-long holding phase. A summary of indentation parameter settings is presented in Tab. 7.2. To verify the isotropy of sample Cpt-M6, in addition to the 10 tests performed on the flat surface, we performed 6 indentation tests on its cross section: 5 of which were with a 20-seconds-long holding phase, one of which was with a 300-seconds-long holding phase. Due to the limited quantity of material, only one test dedicated to the measurement of creep properties was performed on cross-section.

The indentation tests with a 20-seconds-long holding phase were used for determining the Young's modulus E and the indentation hardness H, by applying the analysis presented in section 3.3.2, and those with a 300-seconds-long holding phase were used for determining the creep properties, by applying the analysis presented in section 3.4.2.

M6	E **(GPa)**	H **(GPa)**	C_i **(GPa)**
surface	14.2±0.7	0.306±0.012	22.4±1.1
cross-section	16.0±2.2	0.324±0.012	22.3

Table 7.3: Mechanical properties of compact Cpt-M6 on flat surface and on cross-section obtained by indentation testing.

7.3 Results and discussions

7.3.1 Mechanical properties of compacts

We fitted all the contact creep functions with Eq. 4.3 which yielded for each compact a contact creep modulus C_i and an indentation characteristic time τ_i to reach the logarithmic kinetics of creep. As presented in Fig. 7.7, the applied fit worked very well for all the compacts at 11% relative humidity and for the compact of C-S-H in water-saturated conditions, while the quality of fits was less satisfactory for compact of CH and compact Cpt-M4 in water-saturated conditions: at early times, systematic deviation could be found between the fitted curve and the experimental data points.

A summary of the Young's modulus E (calculated by assuming a Poisson's ratio ν=0.25), the indentation hardness H, the contact creep modulus C_i and the indentation characteristic time τ_i of all compacts are presented in Tab. 7.4. As already mentioned in section 7.2.4, we verified the isotropy of prepared compacts by carrying out indentation testing on both the flat surface and on the cross-section of the compact Cpt-M6. As presented in Tab. 7.3, E, H and C_i obtained from the two surfaces of this sample are quite similar, from which we inferred that the compacts were isotropic mechanically, in spite of the process of compaction.

The contact creep modulus C_i versus Young's modulus E or indentation hardness H are plotted in Fig. 7.8 for samples conditioned in water-saturated conditions and in Fig. 7.9 for those conditioned under 11% relative humdity. In water-saturated conditions, in the C_i-E plane and in the C_i-H plane, the data points for compacts of mixtures gathered around a master curve, but data points for pure phase compacts (both CH and C-S-H) departed from this master curve. At 11% relative humidity, as presented in Fig. 7.9, the contact creep modulus C_i increased with an increasing Young's modulus E and also with an increasing indentation hardness H.

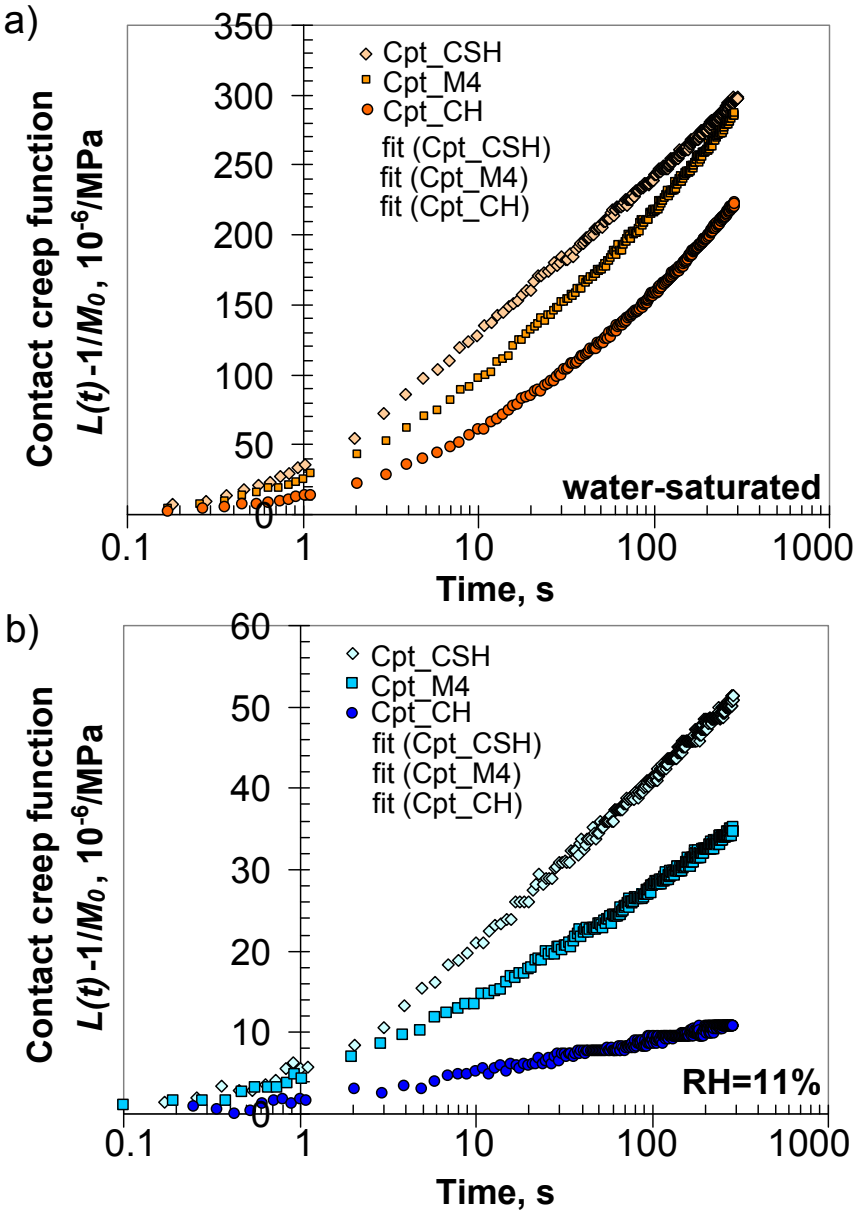

Figure 7.7: Contact creep function $L(t) - 1/M_0$ of compact of C-S-H (Cpt-CSH), compact of CH (Cpt-CH), and compact of mixture Cpt-M4 conditioned a) under water-saturated conditions and b) under 11% relative humidity, at 23°C.

sample	$\boldsymbol{E}$ **(GPa)**	$\boldsymbol{H}$ **(GPa)**	$\boldsymbol{C_i}$ **(GPa)**	$\boldsymbol{\tau_i}$ **(s)**
water-saturated conditions				
Cpt-CSH	7.2±0.8	0.195±0.029	20.0±3.7	1.0±0.7
Cpt-M1	8.3±0.2	0.180±0.001	14.0±0.9	3.7±1.0
Cpt-M2	8.7±0.8	0.178±0.012	14.1±0.8	1.9±0.5
Cpt-M3	8.5±1.7	0.172±0.016	13.2±1.9	3.3±0.7
Cpt-M4	10.0±0.6	0.224±0.017	17.0±1.3	3.7±0.7
Cpt-M5	10.3±1.6	0.233±0.015	18.6±0.6	2.5±1.0
Cpt-M6	14.2±0.7	0.306±0.012	22.4±1.1	4.4±0.9
Cpt-M7	15.7±2.2	0.286±0.008	21.1±2.3	4.6±1.2
Cpt-M8	14.8±1.2	0.321±0.033	21.12±2.5	5.9±2.3
Cpt-CH	25.9±0.3	0.343±0.014	16.4±0.7	8.5±1.5
RH=11%				
Cpt-CSH	18.8±0.5	0.680±0.068	105±17	1.6±0.8
Cpt-M1	21.3±2.2	0.660±0.029	103±9.1	2.0±0.6
Cpt-M2	16.7±1.6	0.665±0.048	97.9±8.6	2.3±0.5
Cpt-M3	21.2±2.0	0.732±0.082	143±15	2.1±0.7
Cpt-M4	22.0±4.2	0.778±0.016	161±15	1.3±0.3
Cpt-M5	18.2±2.2	0.861±0.056	142±21	2.5±1.1
Cpt-M6	22.9±2.2	0.856±0.081	280±20	0.5±0.2
Cpt-M7	23.9±1.2	1.02±0.03	269±46	1.4±0.8
Cpt-M8	22.3±3.3	1.04±0.05	279±33	2.4±1.0
Cpt-CH	32.1±4.9	1.17±0.13	608±139	0.4±0.2

Table 7.4: Young's modulus E, indentation hardness H, contact creep modulus C_i and the characteristic time τ_i obtained by microindentation of compacts of C-S-H, CH and their mixtures.

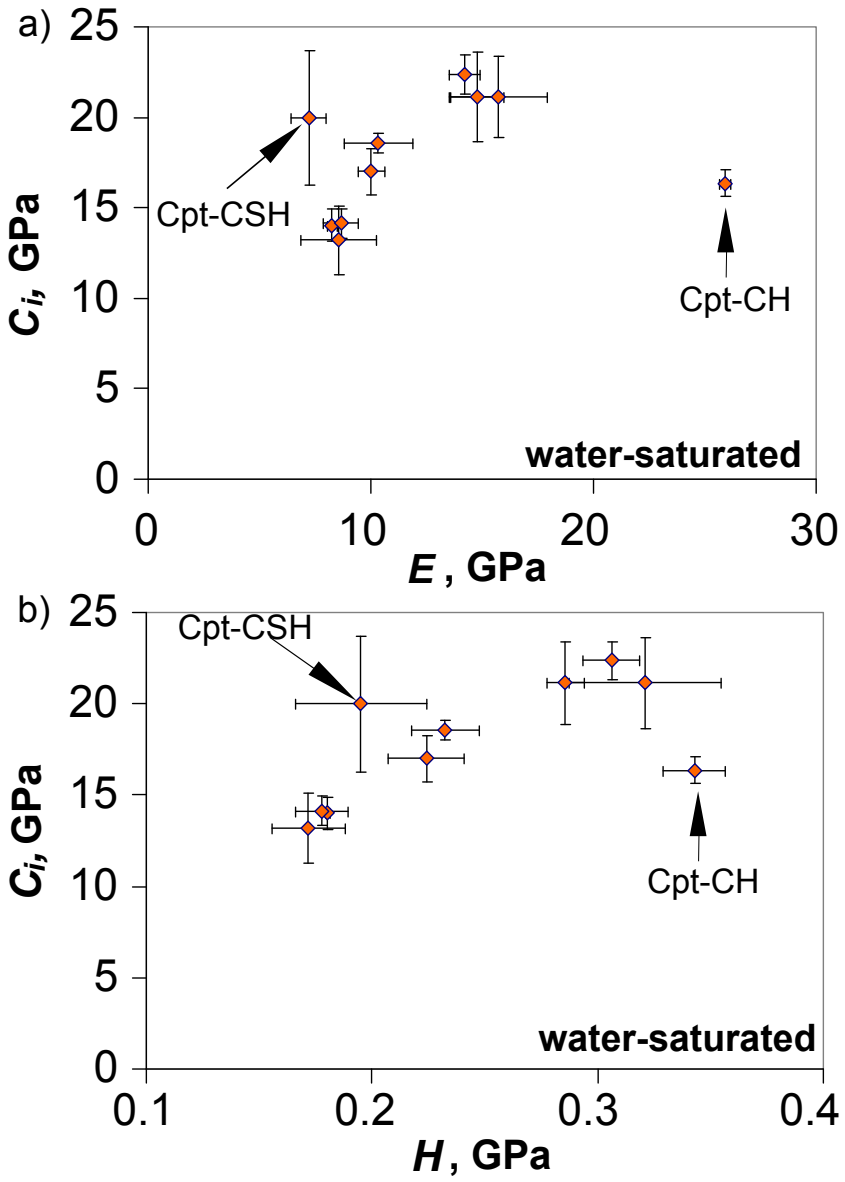

Figure 7.8: Contact creep modulus C_i versus a) Young's modulus E and b) indentation hardness H, from indentation tests performed on compacts in water-saturated conditions and at 23°C.

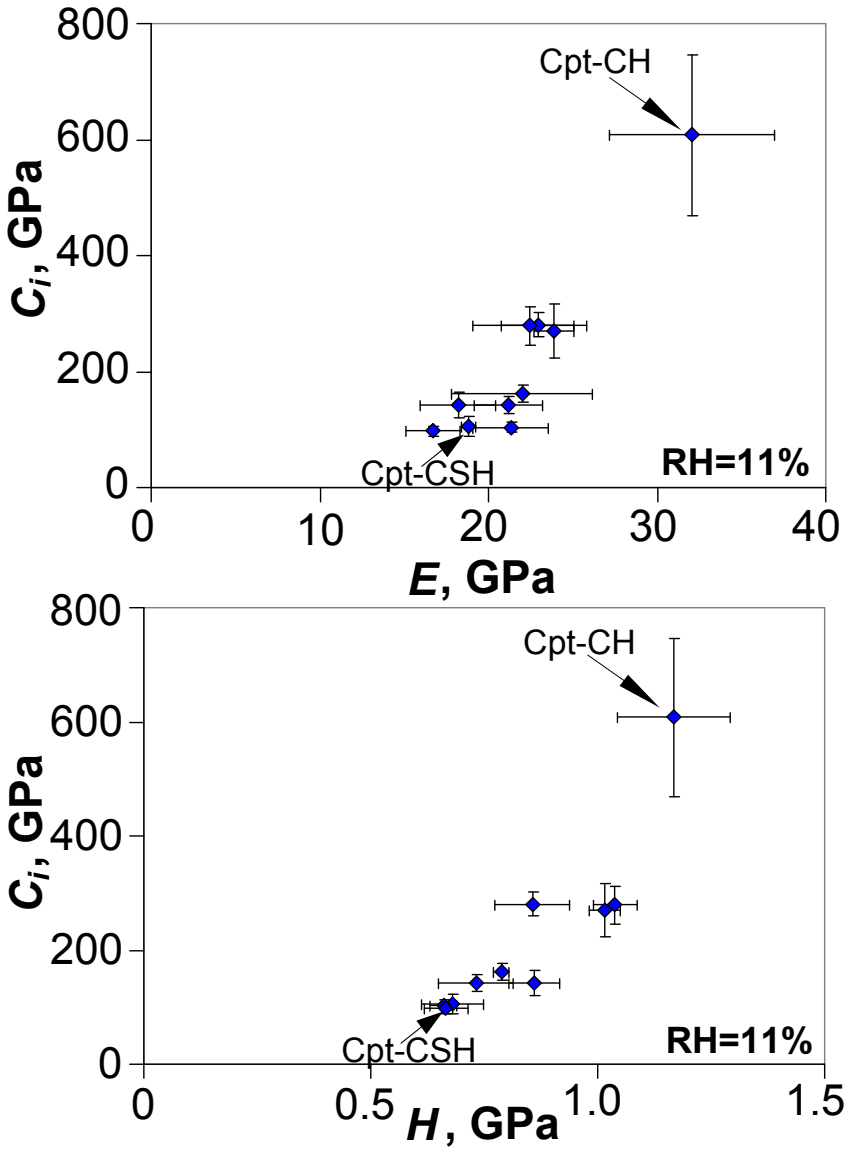

Figure 7.9: Contact creep modulus C_i versus a) Young's modulus E and b) indentation hardness H, from indentation tests performed on compacts at 11% relative humidity and at 23°C.

7.3.2 Link between microstructure and mechanical properties

The porosity of the compacts varied from 0.202 to 0.237, as presented in Tab. 7.1. The main difference between compacts is the proportion of C-S-H and CH. Therefore, we plotted the mechanical properties and the indentation characteristic time in function of the volume fraction $f_{CH}/(f_{CSH} + f_{CH})$ of CH in the solid skeleton. The results are presented in Fig. 7.10 for samples in water-saturated conditions and in Fig. 7.11 for samples at 11% relative humidity.

From Fig. 7.10, one can see that, in water-saturated conditions the Young's modulus E increased with an addition of CH. The indentation hardness H also increased with an addition of CH when the volume fraction of CH in the solid skeleton was higher than 35%, but did not increase when the volume fraction of CH in the solid skeleton was lower than 35%. The evolution of the contact creep modulus C_i in function of the volume fraction of CH in the solid skeleton is non-monotonic: it was a decreasing function of the volume fraction of CH in the solid skeleton when the volume fraction water lower than 35% or greater than 70% but an increasing function of this volume fraction in-between.

For samples conditioned under 11% relative humidity, as presented in Fig. 7.11, generally the indentation hardness H and the contact creep modulus C_i increased with an increasing volume fraction of CH in the solid skeleton. At this relative humidity, the Young's modulus of the compacts was an increasing function of the volume fraction of CH in the solid skeleton, when this volume fraction was greater than 40%. However, the trend at lower volume fractions was unclear.

7.3.3 A glance at the effect of water on the mechanical properties of compacts

Comparing the results from the samples conditioned at 11% relative humidity with those from the samples kept in water-saturated conditions, a strong effect of water on the mechanical properties of the compacts can be found: from the data presented in Tab. 7.4, from water-saturated conditions to 11% relative humidity, the Young's modulus E of the compacts increased by a factor of 1.3 to 2.6; for the

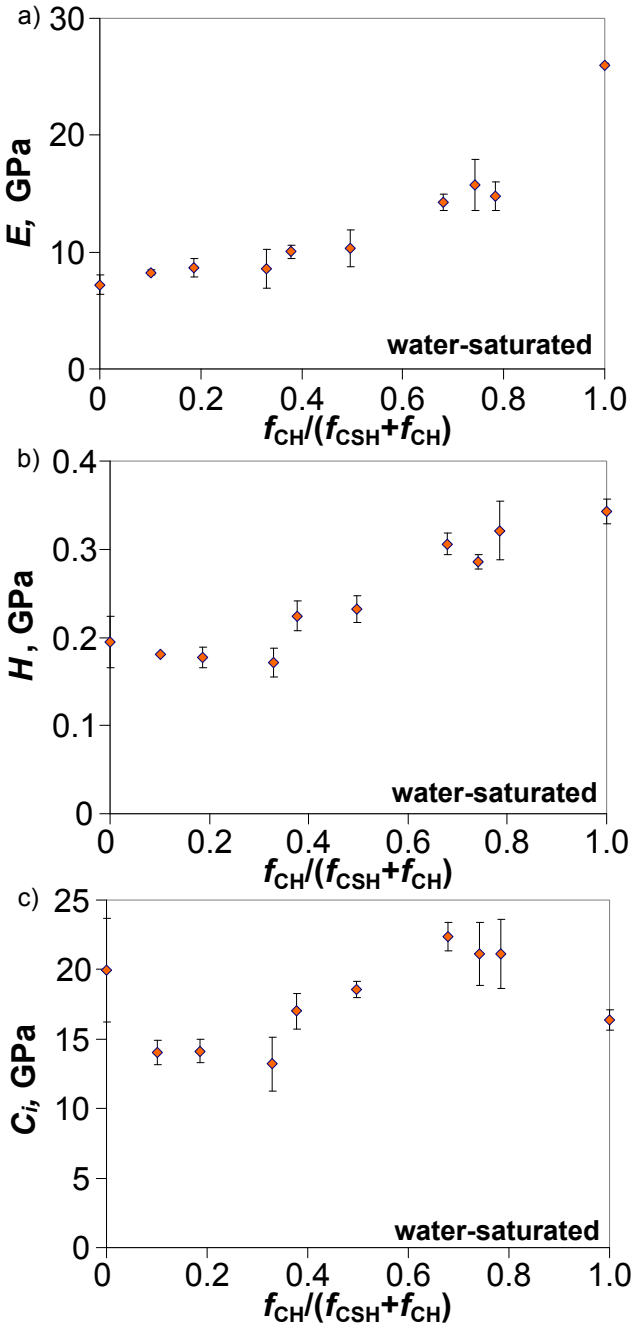

Figure 7.10: a) Young's modulus E, b) indentation hardness H and c) contact creep modulus C_i of compacts from indentation tests on water-saturated compacts. f_{CSH} is the volume fraction of C-S-H and f_{CH} is the volume fraction of CH.

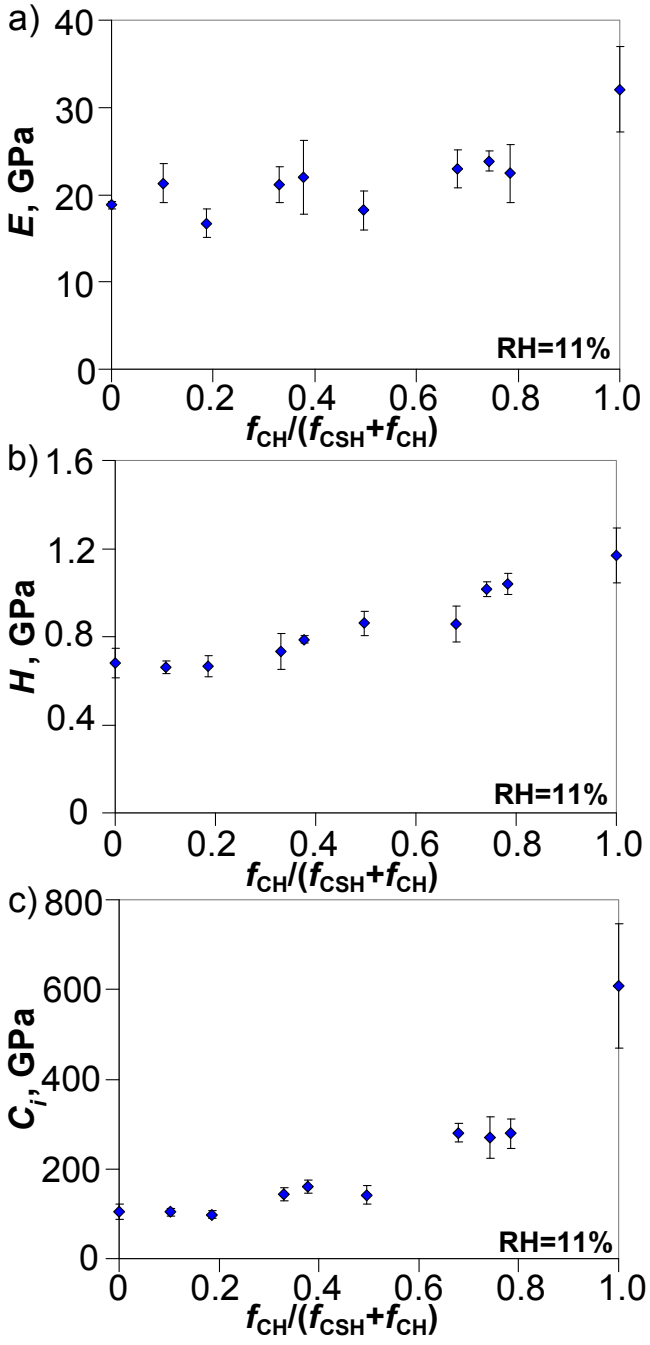

Figure 7.11: a) Young's modulus E, b) indentation hardness H and c) contact creep modulus C_i of compacts from indentation tests performed at 11% relative humidity. f_{CSH} is the volume fraction of C-S-H and f_{CH} is the volume fraction of CH.

indentation hardness H, the factor of increment was between 3.1 and 5.5; and for the contact creep modulus C_i, the increase was by a factor of 7 to 37. On one hand, a general increase of those three mechanical properties was seen for all samples conditioned at 11% relative humidity when compared with those conditioned in water-saturated conditions. On the other hand, the increase of mechanical properties was different for different compacts: the contact creep modulus C_i of the compact of pure CH was found to be more sensitive to the hygral conditions than that of compact of C-S-H. In contrast, the Young's modulus of the compact of CH was found to be less sensitive to hygral conditions than that of compact of C-S-H.

To characterize the creep properties of the compacts, one needs both the contact creep modulus as well as the indentation characteristic time τ_i. Besides the observations presented in last paragraph on the evolution of contact modulus, here we plot in Fig. 7.12 the characteristic time in function of the proportion of CH in solid. As one can see from Fig. 7.12, though the dispersion of the characteristic time τ_i of samples is high, compared with the indentation characteristic time for samples conditioned under 11% relative humdity, for most samples, the characteristic time from samples conditioned in water-saturated conditions was higher. The indentation characteristic time of compact of CH showed the largest increase: from 1s at 11% relative humidity to 8.5s in water-saturated conditons, while for compacts with a volume fraction of CH in the solid skeleton lower than 50%, the difference in the characteristic time between the two hygral conditions was small.

7.4 Chapter conclusions

In this chapter, we presented the experimental methods to prepare samples by compression of powder, to characterize the volume fraction of each phase in the compacts and to perform indentation testing on compacts that were conditioned in either water-saturated conditions or under 11% relative humidity. The relative humidity during indentation test was controlled to avoid any moisture exchange between the tested samples and the environment. The volume fraction of each phase in a compact, its Young's modulus E, its indentation hardness H and its creep properties were measured.

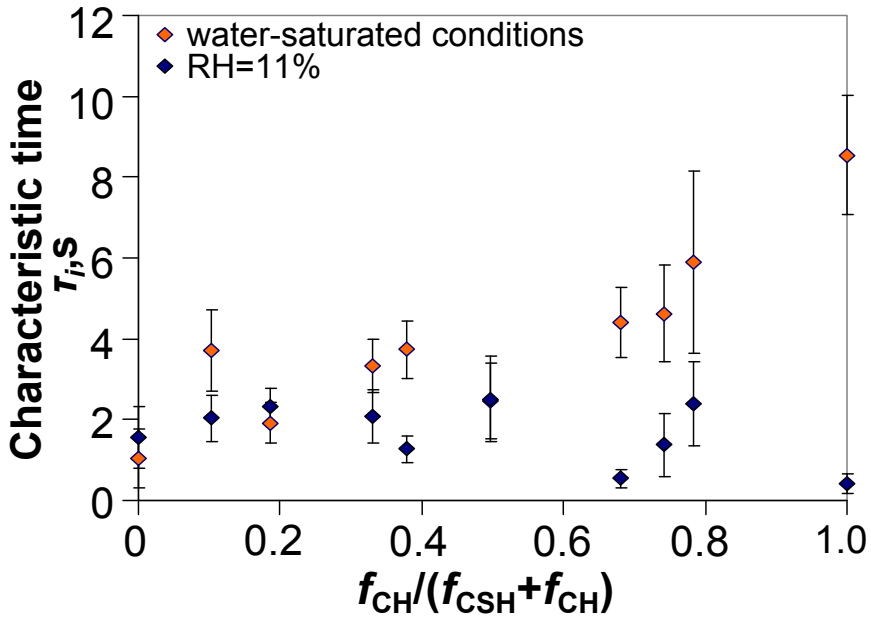

Figure 7.12: Indentation characteristic time τ_i from compacts conditioned in water-saturated conditions and at 11% relative humidity at a temperature of 23°C.

The result of indentation testing on different surfaces of one of the compacts indicates that the compacts are fairly isotropic.

The relation between C_i and E and that between C_i and H for the compacts were found to be different for samples conditioned under 11% relative humidity and for those conditioned in water-satuated conditions. At 11% relative humidity, C_i increased monotonically with Young's modulus E and with indentation hardness H for all the compacts. In water-saturated conditions, in the C_i-E plane or in the C_i-H plane, compacts of pure C-S-H and of pure CH fell out of a master curve formed by the data points of compacts of mixtures.

At 11% relative humidity, the Young's modulus E, indentation hardness H and contact creep modulus C_i were found to increase when increasing the proportion of CH in the solid skeleton, while keeping the porosity constant. In water-saturated conditions, the trend was not clear.

The effect of water on the mechanical properties of compacts was observed. At 11% relative humidity, for all the compacts, their Young's modulus E, indentation hardness H and contact creep modulus C_i increased with respect to those in water-saturated conditions. For the creep properties of compacts, we found that the contact creep modulus increased by a factor of 7 to 37 from water-saturated conditons to 11% relative humidity. Also, the indentation characteristic time τ_i decreased at 11% relative humidity when compared with that in water-saturated conditions, for compacts with high volume fractions of CH.

The remarks above confirm that relative humidity has a major effect on the mechanical properties of cementitious materials: and this effect will be studied in detail in chapter 8.

Chapter 8

Effect of relative humidity on creep properties of cementitious materials

Résumé *Dans ce chapitre, la pâte C_3S, le compact de C-S-H et le compact de CH en équilibre hydrique selon des niveaux d'humidité relative différents ont été testés par microindentation. Pour l'ensemble des matériaux étudiés, il a été observé que la dureté d'indentation H diminuait quand l'humidité relative augmentait. Le module de Young E de la pâte C_3S s'est quant à lui révélé constant à des niveaux d'humidité relative différents, tandis que pour le compact de CH et de C-S-H, une baisse du module de Young E était observée à des humidité relatives élevées. Le module de fluage C_i a baissé de manière générale avec une hausse d'humidité relative. Pour le compact de CH, la baisse du module C_i s'est vérifiée sur l'ensemble d'humidités relatives considérés, alors que pour la pâte C_3S et le compact de C-S-H, nous avons identifié une humidité relative critique en dessous lequel le module C_i variait. En combinant nos observations avec la connaissance de base sur la saturation partielle des solides poreux, nous pouvons conclure que le fait de désaturer les pores capillaires n'a eu aucun effet sur le module de fluage mais que le fait de désaturer les pores dans C-S-H était par contre responsable des variations observées sur le module de fluage à des niveaux d'humidité relative variables. Autrement dit, l'eau dans le C-S-H est responsable du fluage propre à long terme de la pâte C_3S et du compact de C-S-H. Pour tous*

les échantillons analysés, il a été constaté une évolution fragmentée du temps caractéristique d'indentation en fonction de l'humidité relative: il semble qu'il existe une humidité relative critique au-delà duquel τ_i est une fonction décroissante de l'humidité relative et en-deçà duquel τ_i est une fonction croissante de l'humidité relative. Sur la pâte C_3S, en considérant les données sur le module de fluage et l'isotherme de désorption, une relation linéaire reliant le module de fluage et le teneur en eau a été trouvée pour une humidité relative compris entre 11% et 75%.

Abstract *In this chapter, C_3S paste, compact of pure C-S-H and compact of pure CH in hygral equilibrium at various relative humidities were tested by microindentation. For all the materials studied, the indentation hardness H was found to decrease with the increase of relative humidity. The Young's modulus E of C_3S paste was found to be independent of relative humidity, while for compact of CH and C-S-H, a decrease of Young's modulus E was seen in high relative humidities. The contact creep modulus C_i decreased in general with the increase of relative humidity. For compact of CH the decrease of contact creep modulus was observed in the whole range of relative humidities studied, while for C_3S paste and compact of C-S-H, we identified a critical relative humidity below which C_i varied. Combining the observations with basic knowledge on partial saturation of porous solids, we concluded that the removal of water from capillary pores had no effect on the contact creep modulus while the removal of water from pores in C-S-H was responsible for the variation of contact creep modulus in a range of relative humidities. In other words, water in C-S-H was responsible for the long-term basic creep of C_3S paste and of the compact of C-S-H. For all the samples studied, the evolution of indentation characteristic time τ_i in function of relative humidity was also found to be piecewise: there seems to exist a critical relative humidity above which τ_i was an increasing function of relative humidity and below which τ_i was a decreasing function of relative humidity. On C_3S paste, combining the gathered data on contact creep modulus with desorption isotherm, a linear relationship between the contact creep modulus and the water content was found for relative humidities ranging from 11% to 75%.*

8.1 Chapter introduction

As already mentioned in chapter 2, the water content in concrete has an effect on the basic creep of cementitious materials. Several researchers reported that by partially or completely removing water from concrete sample before creep testing, the basic creep strain is decreased [Acker and Ulm, 2001; Bažant et al., 1973; Cilosani, 1964; Wittmann, 1970]. However, even if we know qualitatively that water has an effect on the creep properties of cementitious materials, with the available data in literature, how water influences quantitatively the creep properties of those materials is not clear.

The availability of experimental data is at least partly responsible for the poor understanding of the subject. Indeed, to ensure the hygral equilibrium between sample for macroscopic mechanical testing and the environment takes very long time. In addition, to keep a stable temperature and relative humidity during macroscopic creep testing for a long period to measure the long-term basic creep of cementitious material is not only time consuming but also technically challenging. Of course, to reduce the duration of sample conditioning, one can increase the surface-to-volume ratio of the sample. For example, instead of using cylindrical or prism sample, one can use hollow cylinder [Bažant et al., 1973] with very thin walls, or T-shaped sample [Tamtsia and Beaudoin, 2000]. This approach can guarantee a shorter duration to achieve equilibrium but at the same time increases the risk of getting an inhomogeneous sample with defaults, which could increase the scatterings of measurement with respect to massive samples.

In chapter 4 and chapter 5, we showed that minutes-long indentation creep testing gave access to the long-term basic creep properties of cementitious materials, characterized by contact creep modulus. The duration of the test was largely reduced when compared with macroscopic testing. Furthermore, as the scale of indentation testing was smaller than that of macroscopic testing, sample to test could be made to be very thin, which reduces enormously the time needed for achieving hydraulic equilibrium with environment. Last but not least, from the results presented in former chapters, a typical coefficient of variation of the contact creep modulus obtained by 5 repeats of indentation test was about 10%, which indicated a high repeatability of indentation.

In this chapter, microindentation creep testing is performed on samples that

achieved moisture equilibrium in various relative humidities. Three types of samples are tested: C_3S paste, compact of C-S-H and compact of CH, with the following objectives:

- Obtain abundant data on basic creep of various cementitious materials at various relative humidities.
- To better understand how water content influences the creep of cementitious materials.

8.2 Materials and methods

8.2.1 Description of samples

The C_3S paste sample used in this study was from the C_3S samples prepared for the study in chapter 6. After curing, a cylinder sample was firstly cut into two parts at mid-height. We took the half of sample and applied the polishing procedure indicated in chapter 4 to the surface created by cut so that microindentation test can be carried out on the surface. When the polishing was finished, we did a second cut near the polished surface and a disk of about 5mm thick was obtained. After the second cut, the surface created by the second cut was submitted to a polishing which aimed at reducing the thickness of disk while keeps the parallelism of two flat surfaces: the sample was fixed in a metallic cell which serves as a support and polished on a SiC paper. After the second polishing, the thickness of disk-like sample was reduced to around 3mm to 3.5mm.

Compact samples of C-S-H and CH used in this study were from those prepared for the study presented in chapter 7. After curing in lime water for one week, the compact of C-S-H and that of CH were split into six parts, for indentation tests at various relative humidities.

8.2.2 Conditioning of samples

All the samples were put into desiccator with various relative humidities for conditioning.

The controlled relative humidities for sample conditioning were created by saturated aqueous salt solutions. Each desiccator was carefully cleaned and filled

	LiCl	**$MgCl_2$**	**$Mg(NO_3)_2$**	**NaCl**	**KNO_3**
RH (23°C)	11.3	32.9	53.5	75.4	94.0

Table 8.1: Relative humidity created by various saturated salt solutions at various temperatures. Data is obtained by applying the best-fit function in Tab.1 of [Greenspan, 1977]

with certain saturated salt solution and then moved to a chamber where the temperature was controlled at 23°C±0.2°C one month before the start of conditioning. The chemicals used and the corresponding relative humidities they created was presented in Tab. 8.1. We applied the same procedure as indicated in section 7.2.2 to avoid the carbonation during conditioning.

In order to determine the duration of conditioning necessary for the samples to achieve moisture equilibrium with conditioning environment, the mass evolution of a C_3S paste, part of a compact of C-S-H and a compact of CH being conditioned at 11% relative humidity were measured in parallel with sample coniditionning. The change of mass in function of time was measured and is presented in Fig. 8.1. From Fig. 8.1, a duration of 90 days is enough for compact of C-S-H and C_3S to achieve moisture equilibrium with conditioning envrionment. For compact of CH, the necessary duration is much smaller than that of the other two materials: one day is enough for it to achieve equilibrum. The kinetics of drying of compact of CH is much faster than that of C_3S paste and compact of C-S-H, which shows the necessity of controlling relative humidity around compact of CH during indentation testing.

8.2.3 Indentation testing in relative humidity controlled conditions

After 90 days conditioning, all samples were tested by microindentation testing in relative-humidity-controlled environment. The relative humidities during indentation test were controlled to be very similar to that of conditioning, by circulating air with controlled relative humidity in indentation chamber. The air was obtained by pumping dry CO_2-free air into saturated solutions of various salts (see in Fig. 3.3).

Similarly with other experimental studies presented in former chapters, two

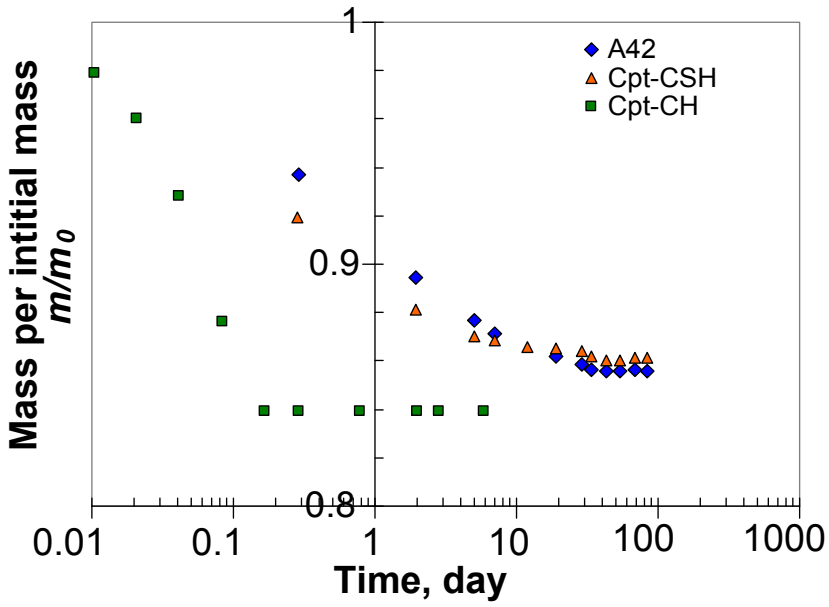

Figure 8.1: Mass evolution of initially water-saturated samples conditioned at 11% relative humidity: the shape of C_3S paste sample and the compact of C-S-H sample is a split part of a 3.5mm-thick disk and the shape of compact of CH is a disk.

Indentation probe	Vickers
Maximum indentation load P_{max}, N	5 to 20
Maximum indentation depth h_{max}, µm	29-38
Holding duration τ_H, s	20 or 300
Temperature T	23°C±0.2°C
Relative humidity RH	11%, 33%, 54%, 75%, 94%

Table 8.2: Experimental parameter settings of indentation experiments on compacts and on C_3S paste at various relative humidities.

types of indentation experiments with different holding duration were performed on each sample, with 5 repeating tests for each type of indentation experiment. A summary of parameters for indentation testing is given in Tab. 8.2. The indentation experiments with a 20-seconds-long holding phase were used to calculate the Young's modulus E (assuming a Poisson's ratio ν=0.25 for all the samples) and indentation hardness H by applying the method mentioned in section 3.3. The indentation experiments with a 300-seconds-long holding phase were used to obtain the contact creep function.

8.3 Results and discussions

8.3.1 Raw results from indentation testing

Five repeats of basic creep function $(L(t) - 1/M_0)$ of C_3S paste, compact of C-S-H and compact of CH at various relative humidities were measured by microindentation testing. The specific basic creep function with median amplitude is presented in Fig. 8.2. As already seen from Fig. 6.3 and Fig. 7.7, the contact creep function of C_3S paste was well captured by a logarithmic function of time, thus similarly to what was applied in former chapters, we fitted the contact creep function curve with Eq. 4.3 to obtain the contact creep modulus C_i and the indentation characteristic time τ_i. The four parameters, i.e., E, H, C_i and τ_i measured from indentation testing are presented in Tab. 8.3.

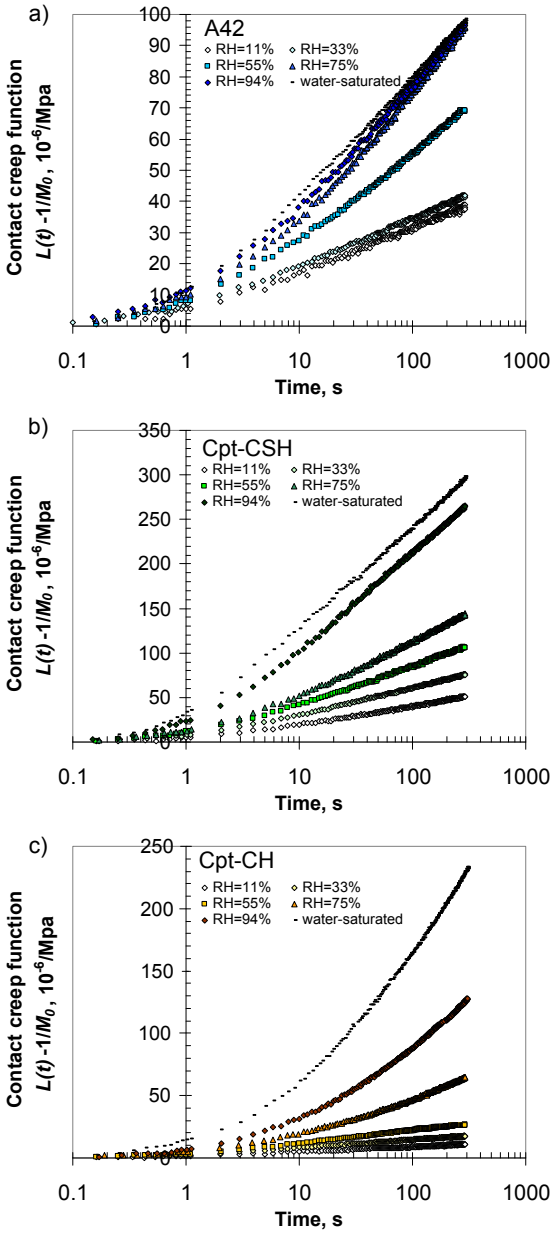

Figure 8.2: Median contact creep function of a) C_3S paste, b) compact of C-S-H and c) compact of CH, at various relative humidities. For C_3S paste in water-saturated conditions, we take C_3S paste tested at age of 56 days in water-saturated conditions from section 6.3. For compacts, the results in water-saturated conditions are from section 7.3.

sample	E **(GPa)**	H **(GPa)**	C_i **(GPa)**	τ_i **(s)**
A42				
RH=11%	18.7±1.0	0.530±0.065	156±3.7	0.8±0.2
RH=33%	21.0±2.9	0.576±0.070	143±0.9	1.0±0.3
RH=54%	20.3±2.0	0.452±0.069	81.5±0.8	1.5±0.8
RH=75%	20.8±0.9	0.384±0.035	48.0±1.9	2.9±0.4
RH=94%	21.5±3.5	0.391±0.029	54.1±1.3	1.4±0.5
water-saturated	21.5±3.5	0.335±0.016	53.2±3.0	1.5±0.4
Cpt-CSH				
RH=11%	18.8±0.5	0.680±0.068	105±17	1.0±0.8
RH=33%	19.1±3.3	0.506±0.051	74.7±4.7	1.6±0.7
RH=54%	18.1±0.3	0.432±0.139	47.2±4.6	1.6±0.2
RH=75%	16.3±2.4	0.360±0.061	35.4±4.4	1.8±0.5
RH=94%	11.7±0.4	0.221±0.026	20.3±4.3	1.8±0.7
water-saturated	7.2±0.8	0.195±0.029	20.0±3.7	1.0±0.7
Cpt-CH				
RH=11%	32.1±4.9	1.17±0.13	608±139	0.4±0.2
RH=33%	33.5±2.3	1.11±0.080	361±31.3	0.6±0.2
RH=54%	29.4±2.5	0.903±0.045	198±20.6	1.3±0.7
RH=75%	30.5±3.9	0.711±0.033	60.6±6.1	8.4±2.1
RH=94%	27.8±1.3	0.585±0.028	26.1±1.5	13.2±2.4
water-saturated	16.4±0.7	0.343±0.016	16.4±0.7	8.5±1.5

Table 8.3: Young's modulus E, indentation hardness H, contact creep modulus C_i and indentation characteristic time τ_i of C_3S paste, with w/c=0.42 (labeled as A42), compact of C-S-H (labeled as Cpt-CSH) and compact of CH (labeled as Cpt-CH) tested in various relative humidities. For C_3S paste in water-saturated conditions, we take the value of C_3S paste tested at age of 56 days in water-saturated conditions (see in Tab. 6.7). For compacts, the results in water-saturated conditions are from Tab. 7.4.

8.3.2 Mechanical properties of C_3S paste and compacts at various relative humidities

As presented in Fig. 8.3a, in H-E plane, the Young's modulus E of compacts increased with the increment of the indentation hardness H. However, for C_3S paste, the evolution of E in function of H was unclear. Fig. 8.3b shows for the three material tested, the contact creep modulus C_i increased with the increment of indentation hardness H. Fig. 8.3c shows that in E-C_i plane, for compacts, C_i increased with the increment of Young's modulus E, but for C_3S paste the trend was unclear.

The contact creep modulus C_i and Young's modulus E and the indentation hardness of C_3S paste, compact of C-S-H and compact of CH at various relative humidities is presented in Fig. 8.4.

As presented in Fig. 8.4a, for both C_3S paste and compact of C-S-H, there exists a critical relative humidity below which the contact creep modulus was a decreasing function of relative humidity and above which the contact creep modulus was constant. For C_3S paste this critical relative humidity, according to Fig. 8.4a, lies somewhere between RH=54% and RH=75%, while for compact of C-S-H, the critical realative humidity lies between 75% and 94%. For compact of CH, C_i decreased with an increasing relative humidity on the whole range of relative humidities studied.

From Fig. 8.4b, the Young's modulus of C_3S paste at various relative humidities varies from 18.7GPa to 21.5GPa. With a coefficient of variation from measurement up to 15% for this parameter, E of C_3S paste can be seen as invariant with the relative humidity. On the other hand, Young's modulus of compacts decreased with the increment of relative humidity. Especially for compact of C-S-H, an obvious drop of the Young's modulus from 18GPa in RH=55%to 11.7GPa in RH=94% and even down to 7.2GPa in water-saturated conditions was observed.

From Fig. 8.4c, one can see that indentation hardness dropped with the increment of relative humidity for the three tested materials.

For all the samples tested, as presented in Fig. 8.5, the indentation characteristic time τ_i increased with the increment of relative humidity up to a critical relative humidity above which τ_i decreased with an increasing relative humidity: for C_3S paste, τ_i increased from 0.8s in RH=11% to 2.9s in RH=75% then decreased

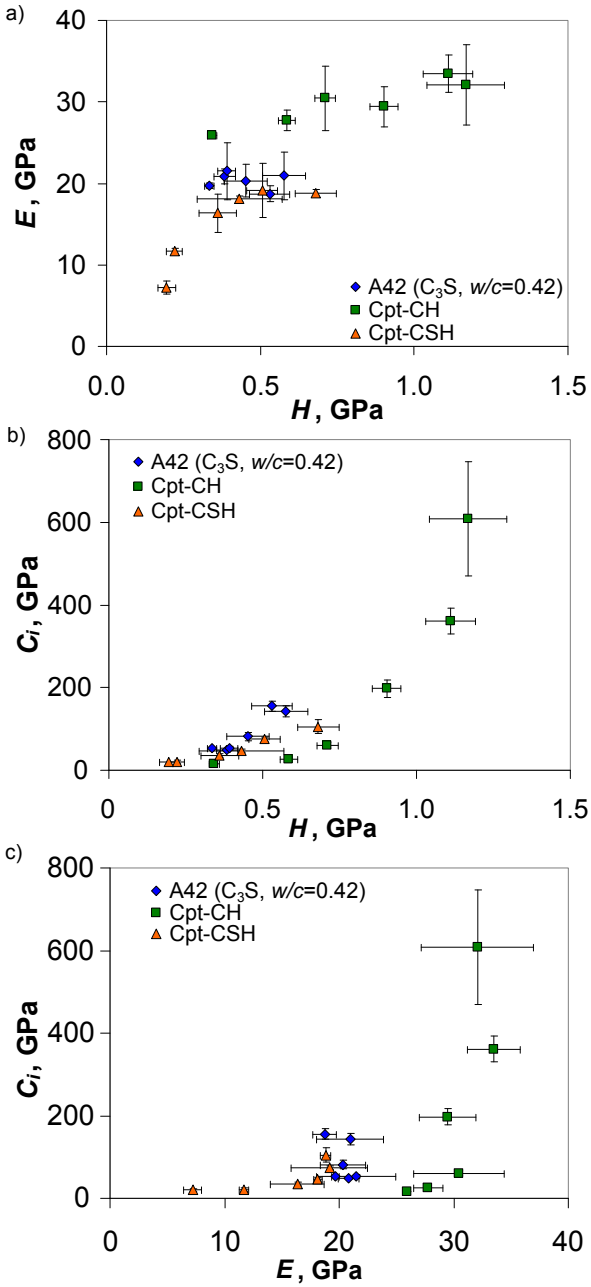

Figure 8.3: Indentation hardness H versus a) Young's modulus E, b) contact creep modulus C_i, and Young's modulus E versus c) contact creep modulus C_i of C_3S paste with w/c=0.42 (A42), compact of C-S-H (Cpt-CSH) and compact of CH (Cpt-CH) at various relative humidities.

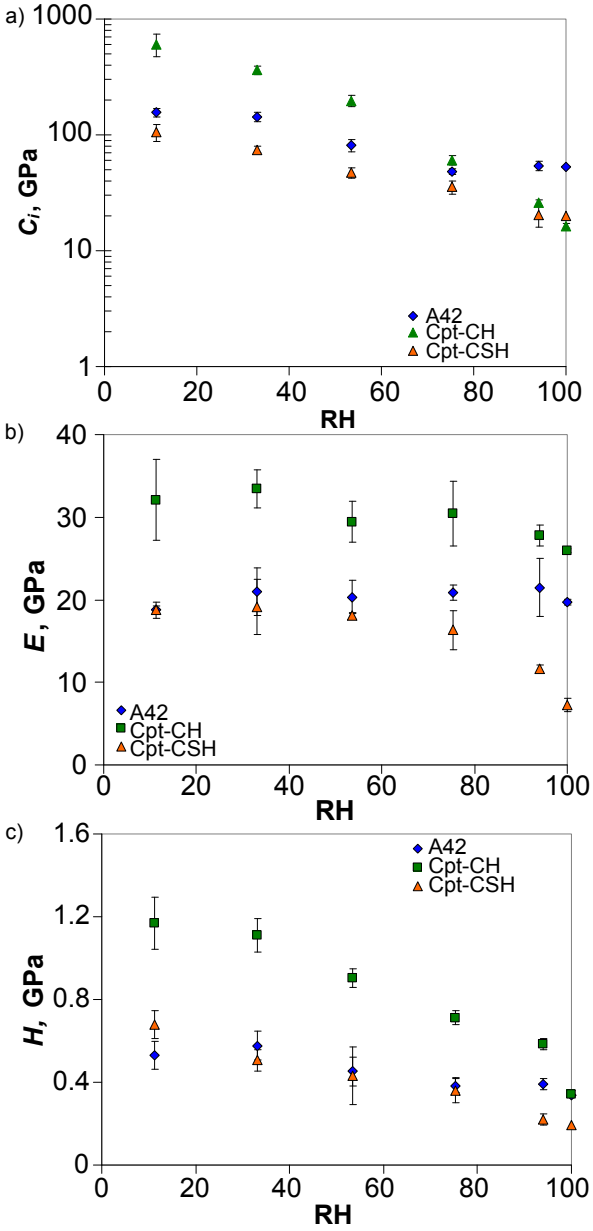

Figure 8.4: Indentation hardness H, contact creep modulus C_i and Young's modulus E of C_3S paste, compact of C-S-H and compact of CH at various relative humidities.

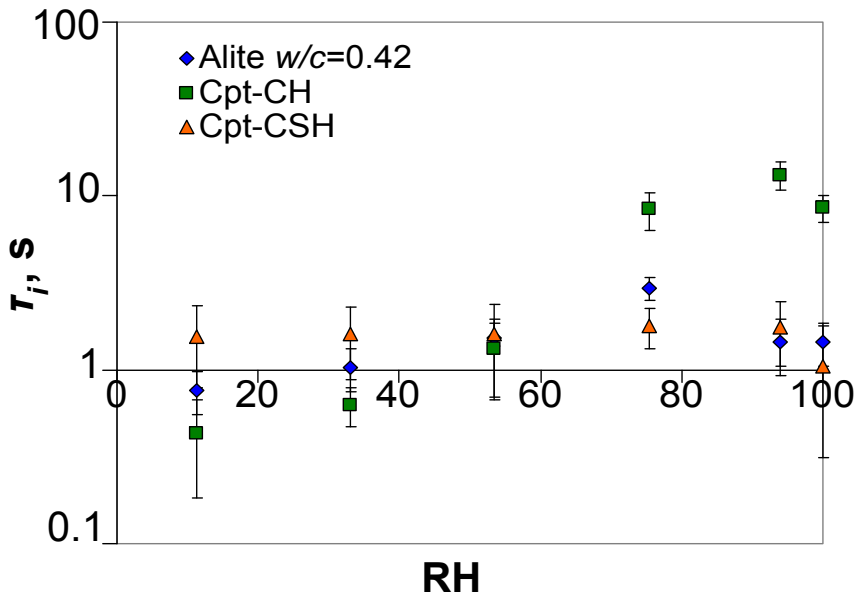

Figure 8.5: Indentation characteristic time τ_i of C_3S paste, compact of C-S-H and compact of CH in equilibrium with various relative humidities.

to 1.5s in water-saturated conditions; for compact of C-S-H, τ_i increased from 1.0s in RH=11% to 1.8s in RH=94% then decreased to 1.0s in water-saturated conditions; for compact of CH, τ_i increased from 0.4s in RH=11% to 13.2s in RH=94% then decreased to 8.5s in water-saturated conditions.

8.3.3 Influence of water content on the creep properties of C_3S paste

The desorption isotherm of a 180-days-old C_3S paste ($w/c = 0.42$) was measured by drying with step decreasing relative humidities starting from 94%, with a dynamic vapor sorption apparatus (many thanks to Gabriel PHAM from Lafarge research center, who carried out dynamic vapor sorption experiment). The water content w of C_3S paste at various relative humidities was obtained with the following equation:

$$w = \frac{m(\mathrm{RH}) - m_{dry}}{m_{dry}} \tag{8.1}$$

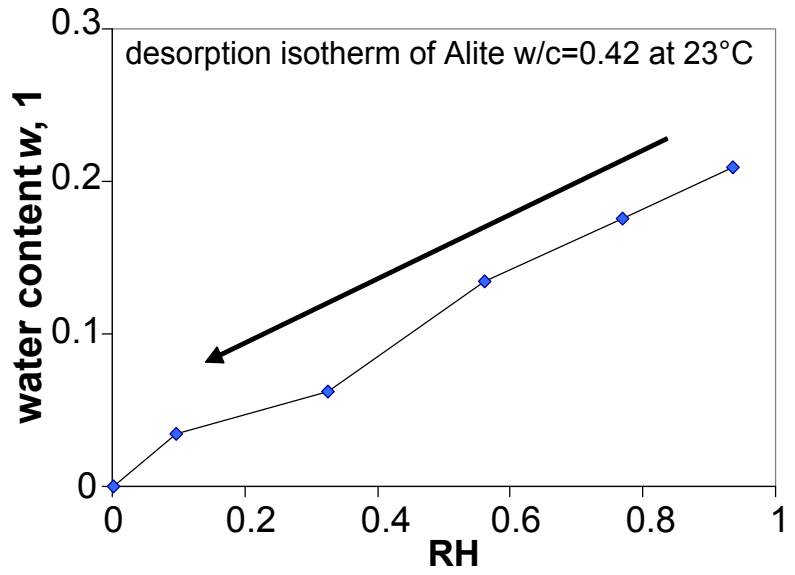

Figure 8.6: Desorption isotherm of a 180-days-old C_3S paste cured in water, with water-to-cement ratio w/c=0.42.

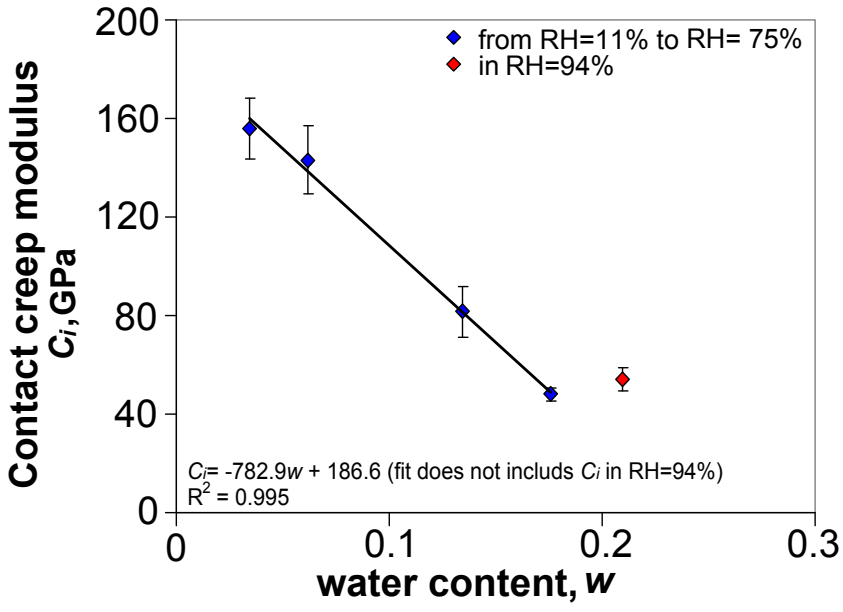

Figure 8.7: The contact creep modulus C_i in function of water content w for C_3S paste.

where $m(\mathrm{RH})$ is the mass of a sample at relative humidity RH and m_{dry} is the dry mass. $m(\mathrm{RH})$ was measured from experiment and the dry mass was approximated as the mass at 3% relative humidity. The first desorption isotherm of C_3S paste is presented in Fig. 8.6.

With the contact creep modulus at various relative humidities displayed in Fig. 8.4a, and the desorption curve, the contact creep modulus C_i in function of the water content w is displayed in Fig. 8.7. A linear relationship between the water content w and the contact creep modulus of C_3S paste in equilibrium with relative humidities between 11% to 75% is found, with a coefficient of determination R^2=0.995.

8.3.4 Effect of relative humidity on creep properties of C_3S paste and compacts

Cured in water, before conditioning, C_3S paste sample was water-saturated. The conditioning at relative humidities lower than 100% dries out water from certain pores in the sample. As presented in Fig. 8.4a, for relative humidities higher than 75%, the contact creep modulus C_i was independent of relative humidity, which means that water dried out at relative humidities higher than 75% had no significant influence on the contact creep modulus of C_3S paste. As presented in Fig. 8.7, starting from 75% relative humidity, C_i increased linearly with the decrease of water content w, which means from 75% relative humidity or lower, the extra dried-out water due to conditioning in those relative humidities accounted for the change of C_i. A critical relative humidity of 75% is thus found for C_3S paste, below which the dried out water influences the contact creep modulus and above which the removal of water has no effect on the contact creep modulus.

For a porous material as cement paste, drying firstly desaturates large pores then smaller pores. Applying the Kelvin-Laplace law for drying, the largest pore entry radius r_{pe} (the largest pore which remains saturated for a porous material in moisture equilibrium with a given relative humidity), can be expressed as the following equation [Coussy, 2004]:

$$r_{pe} = -\frac{2\gamma_{gl}\cos\theta}{RT/V_{m,H_2O}\ln \mathrm{RH}} \tag{8.2}$$

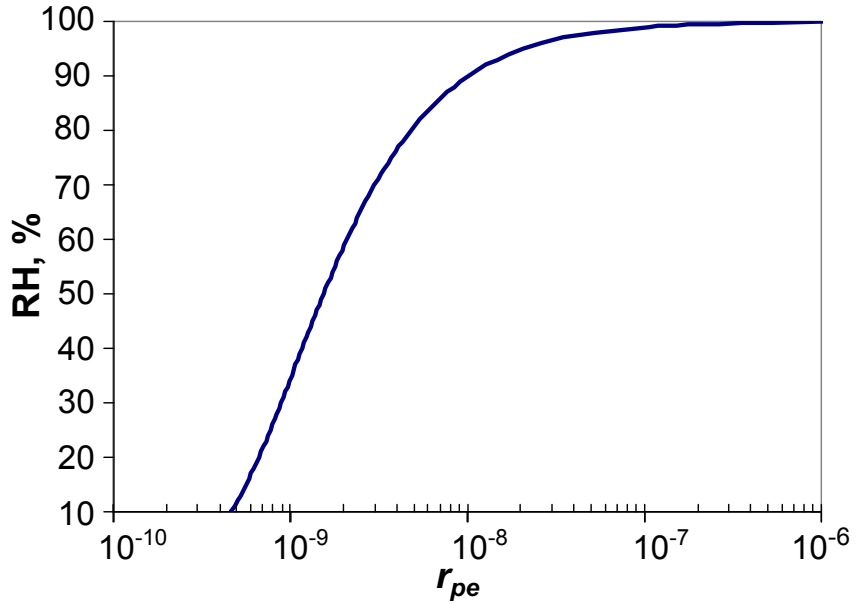

Figure 8.8: Largest radius r_{pe} of pores remaining saturated at various relative humidities.

where γ_{gl} is the air-water interface energy, T is the temperature, R is the ideal gas constant, θ is the wetting angle, V_{m,H_2O} is the molar volume of water and RH is the relative humidity at a given temperature. At a temperature $T = 295$K, with γ_{gl}=73mJ/m^2, θ=0, R=8.31J/(mol·K) and V_{m,H_2O}=18 cm^3/mol, the relation between the relative humidity in sample and the largest pore entry radius (the radius of the largest pore remaining saturated) is presented in Fig. 8.8. As one can see in Fig. 8.8, the lower the relative humidity is, the smaller this radius is. At relative humidity of 75%, the largest radius given by applying Eq. 8.2 is about 4nm.

A similar reasoning can be applied to the compact of C-S-H. Already stated in section 8.3.2, we observed a critical relative humidity above which C_i stayed constant and below which C_i increased with the decrease of relative humidity. This critical relative humidity was between 75% and 94%. By fitting the C_i-RH relation from 11% relative humidity to 75% relative humidity, we found a critical relative humidity of 84%, at which C_i=20GPa. Applying Eq. 8.2 for RH=84%, a radius of the largest pore remaining saturated equal to 6nm is found.

For both C_3S paste and compact of C-S-H, water in pores with an entry radius smaller than 4nm and 6nm, respectively, is therefore linked to the long-term basic creep property. As the capillary pores in cementitious materials are larger than 60nm [Korb et al., 2007; Mehta and Monteiro, 2006], both pores with entry radius of 4nm and 6nm are thus not capillary pores. For both C_3S paste and compact of C-S-H, pores smaller than capillary pores are those in C-S-H, e.g., the gel pores with a characteristic radius of 3nm to 7nm according to different studies [Korb et al., 2007; Muller et al., 2012]. Thus both C_3S paste and compact of C-S-H showed that water in C-S-H is responsible for the long-term basic creep of material studied.

Dissimilarly with what was observed for C_3S paste or for compact of C-S-H, the contact creep modulus of CH evolved with relative humidity on the whole range of relative humidities studied. Applying the above reasoning, one can conclude that water in all types of the pores in compact of CH may influence its basic creep property. An alternative explanation could be that creep of CH is a process influenced by the activity of water itself: such explanation is consistent with the pressure solution theory (see section 2.5) proposed to explain the creep behavior of crystalline materials such as gypsum.

So far, combining the results obtained in this chapter with those from chapter 5, it seems that the basic creep behaviors of pure crystalline materials evolve differently to relative humidity when comparing with those of materials that contain C-S-H. Crystalline materials appear to be more sensitive to relative humidity than materials with amorphous phase C-S-H in terms of creep properties: the contact creep modulus C_i of gypsum plaster and that of compact of CH increased by a factor of 100 and 12 respectively from water-saturated condition to medium relative humidities of about 50%, while for compact C_3S paste and compact of C-S-H the factor was about 2; the indentation characteristic time of gypsum plaster and that of compact of CH increased by a factor of 4 and 7, respectively, from medium relative humidities of about 50% to water-saturated conditions, while for compact C_3S paste and compact of C-S-H, the indentation characteristic time stayed almost unchanged.

8.4 Chapter conclusions

In this chapter, C_3S paste, compact of C-S-H and compact of CH at various relative humidities were tested by microindentation. The Young's modulus E, the indentation hardness H and the contact creep functions of those samples were obtained. The contact creep functions in various relative humidities which represents the specific basic creep of those materials were fitted with a logarithmic function to time (see Eq. 4.3) so that the contact creep modulus C_i and the indentation characteristic time τ_i were applied to characterize the creep properties of those materials in various relative humidities.

For all the materials studied, the indentation hardness H was found to be a decreasing function of relative humidity. The Young's modulus E of C_3S paste was independent of relative humidity. However, for compact of CH a slight drop of E was found in high relative humidities and a much more important drop of E was found for the compact of C-S-H.

The contact creep modulus C_i decreased in general with an increasing relative humidity. For compact of CH, the contact creep modulus decreased on the whole range of relative humidities studied. In contrast, for C_3S paste and the compact of C-S-H, we identified a critical relative humidity below which the contact creep modulus varied and above which it remained constant. By applying the Kelvin-Laplace law, the critical relative humidities were converted into the largest entry radius r_{pe} of largest pore remaining water-saturated when drying. Those largest entry radius indicated that the removal of water from pores in C-S-H was responsible for the evolution of C_i below critical relative humidity, while the removal of water in capillary pores had no influence on the basic creep of the two materials.

For all the samples studied, the evolution of indentation characteristic time in function of relative humidity was also found to exhibit a threshold: there seemed to exist a critical relative humidity above which τ_i decreased with the increment of relative humidity and below which τ_i increased with the increment of relative humidity.

On the C_3S paste, by combining the indentation data with the desorption isotherm, we found a linear relationship between contact creep modulus and water content for relative humidities ranging from 11% to 75%.

Chapter 9

Modeling by micromechanical approach

Résumé *Dans ce chapitre, une approche micromécanique est utilisée pour interpréter les résultats expérimentaux et pour modéliser l'effet de la microstructure et de l'eau sur le fluage. En considérant les propriétés mécaniques et la distribution de chaque phase des matériaux obtenue par expérimentation, nous proposons un modèle de mise à l'échelle pour les pâtes C_3S et C_2S et un autre modèle pour les compacts. Les modèles proposés sont aussi utilisables pour le module de Young E. Pour la pâte C_2S et les compacts, le choix du modèle est guidé par les informations sur la microstructure obtenues par MEB. L'effet de l'humidité relative est en outre intégré aux différents modèles proposés.*

Abstract *In this chapter, a micromechanical approach was applied to decode the experimental results and to model the effect of microstructure and water on creep. With mechanical properties and phase distribution in those materials obtained experimentally, we proposed one upscaling model for C_3S and C_2S pastes and another model for compacts to explain the experimental results on contact creep modulus C_i. The choice of model was guided by information on the microstructures of those materials. The proposed model was also applicable to the Young's modulus E. The effect of relative humidity was also integrated in the proposed models.*

9.1 Short reminder of basic elements of linear homogenization theory

This section is dedicated to presenting a short reminder of basic elements on linear homogenization theory and two homogenization schemes which will be used later in our modeling, namely the Mori-Tanaka scheme and the self-consistent scheme.

Both natural and artificial materials are often heterogeneous: they are composed of various components with different properties and behaviors. Experimental studies are usually carried out on volumes of materials that contain a large number of heterogeneities. Describing these media by using appropriate mathematical models to describe each constituent turns out to be an intractable problem [Auriault et al., 2010]. The aim of homogenization techniques is to model the heterogeneous medium as a simpler equivalent continuous medium, whose description is validated at a scale which is large enough compared to that of heterogeneities. In micromechanics, the representative volume element, noted as RVE, is such a scale large enough to capture the average behavior of all the heterogeneities. At the same time, the RVE should also be small enough when compared with the size l_{sample} of sample studied in the framework of continuum mechanics. In other words, a condition of separation of scales must be satisfied:

$$l_{heter} \ll l_{RVE} \ll l_{sample} \tag{9.1}$$

where l_{heter}, l_{RVE} and l_{sample} are the characteristic sizes of the heterogeneities, of the RVE and of the sample, respectively.

With the separation of scale, the major focus of the linear elastic homogenization theory can be expressed as: to find the homogenized stiffness tensor $\mathbb{C}_{hom}$ which links the macroscopic strain $\boldsymbol{E}(\underline{X})$ to the macroscopic stress $\boldsymbol{\Sigma}(\underline{X}) = \mathbb{C}_{hom} : \boldsymbol{E}(\underline{X})$, from the knowledge of the local distribution of microscopic stiffness tensors $\mathbb{C}(\underline{x})$ which link the local strain $\boldsymbol{\epsilon}(\underline{x})$ to the local stress $\boldsymbol{\sigma}(\underline{x}) = \mathbb{C}(\underline{x}) : \boldsymbol{\epsilon}(\underline{x})$. A summary of the parameters in the two scales and their relations is given in Tab. 9.1. The position, strain and stress at the two scales verify the following relation, which links a quantity $A(\underline{X})$ at the macroscale to

	microscopic	macroscopic (on RVE Ω)
Position	$\underline{x}$	$\underline{X}$
Strain	$\boldsymbol{\epsilon}(\underline{x})$	$\boldsymbol{E}(\underline{X}) = \langle \boldsymbol{\epsilon}(\underline{x}) \rangle_\Omega$
Stress	$\boldsymbol{\sigma}(\underline{x})$	$\boldsymbol{\Sigma}(\underline{X}) = \langle \boldsymbol{\sigma}(\underline{x}) \rangle_\Omega$
Energy	$\boldsymbol{\omega}(\underline{x}) = \boldsymbol{\epsilon}(\underline{x}) : \boldsymbol{\sigma}(\underline{x})$	$\boldsymbol{W}(\underline{X}) = \boldsymbol{E}(\underline{X}) : \boldsymbol{\Sigma}(\underline{X})$
Stiffness	$\mathbb{C}(\underline{x})$	$\mathbb{C}_{hom}(\underline{X})$
Hooke's law	$\boldsymbol{\sigma}(\underline{x}) = \mathbb{C}(\underline{x}) : \boldsymbol{\epsilon}(\underline{x})$	$\boldsymbol{\Sigma}(\underline{X}) = \mathbb{C}_{hom}(\underline{X}) : \boldsymbol{E}(\underline{X})$

Table 9.1: Parameters in microscale and macroscale and their relations.

its corresponding quantity $a(\underline{x})$ at the microscale:

$$A(\underline{X}) = \langle a(\underline{x}) \rangle_{\Omega(\underline{X})} = \frac{1}{|\Omega|} \int_{\Omega(\underline{X})} a(\underline{x}) d\underline{x} \tag{9.2}$$

where Ω is the volume of the RVE and $\langle \rangle_\Omega$ is the volume average of $a(\underline{x})$ on the RVE.

To find the relationship between local stiffness tensor $\mathbb{C}(\underline{x})$ and homogenized stiffness tensor $\mathbb{C}_{hom}(\underline{X})$, one can apply a homogeneous strain $\boldsymbol{E}$ on the boundary $\partial\Omega$ of RVE. The following equations are considered:

- mechanical equilibrium:

$$\text{div}\boldsymbol{\sigma}(\underline{x}) = \mathbf{0} \tag{9.3}$$

- Hooke's law at the microscopic scale:

$$\boldsymbol{\sigma}(\underline{x}) = \mathbb{C}(\underline{x}) : \boldsymbol{\epsilon}(\underline{x}) \tag{9.4}$$

- the boundary conditions:

$$\boldsymbol{\xi}(\underline{x}) = \boldsymbol{E} \cdot \underline{x} \text{ on } \partial\Omega \tag{9.5}$$

Thanks to the linearity of all microscopic material behaviors, one can introduce a fourth-order tensor $\mathbb{A}(\underline{x})$ termed as strain localization tensor which links the local strain $\boldsymbol{\epsilon}(\underline{x})$ to the macroscopic strain $\boldsymbol{E}$ with the following expression:

$$\boldsymbol{\sigma}(\underline{x}) = \mathbb{A}(\underline{x}) : \boldsymbol{E} \tag{9.6}$$

Applying Hooke's law at the microscale yields:

$$\boldsymbol{\sigma}(\underline{x}) = \mathbb{C}(\underline{x}) : \boldsymbol{\epsilon}(\underline{x}) = \mathbb{C}(\underline{x}) : \mathbb{A}(\underline{x}) : \boldsymbol{E} \tag{9.7}$$

By definition, the volume average of local stress $\boldsymbol{\sigma}(\underline{x})$ on Ω is equal to the macroscopic stress $\boldsymbol{\Sigma}(\underline{X})$:

$$\boldsymbol{\Sigma}(\underline{X}) = \langle \boldsymbol{\sigma}(\underline{x}) \rangle_\Omega = \langle \mathbb{C}(\underline{x}) : \mathbb{A}(\underline{x}) \rangle_\Omega : \boldsymbol{E} \tag{9.8}$$

Applying Hooke's law at the macroscale ($\boldsymbol{\Sigma}(\underline{X}) = \mathbb{C}_{hom} : \boldsymbol{E}(\underline{X})$) and combining it with the above equation, one can find a relationship between microscopic local stiffness tensor and homogenized stiffness tensor:

$$\mathbb{C}_{hom} = \langle \mathbb{C}(\underline{x}) : \mathbb{A}(\underline{x}) \rangle_\Omega \tag{9.9}$$

Eshelby [1957] considered the case of an isolated ellipsoidal inclusion with constant stiffness tensor $\mathbb{C}_1$ embedded in an infinite medium with a constant stiffness tensor $\mathbb{C}_0$ and subjected to an uniform strain $\boldsymbol{E}^\infty$ at infinity. He showed that the strain field inside the inclusion was homogeneous and at any point $\underline{x}$ in the inclusion, the strain could be expressed as:

$$\boldsymbol{\epsilon}(\underline{x}) = (\mathbb{I} + \mathbb{P}_{1,0} : (\mathbb{C}_1 - \mathbb{C}_0))^{-1} : \boldsymbol{E}^\infty \tag{9.10}$$

where $\mathbb{I}$ is the four-order unit tensor and $\mathbb{P}_{1,0}$ is Hill's tensor. From now on, we consider that the inclusion phases are all ellipsoidal. Eshelby showed that the Hill's tensor $\mathbb{P}_{1,0}$ depends only on the geometry and the Poisson's ratio of the inclusion, on the elastic properties of the embedding medium, but does not depend on the size of inclusion, as presented by the following equation:

$$\mathbb{P}_{1,0} = \mathbb{S}_1 : \mathbb{C}_0^{-1} \tag{9.11}$$

where $\mathbb{S}_1$ denotes the Eshelby's tensor of phase 1.

Now we consider a multi-phase material with inclusion phases embedded in an infinite medium with stiffness tensor $\mathbb{C}_0$. An inclusion phase r occupies a volume of Ω_r. The stiffness tensor of the phase r is constant, noted as $\mathbb{C}_r$. The volume fraction of phase r is noted as f_r. Applying Eq. 9.10, the mean strain in

each inclusion of phase r can be estimated as:

$$\langle \boldsymbol{\epsilon}(\underline{x}) \rangle_{\Omega_r} = (\mathbb{I} + \mathbb{P}_{r,0} : (\mathbb{C}_r - \mathbb{C}_0))^{-1} : \boldsymbol{E}^{\infty} \tag{9.12}$$

The estimation expressed in the above equation is also known as the diluted model, which applies reasonably well when the inclusions can be regarded as isolated, i.e., without any interaction between inclusions. With the increase of the volume fraction of inclusions, the influence of the interactions of those inclusions can no longer be ignored. To tentatively capture such interactions, instead of considering that each phase is subjected to a strain $\boldsymbol{E}$ at boundary of RVE Ω, one can consider that each phase r is subjected to an auxiliary strain $\tilde{\boldsymbol{E}}$, called screening field:

$$\langle \boldsymbol{\epsilon}(\underline{x}) \rangle_{\Omega_r} = (\mathbb{I} + \mathbb{P}_{r,0} : (\mathbb{C}_r - \mathbb{C}_0))^{-1} : \tilde{\boldsymbol{E}} \tag{9.13}$$

with:

$$\langle \boldsymbol{\epsilon}(\underline{x}) \rangle_{\Omega} = \sum_{r=1}^{N} f_r \langle \boldsymbol{\epsilon}(\underline{x}) \rangle_{\Omega_r} = \boldsymbol{E} \tag{9.14}$$

Combining Eq. 9.13 with Eq. 9.14, one obtains:

$$\langle \boldsymbol{\epsilon}(\underline{x}) \rangle_{\Omega_r} = (\mathbb{I} + \mathbb{P}_{r,0} : (\mathbb{C}_r - \mathbb{C}_0))^{-1} : \left[\sum_{i=1}^{N} f_i (\mathbb{I} + \mathbb{P}_{i,0} : (\mathbb{C}_i - \mathbb{C}_0))^{-1} \right]^{-1} \tag{9.15}$$

Combining the above equation with Eq. 9.6 yields:

$$\begin{aligned} \mathbb{C}_{hom} &= \sum_{r=1}^{N} f_r \mathbb{C}_r : \tilde{\mathbb{A}}_r \\ &= \sum_{r=1}^{N} f_r \mathbb{C}_r : (\mathbb{I} + \mathbb{P}_{r,0} : (\mathbb{C}_r - \mathbb{C}_0))^{-1} : \left[\sum_{i=1}^{N} f_i (\mathbb{I} + \mathbb{P}_{i,0} : (\mathbb{C}_i - \mathbb{C}_0))^{-1} \right]^{-1} \end{aligned} \tag{9.16}$$

where $\tilde{\mathbb{A}}_r$ is termed the mean strain localization tensor of phase r, which is expressed by the following equation [Zaoui, 2002]:

$$\tilde{\mathbb{A}}_r = (\mathbb{I} + \mathbb{P}_{r,0} : (\mathbb{C}_r - \mathbb{C}_0))^{-1} : \left[\sum_{i=1}^{N} f_i (\mathbb{I} + \mathbb{P}_{i,0} : (\mathbb{C}_i - \mathbb{C}_0))^{-1} \right]^{-1} \tag{9.17}$$

When searching for a robust estimation of the homogenized stiffness tensor $\mathbb{C}_{hom}$, besides the information on each phase, namely the volume fraction and the stiffness tensor of each phase, one can also look further on the morphology of studied material. Here we present two classic estimations that take into consideration of the morphology: the Mori-Tanaka scheme and the self-consistent scheme.

The Mori-Tanaka scheme considers that the composite has a clear matrix-inclusion morphology and the matrix is composed of one or some of the constituents of the studied material. The homogenized stiffness tensor obtained with this estimate is denoted as $\mathbb{C}_{MT}$. Supposing phase 1 being the matrix phase, Eq. 9.16 yields the Mori-Tanaka estimate:

$$\mathbb{C}_{MT} = \sum_{r=1}^{N} f_r \mathbb{C}_r : (\mathbb{I} + \mathbb{P}_{r,1} : (\mathbb{C}_r - \mathbb{C}_1))^{-1} : \left[\sum_{i=1}^{N} f_i (\mathbb{I} + \mathbb{P}_{i,1} : (\mathbb{C}_i - \mathbb{C}_1))^{-1} \right]^{-1} \tag{9.18}$$

In contrast, if one considers every phase of the material plays an equivalent role with no phase being the matrix, one can choose the homogenized medium itself as the embedding medium. Such an estimate is called the self-consistent (or polycrystal) scheme. The homogenized stiffness tensor obtained with this estimate is denoted as $\mathbb{C}_{SC}$. $\mathbb{C}_{SC}$ is obtained by combining Eq. 9.16 and Eq. 9.17 and letting $\mathbb{C}_0 = \mathbb{C}_{SC}$, as presented by the following equation:

$$\mathbb{C}_{SC} = \sum_{r=1}^{N} f_r \mathbb{C}_r : (\mathbb{I} + \mathbb{P}_{r,SC} : (\mathbb{C}_r - \mathbb{C}_{SC}))^{-1} : \left[\sum_{i=1}^{N} f_i (\mathbb{I} + \mathbb{P}_{i,SC} : (\mathbb{C}_i - \mathbb{C}_{SC}))^{-1} \right]^{-1} \tag{9.19}$$

Before studying the upscaling of creep modulus, we restrict ourselves to the case of a material that is isotropic at macroscale:

$$\mathbb{C}_{hom} = 3K_{hom}\mathbb{J} + 2G_{hom}\mathbb{K} \tag{9.20}$$

where $\mathbb{J} = 1/3\boldsymbol{I} \otimes \boldsymbol{I}$, $\mathbb{K} = \mathbb{I} - \mathbb{J}$ with $\boldsymbol{I}$ being the two-order unit tensor; K_{hom} and G_{hom} are the bulk modulus and the shear modulus of the macroscopic material, respectively. The material is made of N phases and each phase is isotropic:

$$\mathbb{C}_r = 3K_r\mathbb{J} + 2G_r\mathbb{K} \tag{9.21}$$

where K_r and G_r are the bulk modulus and the shear modulus of phase r. We recall that for ellipsoidal inclusions, the Eshelby's tensor for phase r (see Eq. 9.11) is only a function of the geometry of phase r and the Poisson's ratio ν of the embedding medium. Combining Eq. 9.18, Eq. 9.20 and Eq. 9.21, the Mori-Tanaka estimates K_{MT} and G_{MT} of the macroscopic bulk modulus K_{hom} and shear modulus G_{hom} can be written as:

$$\begin{aligned}
&3K_{MT}\mathbb{J} + 2G_{MT}\mathbb{K} \\
&= \sum_{r=1}^{N} f_r(3K_r\mathbb{J} + 2G_r\mathbb{K}) : \left[\mathbb{I} + \mathbb{S}(\nu_1) : (\frac{K_r - K_1}{K_1}\mathbb{J} + \frac{G_r - G_1}{G_1}\mathbb{K})\right]^{-1} : \\
&\left[\sum_{i=1}^{N} f_i(\mathbb{I} + \mathbb{S}(\nu_1) : (\frac{K_i - K_1}{K_1}\mathbb{J} + \frac{G_i - G_1}{G_1}\mathbb{K}))^{-1}\right]^{-1}
\end{aligned} \tag{9.22}$$

Similarly, under the same hypothesis, combining Eq. 9.19, Eq. 9.20 and Eq. 9.21 yields the following expression for the self-consistent estimates of K_{SC} and G_{SC} of the bulk modulus K_{hom} and shear modulus G_{hom} at macroscale:

$$\begin{aligned}
&3K_{SC}\mathbb{J} + 2G_{SC}\mathbb{K} \\
&= \sum_{r=1}^{N} f_r(3K_r\mathbb{J} + 2G_r\mathbb{K}) : \left[\mathbb{I} + \mathbb{S}(\nu_{SC}) : (\frac{K_r - K_{SC}}{K_{SC}}\mathbb{J} + \frac{G_r - G_{SC}}{G_{SC}}\mathbb{K})\right]^{-1} : \\
&\left[\sum_{i=1}^{N} f_i(\mathbb{I} + \mathbb{S}(\nu_{SC}) : (\frac{K_i - K_{SC}}{K_{SC}}\mathbb{J} + \frac{G_i - G_{SC}}{G_{SC}}\mathbb{K}))^{-1}\right]^{-1}
\end{aligned} \tag{9.23}$$

From Eq. 9.22 and Eq. 9.23, we readily observe that, for both the Mori-Tanaka scheme and the self-consistent scheme, the homogenized bulk modulus and the homogenized shear modulus are homogeneous functions of the bulk moduli and the shear moduli of the phases:

$$nK_{hom} = nK_{hom}(\overbrace{K_1, \cdots, K_N}^{N}, \overbrace{G_1, \cdots, G_N}^{N}) = K_{hom}(\overbrace{nK_1, \cdots nK_N}^{N}, \overbrace{nG_1, \cdots, nG_N}^{N}) \tag{9.24}$$

$$nG_{hom} = nG_{hom}(\overbrace{K_1, \cdots, K_N}^{N}, \overbrace{G_1, \cdots G_N}^{N}) = G_{hom}(\overbrace{nK_1, \cdots nK_N}^{N}, \overbrace{nG_1, \cdots, nG_N}^{N}) \tag{9.25}$$

The homogeneity of the two equations above will be used in the following derivation on the upscaling of creep properties.

9.2 Upscaling of contact creep modulus

This section is dedicated to presenting the method for upscaling contact creep modulus C_i, based on linear homogenization theory, from the knowledge of the creep properties of each phase.

In the following derivation, we prove that if a N-phase material satisfies:

- the material itself is isotropic and each phase of which the material is composed is isotropic material is ellipsoidal, so that Eq. 9.24 and Eq. 9.25 hold;
- the contact creep function is expressed as Eq. 9.26;
- every phase creeps with a time-independent Poisson's ratio;

the following conclusions can be consequently drawn:

- the homogenized material creeps logarithmically respect to time after a transient period;
- the contact creep modulus of the material can be estimated from the contact creep modulus (and the volume fraction, the geometry parameters) of each phase;
- if one applies either the Mori-Tanaka scheme or self-consistent scheme, the function that links the homogenized creep moduli of the material to the creep moduli of each phase of the material is the same function as the one links the elastic moduli of the material with the elastic moduli of each phase of the material (see Eq. 9.46, Eq. 9.52 and Eq. 9.55).

We consider a material made of N phases, and for each phase r, we observe a contact creep function which is logarithmic with respect to time for large times:

$$L_r(t) = \frac{1}{C_{i,r}} \ln\left(\frac{t}{\tau_r} + 1\right) + \frac{1}{M_{0,r}} \tag{9.26}$$

where $C_{i,r}$, τ_r and $M_{0,r}$ are the contact creep modulus, the indentation characteristic time and the indentation modulus at moment of loading of phase r, respectively; The rate $\dot{L}_r(t)$ of contact creep compliance can thus be written as:

$$\dot{L}_r(t) = \frac{1}{C_{i,r}(t + \tau_r)} \tag{9.27}$$

One can notice that the above function satisfies:

$$\lim_{t\to\infty} t\dot{L}_r(t) = \frac{1}{C_{i,r}} \tag{9.28}$$

With the help of the final value theorem and of classical properties of the Laplace transform [Nixon, 1965], the above equation can be written as [Vandamme and Ulm, 2013]:

$$\begin{aligned} C_{i,r} &= \lim_{t\to\infty} t\dot{L}_r = \lim_{s\to 0} s\mathcal{L}(t\dot{L}_r) \\ &= \lim_{s\to 0} -s\frac{d}{ds}\mathcal{L}(\dot{L}_r) = \lim_{s\to 0} -s\frac{d}{ds}\mathcal{L}(L_r - L_r(0)) \\ &= \lim_{s\to 0} -s\frac{d}{ds}(s\mathcal{L}(L_r)) \end{aligned} \tag{9.29}$$

We recall that $\mathcal{L}(f(t))$ is the Laplace transform of the function $f(t)$ and s is the Laplace parameter (see Eq. 3.18). Therefore, from the equation above, $d(s\mathcal{L}(L_r))/ds$ can be approximated by $-1/C_{i,r}s$ for small s, from which follows that $\mathcal{L}(L_r)$ can be approximated by $-\ln s/C_{i,r}s$ for small s [Vandamme and Ulm, 2013]:

$$\mathcal{L}(L_r) \approx -\ln s/C_{i,r}s \text{ for small } s \tag{9.30}$$

For the derivation below, we suppose that the Poisson's ratio is time-invariant: $\nu_r(t) = \nu_{0,r}$. Thus after applying Laplace transform, one obtains:

$$\mathcal{L}(\nu_r(t)) = \nu_{0,r}/s \tag{9.31}$$

Combining Eq. 3.5 with the relations between elastic moduli for an isotropic material, one has:

$$M_r = \frac{2G_r}{1-\nu_r} \tag{9.32}$$

Applying s-multiplied Laplace transform to the above equation, one obtains:

$$s\mathcal{L}(M_r(t)) = \frac{2s\mathcal{L}(G(t))}{1-s\mathcal{L}(\nu_r(t))} \tag{9.33}$$

where $M_r(t)$, $G_r(t)$ are the relaxation indentation modulus and the relaxation shear modulus of phase r. Combining Eq. 9.32 and Eq. 9.33, one obtains:

$$\mathcal{L}(G_r(t)) = \frac{2}{1-\nu_{0,r}}\mathcal{L}(M_r(t)) \tag{9.34}$$

Combining the above equation with equation 3.24 yields:

$$\mathcal{L}(J_{d,r}(t)) = \frac{2}{1-\nu_{0,r}}\mathcal{L}(L_r(t)) \tag{9.35}$$

where $J_{d,r}(t)$ is the deviatoric creep compliance of phase r (see Eq. 3.20). Applying an inverse Laplace transform to the above equation, one obtains in time domain:

$$J_{d,r}(t) = \frac{2}{1-\nu_{0,r}}L_r(t) \tag{9.36}$$

Combining the above equation with Eq. 9.26 yields:

$$\begin{aligned} J_{d,r}(t) &= \frac{2}{1-\nu_{0,r}}\left[\frac{1}{M_{0,r}} + \frac{1}{C_{i,r}}\ln\left(\frac{t}{\tau_r}+1\right)\right] \\ &= \frac{1}{G_{0,r}} + \frac{1}{C_{d,r}}\ln\left(\frac{t}{\tau_r}+1\right) \end{aligned} \tag{9.37}$$

where $G_{0,r} = \frac{1-\nu_{0,r}}{2}M_{0,r}$ is the shear modulus of phase r at moment of loading and $C_{d,r}$ is termed as the deviatoric creep modulus of the phase r. According to Eq. 9.37, it satisfies:

$$C_{d,r} = \frac{1-\nu_{0,r}}{2}C_{i,r} \tag{9.38}$$

Likewise, one can obtain:

$$\begin{aligned} J_{v,r}(t) &= \frac{1-\nu_{0,r}^2}{3(1-2\nu_{0,r})}\left[\frac{1}{M_{0,r}} + \frac{1}{C_{i,r}}\ln\left(\frac{t}{\tau_r}+1\right)\right] \\ &= \frac{1}{K_{0,r}} + \frac{1}{C_{v,r}}\ln\left(\frac{t}{\tau_r}+1\right) \end{aligned} \tag{9.39}$$

where $J_{v,r}(t)$ is the volumetric creep compliance of phase r and $K_{0,r} = \frac{1-\nu_{0,r}^2}{3(1-2\nu_{0,r})}M_{0,r}$ is the bulk modulus of phase r at moment of loading. The parameter $C_{v,r}$ in Eq. 9.38 is termed as the volumetric creep modulus and according to Eq. 9.38, it satisfies:

$$C_{v,r} = \frac{1-\nu_{0,r}^2}{3(1-2\nu_{0,r})}C_{i,r} \tag{9.40}$$

Combining Eq. 9.38 and Eq. 9.40 yields:

$$C_{i,r} = 4C_{d,r}\frac{3C_{v,r}+C_{d,r}}{3C_{v,r}+4C_{d,r}} \tag{9.41}$$

The above derivation also shows that, if the contact creep function is logarithmic with respect to time for large time, and if the Poisson's ratio is time-independent, the volumetric creep compliance $J_{v,r}$ and the deviatoric creep compliance $J_{d,r}$ are also logarithmic with respect to time at large time:

$$\lim_{t\to\infty} t\dot{J}_{v,r} = \frac{1}{C_{v,r}} \text{ and } \lim_{t\to\infty} t\dot{J}_{d,r} = \frac{1}{C_{d,r}} \tag{9.42}$$

and the creep moduli satisfy the relation presented in Eq. 9.41. Similarly to Eq. 9.30, one can obtain:

$$\mathcal{L}(J_{v,r}) \approx -\frac{\ln s}{sC_{v,r}} \text{ and } \mathcal{L}(J_{d,r}) \approx -\frac{\ln s}{sC_{d,r}} \text{ for small } s \tag{9.43}$$

Applying an s-multiplied Laplace transform to Eq. 9.24, one obtains:

$$s\mathcal{L}(K_{hom}(t)) = K_{hom}(s\mathcal{L}(K_1(t)),\ldots,s\mathcal{L}s(K_N(t)),s\mathcal{L}(G_1(t)),\ldots,s\mathcal{L}(G_N(t))) \tag{9.44}$$

Combining the above equation with Eq. 3.23 yields:

$$\begin{aligned}\frac{1}{s\mathcal{L}(J_{v,hom})} =& K_{hom}(\frac{1}{s\mathcal{L}(J_{v,1})},\dots,\frac{1}{s\mathcal{L}(J_{v,N})},\frac{1}{s\mathcal{L}(J_{d,1})},\dots,\frac{1}{s\mathcal{L}(J_{d,N})})\\ =& K_{hom}(\frac{C_{v,1}}{-\ln(s)},\dots,\frac{C_{v,1}}{-\ln(s)},\frac{C_{d,1}}{-\ln(s)},\dots,\frac{C_{v,N}}{-\ln(s)})\\ =& \frac{1}{-\ln(s)}K_{hom}(C_{v,1},\dots,C_{v,N},C_{d,1},\dots,C_{v,N})\end{aligned} \tag{9.45}$$

Let:

$$C_{v,hom} = K_{hom}(C_{v,1},\dots,C_{v,N},C_{d,1},\dots,C_{d,N}) \tag{9.46}$$

so that Eq. 9.45 can be readily written as:

$$s\mathcal{L}(J_{v,hom}) = \frac{-\ln(s)}{C_{v,hom}} \tag{9.47}$$

Consequently, one has:

$$\begin{aligned}\lim_{s\to 0} s\mathcal{L}(tJ_{v,hom}) &= \lim_{s\to 0} -s\frac{d}{ds}\mathcal{L}(\dot{J}_{v,hom}) = \lim_{s\to 0} -s\frac{d}{ds}(s\mathcal{L}(J_{v,hom}) - J_{v,hom}(0))\\ &= \lim_{s\to 0} -s\frac{d}{ds}(s\mathcal{L}(J_{v,hom})) = \lim_{s\to 0} -s\frac{d}{ds}(\frac{\ln(s)}{C_{v,hom}})\\ &= \frac{1}{C_{v,hom}}\end{aligned} \tag{9.48}$$

From the above equation, applying the final value theorem [Nixon, 1965], one can conclude that:

$$\lim_{t\to\infty} t\dot{J}_{v,hom} = \frac{1}{C_{v,hom}} \tag{9.49}$$

which proves that for large times the rate $\dot{J}_{v,hom}$ of the volumetric creep compliance $J_{v,hom}$ of the N-phase material is given by:

$$J_{v,hom} \approx \frac{1}{C_{v,hom}t} \text{ for large time} \tag{9.50}$$

and therefore after a transient period the volumetric creep function of N-phase material is logarithmic with respect to time. The parameter $C_{v,hom}$ can be ob-

tained from Eq. 9.46 as a function of the deviatoric creep moduli and volumetric creep moduli of all phases. Likewise, one can prove:

$$\dot{J}_{d,hom} \approx \frac{1}{C_{d,hom}t} \text{ for large time} \tag{9.51}$$

where the parameter $C_{d,hom}$ can be obtained by:

$$C_{d,hom} = G_{hom}(C_{v,1}, \ldots, C_{v,N}, C_{d,1}, \ldots, C_{d,N}) \tag{9.52}$$

where G_{hom} is the function that links the homogenized shear modulus of the N-phase material to the elastic moduli of each of its phase (see Eq. 9.25).

So far, we proved the deviatoric creep function $J_{d,hom}$ and the volumetric creep function $J_{v,hom}$ of the N-phase material are logarithmic with respect to time for large time if the contact creep function of each phase is logarithmic with respect to time at large time and the Poisson's ratio of each phase is time-invariant. The material is isotropic, so the following expression holds:

$$M_{hom} = 4G_{hom}\frac{3K_{hom} + G_{hom}}{3K_{hom} + 4G_{hom}} \tag{9.53}$$

Performing an s-multiply Laplace transform to the above equation and combining with Eq. 3.24 and Eq. 3.23 enable to get the expression of the contact creep compliance L_{hom} of the N-phase material for small values of the Laplace parameter:

$$L_{hom} \approx -\frac{\ln(s)}{sC_{i,hom}} \text{ for small } s \tag{9.54}$$

The parameter $C_{i,hom}$ in the above equation is the contact creep modulus of the N-phase material, which is given by:

$$C_{i,hom} = 4C_{d,hom}\frac{3C_{v,hom} + C_{d,hom}}{3C_{v,hom} + 4C_{d,hom}} \tag{9.55}$$

where $C_{v,hom}$ and $C_{d,hom}$ are given by Eq. 9.46 and by Eq. 9.52, respectively. Similarly to the derivation expressed in Eq. 9.29, one can find that after a transient period, the contact creep compliance of the N-phase material is logarithmic at

large time:

$$\lim_{t\to\infty} t\dot{L}_{hom} = \frac{1}{C_{i,hom}} \tag{9.56}$$

The rate of contact creep compliance is controlled by $C_{i,hom}$, which can be found as a function of $C_{v,hom}$ and $C_{d,hom}$. Therefore, the derivation above shows that at macroscale, the contact creep compliance of the material is logarithmic with respect to time, if the contact creep function of each phase of the material is logarithmic to time in large time and the Poisson's ratio of each phase is time-invariant. If one applies either the Mori-Tanaka scheme or self-consistent scheme, the function that links the homogenized creep moduli of the material to the creep moduli of each phase of the material is the same function as the one links the elastic moduli of the material with the elastic moduli of each phase of the material (see Eq. 9.46, Eq. 9.52 and Eq. 9.55)

9.3 A two-step homogenization model for C_3S paste or C_2S paste

In this section, we will apply the homogenization approach presented in section 9.2 to predict the contact creep modulus C_i of C_2S paste or C_3S paste with the knowledge of the creep properties of each phase in those materials. Information on the microstructure of those pastes will be used to set up the model. The input parameter of the proposed model will be calibrated with experimental results obtained in chapter 6 and chapter 8.

9.3.1 Description of model

As already mentioned in chapter 6, four distinct phases can be identified in a C_3S paste or in a C_2S paste: the porosity, the C-S-H phase, the CH phase and unhydrated clinker, i.e., unhydrated C_2S in C_2S paste or unhydrated C_3S in C_3S paste. As already stated in section 6.2.3, we recall that, by applying $C_{1.7}$-S-H_4 and a density of 2.06g/m^3 for C-S-H, the C-S-H phase actually includes solid C-S-H and water in gel pores and consequently the porosity represents mainly the pores excluding those included in C-S-H phase.

The concept of the model is inspired from that of Pichler and Hellmich

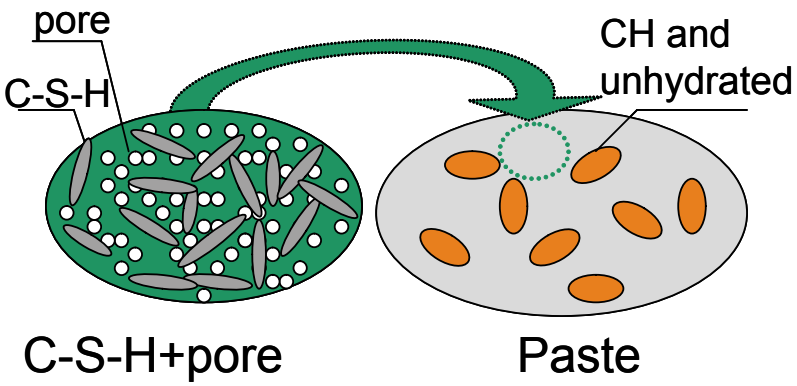

Figure 9.1: Schematic presentation of two-step homogenization model for C_3S and C_2S paste.

[2011]. In the model proposed by Pichler and Hellmich [2011], the hydrate products formed by the hydration of cement clinker were first homogenized by self-consistent scheme with the porosity, then a second homogenization was done by considering the mixture of hydration products and porosity as a matrix in which the unhydrated clinker grains are embedded as inclusions.

In our model, we homogenize only the C-S-H phase with the porosity in the first step. The homogenization yields a 'foam' that consists of C-S-H and porosity. In the second step, we homogenize the remaining phases such as CH and unhydrated phase with the foam obtained in the first homogenization step by considering the other phases are inclusions immersed in the foam. Schematic representation of the model is presented in Fig. 9.1. The major difference between our approach and the model of Pichler and Hellmich [2011] is that, in the first step, instead of homogenizing all the products of hydration with the pores, we homogenize only C-S-H with the porosity. We made this choice based on the features of the microstructure. Observations on the microstructure of C_3S and C_2S pastes by scanning electron microscopy (SEM), with phases identified by energy dispersive X-ray spectrometry guided the way to separate different phases. As one may readily see from Fig. 9.2, for both hydrated C_3S and C_2S pastes:

- The characteristic sizes of C-S-H and pores are much smaller than that of CH. This observation supports the idea of a two-step homogenization

procedure.

- The size of pores in C_3S and C_2S paste is variable and thus can be larger or smaller than the characteristic size of C-S-H. As one can see clearly from the figure, there exists large pores, the size of which is much larger than that of C-S-H. However, C-S-H and pores are well mixed with each other, especially in the C_2S paste: C-S-H and pores can thus be considered to be at the same scale, as two well-intermixed phases, justifying the use of a self-consistent scheme.

- Evidently from the figure, the CH phase can be regarded as inclusions immersed in a 'foam' formed by C-S-H and pores.

In Fig. 9.2, one can hardly observe unhydrated clinker. This is probably due to the small quantity of unhydrated clinker present in well hydrated C_3S paste and C_2S paste. However, logically, the unreacted grains of C_2S or C_3S should be embedded in hydrated products. Thus, similarly as for CH phase, we consider the unhydrated clinker as inclusions immersed in a matrix of 'foam' formed by C-S-H and pores.

The following hypotheses on the creep properties are applied in the model:

- The creep properties of the C-S-H phase in C_3S paste and C_2S paste are the same. C-S-H is considered to creep logarithmically with respect to time in the long term.

- In this section, we consider that the CH phase and the unhydrated clinker exhibit no creep.

- On the time evolution of Poisson's ratio $\nu(t)$ of cementitious material during creep: some believe that Poisson's ratio stays constant during creep and is equal to the initial Poisson's ratio ν_0 at the moment of loading [Bažant and L'Hermite, 1988; Bažant and Xi, 1995], i.e., $\nu(t) = \nu_0$; while others believe that the long-term creep of cement is only deviatoric [Bernard et al., 2003], i.e., the Poisson's ratio $\nu(t)$=0.5 at large time. In this section and also the next section, we consider that the Poisson's ratio of each phase is time-independent.

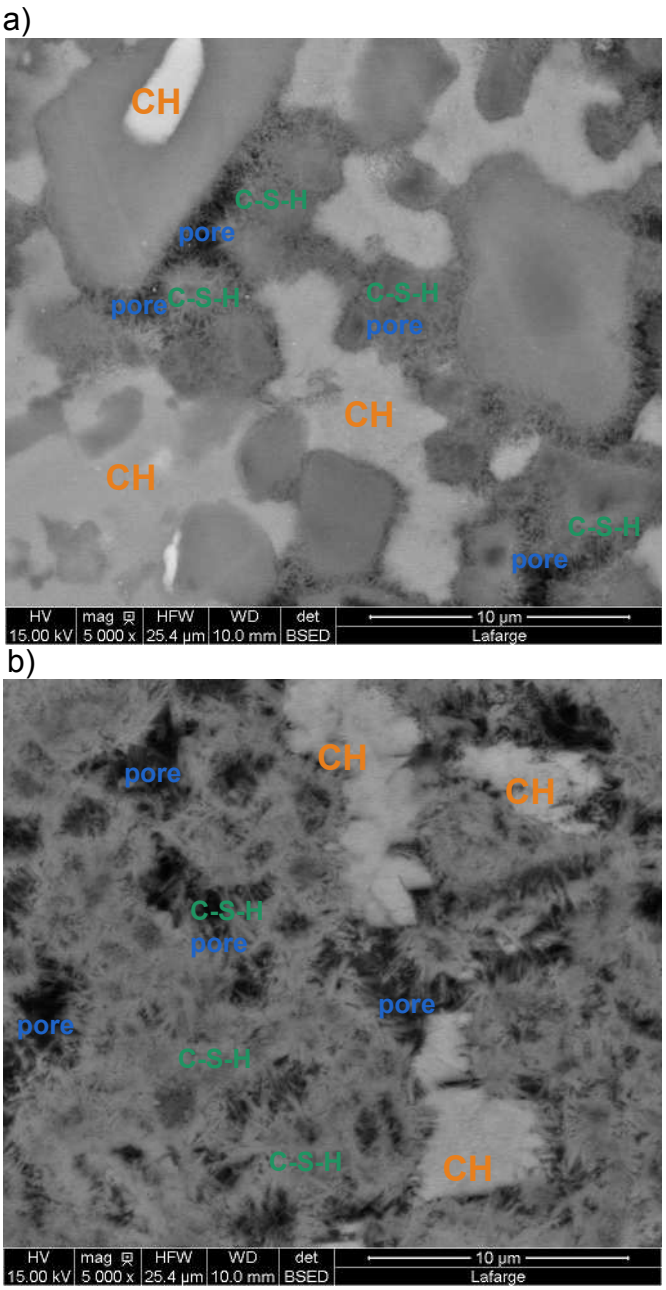

Figure 9.2: SEM observation of a) hydrated C_3S paste with w/c=0.42, imaged at the age of 90 days b) hydrated C_2S paste, with w/c=0.42, imaged at the age of 1 year. CH and C-S-H were identified by X-ray spectrometry. The features were taken and analyzed by C.Bouillon from Lafarge Research Center.

9.3.2 Determination of input parameters

We use our experimental results on C_3S and C_2S pastes presented in chapter 6 to calibrate some of the input parameters of the model. In total 15 pastes (either C_3S pastes or C_2S pastes) with known volume fractions (see Tab. 6.6) and contact creep modulus C_i (see Tab. 6.7) are considered.

To predict the contact creep modulus C_i of a paste, based on the proposed model, one needs the following information for each phase: its volume fraction, its geometry and its contact creep modulus $C_{i,r}$. A summary of input parameters is presented in Tab. 9.2 and they were determined in the following way:

- The volume fraction of each phase was obtained experimentally.
- The geometry of each phase was set as spheroidal, so that the geometry of each phase could be characterized by only one parameter, i.e., the aspect ratio, defined as the ratio of the polar to equatorial lengths of a spheroid. For CH, we set the aspect ratio as 0.25 which yielded an oblate shape (see in Fig. 6.1). In micromechanical modeling of cement paste, the unhydrated grain of clinker is often consider as spherical, i.e., with a aspect ratio equal to 1. Therefore, we set the aspect ratio of unhydrated C_2S or C_3S as 1. As C-S-H phase was homogenized with the porosity, the aspect ratio of C-S-H should be large enough to manage the percolation of the mixture. We set the aspect ratio of the C-S-H phase as 6.0, which is the smallest value that gives non-zero mechanical property for samples with high volume fraction of pore phase.
- As stated before, we consider the Poisson's ratio of each phase is time invariant. The Poisson's ratio of each phase was set to: 0.24 for C-S-H [Constantinides and Ulm, 2004], 0.32 for CH [Monteiro and Chang, 1995], 0.30 for the unhydrated phase [Roland and Van Damme, 2004]. The CH and unhydrated clinker were considered to exhibit no creep, so their contact creep moduli were infinite. The pore phase was considered to creep infinitely fast, thus the contact creep modulus was set to 0. The contact creep modulus of the C-S-H phase was unknown: we obtained it by fitting to the contact creep moduli C_i of C_2S and C_3S pastes measured experimentally.

phase	**C-S-H**	**CH**	**unhydrated**	**pore**
E, GPa	23.8	42.3	135	0
C_i, GPa	57.4	∞	∞	0
ν	0.24	0.32	0.3	0.3
aspect ratio	6.0	0.25	1.0	1.0

Table 9.2: Young's modulus E, contact creep modulus C_i, Poisson's ratio ν and aspect ratio of all phases used in the model. The parameters in blue are calibrated parameters.

- The Young's modulus of each phase is also given in Tab. 9.2, which were used as input parameters to test the proposed model for the estimation of Young's modulus. The major concern on the value of Young's modulus of phases presented in literature is that they were obtained in various hygral conditions. But this is no longer an important issue as we showed in chapter 8 that the relative humidity has little influence on the elastic properties of C_3S paste. We set the Young's modulus of C-S-H phase to 23.8 GPa [Constantinides and Ulm, 2004] and that of CH phase to 42.3GPa [Kamali, 2003]. The Young's modulus of C_2S and of C_3S are quite close from each other, varying from 130GPa to 140GPa according to Acker et al. [2001] and Velez et al. [2001]. Here, we took an unique value of 135GPa for the two phases.

9.3.3 Results of calibration

We display in Fig. 9.3 the contact creep moduli C_i obtained experimentally and those predicted by the model in function of porosity (not including the porosity in C-S-H). This figure shows that the evolution of C_i in function of porosity is well captured by the proposed model. Furthermore, the values obtained with the model are very close to those obtained experimentally, with a coefficient of variation R^2=0.923.

We applied the model to estimate the Young's modulus of C_3S and C_2S pastes, with the same input parameters, i.e., the same aspect ratio and the same Poisson's ratio as those used to estimate the contact creep modulus. As presented in Fig. 9.4, the Young's modulus predicted by the two-step model are in good agreement with the experimental results (R^2=0.806). This result is quite satisfactory as

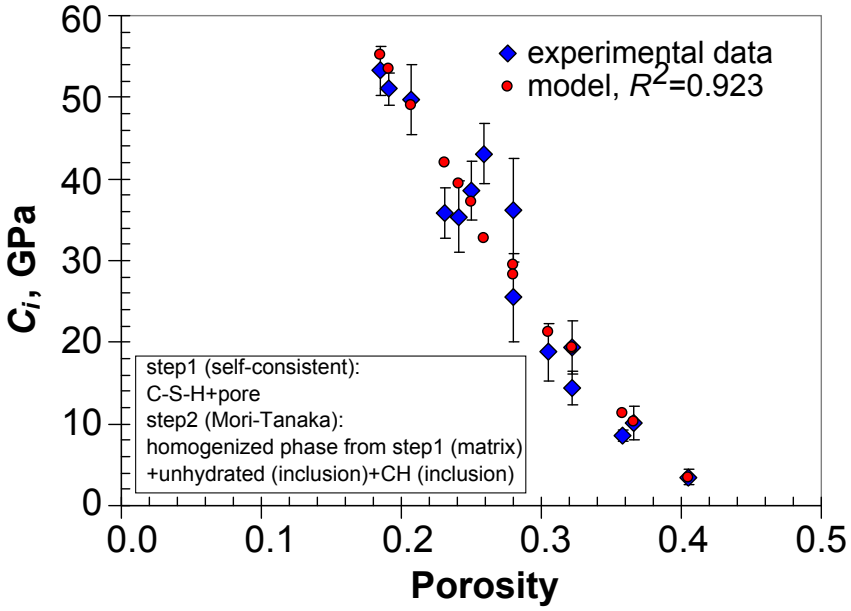

Figure 9.3: Contact creep modulus C_i of C_3S and C_2S pastes obtained from experimental measurement and from the two-step homogenization model.

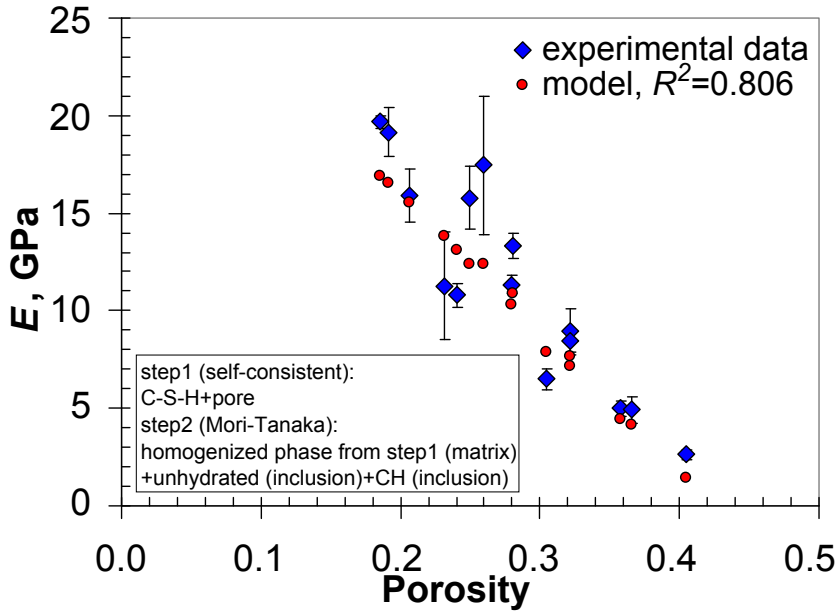

Figure 9.4: Young's modulus E of C_3S and C_2S pastes obtained from microindentation experiment and predicted with the two-step homogenization model.

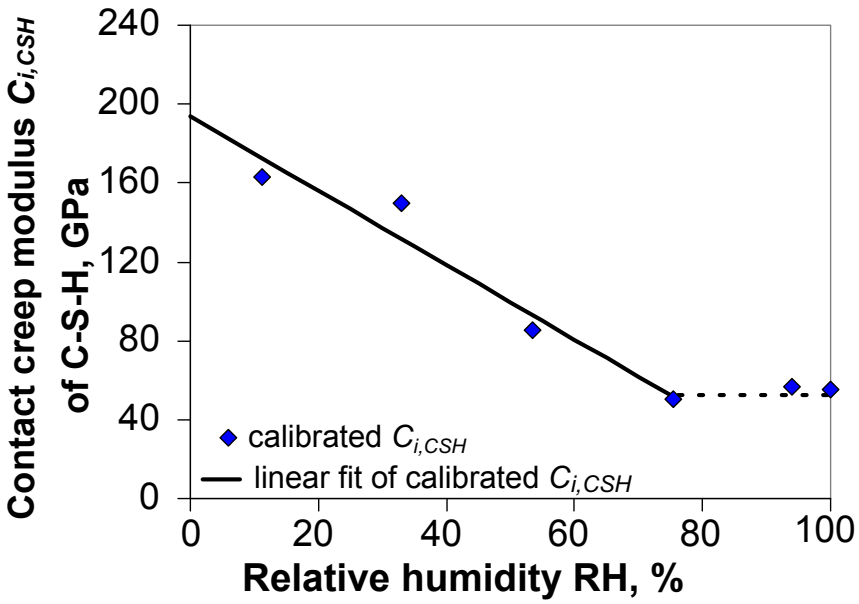

Figure 9.5: Contact creep modulus $C_{i,CSH}$ of C-S-H calibrated by applying the two-step homogenization model presented in section 9.3 and linear fit of the calibrated $C_{i,CSH}$ at relative humidities between 11% and 75%.

all the elastic properties, i.e., the Young's modulus and Poisson's ratio are from literature: none of them were calibrated on the experimental data.

9.3.4 Integrating effect of relative humidity on creep in the model

This section is dedicated to integrating the effect of relative humidity on the contact creep modulus in the model. In chapter 8, we presented how the contact creep modulus of C_3S paste, compact of C-S-H and CH measured by microindentation varied with relative humidity. We showed that the relative humidity has a significant effect on the long-term basic creep of C_3S paste: for hydrated C_3S paste in equilibrium with relative humidities of 11%, 33% 54% and 75%, their contact creep modulus was found to decrease with an increasing relative humidity (see in Fig. 8.4). To integrate this effect of relative humidity in the proposed model for pastes, we assume that the evolution of the contact creep

modulus of C_3S and C_2S pastes with respect to the relative humidity are due to the evolution of creep modulus of the C-S-H phase. By applying the two-step homogenization model presented in section 9.3, with the same input parameter settings presented in Tab. 9.2, we calibrated the contact creep modulus $C_{i,CSH}$ of C-S-H phase with experimental results. The contact creep moduli of phases other than C-S-H were kept constant with respect to relative humidity and only the contact creep modulus of C-S-H varied with the relative humidity. The results of the calibration is displayed in Fig. 9.5. We applied a linear fit for $C_{i,CSH}$ for samples at relatives humidities of 11%, 33% 54% and 75%. At relative humidities above 75% we consider that the contact creep modulus $C_{i,CSH}$ is constant: $C_{i,CSH} = C_{i,CSH}(\text{RH} = 75\%)$ for RH$\geq$75%. Therefore, in the whole range of relative humidity, the contact creep modulus of C-S-H phase can be given by the following equation:

$$\frac{C_{i,CSH}(\text{RH})}{C_{i,CSH}(0)} = \begin{cases} 1 - 0.97 \times \text{RH} & \text{if RH}\leq 75\% \\ 0.27 & \text{if RH}>75\% \end{cases} \tag{9.57}$$

where $C_{i,CSH}(0)$=194GPa is the contact creep modulus of C-S-H phase in conditions obtained from the linear fit presented in Fig. 9.5. With the above equation as well as the distribution of phases, one can predict the contact creep modulus C_i of the paste in equilibrium in a given relative humidity.

9.3.5 Example

We present below an example of using the proposed two-step homogenization model to predict the contact creep modulus of a C_3S paste with $w/c = 0.42$.

As already mentioned in section 6.2.3, the phase distribution in a C_2S paste or a C_3S paste can be obtained with the degree of hydration α. Applying the method indicated in section 6.2.3, one can generate the phase distribution of this paste with given hydration degrees. Then, apply Eq. 9.57 to get the contact creep modulus of the C-S-H phase in given relative humidities. Finally, with the contact creep modulus of C-S-H phase and the other input parameters presented in Tab. 9.2, run the proposed two-step homogenization model: firstly homogenize the C-S-H phase with the porosity by applying a self-consistent scheme, then homogenize the mixture of C-S-H phase and porosity as a matrix with CH and

unhydrated clinker as inclusions by applying Mori-Tanaka scheme.

As presented in Fig. 9.6, the contact creep moduli of a C_3S paste (w/c=0.42, α=0.4 to 1.0, at relative humidities RH=25%, 50%, 75%) is predicted by the model.

9.4 A two-step homogenization model for compacts of mixtures

This section is dedicated to presenting a micromechanical model for compacts of C-S-H, CH and of their mixtures. Similar to what was presented in section 9.3, information on the microstructure of those compacts will be used to set up the model. The input parameter of the proposed model will be calibrated with experimental results obtained in chapter 7 and chapter 8.

9.4.1 Description of model

In our study, we considered two types of compacts: two-phase compacts, i.e., compact of pure C-S-H or pure CH, with a single solid phase and the porosity; three-phase compacts, i.e., compacts of mixtures of C-S-H and CH with two solid phases and porosity. Observations by SEM were performed on compact of CH, C-S-H (see Fig. 9.7) and on compacts of mixture of C-S-H and CH (see Fig. 9.8).

For compacts made with pure C-S-H or pure CH, as presented in Fig 9.7, CH or C-S-H is mixed with the pores. We apply a simple one step micromechanical model for those compacts. Both the self-consistent scheme and Mori-Tanaka scheme should give similar results [Christensen, 1990], as the porosity of compacts is around 22%, which is quite low.

From Fig. 9.8, the following information was obtained:

- Grains of C-S-H could be as large as tens of microns.
- Crystals of portlandite were with a typical size of a micron or less.
- Pores could be found not only around the grains of C-S-H, but also in-between the crystals of portlandite.

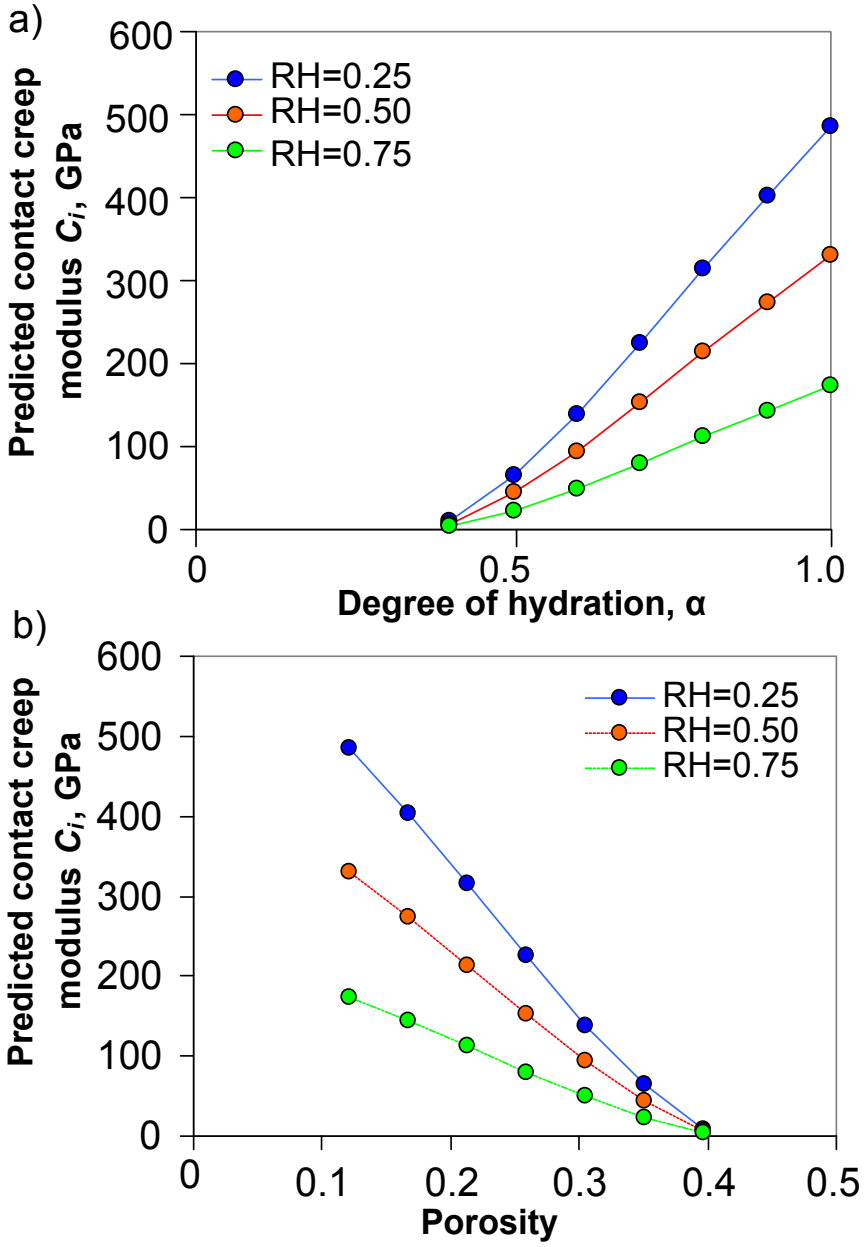

Figure 9.6: Contact creep moduli of C_3S paste (w/c=0.42) at relative humidities of 25%, 50% and 75% predicted by the model in function of a) degree of hydration α and b) porosity (without pores in the C-S-H phase).

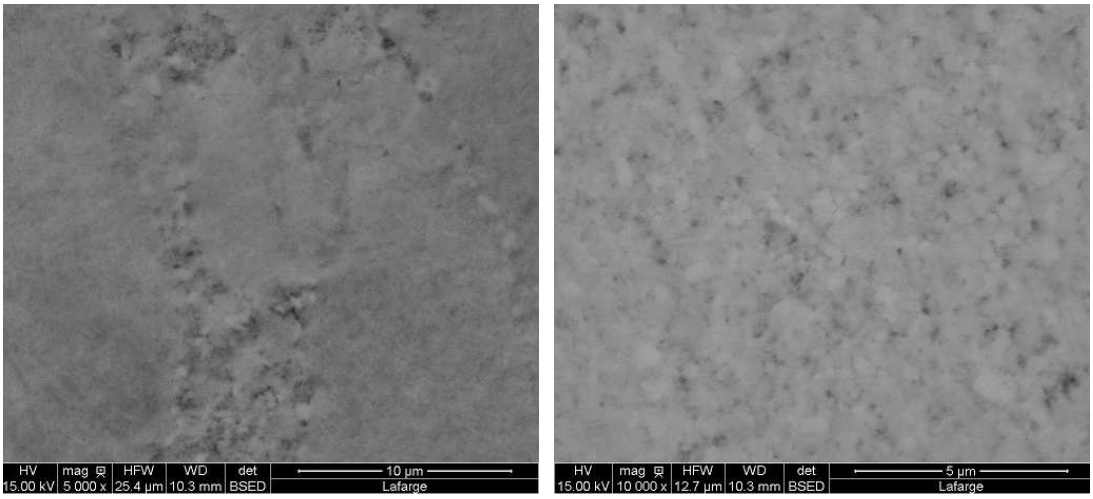

a) compact of C-S-H b) compact of CH

Figure 9.7: SEM observation of a) compact of C-S-H b) compact of CH. The features were taken and analyzed by C. Bouillon from Lafarge Research Center.

- The size of the pores was comparable to the size of portlandite crystals. Both those sizes were much smaller than the size of C-S-H grains.

Based on the observations, we concluded that CH and pores should be located at one scale and C-S-H grains at a larger scale. Such information on the microstructure of compacts of mixtures gives us some clue to use a two-step homogenization model: with CH and pore at a smaller scale and C-S-H at a larger one in the other scale. In our study, the volume fraction of C-S-H and CH varies enormously. Therefore, we apply a self-consistent scheme in both scales in order to avoid wondering what phase plays the matrix and what phase plays the inclusion in function of the volume fraction of solid phases.

To summarize, as presented in Fig. 9.9, we propose a two-step homogenization model for the compacts of mixtures of C-S-H and CH:

- In a first step, we homogenize CH with porosity.
- In a second step, we homogenize C-S-H with the mixture of CH and porosity that was obtained in the first step of homogenization.
- For the two steps of homogenization, we apply a self-consistent scheme. One can thus notice that the compact of C-S-H or CH is just a special case

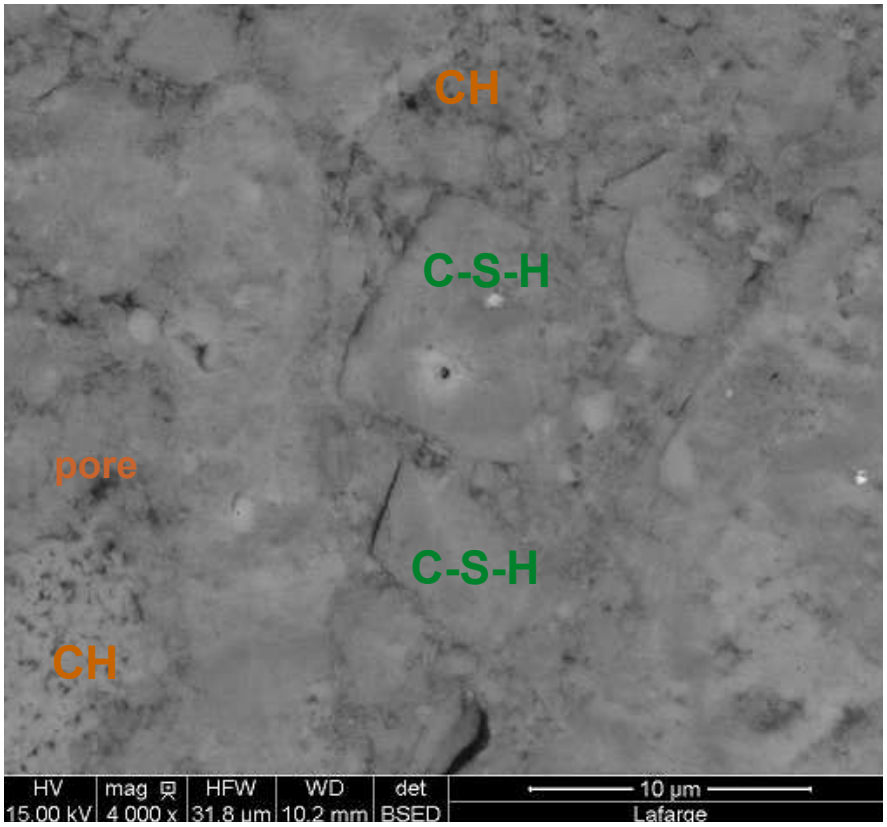

Figure 9.8: SEM observation of compact of mixture Cpt-M3, with (in volume) 52% of C-S-H, 26% of CH and 22% of porosity. The features were taken and analyzed by C. Bouillon from Lafarge Research Center.

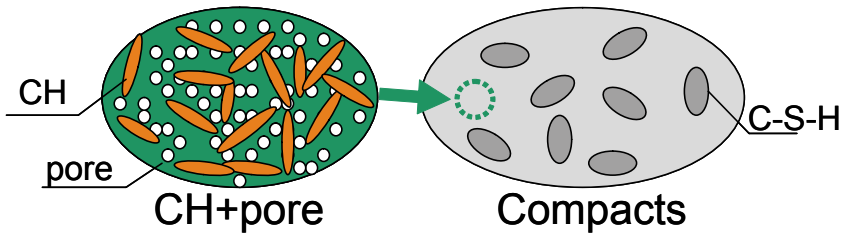

Figure 9.9: Schematic presentation of two-step homogenization model for compacts.

of the proposed two-step homogenization model, with one volume fraction of solid phases equal to 0.

The concept of the model introduced in this section is quite similar to that of the model introduced in section 9.3 for C_3S or C_2S paste. The major difference lies in the organization of phases in the two steps of homogenization.

9.4.2 Hypotheses on creep properties

The main experimental findings presented in chapter 7 and chapter 8 on compacts are recalled as follows:

- Generally, with an increasing volume fraction of CH in the solid phase, the compacts showed higher contact creep modulus, i.e., lower long-term creep. However, a contact creep modulus C_i in function of the volume fraction of CH in solid phase was found to be non-monotonic for compacts saturated with lime water: as presented in Fig. 7.10, when the compacts contained little amount of CH, this contact creep modulus C_i was smaller than that of the compact of pure C-S-H.

- CH also showed creep, especially in water-saturated conditions: as presented in Tab. 7.4, the contact creep modulus of the compact of pure CH is even lower than that of the C-S-H compact in water-saturated conditions.

- Comparing Fig. 7.10 with Fig. 7.11, an effect of water on Young's modulus, indentation hardness and contact creep modulus can be found: the greater the amount of water in those compacts was, the smaller those properties were.

Based on those experimental observations, we suppose that both C-S-H and CH creep, and the contact creep moduli of both CH and C-S-H vary with respect to relative humidity.

Similarly with the hypotheses made on pastes, we also suppose that all phases creep logarithmically with respect to time after a transient period and that the Poisson's ratio of each phase is time invariant and is equal to the initial value at moment of loading, i.e., $\nu(t) = \nu_0$.

9.4.3 Determination of input parameters of the model

In chapter 7 and chapter 8, the basic creep properties as well as the elastic properties of compacts were studied by indentation testing. Those properties of the compacts of pure C-S-H and the compact of CH at 6 relative humidities ranging from 11% to water-saturated conditions were given in Tab. 8.3. For compacts of mixtures of C-S-H and CH, as presented in Tab. 7.4, in total, 8 compacts of different mixtures of C-S-H and CH at 11% relative humidity and in water-saturated conditions were characterized by indentation. The Young's modulus and contact creep modulus of those compacts will be used to determine the input parameters of the model.

The input parameters, i.e., the volume fraction of each phase, the geometry of each phase and the mechanical properties of each phase were determined in the following ways:

- The volume fraction of each phase was obtained experimentally (see in section 7.2.3)
- The geometry of each phase was again set as spheroidal so that it could be characterized by only one parameter, i.e., the aspect ratio. We considered the same aspect ratio of 6.0 for the C-S-H phase, as was applied in the model of C_3S and C_2S pastes (see section 9.3). The aspect ratio of the porosity is set to 1. As the CH phase is homogenized with the porosity, the aspect ratio of CH governs the percolation of the mixture. We set the aspect ratio of CH to 0.07 which gave the CH phase a flat oblate shape and was small enough to assure the percolation for all the compacts. As the second step of homogenization, an extra aspect ratio was needed for mixture of CH and porosity: we set it as 1 for the mixture. One can notice that for the compact of pure C-S-H or the compact of pure CH, the aspect ratio plays little role as the porosity of those compacts is low.
- The Poisson's ratio of each phase was the same as that applied to C_3S and C_2S paste (see. Tab. 9.2).
- The contact creep modulus C_i of the porosity was set to 0. In contrast, the contact creep moduli of C-S-H and CH were not set to a given value and will be fitted on the experimental results.

- The Young's moduli E of CH and C-S-H were not set to a given parameter but were fitted on the experimental results.

On the basis of the above statements, to predict the contact creep modulus of compacts of mixtures, one needs to find out the contact creep moduli of CH and of C-S-H.

9.4.4 Results of calibration

In a first approach, we calibrated the contact creep moduli of C-S-H and CH on the results obtained on the compacts of pure C-S-H and of pure CH at various relative humidities. The contact creep modulus $C_{i,CSH}$ of C-S-H and the contact creep modulus $C_{i,CH}$ of CH calibrated by applying a self-consistent scheme are presented in Fig. 9.10. From this table one can see a significant effect of relative humidity on the contact creep modulus of both phases. Relatively, the contact creep modulus of CH is more sensitive to relative humidities than that of C-S-H. With the contact creep modulus of C-S-H and of CH calibrated on the compacts of pure phases, the contact creep modulus of compacts of mixture can be predicted with the two-step homogenization procedure presented in this section. The predicted contact creep modulus as well as that obtained experimentally are displayed in Fig. 9.11 as black crosses and orange diamonds, respectively. The figure shows that the trend of evolution of C_i with the volume fraction can be well captured. In particular, the non-monotonic evolution of C_i with the volume fraction of CH in the solid skeleton in water-saturated conditions can be captured by the proposed model.

However, the predicted contact creep moduli are quite far from the experimental results for most compacts: the contact creep moduli of compacts are highly overestimated at 11% relative humidy and are understimated in water-saturated conditions. In both conditions, the deviation increases with the volume fraction of CH in the solid skeleton. We know that, with an increasing volume fraction of CH, by homogenization approach, the influence of the CH phase on the macroscopic behaviors becomes higher, which means that the deviation observed at high volume fractions of CH estimated is mainly due to the input value of the contact creep modulus chosen for the CH phase.

Therefore, in a second approach, we calibrated the input parameters, i.e., the

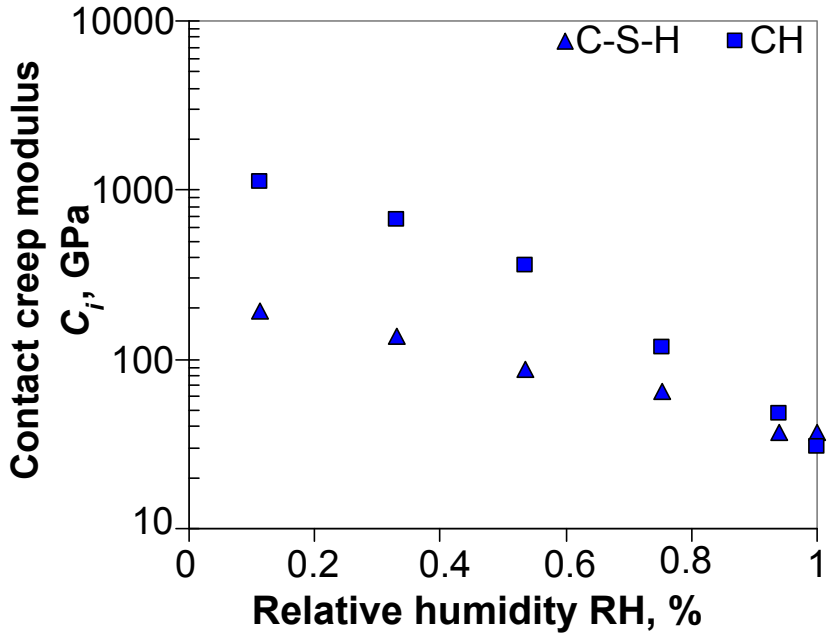

Figure 9.10: Contact creep moduli of C-S-H and CH in various relative humidities, calibrated with a self-consistent scheme on experimental result of compacts of pure C-S-H and pure CH.

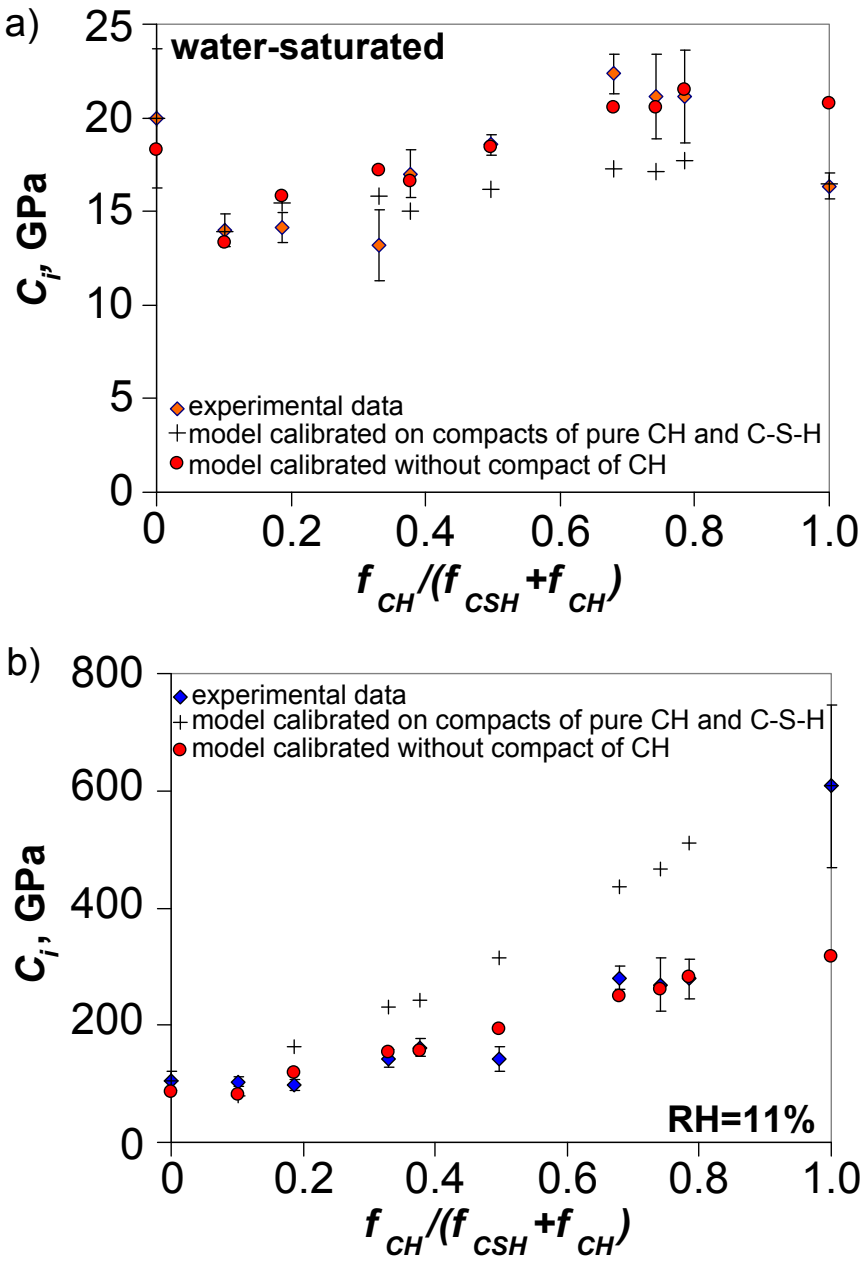

Figure 9.11: Contact creep modulus C_i of compacts from experiments and predicted by the model presented in section 9.4 a) in water-saturated conditions, b) in 11% relative humidity.

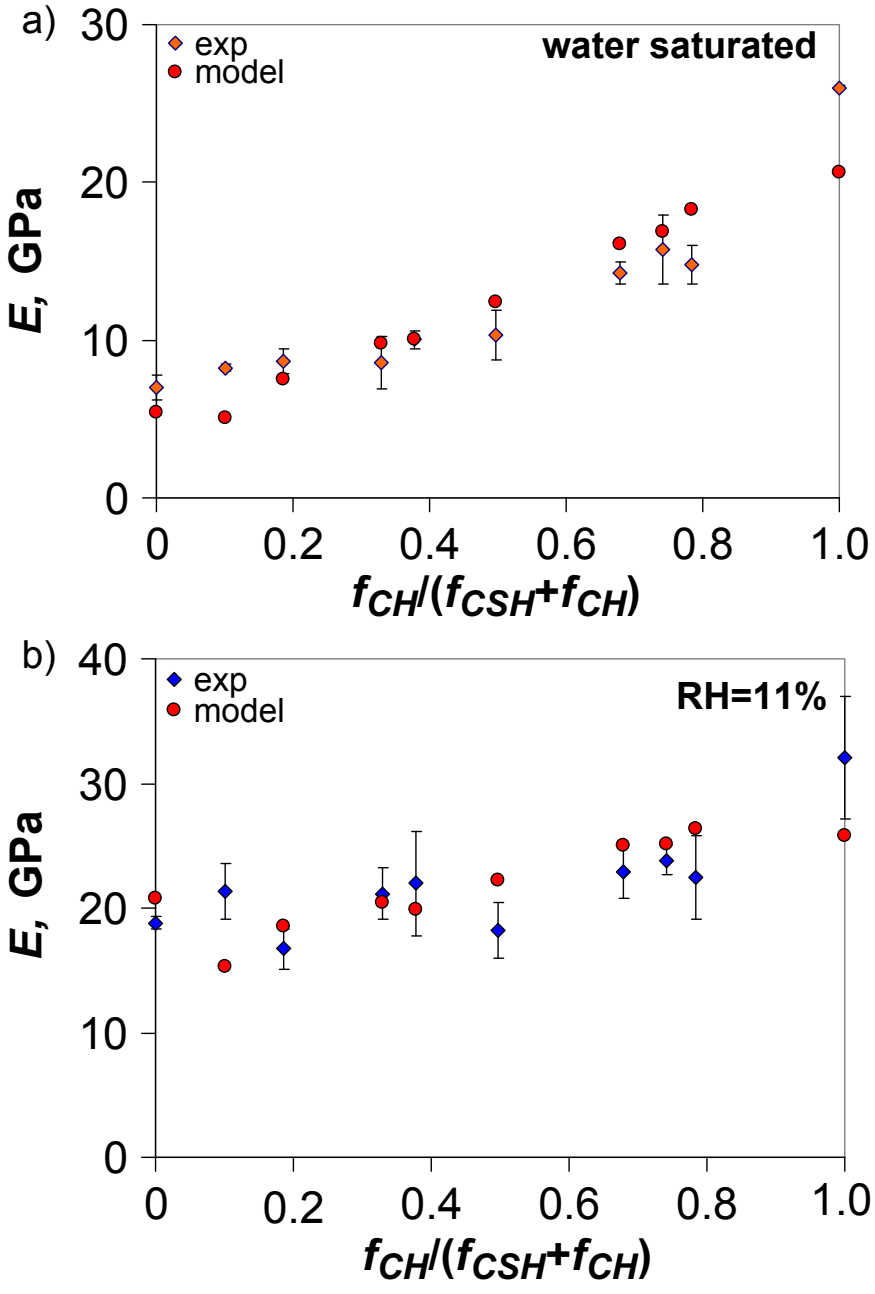

Figure 9.12: Young's modulus E of compacts from experiments and predicted by the model a) in water-saturated conditions and b) at 11% relative humidity.

	C-S-H phase		**CH phase**		**pore phase**	
	saturated	RH=11%	saturated	RH=11%	saturated	RH=11%
C_i, GPa	31.3	149	37.9	579	0	0
E, GPa	5.54	21.1	13.0	17.3	0	0
ν	0.24	0.24	0.32	0.32	0.3	0.3
aspect ratio	6.0	6.0	0.07	0.07	1.0	1.0

Table 9.3: Young's modulus E, contact creep modulus C_i, Poisson's ratio ν and aspect ratio of each phase at 11% relative humidity and in water-saturated conditions used in the model. The parameters in blue are calibrated parameters.

creep modulus of CH phase and the C-S-H phase, by fitting our model on all data expect that of compact of pure CH. Newly calibrated model is displayed in Fig. 9.11 with red circles in both hygral conditions: the trend of evolution of C_i with the volume fraction of CH in the solid skeleton remains well captured, and the quality of the fit is highly improved, with $R^2 = 0.897$ for data in 11% relative humidity (without considering the compact of CH) and $R^2 = 0.732$ for data in water-saturated conditions (without considering the compact of CH). As this second approach gives good fits for all experimental results except that of CH compact, we chose the parameters obtained with this appoarch as input parameters for the proposed model.

With the proposed model, we calibrate the Young's moduli of the C-S-H phase and CH phase in compact in the two hygral conditions on the Young's moduli measured by indentation on all compacts. The result of the calibration is displayed in Fig. 9.12 and the calibrated Young's modulus are given in Tab. 9.3.

In this section, we presented a two-step model for compacts of mixtures of C-S-H and CH. The model was designed based on the information on the microstructure of the compacts. The model gives reasonably good prediction of the elastic and creep properties of those compacts in a wide range of C-S-H to CH volume ratio: in particular, the non-monotonic evolution of contact creep modulus in function of fraction of CH in the solid skeleton is well captured by the model. Compared with the model proposed for C_3S and C_2S pastes (see in section 9.3), the CH phase in the compacts should be considered to exhibit creep too. With the contact creep modulus of C-S-H and CH in various relative humidities in Tab. 9.3, one can predict the contact creep modulus of a compact with given proportions of C-S-H and CH at 11% relative humidity and in water-saturated

condition. Howerer, the proposed model yields poor results for compacts of pure CH, and should therefore be used with caution for compacts with the largest volume fractions of CH, i.e., when the volume fraction of CH in the solid skeleton exceeds 80%.

9.5 Discussion

In the above sections, we presented one micromechanical model for C_3S and C_2S pastes (see in section 9.3) and the other one for compacts (see in section 9.4). The methodologies to set up the two models were quite similar: from information gathered on the microstructure of the materials studied, we chose the homogenization scheme and decided what phase to put at what scale; then we determined the creep properties of each phase by fitting the model to available data; finally, we integrated the effect of relative humidity on the creep properties of the creeping phases. Following the same methodology, the creep properties of various cementitious materials may be predicted. In this section, we will take a close look at the calibrated contact creep modulus of C-S-H phase and CH phase and discuss the similarities and the differences between those calibrated parameters in the pastes and in the compacts.

If we compare the models developed in section 9.3 for pastes with that developed for compacts in section 9.4, two major differences can be observed, described next.

The first difference lies in the spatial organization of different phases: for the model proposed for C_3S and C_2S pastes, C-S-H and the porosity are in the same scale, while for compacts of mixtures of CH and C-S-H, CH and porosity are in the same scale. By doing so, we obtained completely different models. This difference shows the effect of the spatial organization of different phases on the macroscopic mechanical properties of the material. Indeed, although we did not describe it in this chapter, for compacts we also tried homogenization schemes with all possible organization of phases that we could think of, such as putting C-S-H and porosity at the same scale and CH in another scale, or putting all phases in the same scale etc. Among all possible organizations of phases, we found that only the model described in section 9.4 succeeded in explaining the non-monotonic evolution of C_i with respect to the volume fraction of CH in the

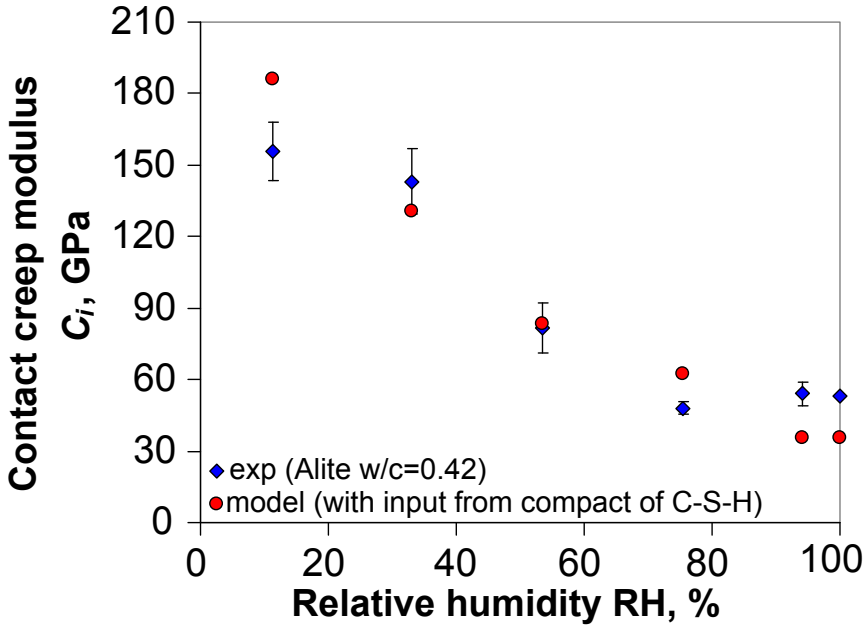

Figure 9.13: Contact creep modulus C_i of C_3S paste, obtained from indentation and predicted by the proposed two-step model for pastes with the input parameter of C-S-H phase calibrated on C-S-H compact.

solid skeleton in water-saturated conditions (see Fig. 9.11).

The second difference lies in the creep property of CH: for pastes, the CH was considered to exhibit no creep while for compacts, CH was considered to creep. This difference introduces an interesting topic for discussion: are the solid phases in the compacts representative of those in a paste obtained by hydration? We will aim at answering this question for C-S-H and CH in the following discussion. We start by comparing the C-S-H phase in paste and in compacts. By applying a self-consistent scheme on the C-S-H compact, we obtained the contact creep modulus of C-S-H in C-S-H compact at various relative humidities (see Fig. 9.10). As already presented in section 9.3, to predict the contact creep modulus of C_3S paste or C_2S paste, one only needs to know the contact creep modulus of C-S-H phase. Therefore, with the contact creep modulus of C-S-H calibrated from compact of pure C-S-H as input parameter, we predicted the contact creep modulus of C_3S paste. The result of this prediction at various relative humidities is displayed in Fig. 9.13 together with the experimental data. One observes that the predicted

values are quite close to the experimental ones: this validates that the long-term basic creep property of synthetic C-S-H in the compacts is representative of that of C-S-H in C_2S paste or C_3S paste. However, one can also observe that, at high relative humidities, the predicted values are 34% lower than the experimental results. This difference between predicted values and experimental ones may be due to the following reasons:

- At the scale of C-S-H phase, as already mentioned in section 7.2.1, the atomic ratio of calcium/silicon of synthetic C-S-H is about 1.4, while this ratio in paste is around 1.7; and the synthetic C-S-H is more crystalline than the C-S-H in paste. Therefore, the fact that C-S-H in paste and synthetic C-S-H are somewhat different could explain the evolution of creep properties of C-S-H with relative humidity.
- At a larger scale, the difference could lie in the presence of interfaces in the compacts. Indeed, those samples were originally under the form of powders, and thus contain interfaces between grains that are not presented in pastes obtained by hydration.

Now we compare CH in compacts with CH in pastes. For C_3S or C_2S paste, the proposed model works well when supposing that CH does not creep. In contrast, the experimental results showed that the compact of CH creeped: the contact creep modulus of compact of CH dropped significantly with an increasing relative humidity. In the model for compacts, we thus considered CH creeps in compacts. But how to explain that CH creeps in a compact, but not in a paste? A potential explanation is the following: already observed in Fig. 9.2, the CH in a C_2S paste or C_3S paste is embedded in a mixture of C-S-H and porosity. Thus, in a paste there are not so many contact points between CH crystals. In contrast, as observed in Fig. 9.7, the CH crystals in compacts are in contact with each other: the small crystals touch each other and porosity is present between the CH crystals. The pressure solution theory applies reasonably well to explain the creep of crystalline materials such as gypsum (see section 2.5). This theory states that creep in such material is due to a local dissolution of the crystals where they are stressed. The organization of CH in compacts is thus much more favorable for the dissolution and precipitation process to happen than that of CH in paste, and

thus CH in compact can exhibit more creep: the numerous contact points between CH crystals in compact favor local stress concentration, i.e., create the sites of dissolution. When CH is dissolved under stress, due to the presence of porosity between the CH crystals, which can be partly or fully saturated with water in high relative humidities, the dissolved CH can be transported and precipitates elsewhere. In contrast, this process is much less likely to happen for a CH crystal isolated in a porous C-S-H matrix. Based on the above reasoning, the contacts betweens CH crystal are thus critical to explain the difference in creep of CH phase in the paste and in compacts.

Last but not least, as stated above, crystalline phases are likely to creep at the interface between crystals, while in the proposed model for compact, the creep of CH is a considered as bulk process which is characterized by contact creep modulus, not an interfacial one. Thus the proposed model might be oversimplified to capture the creep behavior of CH in an accurate manner.

9.6 Chapter conclusions

In this chapter, a micromechanical approach was applied to decode the experimental results and to model the effects of microstructure and water on creep. We proposed one upscaling scheme to explain the experimental results on the Young's modulus and on the contact creep modulus for C_3S and C_2S paste, and another upscaling model to explain the two properties of compacts of mixtures of CH and C-S-H. Information on the microstructure obtained by SEM guided the choice of the models. The effect of relative humidity on the contact creep modulus of those materials was also integrated into the proposed models. A piecewise linear function was proposed to model the evolution of contact creep modulus of C-S-H in function of relative humidity. For the compacts, relative humidity had an effect on both the contact creep modulus of CH and that of C-S-H. With the appropriate calibrated micromechanical models, for each of the two materials, one can predict the contact creep modulus of the two materials for a wide range of C-S-H to CH proportions and at various relative humidities.

We compared the properties of C-S-H and CH in the two types of materials and found the creep properties of synthetic C-S-H in the compacts are representative of the creep properties of C-S-H in the pastes obtained by hydration,

while this is not the case for CH. We explained the discrepancy in terms of creep behavior between compacts and pastes for CH by the spatial organization: due to the numerous contact points between CH crystals in compacts, this phase can also bring creep to the material.

So far, we validated the measurement of long-term basic creep of cementitious materials by microindentation at the scale of paste. With the homogenization tool presented in chapter 4 (see Eq. 4.7), the contact creep modulus of concrete can be predicted from the knowledge of the contact creep modulus of the cement paste in the concrete. With the homogenization models presented in the present chapter, we calibrated the contact creep moduli of each phase in C_3S and C_2S pastes and in compacts, with which the contact creep modulus at the scale of paste or compact can be predicted. In practice, to obtain the long-term basic creep property of cementitious material, the right upscaling model to consider must be chosen between the two models presented in section 9.3 and 9.4: the choice must be guided by observation of the microstructure. One important note from the above discussion is that, for crystalline phases such as CH, if the crystals are in contact with each other, this crystalline phase should be considered to exhibit creep.

Part IV

Conclusions and perspectives

Chapter 10

Conclusions

Résumé *Initié par Lafarge Centre de Recherche et le Laboratoire Navier à l'Ecole des Ponts ParisTech, le projet de recherche visait d'une part à valider la technique d'indentation pour mesurer les propriétés de fluage des matériaux cimentaires et d'autre part à mettre en uvre cette technique pour étudier la manière dont les propriétés de fluage basique évoluent en fonction de leur microstructure et de l'humidité relative. Ce chapitre présente un résumé des principales conclusions du projet de recherche. Sur la base de ces conclusions et des contributions, plusieurs limites et perspectives sont détaillées.*

Abstract *Initiated by Lafarge Research Center and Laboratoire Navier at École des Ponts ParisTech, the research project aimed at validating indentation creep testing for the measurement of creep properties of cementitious materials and at applying this technique to study how their basic creep properties depend on their microstructures and on relative humidity. This Chapter presents a summary of the main findings of the research project. Based on those findings and the contributions, some limitations and perspectives are detailed.*

10.1 Research contributions

In the first part of the research project, we validated indentation creep testing as a technique to measure the long-term logarithmic basic creep of cementitious materials in few minutes, based on the conclusions from two comparative studies:

- In the first study, we compared microindentation creep experiments on cement paste with macroscopic uniaxial creep experiments on both cement paste and concrete. For all experiments, after a transient period, the basic creep was well captured by a logarithmic function of time. We showed that the rate of long-term creep of concrete (characterized by creep modulus C_i) could be quantitatively inferred from minutes-long microindentation experiments at the scale of cement paste, with the help of an upscaling model.

- In the second study, on gypsum plaster, we compared microindentation creep experiments with macroscopic three-point bending creep experiments. For indentation experiments, after a transient period, the basic creep was relatively well captured by a logarithmic function of time. In contrast, for bending creep testing, the basic creep was never logarithmic with respect to time but was well captured by the sum of a logarithmic function of time and of a linear one. Qualitatively, we showed that indentation creep testing enables to capture the trends observed with bending creep testing. Quantitatively, we showed that the creep moduli of gypsum measured by indentation were in very good agreement with that measured by bending for samples without creep-reducing additives. But we found no way of inferring the non-logarithmic part of the bending creep function from indentation creep testing.

In the second part of the research project, we applied the indentation technique to study the basic creep properties of cementitious materials. Abundant experimental data of various materials in various hygral conditions was obtained, with which the basic creep properties, the indentation hardness and the Young's modulus of tested materials can be obtained. A schematic summary of all tested materials and conditions, in the two parts of research project, is presented in Fig. 10.1.

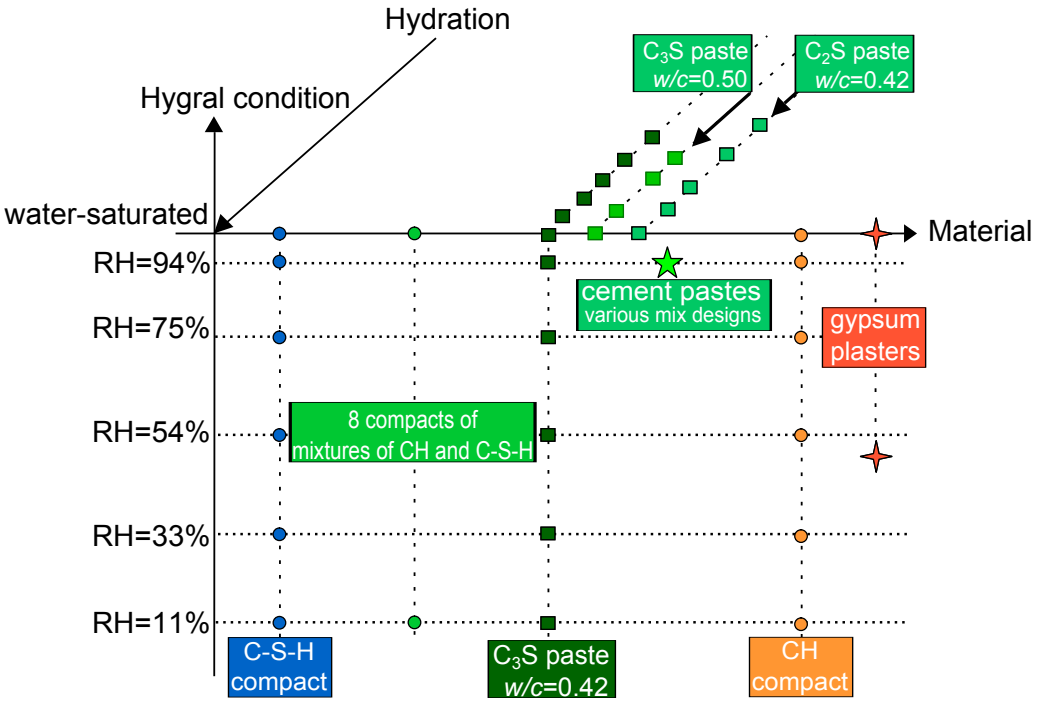

Figure 10.1: Schematic summary of experimental data obtained in the research project.

Based on those experimental results, we derived and calibrated micromechanical models to capture the effects of microstructure and water on creep. We proposed one upscaling scheme to explain the experimental results on the Young's modulus and on the contact creep modulus for C_3S and C_2S pastes, and another upscaling model to explain the two properties of compacts of CH, of synthetic C-S-H and of their mixtures. Information on the microstructure obtained by SEM guided the design of the models. The effect of relative humidity on the contact creep modulus of those materials was also integrated into the proposed models.

10.2 Summary of main findings

The study revealed the following scientific findings on the basic creep properties of cementitious materials:

[**On the contact creep function.**] For all materials studied, the contact creep function was found to be well captured by a logarithmic function respect to time after a transient period. Note however that, although the fit was almost perfect for cement pastes, C_3S and C_2S pastes and for the compact of C-S-H, it was less satisfactory for gypsum and compacts with high volume fractions of CH in water-saturated conditions. The basic creep properties of tested materials could thus be characterized by a contact creep modulus C_i (which controls the long-term basic creep rate) and by an indentation characteristic time τ_i (which controls the time needed to achieve logarithmic kinetics of creep). The contact creep modulus measured by microindentation creep testing was found to be comparable to uniaxial creep modulus and flexural creep modulus from macroscopic creep testing, while indentation characteristic time was orders of magnitude smaller than the characteristic time from macroscopic creep testing.

[**On the effect of microstructure on basic creep.**] From experimental observations and insights from modeling, the effect of microstructure on creep can be summarized as follows:

- The experimental results on C_3S and C_2S pastes showed that the porosity and the volume fraction of C-S-H govern the evolution of contact creep modulus of those materials in first order.

- The experimental results on compacts showed that at a similar level of

porosity, by varying the proportions of C-S-H and CH, the basic creep properties of the compacts is varied: in 11% relative humidity, the contact creep modulus C_i was found to increase with the proportion of CH in the solid skeleton. In water-saturated conditions, the two parameters evolved in non-monotonic manner with respect to each other.

- For a given microstructure, an appropriate micromechanical model can be derived. Information on the microstructure obtained by SEM guided the design of the models. We compared the properties of C-S-H and CH in the materials obtained by hydration and by compaction and found that the contact creep modulus of synthetic C-S-H in the compacts is comparable with that of the C-S-H in the pastes obtained by hydration, while this is not the case for CH. The spatial organization of the various phases may explain the discrepancy in terms of creep behavior observed for CH when comparing hydrated pastes and compacts: in compacts due to the numerous contact points between CH crystals, CH must be considered as a creeping phase; in hydrated C_3S or C_2S pastes, CH crystals are isolated in a matrix and can be considered as non-creeping phase.

[**On the effect of relative humidity on basic creep.**] The effect of relative humidity on creep can be summarized as follows based on experimental observations:

- The contact creep modulus C_i decreased in general with an increasing relative humidity. For compact of CH, the contact creep modulus decreased on the whole range of relative humidities studied. On the other hand, for C_3S paste and the compact of C-S-H, we identified a critical relative humidity below which the contact creep modulus varied and above which it remained constant. The critical relative humidities were converted into the largest entry radius of largest pore remaining water-saturated when drying, the value of which indicated that the removal of water from pores in C-S-H was responsible for the evolution of C_i below critical relative humidity, while the removal of water in capillary pores had no influence on the basic creep of the two materials.

- For all the samples studied, the evolution of indentation characteristic time in function of relative humidity was also found to exhibit a threshold: there

seemed to exist a critical relative humidity above which τ_i decreased with the increment of relative humidity and below which τ_i increased with the increment of relative humidity.

- On the C_3S paste, by combining the indentation data with the desorption isotherm, we found a linear relationship between contact creep modulus and water content for relative humidities ranging from 11% to 75%.

10.3 Industrial benefits

We found mainly two industrial benefits associated with the research project:

- We validated that microindentation testing provides access to the long-term logarithmic kinetics of creep of cementitious materials in minutes.
- We proposed upscaling models which can be used to predict the long-term basic creep property of cementitious materials with a wide range of C-S-H and CH proportions and at various relative humidities. Note however that one must decide whether CH should be considered as creeping phase or not: the choice can be guided by observations of the microstructure.

10.4 Limitations and perspectives

Firstly, we found that further explanations should be searched for some of the experimental results, listed below:

- The measured contact creep moduli did not compare well with the flexural creep moduli on gypsum plaster sample immersed in creep-reducing additives. We attributed this discrepancy to the fact that indentation mostly involved compression, while bending involves both compression and tension. How to fully infer long-term bending creep behavior from indentation test is still not fully resolved.
- The Young's modulus of C_3S paste was found not to depend on relative humidity, while for compact of CH and C-S-H, a decrease of Young's modulus was seen in high relative humidities. For compact of C-S-H, the Young's

modulus decreased as much as 50%. We do not know yet how to explain this discrepancy between compacts and hydrated paste.

Secondly, we found that the some of the methods used for analysis need to be improved. Those methods are listed here:

- For all the materials tested, we applied a logarithmic function to fit the basic creep properties. Such fit was very satisfactory for hydrated pastes and compact of C-S-H, but less satisfactory for crystalline samples such as gypsum or compacts of CH at high relative humidities. For materials with non-logarithmic creep, how to compare quantitatively the creep parameters obtained by macroscopic creep testing and those obtained by indentation testing is still not clear.

- The upscaling model proposed to predict the contact creep modulus of compacts failed to give a good prediction of the contact creep modulus of the compact of pure CH. For materials with high proportion of crystalline phase which also creeps, it seems that the proposed model may be oversimplified for two reasons:

  1. creep of crystalline phases may not be strictly logarithmic with respect to time, especially in high relative humidities;
  2. crystalline phases are likely to creep at the interface between crystals, while in the proposed model, for all phases, creep is a bulk process, not an interface one.

- We validated that microindentation creep testing yields access to long-term logarithmic creep kinetics of cementitious materials. As a counterpart, such microindentation test does not allow to characterize the short-term creep of those materials. Indentation creep testing and the proposed upscaling models only provide information on the contact creep modulus which governs the rate of long-term creep. One needs some information to predict the magnitude of long-term creep: said otherwise: one needs to know the constant of integration to move from the rate to the magnitude. To overcome this shortcoming, a first approach could be to perform regular macroscopic tests that only last long enough in order to measure the short-term kinetics of creep, to which would be juxtaposed the long-term logarithmic creep

characterized by microindentation. By doing so, the whole creep function of cementitious materials could be measured precisely and in a more convenient and faster way than is done today. The second approach would be to predict the characteristic time needed to reach this logarithmic creep at the scale of interest. However, this parameter seems still very mysterious today: why the characteristic time differs so much between various scales of testing? How can this parameter be linked to the properties of the material, of the structure of interest or to the type of solicitation? Further efforts are necessary to answer those questions.

Bibliography

ACI Committee. Prediction of creep, shrinkage, and temperature effects in concrete structures, manual of concrete practice. *American Concrete Institute, Detroit, MI*, 1999. 27

P. Acker and F.-J. Ulm. Creep and shrinkage of concrete: physical origins and practical measurements. *Nuclear Engineering and Design*, 203(2):143–158, 2001. xxv, 5, 19, 20, 84, 155

P. Acker et al. Micromechanical analysis of creep and shrinkage mechanisms. *Creep, Shrinkage, and Durability Mechanics of Concrete and Other Quasi-Brittle Materials,â Proceedings of ConCreep-6@ MIT, Elsevier, London*, pages 15–25, 2001. 189

M. G. Alexander. Deformation properties of blended cement concretes containing blastfurnace slag and condensed silica fume. *Advances in Cement Research*, 6 (22):73–81, 1994. 26

M. G. Alexander. Aggregates and the deformation properties of concrete. *ACI Materials Journal*, 93(6), 1996. 26

L. Amathieu and R. Boistelle. Improvement of the mechanical properties of set plasters by means of four organic additives inducing {101} faces. *Journal of Crystal Growth*, 79(1):169–177, 1986. 83

H. Andrews. The effect of water contents on the strength of calcium sulphate plaster products. *Journal of the Society of Chemical Industry*, 65(5):125–128, 1946. 82

ASTM C-1608-07. *Standard test method for chemical shrinkage and of hydraulic cement paste*. ASTM international, 2007. 115

ASTM E2546 -7. *Standard practice for instrumented indentation testing*. ASTM international, West Conshohocken, 2007. doi: 10.1520/E2546-07. 37

D. S. Atrushi. *Tensile and compressive creep of young concrete: testing and modelling*. PhD thesis, Norwegian University of Science and Technology, 2003. 23

J.-L. Auriault, C. Boutin, and C. Geindreau. *Homogenization of coupled phenomena in heterogenous media*, volume 149. John Wiley & Sons, 2010. 172

E. Badens, S. Veesler, R. Boistelle, and D. Chatain. Relation between Youngâs modulus of set plaster and complete wetting of grain boundaries by water. *Colloids and Surfaces A: Physicochemical and Engineering Aspects*, 156(1-3): 373–379, Oct. 1999. ISSN 09277757. doi: 10.1016/S0927-7757(99)00097-7. 82

Z. P. Bažant. Current status and advances in the theory of creep and interaction with fracture. In *RILEM Proceedings*, pages 291–291. CHAPMAN & HALL, 1993. 28

Z. P. Bažant. Prediction of concrete creep and shrinkage: past, present and future. *Nuclear Engineering and Design*, 203(1):27–38, Jan. 2001. ISSN 00295493. doi: 10.1016/S0029-5493(00)00299-5. 4

Z. P. Bažant and S. Baweja. Justification and refinements of model B3 for concrete creep and shrinkage 2. Updating and theoretical basis. *Materials and Structures*, 28(8):488–495, Oct. 1995. ISSN 0025-5432. doi: 10.1007/BF02473171. 66

Z. P. Bažant and S. Baweja. Creep and shrinkage prediction model for analysis and design of concrete structures: Model B3. *ACI Special Publication*, 194: 1–84, 2000. 30

Z. P. Bažant and R. L'Hermite. *Mathematical modeling of creep and shrinkage of concrete*. Wiley New York, 1988. 186

Z. P. Bažant and G. H. Li. Unbiased statistical comparison of creep and shrinkage prediction models. *ACI Materials Journal*, 105(6):610–621, 2008. 31

Z. P. Bažant and L. Panula. Creep and shrinkage characterization for analyzing prestressed concrete structures. *PCI Journal*, 25(3):86–122, 1980. 3

Z. P. Bažant and S. Prasannan. Solidification theory for concrete creep. I: Formulation. *Journal of Engineering Mechanics*, 115(8):1691–1703, 1989a. 28

Z. P. Bažant and S. Prasannan. Solidification theory for concrete creep. II: Verification and application. *Journal of Engineering Mechanics*, 115(8):1704–1725, 1989b. 28

Z. P. Bažant and F. H. Wittmann. *Creep and shrinkage in concrete structures*. Wiley Chichester, 1982. 11, 12

Z. P. Bažant and Y. Xi. Continuous retardation spectrum for solidification theory of concrete creep. *Journal of Engineering Mechanics*, 121(2):281–288, 1995. 186

Z. P. Bažant, J. H. Hemann, H. Koller, and L. J. Najjar. A thin-wall cement paste cylinder for creep tests at variable humidity or temperature. *Materials and Structures*, 6(34):227–281, 1973. xxv, 5, 19, 20, 155

Z. P. Bažant, A. A. Asghari, and J. Schmidt. Experimental study of creep of hardened Portland cement paste at variable water content. *Matériaux et Construction*, 9(4):279–290, 1976. 22

Z. P. Bažant, A. B. Hauggaard, S. Baweja, and F.-J. Ulm. Microprestress-solidification theory for concrete creep. I: Aging and drying effects. *Journal of Engineering Mechanics*, 123(11):1188–1194, 1997. 28, 84

Z. P. Bažant, G. Cusatis, and L. Cedolin. Temperature effect on concrete creep modeled by microprestress-solidification theory. *Journal of Engineering Mechanics*, 130(6):691–699, 2004. 21

Z. P. Bažant, M. H. Hubler, and Q. Yu. Pervasiveness of excessive segmental bridge deflections: wake-up call for creep. *ACI Structure Journal*, 108(6):766–774, 2011. 75

Z. P. Bažant and X. Yunping. Drying creep of concrete: constitutive model and new experiments separating its mechanisms. *Materials and Structures*, 27(1): 3–14, 1994. 12

B. Beake. Modelling indentation creep of polymers: a phenomenological approach. *Journal of Physics D: Applied Physics*, 39:4478–4485, 2006. ISSN 00223727. doi: 10.1088/0022-3727/39/20/027. 18

J. J. Beaudoin. Comparison of mechanical properties of compacted calcium hydroxide and portland cement paste systems. *Cement and Concrete Research*, 13(3):319–324, 1983. 130

J. J. Beaudoin, P. Gu, and R. Myers. The fracture of csh and csh/ch mixtures. *Cement and concrete research*, 28(3):341–347, 1998. 130

J. J. Beaudoin, L. Raki, and J. Marchand. The use of compacts for durability investigation of cement-based materials. *Journal of Materials Science*, 38(24): 4957–4964, 2003. 130

O. Bernard, F.-J. Ulm, and J. T. Germaine. Volume and deviator creep of calcium-leached cement-based materials. *Cement and Concrete Research*, 33(8):1127–1136, 2003. ISSN 0008-8846. doi: http://dx.doi.org/10.1016/S0008-8846(03)00021-8. 13, 186

A. K. Bhattacharya and W. D. Nix. Analysis of elastic and plastic deformation associated with indentation testing of thin films on substrates. *International Journal of Solids and Structures*, 24(12):1287–1298, 1988. 18

B. Bhushan and X. Li. Nanomechanical characterisation of solid surfaces and thin films. *International Materials Reviews*, 48(3):125–164, 2003. 40

B. Bissonnette and M. Pigeon. Tensile creep at early ages of ordinary, silica fume and fiber reinforced concretes. *Cement and Concrete Research*, 25(5): 1075–1085, 1995. 19

B. Bissonnette and M. Pigeon. Le comportement viscoélastique du béton en traction et la compatibilité déformationnelle des réparations. *Materials and Structures*, 33(2):108–118, 2000. 24, 27

J. A. Brinell. Mémoire sur les épreuves a bille en acier. In *Congrès international des méthodes d'essai des matériaux de construction*, volume 2, pages 83–94, 1901. 42

J. J. Brooks and M. Johari. Effect of metakaolin on creep and shrinkage of concrete. *Cement and Concrete Composites*, 23(6):495–502, 2001. 26

S. Brunauer. A discussion of the helium flow results of RF Feldman. *Cement and Concrete Research*, 2(4):489–492, 1972. 109

S. I. Bulychev, V. P. Alekhin, M. K. Shorshorov, A. P. Ternovskii, and G. D. Shnyrev. Determination of young's modulus according to indentation diagram. *Zavodskaya Laboratoria*, 41:1137, 1975. 38

M. A. Carreira and J. D. Chiorino. Factors affecting creep and shrinkage of hardened concrete and guide for modelling - A state-of-art report on international recommendations and scientific debate. *The India Concrete Journal*, December:11–23, 2012. 30

G. A. Chami, M. Thériault, and K. W. Neale. Creep behaviour of CFRP-strengthened reinforced concrete beams. *Construction and Building Materials*, 23(4):1640–1652, 2009. ISSN 0950-0618. doi: http://dx.doi.org/10.1016/j.conbuildmat.2007.09.006. 13

J. Chen, W. Wang, L. Lu, and K. Lu. Measurement of creep rate sensitivity of copper at room temperature by using nanoindentation. *Jinshu XuebaoActa Metallurgica Sinica*, 37:1179–1183, 2001. 18

J. J. Chen, J. J. Thomas, H. F. Taylor, and H. M. Jennings. Solubility and structure of calcium silicate hydrate. *Cement and Concrete Research*, 34(9): 1499–1519, 2004. 133

X. Chen, N. Ogasawara, M. Zhao, and N. Chiba. On the uniqueness of measuring elastoplastic properties from indentation: the indistinguishable mystical materials. *Journal of the Mechanics and Physics of Solids*, 55(8):1618–1660, 2007. 43

Y. T. Cheng and C. M. Cheng. Scaling, dimensional analysis, and indentation measurements. *Materials Science Engineering: R: Reports*, 44:91–149, 2004. ISSN 0927796X. 18, 39, 43

R. M. Christensen. A critical evaluation for a class of micro-mechanics models. *Journal of the Mechanics and Physics of Solids*, 38(3):379–404, 1990. 193

Z. N. Cilosani. On the true mechanism of creep of concrete. *Beton i Zhelezobeton*, 2:75–78, 1964. 6, 19, 155

J.-L. Clément and F. Le Maou. Étude de la répétabilité des essais de fluage sur éprouvette de béton. *Bulletin des Laboratoires des Ponts et Chaussées*, 228 (4329):59–69, 2000. 76

R. L. Coble. A model for boundary diffusion controlled creep in polycrystalline materials. *Journal of Applied Physics*, 34:1679, 1963. 28

X. Cong and R. J. Kirkpatrick. 17O MAS NMR investigation of the structure of calcium silicate hydrate gel. *Journal of the American Ceramic Society*, 79(6): 1585–1592, 1996. 109

G. Constantinides and F.-J. Ulm. The effect of two types of C-S-H on the elasticity of cement-based materials: Results from nanoindentation and micromechanical modeling. *Cement and Concrete Research*, 34(1):67–80, 2004. ISSN 00088846. doi: 10.1016/S0008-8846(03)00230-8. 188, 189

L. E. Copeland, D. Kantro, and G. J. Verbeck. *Chemistry of hydration of Portland cement*. Portland Cement Association, Research and Development Laboratories, 1960. 115

O. Coussy. *Poromechanics*. Wiley. com, 2004. 167

D. Davydov, M. Jirasek, and L. Kopecký. Critical aspects of nano-indentation technique in application to hardened cement paste. *Cement and Concrete Research*, 41(1):20–29, Jan. 2011. ISSN 00088846. doi: 10.1016/j.cemconres.2010.09.001. 5, 18

S. De Meer and C. J. Spiers. Uniaxial compaction creep of wet gypsum aggregates. *Journal of Geophysical Research: Solid Earth (1978–2012)*, 102:875–891, 1997. xxviii, 100, 102

S. De Meer and C. J. Spiers. Influence of pore-fluid salinity on pressure solution creep in gypsum. *Tectonophysics*, 308(3):311–330, 1999. 29, 100

S. De Meer, C. J. Spiers, and C. J. Peach. Pressure solution creep in gypsum: Evidence for precipitation reaction control. *Physics and Chemistry of the Earth*, 22(1):33–37, 1997. 29, 100

G. De Schutter and L. Taerwe. Fictitious degree of hydration method for the basic creep of early age concrete. *Materials and Structures*, 33(6):370–380, 2000. 23, 24

M. F. Doerner and W. D. Nix. A method for interpreting the data from depth-sensing indentation instrurnents. *Journal of Materials Research*, 1(4), 1986. 18

A. Domingo-Cabo, C. Lázaro, F. López-Gayarre, M. A. Serrano-López, P. Serna, and J. O. Castaño Tabares. Creep and shrinkage of recycled aggregate concrete. *Construction and Building Materials*, 23(7):2545–2553, 2009. 26

D. Dorner, K. Röller, B. Skrotzki, B. Stöckhert, and G. Eggeler. Creep of a TiAl alloy: a comparison of indentation and tensile testing. *Materials Science and Engineering: A*, 357(1):346–354, 2003. 18

J. Escalante-Garcia and J. Sharp. Effect of temperature on the hydration of the main clinker phases in portland cements: Part i, neat cements. *Cement and concrete research*, 28(9):1245–1257, 1998. 22

J. D. Eshelby. The determination of the elastic field of an ellipsoidal inclusion, and related problems. *Proceedings of the Royal Society of London. Series A. Mathematical and Physical Sciences*, 241(1226):376–396, 1957. 174

H. M. Fahmi, M. Polivka, and B. Bresler. Effects of sustained and cyclic elevated temperature on creep of concrete. *Cement and Concrete Research*, 2(5):591–606, 1972. 23

Fédération Internationale du Béton. *Section 7.2.4 Analysis of structural effects of time-dependent behaviour of concrete*. Fédération Internationale du Béton fib/International Federation for Structural Concrete, 2013. 3

R. F. Feldman. Helium flow and density measurement of the hydrated tricalcium silicate-water system. *Cement and Concrete Research*, 2(1):123–136, 1972. 109, 116

R. F. Feldman and J. J. Beaudoin. Microstructure and strength of hydrated cement. *Cement and Concrete Research*, 6(3):389–400, 1976. 130

R. F. Feldman and P. J. Sereda. A model for hydrated portland cement paste as deduced from sorption-length change and mechanical properties. *Matériaux et Construction*, 1(6):509–520, 1968. 109

R. F. Feldman and P. J. Sereda. A new model for hydrated portland cement and its practical implications. *Engineering Journal*, 53(8-9):53–59, 1970. 10

M. C. Fernandez. *Effect of particle size on the hydration kinetics and microstructural development of tricalcium silicate*. PhD thesis, Ph. D. thesis. École Polytechnique Federale De Lausanne, 2008. 116

M. Fujiwara and M. Otsuka. Indentation creep of β-Sn and Sn–Pb eutectic alloy. *Materials Science and Engineering: A*, 319:929–933, 2001. 18

L. A. Galin, H. Moss, and N. I. Sneddon. Contact problems in the theory of elasticity. 1961. 38

V. Y. Garas, L. F. Kahn, and K. E. Kurtis. Short-term tensile creep and shrinkage of ultra-high performance concrete. *Cement and Concrete Composites*, 31(3): 147–152, 2009. 26

N. Gardner. Comparison of prediction provisions for drying shrinkage and creep of normal-strength concretes. *Canadian Journal of Civil Engineering*, 31(5): 767–775, 2004. 30

N. Gardner and M. Lockman. Design provisions for drying shrinkage and creep of normal-strength concrete. *ACI Materials Journal*, 98(2), 2001. 30

E. M. Gartner. Cohesion and expansion in polycrystalline solids formed by hydration reactions – The case of gypsum plasters. *Cement and Concrete Research*, 39(4):289–295, 2009. ISSN 0008-8846. doi: http://dx.doi.org/10.1016/j.cemconres.2009.01.008. 82

A. Geranmayeh and R. Mahmudi. Power law indentation creep of sn-5% sb solder alloy. *Journal of Materials Science*, 40(13):3361–3366, 2005. 18

E. Ghossein and M. Lévesque. A fully automated numerical tool for a comprehensive validation of homogenization models and its application to spherical particles reinforced composites. *International Journal of Solids and Structures*, 49(11-12):1387–1398, June 2012. ISSN 00207683. doi: 10.1016/j.ijsolstr.2012.02.021. 74

L. Greenspan. Humidity fixed points of binary saturated aqueous solutions. *Journal of Research of the National Bureau of Standards, A. Physics and Chemistry A*, 81:89–96, 1977. xxxv, 157

J.-P. Guin, T. Rouxel, V. Keryvin, J.-C. Sanglebœ uf, I. Serre, and J. Lucas. Indentation creep of Ge–Se chalcogenide glasses below T g: elastic recovery and non-Newtonian flow. *Journal of Non-crystalline Solids*, 298(2):260–269, 2002. 18

Y. C. Guo, C. L. Xin, M. S. Song, and Y. D. He. Study on short- and long-term creep behavior of plastics geogrid. *Polymer Testing*, 24(6):793–798, 2005. ISSN 0142-9418. doi: http://dx.doi.org/10.1016/j.polymertesting.2005.02.014. 13

L. H. Han and Y. F. Yang. Analysis of thin-walled steel RHS columns filled with concrete under long-term sustained loads. *Thin-Walled Structures*, 41(9):849–870, 2003. ISSN 0263-8231. doi: http://dx.doi.org/10.1016/S0263-8231(03)00029-6. 13

W. K. Hatt. Notes on the effect of time element in loading reinforced concrete beams. In *Proceedings: American Society for Testing Materials*, volume 7, pages 421–433, 1907. 3

J. C. Hay, A. Bolshakov, and G. M. Pharr. A critical examination of the fundamental relations used in the analysis of nanoindentation data. *Journal of*

Materials Research, 14:2296–2305, 1999. ISSN 08842914. doi: 10.1557/JMR.1999.0306. 39

T. Hidenari, F. Masami, and D. Ming. Determination of constitutive parameters for self-similar indentation creep and its applications. In *11th International Conference on Fracture*, pages 1–6, 2005. 18

E. Holt. Contribution of mixture design to chemical and autogenous shrinkage of concrete at early ages. *Cement and Concrete Research*, 35(3):464–472, 2005. 11

C. Y. Hua. *Analyse et modélisation du retrait d'autodessication de la pâte de ciment durcissante*. PhD thesis, 1995. 11

C. Huet, P. Acker, and J. Baron. Fluage et autres effets rhéologiques du béton. In *Le Béton Hydraulique*, chapter 19, pages 355–364. Presses de l'Ecole Nationale des Ponts et Chaussées, 1982. 57

O. Ishai and L. J. Coheno. Effect of fillers and voids on compressive yield of epoxy composites. *Journal of Composite Materials*, 2(3):302–315, 1968. 27

H. Jaffel, J.-P. Korb, J.-P. Ndobo-Epoy, J.-P. Guicquero, and V. Morin. Multi-scale approach continuously relating the microstructure and the macroscopic mechanical properties of plaster pastes during their settings. *The journal of physical chemistry. B*, 110(37):18401–7, Sept. 2006. ISSN 1520-6106. doi: 10.1021/jp062832a. xxvii, 82, 83, 88

H. M. Jennings. A model for the microstructure of calcium silicate hydrate in cement paste. *Cement and Concrete Research*, 30(1):101–116, 2000. 109, 116

H. M. Jennings. Refinements to colloid model of csh in cement: Cm-ii. *Cement and Concrete Research*, 38(3):275–289, 2008. 109, 116, 138

O. M. Jensen and P. F. Hansen. Water-entrained cement-based materials: I. principles and theoretical background. *Cement and concrete research*, 31(4): 647–654, 2001. xxviii, 113

Z. W. Jiang, Z. P. Sun, and P. M. Wang. Autogenous relative humidity change and autogenous shrinkage of high-performance cement pastes. *Cement and*

Concrete Research, 35(8):1539–1545, Aug. 2005. ISSN 00088846. doi: 10.1016/j.cemconres.2004.06.028. 60

M. Jirásek and S. Dobruskỳ. Accuracy of concrete creep predictions based on extrapolation of short-time data. In *Proceedings of the 5th international conference on reliable engineering computing,(197-207)*, 2012. 4

B.-W. Jo, G.-H. Tae, and C.-H. Kim. Uniaxial creep behavior and prediction of recycled-PET polymer concrete. *Construction and Building Materials*, 21(7):1552–1559, 2007. ISSN 0950-0618. doi: http://dx.doi.org/10.1016/j.conbuildmat.2005.10.003. 13

S. Kamali. *Comportement et simulation des matériaux cimentaires en environnements agressifs: lixiviation et température*. Laboratoire de mécanique et technologie, 2003. 189

A. Kamen, E. Denarié, and E. Brühwiler. Time dependent behaviour of ultra high performance fibre reinforced concrete (UHPFRC). In *6th PhD Symposium in Civil Engineering, Zürich, Switzerland, paper submitted*, 2006. 19

A. Kamen, E. Denarié, and E. Brühwiler. Viscoelastic behavior of a strain hardening Ultra High Performance Fiber Reinforced Concrete. In *Advances in Construction Materials 2007*, pages 157–164. Springer, 2007. 24

F. Khadraoui. Creep and shrinkage behaviour of CFRP-reinforced mortar. *Construction and Building Materials*, 28(1):282–286, 2012. ISSN 0950-0618. doi: http://dx.doi.org/10.1016/j.conbuildmat.2011.07.048. 13

K. O. Kjellsen, R. J. Detwiler, and O. E. Gjørv. Pore structure of plain cement pastes hydrated at different temperatures. *Cement and Concrete Research*, 20 (6):927–933, 1990a. 22

K. O. Kjellsen, R. J. Detwiler, and O. E. Gjørv. Backscattered electron imaging of cement pastes hydrated at different temperatures. *Cement and concrete research*, 20(2):308–311, 1990b. 115

G. J. Kommendant, M. Polivka, and D. Pirtz. Study of concrete properties for prestressed concrete reactor vessels, final report-part II, Creep and strength

characteristics of concrete at elevated temperatures. *Report No. UCSESM*, pages 73–76, 1976. 22

J.-P. Korb, L. Monteilhet, P. McDonald, and J. Mitchell. Microstructure and texture of hydrated cement-based materials: A proton field cycling relaxometry approach. *Cement and concrete research*, 37(3):295–302, 2007. 169

R. Le Roy. *Déformations instantanées et différées des bétons à hautes performances*. PhD thesis, 1996. ix, xxvi, 4, 25, 26, 50, 51, 52, 56, 62

F. M. Lea and C. R. Lee. Shrinkage and creep in concrete. In *Proc., Symposium on the Shrinkage and Cracking of Cementative Materials. Society of Chemical Industry, London*, 1947. 27

Y. Lee, S.-T. Yi, M.-S. Kim, and J.-K. Kim. Evaluation of a basic creep model with respect to autogenous shrinkage. *Cement and Concrete Research*, 36(7): 1268–1278, July 2006. ISSN 00088846. doi: 10.1016/j.cemconres.2006.02.011. xxv, 15, 23, 24

J. Y. Li and Y. Yao. A study on creep and drying shrinkage of high performance concrete. *Cement and Concrete Research*, 31(8):1203–1206, 2001. 25, 26

X. Li, X. L. Gu, Y. Ouyang, and X. B. Song. Long-term behavior of existing low-strength reinforced concrete beams strengthened with carbon fiber composite sheets. *Composites Part B: Engineering*, 43(3):1637–1644, 2012. ISSN 1359-8368. doi: http://dx.doi.org/10.1016/j.compositesb.2012.01.016. 13

Z. J. Li. *Advanced concrete technology*. Wiley, 2011. 3

A. Love. *The mathematical theory of elasticity*. 1927. 37

H. Lu, B. Wang, J. Ma, G. Huang, and H. Viswanathan. Measurement of creep compliance of solid polymers by nanoindentation. *Mechanics of Time-Dependent Materials*, 7:189–207, 2003. ISSN 13852000. 18

C. G. Lynam. *Growth and movement in Portland cement concrete*. London, 1934. 27

X. Ma and F. Yoshida. Rate-dependent indentation hardness of a power-law creep solder alloy. *Applied Physics Letters*, 82:188, 2003. ISSN 00036951. doi: 10.1063/1.1537513. 18

D. D. Magura, M. A. Sozen, and C. P. Siess. *A study of stress relaxation in prestressing reinforcement*. University of Illinois, 1963. 3

R. Mahmudi, A. R. Geranmayeh, H. Noori, H. Khanbareh, and N. Jahangiri. A comparison of impression, indentation and impression-relaxation creep of lead-free Snâ9Zn and Snâ8Znâ3Bi solders at room temperature. *Journal of Materials Science: Materials in Electronics*, 20:312–318, 2009. ISSN 09574522. doi: 10.1007/s10854-008-9726-x. 18

P. S. Mangat and M. M. Azari. Compression creep behaviour of steel fibre reinforced cement composites. *Materials and Structures*, 19(5):361–370, 1986. 26

S. Manzi, C. Mazzotti, and M. C. Bignozzi. Short and long-term behavior of structural concrete with recycled concrete aggregate. *Cement and Concrete Composites*, 37(0):312–318, 2013. ISSN 0958-9465. doi: http://dx.doi.org/10.1016/j.cemconcomp.2013.01.003. 13

J. Marchand. Résistance et module des pâtes de ciment à hautes performances. Technical report, LCPC, Paris, 1992. xxvi, 64

A. S. Maxwell, M. A. Monclus, N. M. Jennett, and G. Dean. Accelerated testing of creep in polymeric materials using nanoindentation. *Polymer Testing*, 30(4):366–371, June 2011. ISSN 01429418. doi: 10.1016/j.polymertesting.2011.02.002. 18

P. K. Mehta and P. J. Monteiro. *Concrete: microstructure, properties, and materials*. McGraw-Hill New York, 2006. xxv, 9, 10, 169

S. Meille. *Etude du comportement mécanique du platre pris en relation avec sa microstructure*. PhD thesis, INSA de Lyon, 2001. 82

C. Miàs, L. Torres, A. Turon, and C. Barris. Experimental study of immediate and time-dependent deflections of GFRP reinforced concrete beams. *Composite*

Structures, 96(0):279–285, 2013. ISSN 0263-8223. doi: http://dx.doi.org/10.1016/j.compstruct.2012.08.052. 13

M. Miller, C. Bobko, M. Vandamme, and F.-J. Ulm. Surface roughness criteria for cement paste nanoindentation. *Cement and Concrete Research*, 38(4):467–476, Apr. 2008. ISSN 00088846. doi: 10.1016/j.cemconres.2007.11.014. 58

G. Monfore and B. Ost. An 'isothermal' conduction calorimeter for study of the early hydration reactions of portland cements. Technical report, 1900. 115

P. J. Monteiro and C. Chang. The elastic moduli of calcium hydroxide. *Cement and Concrete Research*, 25(8):1605–1609, 1995. 188

A. C. Muller, K. L. Scrivener, A. M. Gajewicz, and P. J. McDonald. Densification of c–s–h measured by 1h nmr relaxometry. *The Journal of Physical Chemistry C*, 117(1):403–412, 2012. 10, 169

A. M. Neville. *Creep of concrete: plain, reinforced, and prestressed*. North-Holland Pub. Co., 1971. 3, 4

A. M. Neville, W. H. Dilger, and J. J. Brooks. *Creep of plain and structural concrete*. Construction Press London and New York, 1983. 11, 28

D.-T. Nguyen, R. Alizadeh, J. J. Beaudoin, and L. Raki. Microindentation creep of secondary hydrated cement phases and c–s–h. *Materials and Structures*, 46:1519–1525, 2013. 130

F. E. Nixon. *Handbook of Laplace Transformation: Tables and Examples. Workbook (with Answers)*. Prentice-Hall, 1965. 179, 182

A. Nonat. The structure and stoichiometry of csh. *Cement and Concrete Research*, 34(9):1521–1528, 2004. 109

N. Ogbonna, N. A. Fleck, and A. C. F. Cocks. Transient creep analysis of ball indentation. *International Journal of Mechanical Sciences*, 37:1179–1202, 1995. 18

W. C. Oliver and G. M. Pharr. An improved technique for determining hardness and elastic modulus using load and displacement sensing indentation experiments. *Journal of Materials Research*, 7(6):1564–1583, Jan. 1992. ISSN 0884-2914. doi: 10.1557/JMR.1992.1564. xxvi, 18, 40, 42

W. C. Oliver and G. M. Pharr. Measurement of hardness and elastic modulus by instrumented indentation: Advances in understanding and refinements to methodology. *Journal of Materials Research*, 19(01):3–20, 2004. 18

L. Østergaard, D. A. Lange, S. A. Altoubat, and H. Stang. Tensile basic creep of early-age concrete under constant load. *Cement and concrete research*, 31(12): 1895–1899, 2001. 24

M. L. Oyen. Spherical indentation creep following ramp loading. In *MRS Proceedings*, volume 841, pages R5—-9. Cambridge Univ Press, 2004. 18

E.-A. Pachon-Rodriguez. *Étude de l'influence de la dissolution sous contrainte sur les propiétés mécaniques des solides - Fluage du Plâtre*. PhD thesis, Université Lyon 1, 2011. x, xxvii, 80, 81, 83, 86, 94, 95

E.-A. Pachon-Rodriguez, E. Guillon, G. Houvenaghel, and J. Colombani. Wet creep of hardened hydraulic cements - example of gypsum plaster and implication for hydrated Portland cement. 29

E. A. Pachon-Rodriguez, E. Guillon, G. Houvenaghel, and J. Colombani. Pressure solution as origin of the humid creep of a mineral material. *Physical Review E*, 84(6):066121, 2011. 29

P. Padevět, P. Tesárek, and T. Plachý. Evolution of mechanical properties of gypsum in time. *International Journal of Mechanics*, 5(1):1–9, 2011. 82

L. J. Parrott, M. Geiker, W. A. Gutteridge, and D. Killoh. Monitoring portland cement hydration: comparison of methods. *Cement and Concrete Research*, 20 (6):919–926, 1990. 115

D. L. Peng, M. Yan, J. F. Sun, J. Shen, Y. Y. Chen, and D. G. Mccartney. Indentation creep behavior of a Zr-based bulk metallic glass. *Journal of Alloys and Compounds*, 400:197–201, 2007. ISSN 09258388. doi: 10.1016/j.jallcom.2006.08.103. 18

B. Pichler and C. Hellmich. Upscaling quasi-brittle strength of cement paste and mortar: A multi-scale engineering mechanics model. *Cement and Concrete Research*, 41(5):467–476, 2011. 184, 185

C. Pichler and R. Lackner. Identification of Logarithmic-Type Creep of Calcium-Silicate-Hydrates by Means of Nanoindentation. *Strain*, 45(1):17–25, 2009. ISSN 00392103. doi: 10.1111/j.1475-1305.2008.00429.x. 5, 18

G. Pickett. The Effect of Chang in Moisture-Content on the Creep of Concrete Under a Sustained Load. In *ACI Journal Proceedings*, volume 38. ACI, 1942. 19

W. H. Poisl, W. C. Oliver, and B. D. Fabes. The relationship between indentation and uniaxial creep in amorphous selenium. *Journal of Materials Research*, 10 (8):2024–2032, 1995. 18

T. Powers. The thermodynamics of volume change and creep. *Materials and Structures*, 1(6):487–507, 1968. 27

T. Powers and T. Brownyard. Studies of the physical properties of hardened portland cement paste. *Bulletin*, 22, 1947. 109, 116

R. Raj. Creep in polycrystalline aggregates by matter transport through a liquid phase. *Journal of Geophysical Research: Solid Earth (1978–2012)*, 87(B6): 4731–4739, 1982. 28

N. Ranaivomanana, S. Multon, and A. Turatsinze. Tensile, compressive and flexural basic creep of concrete at different stress levels. *Cement and Concrete Research*, 52(0):1–10, 2013. ISSN 0008-8846. doi: http://dx.doi.org/10.1016/j.cemconres.2013.05.001. 24

F. Renard and P. Ortoleva. Water films at grain-grain contacts: Debye-Hückel, osmotic model of stress, salinity, and mineralogy dependence. *Geochimica et Cosmochimica Acta*, 61(10):1963–1970, 1997. 29

I. Richardson. The nature of the hydration products in hardened cement pastes. *Cement and Concrete Composites*, 22(2):97–113, 2000. 109

I. Richardson. Tobermorite/jennite-and tobermorite/calcium hydroxide-based models for the structure of csh: applicability to hardened pastes of tricalcium silicate, β-dicalcium silicate, portland cement, and blends of portland cement with blast-furnace slag, metakaolin, or silica fume. *Cement and Concrete Research*, 34(9):1733–1777, 2004. 109

J.-M. P. Roland and H. Van Damme. Why does concrete set?: The nature of cohesion forces in hardened cement-based materials. *Mrs Bulletin*, page 319, 2004. 188

P. Rossi, J.-L. Tailhan, F. Le Maou, L. Gaillet, and E. Martin. Basic creep behavior of concretes investigation of the physical mechanisms by using acoustic emission. *Cement and Concrete Research*, 42(1):61–73, 2012. ISSN 0008-8846. doi: http://dx.doi.org/10.1016/j.cemconres.2011.07.011. 28

P. Rossi, J.-L. Tailhan, and F. Le Maou. Creep strain versus residual strain of a concrete loaded under various levels of compressive stress. *Cement and Concrete Research*, 51(0):32–37, 2013a. ISSN 0008-8846. doi: http://dx.doi.org/10.1016/j.cemconres.2013.04.005. 24

P. Rossi, J.-L. Tailhan, and F. Le Maou. Comparison of concrete creep in tension and in compression: Influence of concrete age at loading and drying conditions. *Cement and Concrete Research*, 51(0):78–84, 2013b. ISSN 0008-8846. doi: http://dx.doi.org/10.1016/j.cemconres.2013.04.001. xxv, 16, 19

W. Ruetz. A hypothesis for the creep of hardened cement paste and the influence of simultaneous shrinkage. *Proceedings of the Structure of Concrete and its Behavior under Load*, pages 365–387, 1968. 27

E. H. Rutter. Pressure solution in nature, theory and experiment. *Journal of the Geological Society*, 140(5):725–740, 1983. 28

E. H. Rutter and D. Elliott. The kinetics of rock deformation by pressure solution [and Discussion]. *Philosophical Transactions of the Royal Society of London. Series A, Mathematical and Physical Sciences*, 283(1312):203–219, 1976. 28

W. Saengsoy, T. Nawa, and P. Termkhajornkit. Influence of relative humidity on compressive strength of fly ash cement paste. *Journal of Structural and Construction Engineering*, 73(631):1433–1441, 2008. 60

K. Sakata. Prediction of concrete creep and shrinkage. In *RILEM Proceedings*, pages 649–649. CHAPMAN & HALL, 1993. 22

M. A. Salau. Long-term deformations of laterized concrete short columns. *Building and Environment*, 38(3):469–477, 2003. ISSN 0360-1323. doi: http://dx.doi.org/10.1016/S0360-1323(02)00014-8. 13

J. Salençon. *Viscoélasticité*. Presses de l'Ecole Nationale des Ponts et Chaussées, 1981. 43, 44, 57

P. M. Sargent and M. F. Ashby. Indentation creep. *Materials Science and Technology*, 8(7):594–601, 1992. 18

I. Schrage and R. Springenschmid. Creep and shrinkage data of high-strength concrete. In *Proceedings, 4th International Symposium on High-Strength/High-Performance Concrete*, pages 331–338, 1996. 19

R. Seltzer and Y.-W. Mai. Depth sensing indentation of linear viscoelastic-plastic solids: A simple method to determine creep compliance. *Engineering Fracture Mechanics*, 75:4852–4862, 2008. ISSN 00137944. doi: 10.1016/j.engfracmech.2008.06.012. 18

P. J. Sereda and R. F. Feldman. Compacts of powdered material as porous bodies for use in sorption studies. *Journal of Applied Chemistry*, 13(4):150–158, 1963. 130

P. J. Sereda, R. F. Feldman, and E. G. Swenson. Effect of sorbed water on some mechanical properties of hydrated portland cement pastes and compacts. *Highway Research Board Special Report*, (90), 1966. 130

U. F. J. Shahsavari R. Indentation analysis of fractional viscoelastic solids. *Journal of Mechanics of Materials and Structures*, 4:523–550, 2009. ISSN 15593959. doi: 10.2140/jomms.2009.4.523. 18

E. D. Shchukin and E. A. Amelina. bridging of crystal in the process of hydration of gypsum. In *RILEM Proceedings*, pages 219–233, 1992. 82

H. Shkoukani and J. C. Walraven. Creep and relaxation of concrete subjected to imposed thermal deformations. In *RILEM Proceedings*, page 45. Chapman & Hall, 1993. 23

V. Sicard, J. F. Cubaynes, and G. Pons. Modélisation des déformations différées des bétons à hautes performances: relation entre le retrait et le fluage. *Materials and Structures*, 29(6):345–353, 1996. 11

L. Skinner, S. Chae, C. Benmore, H. Wenk, and P. Monteiro. Nanostructure of calcium silicate hydrates in cements. *Physical Review Letters*, 104(19):195502, 2010. 109

F. O. Slate and K. C. Hover. Microcracking in concrete. In *Fracture mechanics of concrete: Material characterization and testing*, pages 137–159. Springer, 1984. 27

I. N. Sneddon. The relation between load and penetration in the axisymmetric boussinesq problem for a punch of arbitrary profile. *International Journal of Engineering Science*, 3(1):47–57, 1965. 41

I. Soroka and P. J. Sereda. The structure of cement-stone and the use of compacts as structural models. 1970. xxix, 130, 131

N. Stilwell and D. Tabor. Elastic recovery of conical indentations. *Proceedings of the Physical Society*, 78(2):169, 1961. 40

D. Tabor. *The hardness of metals*. Oxford university press, 2000. 43

H. Takagi, M. Dao, and M. Fujiwara. Creep characterization of power-law materials through pseudosteady indentation tests and numerical simulations. *Journal of Physics Conference Series*, 240:12064, 2010. 18

B. T. Tamtsia and J. J. Beaudoin. Basic creep of hardened cement paste A re-examination of the role of water. *Cement and Concrete Research*, 30(9): 1465–1475, Sept. 2000. ISSN 00088846. doi: 10.1016/S0008-8846(00)00279-9. xxv, 13, 21, 22, 155

H. F. Taylor. Proposed structure for calcium silicate hydrate gel. *Journal of the American Ceramic Society*, 69(6):464–467, 1986. 109

H. F. Taylor. *Cement chemistry*. Thomas Telford, 1997. 22, 114, 134

E.-i. Tazawa. Autogenous shrinkage of concrete. In *Proceeding of the international workshop organized by JCI, New York*, 1998. 11

E.-i. Tazawa and S. Miyazawa. Influence of cement and admixture on autogenous shrinkage of cement paste. *Cement and Concrete Research*, 25(2):281–287, 1995. 11

P. D. Tennis and H. M. Jennings. A model for two types of calcium silicate hydrate in the microstructure of portland cement pastes. *Cement and Concrete Research*, 30(6):855–863, 2000. 10

N. A. Testwell and D. Tabor. Elastic recovery of conical indentations. *Proceedings of the Physical Society*, 78(2):169, 1961. xxv, 17

R. Tewari, G. K. Dey, T. R. G. Kutty, A. K. Sengupta, N. Prabhu, and S. Banerjee. Deformation behavior of Zr3Al-Nb alloys II: Indentation creep studies. *Metallurgical and Materials Transactions aPhysical Metallurgy and Materials Science*, 35A:205–216, 2004. ISSN 10735623. 18

F. G. Thomas. Creep of concrete under load. *International Association of Testing Materials, London, UK*, pages 292–294, 1937. 27

J. J. Thomas, S. A. FitzGerald, D. A. Neumann, and R. A. Livingston. State of water in hydrating tricalcium silicate and portland cement pastes as measured by quasi-elastic neutron scattering. *Journal of the American Ceramic Society*, 84(8):1811–1816, 2001. 109

P. J. Tikalsky, P. M. Carrasquillo, and R. L. Carrasquillo. Strength and durability considerations affecting mix proportioning of concrete containing fly ash. *ACI Materials Journal*, 85(6), 1988. 25

F. Toutlemonde and F. Le Maou. Protection des éprouvettes de béton vis-à-vis de la dessiccation -Le point sur quelques techniques de laboratoire. *Bulletin des Laboratoires des Ponts et Chaussées*, 203:105–119, 1996. 77

F.-J. Ulm, F. Le Maou, and C. Boulay. Creep and shrinkage coupling: new review of some evidence. *Revue Française de Génie Civil*, 3(3-4):21–37, 1999. 13, 66

M. Vandamme. *The nanogranular origin of concrete creep: a nanoindentation investigation of microstructure and fundamental properties of calcium-silicate-hydrates*. PhD thesis, Massachusetts Institute of Technology, 2008. xxv, 5, 9, 48

M. Vandamme and F.-J. Ulm. Viscoelastic solutions for conical indentation. *International Journal of Solids and Structures*, 43:3142–3165, 2006. ISSN 00207683. doi: 10.1016/j.ijsolstr.2005.05.043. 18

M. Vandamme and F.-J. Ulm. Nanogranular origin of concrete creep. *Proceedings of the National Academy of Sciences*, 106(26):10552–10557, 2009. 5, 18, 75, 123

M. Vandamme and F.-J. Ulm. Nanoindentation investigation of creep properties of calcium silicate hydrates. *Cement and Concrete Research*, 52(0):38 – 52, 2013. ISSN 0008-8846. doi: http://dx.doi.org/10.1016/j.cemconres.2013.05.006. 5, 18, 69, 79, 179

M. Vandamme, C. A. Tweedie, G. Constantinides, F.-J. Ulm, and K. J. Van Vliet. Quantifying plasticity-independent creep compliance and relaxation of viscoelastoplastic materials under contact loading. *Journal of Materials Research*, 27:302–312, 2011. ISSN 08842914. doi: 10.1557/jmr.2011.302. 46, 47, 48

L. Vandewalle. Concrete creep and shrinkage at cyclic ambient conditions. *Cement and Concrete Composites*, 22(3):201–208, 2000. 19, 21

M. R. VanLandingham. Review of instrumented indentation. *Journal of Research of the National Institute of Standards and Technology*, 108(4), 2003. 4

M. R. VanLandingham, N. K. Chang, P. L. Drzal, C. C. White, and S. H. Chang. Viscoelastic characterization of polymers using instrumented indentation. I. Quasi-static testing. *Journal of Polymer Science Part B: Polymer Physics*, 43:1794–1811, 2005. ISSN 08876266. doi: 10.1002/polb.20454. 18

K. Velez, S. Maximilien, D. Damidot, G. Fantozzi, and F. Sorrentino. Determination by nanoindentation of elastic modulus and hardness of pure constituents of portland cement clinker. *Cement and Concrete Research*, 31(4):555–561, 2001. 189

M.-H. Vu, J. Sulem, S. Ghabezloo, J.-B. Laudet, A. Garnier, and S. Guédon. Time-dependent behaviour of hardened cement paste under isotropic loading. *Cement and Concrete Research*, 42(6):789–797, 2012. 22

T.-S. Vu, G. Ovarlez, and X. Chateau. Macroscopic behavior of bidisperse suspensions of noncolloidal particles in yield stress fluids. *Journal of Rheology*, 54 (4):815, 2010. ISSN 01486055. doi: 10.1122/1.3439731. xxvii, 72, 74, 75, 78

F. J. Wang, X. Ma, and Y. Y. Qian. Indentation rate-dependent creep behavior of Sn-Ag-Cu Pb-free ball grid array (BGA) solder joint. *Materials Science Forum*, 502:399–404, 2005. 18

R. Wendner, M. Hubler, and Z. Bažant. The B4 model for multi-decade creep and shrinkage prediction. *CONCREEP-9, MIT*, 2013. 30

P. K. Weyl. Pressure solution and the force of crystallization: A phenomenological theory. *Journal of Geophysical Research*, 64(11):2001–2025, 1959. 28

K. Wiegrink, S. Marikunte, and S. P. Shah. Shrinkage cracking of high-strength concrete. *ACI Materials Journal*, 93(5), 1996. 25

F. Wittmann. Influence of moisture content on the creep of hardened cement. *Rheologica Acta*, 9(2):282–87, 1970. 6, 155

World Business Council for Sustainable Development. Sustainability benefits of Concrete, 2013. 3

G. P. York, T. W. Kennedy, and E. S. Perry. *Experimental investigation of creep in concrete subjected to multiaxial compressive stresses and elevated temperatures*. Department of Civil Engineering, University of Texas at Austin, 1970. 22

A. Zaoui. Continuum micromechanics: survey. *Journal of Engineering Mechanics*, 128(8):808–816, 2002. 175

C. Zhang, Y. Zhang, K. Zeng, and L. Shen. Nanoindentation of polymers with a sharp indenter. *Journal of materials research*, 20(06):1597–1605, 2005. 18

K. Zhang, J. R. Weertman, and J. A. Eastman. The influence of time, temperature, and grain size on indentation creep in high-purity nanocrystalline and ultrafine grain copper. *Applied Physics Letters*, 85(22):5197–5199, 2004. 18